Bacterial Cellulose For Use in: Hierarchical Composites, Macroporous Foams, Bioinorganic Nanohybrids and Bacterial-Based Nanocomposites



Anthony Abbott

Department of Chemical Engineering and Chemical Technology

Imperial College London

Submitted in part fulfilment of the requirements for the degree of Doctor of Philosophy of Imperial College London and the Diploma of Imperial College,

2011 February

Abstract

The growing environmental awareness and the not so distant scarcity of fossil feedstocks are promoting nowadays a renewed interest in the use of renewable raw materials derived from biomass, *i.e.*, cellulosic products. Recently, a relatively novel type of cellulose product namely, bacterial cellulose, biosynthesised by cellulose-producing bacteria *Gluconobacter xylinus*, has appeared as a promising raw material for the development of advanced renewable (nano-) materials owing to its outstanding properties such as inherent nanosize (width: 1 to 25 nm; length: 1 to 9 μm), high degree of crystallinity (70% to 90%) and impressive mechanical properties (Young's modulus: 78 to 155 GPa).

This thesis describes the preparation of different types of renewable (nano-) materials composed of bacterial cellulose, which includes all-cellulose hierarchical composites, macroporous cryogel microspheres, functional bioinorganic nanohybrids and entirely bacterial-based nanocomposites.

Bacterial cellulose was deposited around the surface of sisal fibres by *Gluconobacter xylinus*, which resulted in a dense bacterial cellulose coating of the surfaces of sisal fibres. Furthermore, the bacterial cellulose coated sisal fibres obtained after surface modification of fibres enhanced the mechanical performance of all-cellulose hierarchical composites owing to an improvement of the quality of the sisal fibres-regenerated cellulose matrix interface.

Bacterial cellulose nanofibrils were dissolved in DMAc/LiCl cosolvent, then templated into a microsphere shape, regenerated in H_2O and freeze-dried to obtain highly porous cryogel microspheres composed exclusively of regenerated bacterial cellulose, which possessed a Brunauer-Emmet-Teller (BET) surface area ranging from 55 m^2/g to 123 m^2/g.

Thioether functionalised bacterial cellulose nanofibrils were synthesised using a "grafting from" approach during the free radical grafting polymerisation of a

monomer containing thioether moieties, namely 2-(methylthio)ethyl methacrylate. The thioether moieties grafted from the bacterial cellulose (MTEMA-g-BC) nanofibrils subsequently enabled the preparation of optically functional bioinorganic nanohybrids, where either gold nanoparticles or cadmium telluride quantum dots were chemisorbed onto the thioether moieties functionalised bacterial cellulose nanofibrils.

Hydrophobised bacterial cellulose nanofibrils were also synthesised using the same "grafting from" approach using free radical grafting polymerisation of a hydrophobic caprolactone-based macromonomer, caprolactone 2- (methacryloyloxy)ethyl ester. Then, entirely bacterial-based nanocomposites composed of caprolactone grafted bacterial cellulose (PCLMA-g-BC) nanofibrils reinforced poly(3- hydroxybutyrate) (PHB) matrix were produced by solution casting. The tensile strength and Young's modulus of bacterial-based nanocomposites reinforced with PCLMA-g-BC nanofibrils (*i.e.*, nanofiller content of 10 wt./wt.%) increased by 101% and 170%, respectively, as compared to the neat PHB film.

The findings reported in this thesis highlight the potential and versatility of bacterial cellulose to produce novel and innovative types of renewable advanced (nano-) materials and composites.

Declaration

This dissertation is a description of the work carried out by the author in the Department of Chemical Engineering, Imperial College London, United Kingdom between October 2006 and June 2010 under the supervision of Prof. Alexander Bismarck. Except where acknowledged, the material is the original work of the author and includes nothing, which is the outcome of work in collaboration, and no part of it, has been submitted for a degree at this or any other university.

Anthony Abbott

Acknowledgements

First off all, I would like to thank Prof. Alexander Bismarck, my academic supervisor, for the great freedom he has given me during my PhD research and his great enthusiasm and support. Also, I would like to acknowledge Alexander for his feedback and patience while reviewing the present manuscript and correcting our papers. I also remember his keenness to have me embarked on this PhD research within the Polymer and Composite Engineering (PaCE) group, it has been quite a journey punctuated by enriching experiences, exciting knowledge and learning, it has been worthwhile.

I would like to thank the Challenging Engineering Programme (EP/E007538/1) of the UK Engineering and Physical Sciences Research Council (EPSRC) for supporting the research and "Le Conseil Regional de la Martinique" for financial support.

I am also grateful to the following academics who kindly allowed me to use their laboratories or/and equipment: Prof. Athanasios Mantalaris, Prof. Sergei Kazarian, Dr. Jerry Heng, Dr. Daryl Williams and Prof. Milo Shaffer.

I would like to express my gratitude to Dr. Julasak Juntaro and Dr. Marion Pommet for their help and guidance while I was discovering this rather new and exciting research field on renewable (nano-) composite materials.

I am indeed grateful to Dr. Jonathan Blaker, Nadiene Graeber, Dr. Kingsley Ho, Dr. Steven Lamoriniere, Koon Yang Lee, Dr. Angelika Menner, Dr. Robert Menzel, Dr. Francesca Palombo, Dr. Gabriela Salejova, Dr. Natasha Shirshova, Dr. Feng Tay, Dr. Michael Tran and George Duo Wang (by alphabetical order), for the interesting and instructive discussions, as well as, for sharing their diverse experiences and vast knowledge with me over the years. Great regards are directed to all PaCE group members past and present, for their advice and constructive exchanges.

I would like to thank my office colleagues for the nice and fun atmosphere while studying Dr. James Griffin, Michelle Lewis, Dr. Ruth Blackwell, Dr. Shu San Manley, Dr. Jonathan Blaker, Dr. Yuan-Min Lin, Nadine Graeber, Ling Ching Wong and Qixiang Jiang (in chronological order). A warm thanks to all the friends have made during all those years both at Imperial College and in London Gabriela, Steven, Juntaro (Jay), Kingsley, Charnwit (Jo), Ivan, Rio, Vivian, Shu San, Hazel, Feng, George, Jonny, Michael, Henri, Tomi, Jasper, Irene, Giulia,... and Rotaract friends, for the great time, fun, euphoria and hardship. Their names are too many to mention everyone.

I would also thank Sarah Payne, Susi Underwood, Anusha Sri-Pathmanathan, Aleksandra Szymanska, Sripriya Niranjan, Patricia Carry, Tawanda Nyabango, Keith Walker, Pim Amrit and Joseph Meggyesi, for having dealt with my numerous and various requests over the years, which often resulted in a positive outcome or fair agreement.

I would like to express my special and deepest thanks to my dearest parents for supporting and encouraging me since I left my brothers, my house and home country "Martinique" in 2001 to pursue such a long and exciting academic journey, as well as personal growth and development. Thank you mother for your unconditional support, listening and wise advice along that tortuous path and not the least father for your never resting and always pushing spirit, as well as for your very pragmatic and concise points of view but nevertheless very wise, indeed. I feel very much indebted and grateful towards both of you for your unquantifiable help.

Contents

List of Figures **xi**

List of Tables **xx**

Nomenclature **xxiii**

1 General Introduction **1**

1.1 Research context 1

1.2 Motivation 3

1.3 Roadmap of the thesis 3

2 Methods **5**

2.1 Optical density 6

2.2 ATR-FTIR spectroscopy 7

2.3 UV-Vis spectroscopy 8

2.4 Particle sizing 9

2.5 X-ray diffraction 10

2.6 BET surface area 11

2.7 Elemental analysis 13

2.8 Thermogravimetric analysis 13

2.9 Differential scanning calorimetry 14

2.10 Dynamic mechanical thermal analysis 15

2.11 Mechanical testing of tensile properties 17

2.12 Scanning electron microscopy 18

2.13 Dynamic vapour sorption 19

2.14 Summary of analytical methods 19

3 Production of Bacterial Cellulose **21**

3.1 Introduction 21

3.1.1 Aims and objectives 21

3.1.2 Sources of cellulose materials 22

3.1.3 Source of bacterial cellulose 23

3.1.4 Biosynthesis of bacterial cellulose 24

3.1.5 Fermentation process of *Gluconobacter xylinus* for biosynthesis of BC 26

3.1.6 Properties of bacterial cellulose 27

3.1.7 Applications of bacterial cellulose 29

3.2 Experimental 30

3.2.1 Materials 30

3.2.2 Cultivation of *Gluconobacter xylinus* bacteria 30

3.2.3 Conditions for bacterial cellulose production 32

3.3 Characterisation of *Gluconobacter xylinus* and biosynthesised BC 33

3.3.1 Biosynthesised bacterial cellulose 33

3.3.2 BC productivity and growth of *Gluconobacter xylinus* population . . . 35

3.3.3 Improvement of BC production using a bioreactor 35

3.4 XRD characterisation of BC cultured in different culture conditions 38

3.5 ATR-FTIR characterisation of biosynthesised BC 38

3.6 Thermal degradation of biosynthesised BC 41

3.7 Conclusions 44

3.8 Future work 45

4 Self-Reinforced Cellulose Nanocomposites & Bacterial Cellulose Coated Sisal Fibres Reinforced Cellulose Composites **46**

4.1 Introduction 46

4.1.1 Aims and objectives 46

4.1.2 Sustainable composite materials 47

4.1.3 All-cellulose nanocomposites and composites 48

4.1.4 Dissolution of cellulose 48

4.1.5 Properties of sisal fibres 49

4.1.6 Modification of natural fibre/matrix interface 51

4.2 Experimental 52

4.2.1 Materials . . . 52
4.2.2 Preparation of self-reinforced cellulose nanocomposites . . . 53
4.2.3 BC coating of sisal fibres using *Gluconobacter xylinus* bacteria . . . 54
4.2.4 Preparation of hierarchical all-cellulose composites . . . 54
4.3 Characterisation of self-reinforced regenerated cellulose nanocomposites . . . 55
4.3.1 Crystallinity evolution in self-reinforced regenerated cellulose nanocomposites . . . 55
4.3.2 Investigation of the crystallinity of regenerated cellulose using ATR-FTIR spectroscopy . . . 58
4.3.3 Thermal behaviour of self-reinforced regenerated cellulose nanocomposites . . . 59
4.3.4 Dynamic mechanical analysis of self-reinforced regenerated cellulose nanocomposites . . . 62
4.3.5 Mechanical properties of self-reinforced regenerated cellulose nanocomposites . . . 63
4.3.6 SEM observation of fracture surfaces of self-reinforced of regenerated cellulose nanocomposites . . . 65
4.3.7 Moisture uptake behaviour of self-reinforced regenerated cellulose nanocomposites . . . 67
4.4 Characterisation of hierarchical all-cellulose composites . . . 69
4.4.1 Surface morphology of sisal fibres and BC-coated sisal fibres. . . . 69
4.4.2 XRD characterisation of sisal fibres and BC-coated sisal fibres . . . 70
4.4.3 Mechanical properties of single (modified) sisal fibres . . . 72
4.4.4 Dynamic mechanical analysis of hierarchical all-cellulose composites . 72
4.4.5 Mechanical properties of hierarchical all-cellulose composites . . . 73
4.4.6 SEM observation of fracture surfaces of hierarchical all-cellulose composites . . . 75
4.5 Conclusions . . . 77
4.6 Future work . . . 79

5 Regenerated Bacterial Cellulose Cryogels: Microsphere Templating and Morphology of Porous Structure 81
5.1 Introduction . . . 81

5.1.1 Aims and objectives . . . 81
5.1.2 Introduction to highly porous materials . . . 82
5.1.3 Various preparation routes to highly porous aerogel-like materials . . . 83
5.1.4 Applications of aerogels . . . 85
5.1.5 Cellulose-based porous materials: state of the art . . . 85
5.1.5.1 Cellulose aerogels . . . 86
5.1.5.2 Aerogels made from cellulose derivatives . . . 87
5.1.5.3 Bacterial cellulose aerogel . . . 87
5.1.6 Manufacturing routes to highly porous cellulose materials . . . 88
5.1.6.1 Preparation of cellulose precursors for aerogels . . . 88
5.1.7 Potential applications of porous microspheres . . . 89
5.2 Experimental . . . 90
5.2.1 Materials . . . 90
5.2.2 Preparation of regenerated BC cryogel microspheres . . . 90
5.2.3 Schematic of preparation of regenerated BC cryogel microspheres . . . 91
5.3 Characterisation of BC cryogels and regenerated BC microspheres . . . 93
5.3.1 X-ray diffraction of regenerated BC cryogel microspheres . . . 93
5.3.2 ATR-FTIR spectroscopy of regenerated BC cryogel microspheres . . . 95
5.3.3 Thermal degradation of regenerated BC porous microspheres . . . 96
5.3.4 Nitrogen sorption isotherm for regenerated BC cryogel microspheres . 97
5.3.5 SEM observation of regenerated BC cryogel microspheres . . . 99
5.4 Conclusions . . . 105
5.5 Future work . . . 105

6 Bacterial Cellulose-based Bioinorganic Nanohybrids 107
6.1 Introduction . . . 107
6.1.1 Aims and objectives . . . 107
6.1.2 Introduction to (bio)organic-inorganic materials . . . 108
6.1.3 Routes to organic-inorganic hybrid materials . . . 109
6.1.4 Cellulose-based bioinorganic hybrid materials: state of the art . . . 110
6.1.5 Applications of bioinorganic hybrid materials . . . 114
6.2 Experimental . . . 116
6.2.1 Materials . . . 116

6.2.2 Preparation of 2-(methylthio)ethyl methacrylate (MTEMA) grafted BC nanofibrils . . . 116
6.2.3 Schematic of free radical grafting polymerisation of MTEMA from BC nanofibrils . . . 117
6.2.4 Synthesis of Au nanoparticles and preparation of MTEMA-g-BC-Au nanohybrids . . . 118
6.2.5 Synthesis of CdTe quantum dots and preparation of MTEMA-g-BC-CdTe nanohybrids . . . 120
6.2.6 Preparation of photoluminescent nanocomposites containing MTEMA-g-BC-CdTe nanohybrids . . . 123
6.3 Characterisation of MTEMA-g-BC Nanofibrils . . . 124
6.3.1 Evolution of X-ray diffraction of cerium (IV) oxidised BC nanofibrils . 124
6.3.2 Evolution of X-ray diffraction of MTEMA-g-BC nanofibrils . . . 125
6.3.3 ATR-FTIR spectroscopy of MTEMA-g-BC nanofibrils . . . 126
6.3.4 Elemental analysis of MTEMA-g-BC nanofibrils . . . 131
6.3.5 Thermal degradation behaviour of MTEMA-g-BC nanofibrils . . . 132
6.3.6 SEM observation of MTEMA-g-BC nanofibrils . . . 133
6.4 Characterisation of MTEMA-g-BC-Au Nanohybrids . . . 136
6.4.1 UV-Vis spectroscopy of MTEMA-g-BC-Au nanohybrids . . . 136
6.4.2 SEM of MTEMA-g-BC-Au nanohybrids . . . 140
6.5 Characterisation of MTEMA-g-BC-CdTe Nanohybrids . . . 142
6.5.1 UV-Vis spectroscopy of CdTe quantum dots . . . 144
6.5.2 UV-Vis of MTEMA-g-BC-CdTe nanohybrids . . . 145
6.5.3 SEM of MTEMA-g-BC-CdTe nanohybrids . . . 146
6.6 Observation of photoluminescent nanocomposite films containing MTEMA-g-BC-CdTe nanohybrids . . . 148
6.7 Conclusions . . . 150
6.8 Future work . . . 152

7 Bacterial-Based Nanocomposites: Hydrophobised Bacterial Cellulose Nanofibril Reinforced Poly−3−Hydroxybutyrate 153
7.1 Introduction . . . 153
7.1.1 Aims and objectives . . . 153

7.1.2 Introduction to renewable-based nanocomposites reinforced with cellulosic nanofillers . . . 154
7.1.3 Bacterial−based nanocomposite materials: state of the art . . . 156
7.1.4 Surface hydrophobicity of cellulose-based materials: state of the art . 158
7.1.5 Bacterial−synthesised biopolymers: polyhydroxyalkanoates as advanced materials . . . 159
7.2 Experimental . . . 161
7.2.1 Materials . . . 161
7.2.2 Preparation of polycaprolactone 2−(methacryloyloxy)ethyl ester grafted BC nanofibrils . . . 162
7.2.3 Schematic of free radical grafting polymerisation of PCLMA from BC nanofibrils . . . 163
7.2.4 Preparation of PCLMA−g−BC nanofibril reinforced PHB nanocomposites . . . 163
7.2.5 Schematic of preparation of PCLMA-g-BC/PHB nanocomposites . . . 164
7.3 Characterisation of PCLMA−g−BC nanofibrils . . . 165
7.3.1 Crystallinity evolution of PCLMA−g−BC nanofibrils . . . 165
7.3.2 ATR-FTIR spectroscopy of PCLMA−g−BC nanofibrils . . . 169
7.3.3 Elemental analysis of PCLMA−g−BC nanofibrils . . . 170
7.3.4 Thermal degradation of PCLMA−g−BC nanofibrils . . . 171
7.3.5 Surface characterisation of PCLMA−g−BC nanofibrils . . . 173
7.3.6 Surface morphology of PCLMA−g−BC nanofibrils . . . 174
7.4 Characterisation of bacterial-based nanocomposite films with PCLMA-g-BC nanofibrils . . . 176
7.4.1 Thermal behaviour of PCLMA−g−BC nanofibril reinforced PHB nanocomposites . . . 176
7.4.2 Dynamic mechanical analysis of PCLMA−g−BC nanofibril reinforced PHB nanocomposites . . . 177
7.4.3 Mechanical properties of PCLMA−g−BC nanofibril reinforced PHB nanocomposites . . . 180
7.5 Conclusions . . . 182
7.6 Future work . . . 184

8 General Conclusions **185**

8.1 Biosynthesis of bacterial cellulose by *Gluconobacter xylinus* BPR2001 185

8.2 Surface modification of sisal by bacterial cellulose coating and preparation of hierarchical all-cellulose composites 186

8.3 Preparation of bacterial cellulose based porous cryogel microspheres 186

8.4 Thioether functionalisation of bacterial cellulose and synthesis of bioinorganic nanohybrids 187

8.5 Hydrophobisation of bacterial cellulose nanofibrils and processing of bacterial-based nanocomposites 188

8.6 Concluding remarks 188

References 190

List of Figures

1.1 Summary of the annual number of scientific publications related to cellulose-based materials from the year 2000 to 2010 indexed within the Web of Science®. The keywords for the search included the combination of the terms: cellulose, nanocomposite, composite, hybrid and functional, while excluding the terms: lignin, chitin, chitosan and starch. 2

2.1 Schematic description of electronic cloud displacements in nanoparticles in an electromagnetic wave (reproduced from [1]). 9
2.2 DMA principle, stress-strain relationship for linear viscoelastic material. . . . 17

3.1 Molecular structure of cellulose (n=DP, degree of polymerisation) (reproduced from [2]). 23
3.2 Schematic diagrams of (**a**) antiparallel orientation and (**b**) all-parallel orientation. All polymer chains within the same stack or sheet are parallel (reproduced from [3]). 23
3.3 The cellulose and *Gluconobacter xylinus* cell in an H&S medium a.) A negatively stained cell producing a cellulose ribbon. The ribbon is formed parallel to the longitudinal axis of the cell. b.) Higher magnification of cellulose ribbons showing striations and twists (arrow). c.) A negatively stained cellulose ribbon prepared by rapid-freeze and substitution (RFS) method. d.) A shadowed cellulose ribbon. Scale bars: 0.5 (a) and 0.2 (b-d) μm. (reproduced from [4]) 25

3.4 Generalised model of ribbon assembly in *Gluconobacter xylinus*, showing a possible mechanism of origin of microfibrils and separate fibrillar subunits within the ribbon. Shown in the boxes are possible packing arrangements of the 1.5-nm tactoidal aggregates (reproduced from [5]). 26
3.5 Shape of biosynthesised BC by *Gluconobacter xylinus* BPR2001 after 3 d of culture at $30°C$ under; a) static Erlenmeyer flask; b) agitated Erlenmeyer flask. 28
3.6 a) Photograph of Erlenmeyer flasks placed onto an orbital shaker in the case of agitated culture; b) Photograph of instrumented-bioreactor equipped with feedback control-loop. 33
3.7 SEM micrographs of dried BC pellicle with attached *Gluconobacter xylinus* cells after 7 d of static culture. 34
3.8 SEM micrographs of dehydrated BC nanofibrils after 7 d of static culture and subsequent treatment with 0.1 N NaOH to lyse *Gluconobacter xylinus* cells (Section 3.2.2). 34
3.9 BC productivity, growth of *Gluconobacter xylinus* bacteria and variation of pH in the case of agitated culture in Erlenmeyer flasks using modified H&S culture medium. 36
3.10 Photographs of bioreactor vessel with different internal configurations. a) standard configuration; b,c) modified configuration with additional stainless-steel meshes to create a greater surface area. 37
3.11 X-ray diffractogram of dried biosynthesised BC produced by *Gluconobacter xylinus* cultured in various conditions: static, agitated and in a bioreactor, respectively. 39
3.12 ATR-FTIR spectra of biosynthesised BC in various culture conditions namely, static, agitated and in a bioreactor. 42
3.13 **I**) Thermal degradation in N_2 atmosphere of BC cultured in static, agitated Erlenmeyer flask and in a bioreactor. **II**) Derivative weight loss in N_2 atmosphere of BC synthesised in static, agitated Erlenmeyer flask and in a bioreactor. 43

4.1 Classification of various cellulose solvents (reproduced from [6]). 50
4.2 a) Structure of natural plant fibre (reproduced from [7]); b) Schematic of cross-section of a flax fibre (reproduced from [8]) 51
4.3 Schematic of preparation of hierarchical all-cellulose composites. 54

4.4 X-ray diffractogram of received microcrystalline cellulose powder and self-reinforced regenerated cellulose regenerated from DMAc/LiCl cosolvent after increasing dissolution times and amorphous regenerated cellulose obtained by dissolution of 1 wt./v.% of MCC in DMAc/LiCl for 48 h and subsequent regeneration. 56
4.5 Degree of crystallinity as determined using Segal's equation and crystal size of self-reinforced regenerated cellulose as determined using the Scherrer's equation as a function of dissolution time of MCC in DMAc/LiCl cosolvent 57
4.6 ATR-FTIR spectra of self-reinforced regenerated cellulose with different degree of crystallinity. 60
4.7 Change in degree of crystallinity of self-reinforced regenerated cellulose defined by ATR-FTIR A_{1430}/A_{900} ratio as a function of degree of crystallinity measured by XRD. 60
4.8 Modification of cellulose crystal polymorph type-I to type-II as characterised by ATR-FTIR A_{1370}/A_{670} ratio as a function of degree of crystallinity of self-reinforced regenerated cellulose. 61
4.9 Weight loss due to thermal degradation in N_2 as a function of temperature of microcrystalline and self-reinforced regenerated cellulose as a function of degree of crystallinity. 62
4.10 Change of flexural E' modulus of self-reinforced regenerated cellulose at different degree of crystallinity 64
4.11 Ultimate tensile strength and Young's modulus of self-reinforced regenerated cellulose conditioned at 65% RH as a function of the degree of crystallinity. . 66
4.12 Work to fracture of self-reinforced regenerated cellulose tested in tensile mode with respect to degree of crystallinity. 66
4.13 SEM micrographs of cryo-fractured surface of self-reinforced regenerated cellulose at different degree of crystallinity: 66% for a & b); 38% for c & d). . . 68
4.14 Moisture absorption profiles for self-reinforced regenerated cellulose at 95% RH for different degree of crystallinity. 69
4.15 **a** & **c**) SEM micrograph of sisal fibres after autoclaving, soaking for 7 d in culture medium and after NaOH treatment; **b** & **d**) SEM micrograph of BC-coated sisal fibres, where the BC coating was obtained using the procedure described in Section 4.2.3. 70

4.16 Effect of BC coating procedure on crystallinity of sisal fibres. (a) Original sisal; (b) NaOH treated sisal; (c) BC-coated and NaOH treated sisal; and (d) BC nanofibrils extracted from BC pellicle and NaOH treated. 71
4.17 Change of flexural E' modulus of all-cellulose composites reinforced with: a) original sisal fibres; b) BC-coated sisal fibres. 74
4.18 Photograph of typical tensile test coupons of hierarchical all-cellulose composite reinforced with BC-coated sisal fibres with a fibre fraction of 40 wt./wt.%: top, before testing; bottom, after testing. 75
4.19 Tensile strength of all-cellulose composites as a function of degree of crystallinity of regenerated cellulose matrix and sisal fibre reinforcement (40 wt./wt.%). 76
4.20 Young's modulus of all-cellulose composites as a function of degree of crystallinity of regenerated cellulose matrix and sisal fibre reinforcement (40 wt./wt.%). 76
4.21 Typical SEM micrograph of a fracture surface of all-cellulose cellulose composites reinforced with: **a**, sisal fibres and **b**, BC-coated sisal fibres (fibre fraction of 40 wt./wt.%). 78

5.1 Description of the sol-gel process by Pajonk: (a) sol; (b) gel[9]. 84
5.2 Scanning electron microscopy micrograph at various magnifications (x200, x500, x3 000; from left to right) of a $scCO_2$ dried aerogel from bacterial cellulose[10]. 88
5.3 Schematic setup for preparation of regenerated BC cryogel microspheres. . . . 92
5.4 X-ray diffractogram of freeze-dried BC, amorphous regenerated BC and regenerated BC cryogel microsphere at BC concentration of 2.5 wt.% and 5 wt.% for 1 h of dissolution in DMAc/LiCl. 94
5.5 ATR-FTIR spectra of freeze-dried BC and regenerated BC cryogel microspheres at various dissolution time and BC concentration of 2.5 wt.% and 5 wt.%. 96
5.6 **I**) Thermal degradation of freeze-dried BC and regenerated BC cryogel microspheres in N_2 atmosphere for BC concentration of 2.5 wt.%/ and 5 wt.%. **II**) Derivative weight loss of freeze-dried BC and regenerated BC cryogel microspheres in N_2 atmosphere for BC concentration of 2.5 wt.%/ and 5 wt.%. . . 97

5.7 **I**) N_2 adsorptiondesorption at 77K for Freeze-dried BC (a), rBC cryogel microspheres with a BC concentration of 2.5 wt.% (b) and 5 wt.% (c). **II**) BJH pore size distribution (N_2 adsorption) obtained for freeze-dried BC and rBC cryogel microspheres. 100
5.8 SEM micrographs at various magnifications of surface of rBC cryogel microspheres with a BC concentration of 2.5 wt.% after 1 h of dissolution in DMAc/LiCl. With **a**) x100; **b**) x500; **c**) x5K and **d**) x10K. 102
5.9 SEM micrographs at various magnifications (x100 and x2K; from left to right) of surface and cross-section (inserts) of rBC cryogel microspheres with a BC concentration of 5 wt.% for different dissolution time in DMAc/LiCl. With: **a** & **b**) for 1h; **c** & **d**) for 2 h and **e** & **f**) for 4 h, respectively. 103
5.10 SEM micrographs at various magnifications (x250 and x2.5K; from left to right) of both surface and cross-section of amorphous rBC cryogel microsphere with a BC concentration of 2.5 wt.% after 24 h of dissolution in DMAc/LiCl. 104
5.11 SEM micrographs at various magnifications (x2.5K, x10K and x50k; from left to right) of a pore cross-section of amorphous rBC cryogel microsphere with a BC concentration of 2.5 wt.% after 24 h of dissolution in DMAc/LiCl. 104

6.1 Schematic of the synthetic routes for the development of organic-inorganic hybrid materials (reproduced from reference [11]). 110
6.2 Schematic of free radical grafting from BC polymerisation reaction of 2−(methylthio) ethyl methacrylate. **a**) Initiation phase and free radical formation; **b**) propagation phase. 118
6.3 Schematic of preparation of MTEMA-g-BC-Au nanohybrids obtained by *in situ* immobilisation of Au NPs during Au NPs synthesis in the presence of MTEMA-g-BC nanofibrils. **a**) aqueous suspension of MTEMA-g-BC; **b**) nucleation step of Au NPs by reduction of Au^{3+} to Au^{+} by addition of $Na_3C_6H_5O_7{\cdot}2H_2O$; **c**) thermal growth of Au NPs in presence of MTEMA-g-BC and **d**) formation of MTEMA-g-BC-Au nanohybrid by chemisorption of Au NPs to MTEMA-g-BC nanofibrils. 121
6.4 Schematic of preparation of MTEMA-g-BC-CdTe nanohybrids obtained by transfer of CdTe QDs to MTEMA-g-BC via ligand exchange in acetone between thioglycolic acid and thioether moieties. 123

6.5 X-ray diffractograms of HCl hydrolysed BC and CAN oxidised BC nanofibrils. 127
6.6 X-ray diffractograms of HCl hydrolysed BC and MTEMA-g-BC nanofibrils at various concentration of MTEMA & CAN). 127
6.7 ATR-FTIR spectra HCl hydrolysed BC and CAN oxidised BC nanofibrils as a function of concentration of CAN. 130
6.8 ATR-FTIR spectra of HCl hydrolysed BC and MTEMA-g-BC nanofibrils at various concentrations of MTEMA and CAN. 130
6.9 **I**) Thermal degradation behaviour of HCl hydrolysed BC and CAN oxidised BC nanofibrils (CAN conc. 1 & 2.5 mmol) in N_2 atmosphere. **II**) Derivative weight loss of HCl hydrolysed BC and CAN oxidised BC nanofibrils (CAN conc. 1 & 2.5 mmol) in N_2 atmosphere. 134
6.10 **I**) Thermogravimetric analysis of HCl hydrolysed BC and MTEMA-g-BC nanofibrils at various concentrations of MTEMA: 1, 5 and 10 mmol & CAN: 1 and 2.5 mmol in N_2 atmosphere. **II**) Derivative weight loss of HCl hydrolysed BC and MTEMA-g-BC nanofibrils at various concentrations of MTEMA: 1, 5 and 10 mmol & CAN: 1 and 2.5 mmol) in N_2 atmosphere. 135
6.11 SEM micrographs of: $\mathbf{a}, \mathbf{b}$) HCl hydrolysed BC nanofibrils, as prepared in Chapter 3; $\mathbf{c}, \mathbf{d}$) BC nanofibrils oxidised with CAN conc. of 2.5 mmol and $\mathbf{e}, \mathbf{f}$) MTEMA-g-BC nanofibrils after FRGP (MTEMA with conc. of 10 mmol and CAN with conc. of 2.5). 137
6.12 **I**) UV-Vis absorption of colloidal suspensions of Au NPs non-chemisorbed to the thioether moieties (SCH_3) of polyMTEMA chains during the thermal growth of Au NPs in the presence of MTEMA-g-BC nanofibrils. **II**) UV-Vis absorption of MTEMA-g-BC-Au nanohybrids prepared *in situ* by thermal growth of Au NPs in the presence of MTEMA-g-BC nanofibrils synthesised using different concentrations of MTEMA and CAN. 141

6.13 Photograph of MTEMA-g-BC-Au nanohybrids suspended in EtOH (conc. of 0.1 wt./v.%), where the red colour reflected the presence of Au NPs chemisorbed to thioether moieties of polyMTEMA chains of MTEMA-g-BC nanofibrils. MTEMA-g-BC-Au nanohybrids prepared with MTEMA-g-BC nanofibrils synthesised using various concentrations of MTEMA and CAN: **a**) 1 mmol & 1 mmol; **b**) 5 mmol & 1 mmol; **c**) 10 mmol & 1 mmol; **d**) 1 mmol & 2.5 mmol; **e**) 5 mmol & 2.5 mmol; **f**) 10 mmol & 2.5 mmol. **g**) MTEMA-g-BC nanofibrils synthesised using a concentration of MTEMA of 10 mmol and a concentration of CAN of 2.5 mmol, respectively. **h**) pure Au colloid. 142

6.14 SEM micrographs of MTEMA-g-BC-Au nanohybrid at various magnifications: **a**) x75k; **b**) x100k. MTEMA-g-BC synthesised using a concentration of MTEMA of 1 mmol and CAN of 2.5 mmol. 143

6.15 **I**) UV-Vis absorption of CdTe QD colloids as a function of refluxing time. **II**) Photograph of CdTe QDs colloid visualised under daylight. **III**) Photograph of CdTe QDs colloid visualised under UV irradiation. Refluxing time: (a) 10 min; (b) 20 min; (c) 30 min; (d) 60 min; (e) 120 min; (f) 180 min. 144

6.16 **I**) UV-Vis absorption of MTEMA-g-BC-CdTe nanohybrid nanofibrils with increasing concentration of CdTe QDs. **II**) Photograph of MTEMA-g-BC-CdTe nanohybrids (0.1 wt./v.%) suspensions in EtOH visualised under daylight. **III**) Photograph of MTEMA-g-BC-CdTe nanohybrids (0.1 wt./v.%) suspension in EtOH visualised under UV irradiation. The corresponding concentration of CdTe QDs in MTEMA-g-BC-CdTe nanohybrids: (a) CdTe QDs only; (b) 11.6 wt./wt.%; (c) 14.8 wt./wt.%; (d) 21.5 wt./wt.%; (e) 37.1 wt./wt.%. 147

6.17 SEM micrographs of MTEMA-g-BC-CdTe nanohybrids at a magnification of x75k; **a**) and x100k; **b**) 149

6.18 Photographs of suspensions of MTEMA-g-BC-CdTe nanohybrids (1 wt./v.%) in DCM: **I**) under daylight & **II**) under UV irradiation. The corresponding concentration of CdTe QDs immobilised on MTEMA-g-BC substrates were: (a) 11.6 wt./wt.%; (b) 14.8 wt./wt.%; (c) 21.5 wt./wt.%; (d) 37.1 wt./wt.%. . 150

6.19 Photographs of PHBHHX nanocomposite films containing MTEMA-g-BC-CdTe nanohybrids (4 wt./wt.%) under UV irradiation. The corresponding concentration of CdTe QDs immobilised onto MTEMA-g-BC substrates were: (a) 11.6 wt./wt.%; (b) 14.8 wt./wt.%; (c) 21.5 wt./wt.%; (d) 37.1 wt./wt.%. . 150

7.1 Schematic presentation of functionalisation of polysaccharide backbone by esterification reactions (top) and etherification reactions (bottom) (reproduced from [12]). 160
7.2 Preparation of polymer brushes by "grafting-to" and "grafting-from" (reproduced from [13]). 160
7.3 **a**) General structure of polyhydroxyalkanoates (adapted from [14]); **b**) Structure of poly(3-hydroxybutyrate); **c**) transmission electron micrograph of thin sections of recombinant *R. eutropha* PHB24 cells containing large amounts (90% of the dry cell weight) of P(3HB-co-5 mol% 3HHx) (reproduced from [15]). 162
7.4 Schematic of free radical grafting polymerisation reaction of polycaprolactone 2-(methacryloyloxy) ethyl ester macromonomer from BC nanofibrils. **a**) Initiation phase and free radical formation; **b**) grafting and propagation phase of monomer. 164
7.5 Schematic of preparation of PCLMA-g-BC nanofibril reinforced PHB nanocomposite films. **a**) Aqueous suspension of BC nanofibrils; **b**) sedimentation of PCLMA-g-BC nanofibrils in H_2O; **c**) dispersion of PCLMA-g-BC nanofibrils in DCM and **d**) dispersion of PCLMA-g-BC nanofibrils in PHB solution prior to solution-casting. 166
7.6 X-ray diffractograms of HCl hydrolysed BC and PCLMA-g-BC nanofibrils for various concentration of PCLMA and duration of FRGP reaction. (At a fixed concentration of CAN of 1 mmol). 168
7.7 ATR-FTIR spectra of HCl hydrolysed BC and PCLMA-g-BC nanofibrils produced using increasing concentration of PCLMA and duration of FRGP reaction (Fixed concentration of CAN of 1 mmol). 169
7.8 **I**) Thermal degradation behaviour and **II**) derivative weight loss of HCl hydrolysed BC and PCLMA-g-BC nanofibrils produced using various concentrations of PCLMA (*i.e.*, 1 mmol and 5 mmol) and increasing time of FRGP reaction (*i.e.*, 15 min, 30 min, 1 hr and 2 hr) in N_2 atmosphere (Fixed conc. of CAN, 1 mmol). 172
7.9 Evolution of advancing contact angles on surface of "nanopaper" made from HCl hydrolysed BC and PCLMA-g-BC nanofibrils, respectively, as function of duration of FRGP reaction and concentration of PCLMA used for FRGP reaction. 174

7.10 Photographs of suspension of (**a**, **c**) HCl hydrolysed BC nanofibrils and (**b**, **d**) PCLMA-g-BC* nanofibrils, respectively, with a concentration of 0.1% wt./v. in dichloromethane. After dispersion using an ultrasonic probe (**a**; **b**) and 24 h after sonication (**c**; **d**). (* conc. of PCLMA, 1 mmol; conc. of CAN, 1 mmol & duration FRGP 30 min) 175
7.11 SEM micrographs of PCLMA-g-BC nanofibrils produced using a concentration of PCLMA of: **a**) 1 mmol and **b**) 5 mmol, respectively, at a fixed concentration of CAN of 1 mmol and a reaction time of 30 min. 175
7.12 DSC thermograms of neat PHB and PCLMA-g-BC/PHB nanocomposites as a function of fraction (%wt.) of reinforcing nanofillers: **I**) second heating profile, **II**) first cooling profile, as described in Chapter 2 177
7.13 E$'$ and $\tan\delta$ for neat PHB film and PHB nanocomposites as a function of nanofiller content and temperature: **I** & **II**, HCl hydrolysed BC nanofibrils; **III** & **IV**, PCLMA-g-BC nanofibrils (conc. of PCLMA, 1 mmol; conc. of CAN, 1 mmol & duration FRGP, 30 min); **V** & **VI**, PCLMA-g-BC nanofibrils (conc. of PCLMA, 5 mmol; conc. of CAN. 1 mmol & duration FRGP, 30 min) . . . 181
7.14 Tensile strength of bacterial-based nanocomposites reinforced with HCl hydrolysed BC and PCLMA-g-BC nanofibrils as a function of nanofiller content and state of chemical modification. 183
7.15 Young's modulus of bacterial-based PHB reinforced with HCl hydrolysed BC and PCLMA-g-BC nanofibrils as a function of nanofiller content and state of chemical modification. 183

List of Tables

2.1 Summary of various analytical methods described in the present chapter. . . 20

3.1 Effects of internal configuration of stirred tank vessel on BC biosynthesis by *Gluconobacter xylinus* under agitated culture. 38
3.2 Crystal size of lattice [101], [10$\bar{1}$] and [002], and degree of crystallinity of bacterial cellulose synthesised by *Gluconobacter xylinus* under various culture conditions. 39
3.3 Summary of main absorption bands and assignment for the ATR-FTIR spectra of bacterial cellulose. 41
3.4 Fraction of cellulose allomorph I_α and I_β constituting the BC structure produced under various culture conditions. 41
3.5 Onset degradation temperature, maximum degradation temperature, weight loss rate and char yield of the thermal degradation process in N_2 of BC synthesised under various culture conditions. 44

4.1 Degree of crystallinity, full width half maximum (FWHM) peak for [002] lattice and crystal size of self-reinforced regenerated cellulose as a function of dissolution time of MCC in DMAc/LiCl cosolvent. 57
4.2 Summary of absorption bands and assignment for the ATR-FTIR spectra of regenerated cellulose. 59
4.3 Onset degradation temperature, degradation temperature, weight loss rate, char yield and activation energy of the thermal degradation process in N_2 of self-reinforced regenerated cellulose with various degrees of crystallinity. . . . 63
4.4 Moisture uptake and content of self-reinforced regenerated cellulose exposed to 95% RH at 30°C. 68

4.5 Evolution of the degree of crystallinity of sisal fibre after bacterial cellulose coating; full width half maximum (FWHM) peak for [002] lattice, crystal size and degree of crystallinity. 72
4.6 Young's modulus, tensile strength and strain of sisal fibres for immersion in culture medium, NaOH treatment and BC coating procedure. 73

5.1 Identification of aerogel properties and features, and associated potential applications[16]. 86
5.2 Degree of crystallinity, BC concentration, crystal size and peak location for [002] lattice of BC cryogels and rBC cryogel microspheres as a function of dissolution time of BC in DMAc/LiCl cosolvent. 95
5.3 Onset degradation temperature, degradation temperature, weight loss rate and char yield of the thermal degradation process in N_2 of freeze-dried BC and regenerated BC with various dissolution time and BC concentration 98
5.4 Average pore diameter, specific pore volume and specific (BET) surface area determined by N_2 sorption measurements at 77 K for freeze-dried BC cryogel and rBC cryogel microspheres at various dissolution time in DMAc/LiCl and BC concentration. 100

6.1 Sampling of the composition of various types of bioinorganic hybrid materials as a function of their composition and shape of organic component and nature of inorganic NPs and corresponding references. 115
6.2 Crystal size of [101], [$10\bar{1}$] and [002] lattice determined using using Scherrer's equation (see Chapter 2); peak location for [002] lattice and degree of crystallinity for BC, CAN oxidised BC and MTEMA-g-BC nanofibrils, respectively, as a function of concentration of CAN and MTEMA. 128
6.3 Summary of main absorption bands and assignment for the ATR-FTIR spectra of CAN oxidised BC and MTEMA-g-BC. 129
6.4 Elemental weight composition for HCl hydrolysed BC, CAN oxidised BC and MTEMA-g-BC nanofibrils as a function of concentration of CAN and MTEMA as determined by elemental analysis. 132

6.5 Onset degradation temperature, degradation temperature, weight loss rate and char yield of the thermal degradation in N_2 atmosphere of BC, CAN oxidised BC and MTEMA-g-BC nanofibrils with various concentrations of CAN and MTEMA. 134
6.6 SPR absorbance peak of colloidal suspensions of Au NPs and aqueous suspensions of MTEMA-g-BC-Au nanohybrids; aggregate sizes of Au NPs in colloidal suspensions measured by dynamic light scattering (DSL). 140
6.7 SPR absorbance peak (UV-Vis spectroscopy) of CdTe QD colloids as a function of refluxing time. 145
6.8 SPR absorbance peak (UV-Vis spectroscopy) of MTEMA-g-BC-CdTe nanohybrids (0.1 wt./v.%) in suspension as a function of concentration of CdTe QDs. 147

7.1 Crystal size of [101], [$10\bar{1}$] and [002] lattice; peak location for [002] lattice and degree of crystallinity for PCLMA-g-BC nanofibrils, respectively, as a function of concentration of PCLMA and duration of the FRGP reaction for a fixed concentration of CAN of 1 mmol. 167
7.2 Elemental weight decomposition for HCl hydrolysed BC and PCLMA-g-BC nanofibrils as a function of concentration of PCLMA macromonomer and duration of FRGP reaction using EA. 170
7.3 Onset degradation temperature, degradation temperature, weight loss rate and char yield of the thermal degradation process in N_2 atmosphere of PCLMA-g-BC nanofibrils as a function of concentration of PCLMA and duration of FRGP reaction (Fixed concentration of CAN of 1 mmol). 171
7.4 Summary of thermal characteristics of PHB nanocomposites reinforced with various fraction (%wt.) of PCLMA$-$g$-$BC† nanofibrils (conc. of PCLMA, 1 mmol; conc. of CAN, 1 mmol & duration FRGP, 30 min). 178

Nomenclature

$D\bar{P}w$	Weight-average degree of polymerisation
ΔH_f^0	Heat of fusion
E'	Storage modulus
AGU	Anhydroglucose unit
Al_2Te_3	Aluminium telluride
ATR-IR	Attenuated total reflectance-Infrared
Au NPs	Gold nanoparticles
BC	Bacterial cellulose
BC-coated	Bacterial cellulose coated
BET	Brunauer-Emmet-Teller method
BJH	Barrett-Joyner-Halenda method
CA	Contact angle
CAN	Cerium (IV) ammonium nitrate
$Cd(ClO_4)_2 \cdot xH_2O$	Cadmium perchlorate hydrate
$CdCl_2$	Cadmium chloride
CdS QDs	Cadmium sulphide quantum dots
CdTe QDs	Cadmium telluride quantum dots

Ce Cerium

CHNS Carbon hydrogen nitrogen sulphur

CSL Corn steep liquor

DCM Dichloromethane

DLS Dynamic light scattering

DMAc Dimethylacetamide

DMTA Dynamic mechanical thermal analysis

DSC Differential scanning calorimetry

DTG Derivative thermogravimetric

DVS Dynamic vapour sorption

EA Elemental analysis

FRGP Free radical grafting polymerisation

FWHM Full width at half maximum

H_2Te Hydrogen telluride

H-bonded hydrogen-bonded

H&S medium Hestrin and Schramm medium

$HAuCl_4 \cdot 3H_2O$ Gold (III) chlorite trihydrate

HCl Hydrochloric acid

I.U.P.A.C. International Union of Pure and Applied Chemistry

IL Ionic liquid

IR Infrared

LiCl Lithium chloride

MCC Microcrystalline cellulose

MMA Methyl methacrylate

MTEMA 2-(methylthio)ethyl methacrylate

MTEMA-g-BC MTEMA-grafted-bacterial cellulose

MTEMA-g-BC-Au MTEMA-grafted-bacterial cellulose-gold nanoparticles

MTEMA-g-BC-CdTe MTEMA-grafted-bacterial cellulose-cadmium telluride quantum dots

N_2 Nitrogen

NBB Nanobuilding block

NPs Nanoparticles

OD_{600} Optical density at 600 nm

OH group Hydroxyl group

PCL Poly(caprolactone)

PCLMA Caprolactone 2−(methacryloyloxy)ethyl ester

PCLMA-g-BC PCLMA-grafted-bacterial cellulose

PHA Polyhydroxyalkanoate

PHB Poly-3-hydroxybutyrate

PHBHHx Poly(3-hydroxybutyrate-co-3-hydroxyhexanoate)

PLLA Poly(L-lactic acid)

QDs Quantum dots

rBC Regenerated bacterial cellulose

RH Relative humidity

RT Room temperature

SAXS Small angle X-ray scattering

scCO$_2$ Super critical CO_2

SCH$_3$ Methylthiol moiety

SEM Scanning electron microscopy

SiO$_2$ Silica

SPR Surface plasmon resonance

TEM Transmission electron microscopy

TGA Thermogravimetric analysis

UV-VIS Ultraviolet-Visible

WAXD Wide angle X-ray diffraction

X-linking Cross-linking

XRD X-Ray diffraction

1

General Introduction

1.1 Research context

In recent years, a renewed interest for the development of bio-based materials and the utilisation of renewable resources as raw materials has been observed in both academia and industry. This propensity towards "greener" materials is ascribed to the not so distant scarcity of fossil resources, which are extensively used nowadays in our society and also to the awakening environmental awareness across the globe.

Polysaccharides, and particularly cellulose, are the most abundant and ubiquitous biopolymers on earth, thus establishing them to be the prime candidates for replacing petroleum-based feedstock. Cellulose is the skeletal component of plants and the main product of their photosynthesis. Biosynthesised cellulosic materials currently account for 1.5×10^{12} tonnes of the total yearly biomass production[2]. Besides, only a small fraction of this biomass, 2%, is processed and transformed industrially in to papers (and other absorption media), cardboards, regenerated cellulose materials (*i.e.*, fibres and films) and cellulose derivatives (*e.g.*, cellulose esters or cellulose ethers) used in building materials, pharmaceuticals, foodstuff and cosmetics[17]. Therefore, there is a strong impetus to take advantage of the intrinsic properties of cellulose, *i.e.*, the ease of chemical functionalisation, biodegradability, renewability, high strength and stiffness, to develop novel materials for innovative applications such as smart coatings, pharmaceutical applications, nanocomposites, electronic materials[18], besides the customary usages of cellulose. As a consequence, the number of research publications dealing with cellulose-based materials has grown steadily over the last decade[19], as seen in Figure 1.1.

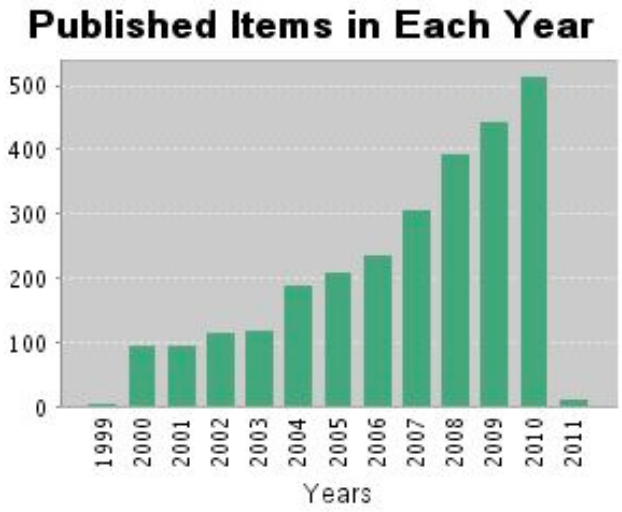


Figure 1.1: Summary of the annual number of scientific publications related to cellulose-based materials from the year 2000 to 2010 indexed within the Web of Science®. The keywords for the search included the combination of the terms: cellulose, nanocomposite, composite, hybrid and functional, while excluding the terms: lignin, chitin, chitosan and starch.

There is currently a tremendous amount of attention for bacterial cellulose; an inherent nanoscale cellulose material, which exhibits a nanofibrillar network structure composed exclusively of crystalline cellulose contrary to cellulose originating from plants. Bacterial cellulose was first identified in 1954 by Hestrin and Schramm [20,21], who isolated it from an acetic-producing bacteria strain, namely *Acetobacter xylinum*. Since then, bacterial cellulose has remained an intriguing material for microbiologists, thus attempting to understand its morphology and the mechanism by which it was biosynthesised in certain strains of bacteria [22]. Recently, the drive for the usage of bacterial cellulose in materials science was initiated by its unique physical properties, *i.e.*, hydrophilicity, biocompatibility, nanosize and high tensile modulus [23,24]. In addition, bacterial cellulose was proclaimed by Iguchi *et al.* [25] and Brown [26] to have great potential and be a promising biopolymer in a wide range of applications such as medicine, biomaterials engineering, membranes and polymer nanocomposites [27,28,29], which has been confirmed by the recent and steep increase of the number publications about advanced materials making use of bacterial cellulose.

1.2 Motivation

The purpose of the study was to investigate and identify potential and novel applications of bacterial cellulose in various areas (or aspects) of materials science, which covered bio-processing, renewable hierarchical composites, macroporous foams, functional bioinorganic nanohybrids and bacterial-based nanocomposites.

The findings reported in the following chapters aimed to demonstrate the versatile use of bacterial cellulose to produce different types of renewable advanced (nano-) materials. Moreover, bacterial cellulose revealed an ability for tailoring its physical properties, *i.e.*, surface chemistry, surface functionality, dissolution/regeneration, shape, morphology and *etc.*, thus enabling the preparation of advanced (nano-) materials having properties compliant with their application requirements.

1.3 Roadmap of the thesis

The author would like to emphasise on the fact that each individual chapter contains its respective introductory part and literature review followed by the experimental, results/discussion and conclusion parts. The atypical layout (*i.e.*, for British PhD-theses) of the chapters presented in this thesis was adopted for the sake of clarity and coherence since the research described in the following chapters is proposing to make use of bacterial cellulose nanofibrils in different fields of materials science ranging from hierarchical composites, porous media, functional bioinorganic nanohybrids and bacterial-based nanocomposites. Therefore, it would have been a very convoluted narrative to draw a unifying introduction encompassing the various aspects of the author's research in a single chapter.

The present thesis is divided into 8 chapters, as follows:

- Chapter 1 introduces the context of the research, motivation and the roadmap to this thesis.
- Chapter 2 provides a background and introduction to the analytical methods used and the experimental methodology followed.
- In Chapter 3, the biosynthesis of bacterial cellulose by the *Gluconobacter xylinus* strain in static and agitated fermentation conditions is characterised. An increase of the productivity of bacterial cellulose in an instrumented stirred-tank bioreactor was achieved by

the addition of a stainless-steel mesh support inside the bioreactor vessel. The physical, chemical and thermal characteristics of the bacterial cellulose nanofibrils produced in static and agitation fermentation conditions have been characterised and compared.

- Chapter 4 describes the characterisation of all-cellulose nanocomposites produced by dissolution and subsequent regeneration of microcrystalline cellulose. The surface modification procedure of sisal fibre, which consists of coating of bacterial cellulose onto the surfaces of sisal fibres *in situ* during fermentation of *Gluconobacter xylinus* is discussed. The mechanical properties of bacterial cellulose coated sisal fibres are characterised. The effect of both surface modification of sisal fibres and degree of crystallinity of the regenerated cellulose matrix on the mechanical properties of hierarchical all-cellulose composites is evaluated and discussed.

- Chapter 5 describes the preparation and characterisation of porous cryogel microspheres composed of regenerated bacterial cellulose nanofibrils. The physical and structural properties of the regenerated bacterial cellulose cryogel microspheres are reported as a function of the dissolution time and concentration of bacterial cellulose nanofibrils in the DMAc/LiCl cosolvent. The evolution of the morphology of the porous network and BET surface area of the regenerated bacterial cellulose cryogel microspheres are discussed.

- Chapter 6 describes the synthesis and characterisation of thioether functionalised bacterial cellulose nanofibrils by free radical grafting polymerisation reaction in an aqueous medium. The preparation and characterisation of bioinorganic nanohybrids composed of either gold nanoparticles or cadmium telluride quantum dots chemisorbed onto the thioether functionalised bacterial cellulose nanofibrils are reported.

- The synthesis and characterisation of hydrophobised bacterial cellulose nanofibrils by free radical grafting polymerisation in aqueous medium are reported in Chapter 7. BC was hydrophobised by the grafting of polycaprolactone chains from its surface. The thermal and mechanical properties of entirely bacterial-based nanocomposites composed of poly(3-hydroxybutyrate) (PHB) biopolymer matrix reinforced with hydrophobised bacterial cellulose nanofibrils are characterised and discussed.

- The general conclusions are then drawn in Chapter 8.

2

Methods

The aim of this chapter is to summarise the various analytical methods employed to characterise the different specimen presented subsequently in the present thesis. Each analytical method is introduced succinctly with its relevant background theory. The methodology and apparatus used for the characterisation of the specimen are also described. The list of analytical methods used is as follows:

- The optical properties of bacterial suspension of *Gluconobacter xylinus* strain was characterised by optical density at wavelength of 600 nm (OD_{600}).
- The cellulose polymorphs, allomorphs and functional groups grafted from bacterial cellulose (BC) nanofibrils were characterised by ATR-FTIR spectroscopy.
- The surface plasmon resonance of colloidal suspension of gold nanoparticles (Au NPs) and cadmium telluride quantum dots (CdTe QDs) as well as suspension of functional bioinorganic nanohybrids were characterised by UV-Vis spectroscopy.
- The diameter of Au NPs was determined by dynamic light scattering technique.
- The crystal structure of cellulose specimen was analysed by X-ray diffraction (XRD).
- The surface area of freeze-dried BC nanofibrils and macroporous cryogel (*i.e.*, freeze-dried) microspheres composed of regenerated BC nanofibrils was quantified by nitrogen BET adsorption.
- The chemical composition of functionalised BC nanofibrils was quantified using elemental analysis (EA).

- The thermal and thermomechanical properties of various type of specimen were characterised using thermogravimetric analysis (TGA), differential scanning calorimetry (DSC) and dynamic mechanical thermal analysis (DMTA).
- The mechanical properties of various (nano-) composites were characterised by tensile testing.
- The morphology of various specimens was observed using scanning electron microscopy (SEM).
- The moisture sorption behaviour of regenerated cellulose was assessed by dynamic vapour sorption (DVS).

2.1 Optical density

The growth of a bacterial population of *Gluconobacter xylinus* strain was monitored using optical density measurements at a wavelength of 600 nm (OD_{600}) of a broth containing bacterial cells, as discussed later in Sections 3.2.2 & 3.3.2, respectively. The change in OD_{600} provides information about the rate of growth of the bacterial population during cultivation.

The OD_{600} analysis (also referred as turbidity) is based on the Lambert-Beer law, where there is a direct and linear relationship between the amount of light adsorbed and the concentration of constituents in the sample, as long as it adsorbs or scatters the incident light. The Lambert-Beer law is expressed as follows:

$$A_\lambda = \log \frac{1}{T} = -\log T \tag{2.1}$$

where A_λ is the sample absorbance at a specific wavelength, T is the transmittance expressed as the ratio of intensity of transmitted light I_t over intensity of light beam I_0.

$$T = \frac{I_t}{I_0} \tag{2.2}$$

In the case of a dilute substance, as for culture broth, the Lambert-Beer law is rewritten as follows:

$$A_\lambda = \epsilon_\lambda c d \tag{2.3}$$

where ϵ_λ represents the coefficient of adsorption at a specific wavelength ($L \cdot mol^{-1}$), c is the concentration of the sample ($mol \cdot L^{-1}$) and d is the path length of light through the

sample (cm). The coefficient of adsorption is different for each sample, however for a specific wavelength and sample type, the parameters ϵ_λ and d are constant.

The OD_{600} of aliquot (200 μl) containing a suspension of bacterial cells of *Gluconobacter xylinus* placed in a UV-transparent plastic cuvette was measured using a BioPhotometer (Eppendorf, UK).

2.2 ATR-FTIR spectroscopy

ATR-FTIR spectroscopy was used to characterise various aspects of cellulose specimens such as cellulose polymorphs, allomorphs and functional groups. ATR-FTIR spectroscopy enabled the distinction of crystal allomorphs (I_α and I_β) and polymorphs (type I and II) of cellulose specimen, as discussed in Section 3.5, Section 5.3.2 and Section 4.3.2, respectively. Furthermore, surface modifications performed on BC nanofibrils were characterised by ATR-FTIR spectroscopy to characterise the functional moieties grafted from the cellulose backbone.

IR spectroscopy allows to characterise the functional groups present in a specimen in any physical state or form. The incident IR radiation is absorbed by the molecules constituting a specimen. The intensity of absorption varies as a function of molecular structure and composition such as functional groups. Moreover, the corresponding vibrational and rotational modes of a molecule vary for various excitation frequencies of IR radiation. The intensity of energy adsorption by a molecule relates to its dipole moment with respect to frequency of IR radiation. Traditional IR spectroscopy consists in measuring light transmission through a sample. Whereas, the principle of ATR-FTIR spectroscopy consists of multiple reflection of an incident light beam using an internal reflectance element (IRE), where the intensity of light beam is attenuated as a function of absorption by a specimen [30]. Thus, ATR-FTIR is more sensitive to the surface volume. ATR-FTIR requires intimate contact between IRE and the specimen. In ATR-FTIR, the reflected light beam penetrates into specimen by a few micrometers, where it is absorbed. The depth of penetration, D_p (μm) of the reflected light beam is expressed as follows:

$$D_p = \frac{\lambda}{2\pi n_1 \sqrt{\sin^2\theta - n_{12}^2}} \tag{2.4}$$

where λ (μm) is the wavelength, π is a mathematical constant (equal to 3.14159), n_1 the index of refraction of the IRE, θ the incidence angle and n_{12} the ratio of refraction index of specimen and IRE.

The ATR-FTIR measurements were performed using a Bruker FTIR spectrometer (Equinox 55, Bruker, Germany), equipped with a Golden Gate diamond crystal ATR accessory (Specac Ltd, Orpington, UK) with 45° incident angle configuration. Throughout measurements the room temperature was set to $20°C$ using an air-conditioning unit. In addition, the ATR accessory was continuously purged with N_2 (O_2-free; BOC, UK) to remove H_2O vapour. All FTIR absorption spectra were recorded over a range from 4000 to 400 cm^{-1} wavenumbers, at a resolution of 2 cm^{-1} using a liquid nitrogen-cooled mercury-cadmium-telluride (MCT) detector. The dried and flat specimens were clamped in a reproducible fashion on the IRE within the measuring cell. For each specimen, 64 scans were co-added to achieve an appropriate signal-to-noise ratio. All spectra were normalised with respect to area under the C-H stretching band located between 2220 cm^{-1} and 3000 cm^{-1}.

2.3 UV-Vis spectroscopy

UV-Visible (UV-Vis) spectroscopy was employed to monitor the transition of surface plasmon resonance (SPR) of Au NPs, CdTe QDs and BC- based bioinorganic nanohybrids. In the case of Au NPs or CdTe QDs with a diameter smaller than the wavelength of incident light and at specific frequency, the surface of these nanoparticles exhibits an SPR band under UV-Vis excitation. The SPR consists of an interaction between surface of nanoparticle and incident light beam, which modifies the electron field by collective and coherent oscillations of electrons on its outer layer. Thus, the oscillation of electrons induced the formation of dipole within the nanoparticle[31]. The excited cloud of negatively charged electrons gather on the side of nanoparticle radiated by incident light beam, thus rendering its opposite side positively charged, as seen in Figure 2.1. Moreover, the frequency at which SPR occurs and the energy associated are a function of size, shape and dielectric properties of nanoparticles as well as the refractive index of the medium in which they are dispersed[32].

The Lambert-Beer law can also be used for UV-Vis spectroscopy to quantify the concentration of absorbing species, as presented in equation 2.3. The extinction cross-section for a spherical particle, σ_{ext}, corresponds to the absorption frequency of SPR established by the Mie theory[33,34], expressed as follows:

$$\sigma_{ext} = \frac{24\pi^2 R^3 \epsilon_m^{3/2}}{\lambda} \left(\frac{\epsilon_2}{(\epsilon_1 + 2\epsilon_m)^2 + \epsilon_2^2} \right) \tag{2.5}$$

where σ_{ext} is the extinction cross-section composed of the sum of scattering and absorption cross-sections (σ_{ext}=σ_{sca}+σ_{abs}) (nm), R^3 is the mean radius of nanoparticles (nm), λ the wavelength of the incident light beam (nm), ϵ_m the dielectric constant of the medium, ϵ_1 and ϵ_2 are the real and imaginary parts of dielectric function of the nanoparticle, respectively.

The UV-Vis measurements were performed using a Varian Cary 50 UV/Vis Spectrophotometer. The specimen absorption was measured using a dual beam configuration with a scanning range set between 800 nm and 200 nm, with an average data point acquisition of 12.5 ms at a wavelength interval of 1 nm. Prior to measurement the baseline was corrected using two quartz cuvettes with matched reflective index containing the medium without nanoparticles. Suspensions of various particles in EtOH were prepared with a concentration of 0.01 wt./v.% and sonicated for 2 min using an ultrasonic probe UP50H (Hielscher Ultrasonics GmbH, Germany).

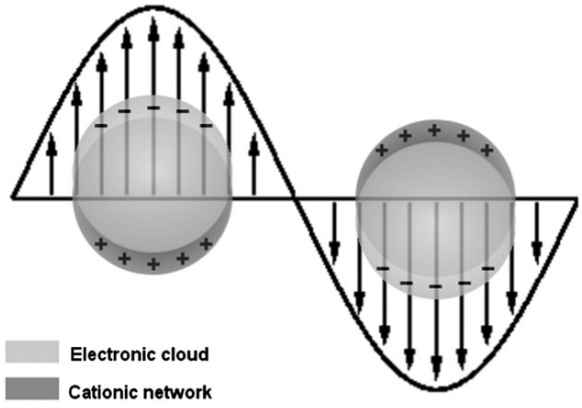


Figure 2.1: Schematic description of electronic cloud displacements in nanoparticles in an electromagnetic wave (reproduced from [1]).

2.4 Particle sizing

Dynamic light scattering (DLS) technique was used for the determination of diameters of various synthesised nanoparticles. An incident light beam is directed through a medium containing particles undergoing diffusive Brownian motion, where the detector records scattered waves at a fixed angle (90°) with respect to incident light beam. When the light is scattered by a moving particle, a Doppler shift occurs, hence changing of the wavelength

of light scattered by the particle. Thus, intensity and frequency shift of the scattered light is a function of the particle size (and shape) in the medium. The theory of dynamic light scattering is derived from the probability density function of Brownian motion for spherical particle, expressed as follows:

$$P(r,t|0,0) = (4\pi Dt)^{3/2} \exp\left(\frac{-r^2}{4Dt}\right) \tag{2.6}$$

where t is the time, r the radius of spherical particle and D is the diffusion coefficient, which is expressed as follows:

$$D = \frac{k_b T}{6\pi\eta r} \tag{2.7}$$

where k_b is the Boltzmann constant (1.38^{-23} $J.K^{-1}$), T is the temperature in Kelvin (K), η is the viscosity of medium (Ns/m^2) and r is the radius of particle (nm).

The particle analysis was performed using a ZetaPALS (Zeta potential analyser) (Brookhaven, Lancashire, UK) at a fixed temperature of $30°C$. A diluted suspension in H_2O or ethanol containing the nanoparticles to characterise was sonicated for 2 min and placed in a quartz cuvette, prior to measurement.

2.5 X-ray diffraction

The degree of crystallinity, the crystal structure and size of cellulose crystals were determined using X-ray diffraction (XRD) technique for cellulose specimen. XRD characterisation was carried out for BC nanofibrils, microcrystalline cellulose (MCC), regenerated MCC, sisal fibres, regenerated BC and chemically modified BC nanofibrils, respectively. XRD consists in irradiating a specimen with an incident X-ray beam with a wavelength of few Angstroms (herein, 1.5405 Å). When an X-ray beam impinges on a specimen at a various incidence angle, only a fraction of incident X-ray beam amplitude is diffracted by the layers of atomic planes constituting a crystal. The diffraction mechanism is thoroughly discussed elsewhere [35]. Bragg's law correlates the spacing of atomic planes, so called lattice planes, from one another with the angle of incidence of the X-ray beam. Bragg's law is expressed as follows:

$$n\lambda = 2d\sin\theta \tag{2.8}$$

where n is the reflection order, λ is the wavelength of incident X-ray beam (Å), d is the lattice plane distance and θ is the incident angle between the X-ray beam (°) and the scattering

lattice planes (Å). The degree of crystallinity of cellulose specimen χ_{cr} was determined using the empirical Segal's equation [36], expressed as follows:

$$\chi_{cr} = \frac{I_{[002]} - I_{[am]}}{I_{[002]}} \tag{2.9}$$

where $I_{[002]}$ and $I_{[am]}$ are the intensity of the diffraction peaks corresponding to lattice planes [002] and amorphous cellulose, respectively. The size of cellulose crystals for their respective lattice plane $L_{[lattice]}$ was evaluated using Scherrer's equation [35], expressed as follows:

$$L_{[lattice]} = \frac{k\lambda}{\beta_{[lattice]} \cos\theta} \tag{2.10}$$

where k is the Scherrer constant for cellulose ($k = 0.84$ [35]), λ is the wavelength of incident X-ray beam (Å) and $\beta_{[lattice]}$ is the full width at half peak intensity for the specific lattice (in radian).

Two diffractometers were used to perform XRD measurement on cellulose specimen of various natures. A Philips PW1700 series automated diffractometer (Philips, The Netherlands) was used for regenerated cellulose specimen. On this apparatus, diffractograms were collected with an angle of incidence 2θ ranging from 5° to 45° with incremental steps of 0.04°. X-rays were generated using CuK_α radiation at $\lambda = 1.5405$ Å. A Goniometer PW3064/60 XPert PRO diffractometer (PANalytical, The Netherlands) was used for all other specimen. On this later apparatus, diffractograms were collected with an angle of incidence 2θ ranging from 5° to 60° with incremental steps of 0.03°. X-ray were generated using CuK_α radiation at $\lambda = 1.5405$ Å with an accelerated voltage of 40 kV and a current of 40 mA. Specimen were mounted onto a spinning stage rotating at 0.1 r.p.s.. For analysis, diffractograms were corrected with an appropriate baseline and subsequently, the various diffraction peaks were fitted using a pseudo-Voigt function.

2.6 BET surface area

The surface area of freeze-dried BC nanofibrils and regenerated BC macroporous cryogels microspheres were characterised using N_2 isotherm sorption technique at $77°K$. Brunauer-Emmet-Teller (BET) surface area consists in measuring the pressure change in a known volume as a function of the partial pressure of N_2, which allows to determine the amount of gas adsorbed on a surface, thus forming mono- or multi-layers. The sorption behaviour of

gas molecules varies with nature, morphology and size distribution of pore walls in any given specimen. Thus, the International Union of Pure and Applied Chemistry (I.U.P.A.C.) has identified six different types of gas adsorption isotherms [37]. According to the I.U.P.A.C., the type of pores in a porous structure is classified as a function of pore width. Where, a micropore is a pore with an internal width of less than 2 nm, a mesopore is a pore with an internal width between 2 nm and 50 nm and a macropore is a pore with an internal width greater than 50 nm [37]. The BET theory is an extension of Langmuir's adsorption isotherm, which assumes that a single monolayer of molecules is adsorbed onto sample surface [38]. The BET theory enables determination of the number of gas molecules adsorbed onto a surface assuming the formation of multi-layers, where the monomolecular layer, the layer farthest from the adsorbent surface is in dynamic equilibrium with the vapour phase. The equation for BET theory is expressed, as follows:

$$\frac{1}{W\left[\frac{P}{P_0}-1\right]} = \frac{1}{W_m C} + \frac{C-1}{W_m C}\left(\frac{P}{P_0}\right) \tag{2.11}$$

where $\frac{P}{P_0}$ is the relative pressure, W and W_m are the weight of molecules (g/mol) adsorbed in the incomplete and complete monolayer and C is an empirical constant, which gives an indication of the order of magnitude of the attractive adsorbent-adsorbate interactions [39]. The specific surface area, S_t (m^2/g) of BC and regenerated BC cryogels was determined by equation 2.12, as follows:

$$S_t = \frac{W_m \bar{N} A_x}{\bar{M}} \tag{2.12}$$

where $\bar{N}$ is the Avogadro's number, A_x is the cross-sectional area of N_2 and $\bar{M}$ is the molecular weight of N_2 (g/mol). Moreover the variables W_m and C are deduced from BET plot based on equation 2.11. The pore size distribution within BC and regenerated BC cryogels was determined using Barrett-Joyner-Halenda (BJH) method [40], which assumes that, pores are cylindrical and that the phase equilibrium between adsorbate and adsorbent is reached by physical adsorption on the pore walls and capillary condensation occurs in the inner capillary volume. Thus, the BJH method provides a correlation between pore diameter and pore condensation pressure, expressed as follows:

$$\ln\left(\frac{P}{P_0}\right) = \frac{-2\gamma\bar{V}}{rRT} \tag{2.13}$$

where $\frac{P}{P_0}$ is the relative pressure, γ the surface tension of liquid N_2 (mN/m), $\bar{V}$ the molar volume of condensed liquid N_2 (m^3/mol), r the radius of the pore (m), R the universal gas

constant ($J/K \cdot mol$) and T the temperature of liquid N_2 ($77°K$). Since several parameters are constants, BJH method is simplified, as follows:

$$r = \frac{-4.14}{\ln\left(\frac{P}{P_0}\right)} \tag{2.14}$$

The surface area of freeze-dried BC nanofibrils and regenerated BC macroporous cryogels microspheres were characterised using a physisorption analyser ASAP 2010 (Micromeritics, UK). N_2 sorption was performed at $77°K$, the weight of specimen was approximately 50 mg. Prior to measurement the specimen was outgassed for 8 h at $105°C$ in inert helium (Grade A; BOC, UK) atmosphere. The determination of specific surface area and pore size distribution for both BC and regenerated BC cryogels was based on equations 2.12 and 2.13, respectively.

2.7 Elemental analysis

The elemental composition of BC nanofibrils, cerium (IV) ammonium nitrate oxidised BC nanofibrils, thioether grafted BC nanofibrils and polycaprolactone grafted BC nanofibrils was assessed using a CHNS elemental analysis (EA). EA technique enables the quantification of elemental fraction of carbon, hydrogen, nitrogen and sulphur in a specimen. EA is based on analysis of the composition of a reduced combustion gas that emanated from complete and instantaneous oxidation of a specimen in furnace at $1000°C$, where the atmosphere was temporarily enriched with oxygen. EA measurements were performed using a Carlo Erba CE1108 Elemental Analyser operated by Mr. Stephen Boyer based at the London Metropolitan University. The analysis and interpretation of the raw data was performed by the author.

2.8 Thermogravimetric analysis

Thermogravimetric analysis (TGA) was used to determine thermal stability of various cellulose-based materials. The effect of degree of crystallinity of regenerated cellulose and regenerated BC on the degradation behaviour was evaluated by TGA, as will be discussed in Chapter 4 and Chapter 5, respectively. The change of degradation behaviour of thioether and polycaprolactone grafted BC nanofibrils was also assessed by TGA, as will be discussed in Chapter 6 and Chapter 7, respectively. TGA enables characterisation of the thermal stability of a specimen by measuring its weight change as a function of temperature using a thermobalance.

The degradation behaviour of cellulose and BC specimen was assessed using a TA Q500 (TA Instruments, UK) in an inert nitrogen atmosphere to avoid premature degradation by oxidation. Specimens of 50 ± 5 mg were tested in the temperature range from $35°C$ to $800°C$ at a heating rate of $5°C/min$. The weight-loss rate was obtained from derivative thermogravimetric data (DTG); expressed as $\frac{dm}{dT}$. Moreover, the activation energy (E_a) of the degradation process was obtained using Broido's method[41]. The activation energy E_a was determined from the slope of the graph $\ln(\ln \frac{1}{y})$ versus $\frac{1}{T}$[41,42,43,44]:

$$\ln\left(\ln\frac{1}{y}\right) = -\frac{E_a}{R}\frac{1}{T} + C \tag{2.15}$$

where, T is the sample temperature ($°K$), R the universal gas constant ($J/K \cdot mol$) and C the temperature independent constant. The parameter y corresponds to the remaining material weight (W) at any given reaction time.

$$y = \frac{W - W_{final}}{W_{initial} - W_{final}} \tag{2.16}$$

2.9 Differential scanning calorimetry

The thermal behaviour of nanocomposites was assessed by differential scanning calorimetry (DSC). DSC monitors the difference of power output required for a reference pan and a specimen pan to reach a specified temperature. During heating and cooling cycles the heat flux, $\frac{dH}{dt}$ varies in the specimen when exothermic or endothermic transitions occur. This results in the variation of the heat capacity of the sample, ΔC_p and thus enables the characterisation of phase transitions as a function of temperature, such as glass transition, melting and crystallisation. The heat flux is expressed as follows:

$$\Delta\frac{dH}{dt} = \left(\frac{dH}{dt}\right)_{specimen} - \left(\frac{dH}{dt}\right)_{reference} \tag{2.17}$$

$$\Delta C_p = \Delta\left(\frac{dH}{dT}\right) = \Delta\frac{dH}{dt}\frac{dt}{dT} \tag{2.18}$$

where t is time (s) and T is the temperature ($°C$). Moreover, the degree of crystallinity of polymeric specimen, X_c, can be calculated from the enthalpy of fusion associated with the area of melting endothermic phase. X_c is expressed as follows

$$X_c = \frac{\Delta H_f(T_m)}{\phi\Delta H_f^0(T_m^0)} \tag{2.19}$$

where ΔH_f is the enthalpy of fusion measured at the melting point, T_m and T_m^0 are the melting temperatures ($^\circ C$), ΔH_f^0 are the enthalpy of fusion ($J \cdot g^{-1}$) of an 100% crystalline polymeric specimen measured at the equilibrium melting temperature T_m^0 and ϕ is the weight fraction of polymer in the specimen [45]. In addition the heat of fusion, ΔH_f^0, as determined for fully crystalline poly(3-hydroxybutyrate) (PHB) was reported to be 146 $J \cdot g^{-1}$ [46,47].

The DSC measurement was carried out in an inert helium atmosphere using a DSC Q2000 (TA Instruments, UK). Prior to measurement, all the specimens were conditioned in a drying oven at $40^\circ C$ for 1 d. Approximately, 5-9 mg of a specimen was weight and sealed in an aluminium pan. During measurement, the thermal cycle experienced by specimen was composed of subsequent heating-cooling-heating profiles. The specimen was heated from $20^\circ C$ to $200^\circ C$ with a heating rate of $5^\circ C/min$. The first heating enabled the suppression of the thermal history. The following cooling was carried out from $200^\circ C$ down to $-20^\circ C$ at a cooling rate of $-5^\circ C/min$. The second heating was carried out from $-20^\circ C$ up to $200^\circ C$ at a heating rate of $5^\circ C/min$. This temperature program was the same for all the specimens tested.

2.10 Dynamic mechanical thermal analysis

The viscoelastic properties of self-reinforced cellulose nanocomposites and all-cellulose hierarchical composites were investigated using dynamic mechanical thermal analysis (DMTA) as a function of the degree of crystallinity of the regenerated cellulose matrix. The viscoelastic properties of hydrophobised BC nanofibrils reinforced poly-3-hydroxybutyrate (PHB) biopolymer nanocomposites were also investigated using DMTA as a function of both nanofiller content and degree of hydrophobicity of modified BC nanofibrils. DMTA consists in measuring the linear viscoelastic response of a polymeric material, which is subjected to an external sinusoidal oscillatory stress. The response of a polymeric material is a function of both temperature and oscillation frequency [48,49]. The intrinsic properties of a viscoelastic polymeric material can be described by a linear response complying with Hooke's law and another non-linear complying with Newton's law. Hooke's law defined the elastic response as follows:

$$\sigma = E \times \epsilon \tag{2.20}$$

where σ is the stress (MPa), E the Young's modulus (GPa) and ϵ the strain (%). Newton's law for Newtonian viscous flow is expressed as follows:

$$\tau = \eta\dot{\gamma} = \eta\frac{\partial\gamma}{\partial t} \tag{2.21}$$

where τ is the shear stress (Pa), η the viscosity ($Pa \cdot s$) and $\dot{\gamma}$ the shear rate (s^{-1}). When a polymeric material is subjected to oscillatory strain, the material response exhibits a phase-lag δ, as shown in Figure 2.2. Therefore the strain and stress waves are expressed as follows:

$$\epsilon = \epsilon_0 \sin(wt) \tag{2.22}$$

$$\sigma = \sigma_0 \sin(wt + \delta) \tag{2.23}$$

where ϵ_0 is the maximum strain, σ_0 the maximum stress, w the frequency and t the time. Therefore, the equation representing the stress wave is expressed as follows [50]:

$$\sigma = \sigma_0 \sin(wt)\cos(\delta) + \sigma_0 \cos(wt)\sin(\delta) \tag{2.24}$$

Equation 2.24 expresses the elastic term and the viscosity term, corresponding to in-phase and out-phase stress, respectively. Therefore, the storage modulus E' and the loss modulus E'' corresponding to elastic and viscous modulus, respectively, are expressed as follows:

$$E' = \frac{\sigma_0}{\epsilon_0}\cos(\delta) \tag{2.25}$$

$$E'' = \frac{\sigma_0}{\epsilon_0}\sin(\delta) \tag{2.26}$$

Furthermore, loss tangent δ corresponding to the damping factor is expressed as follows:

$$\tan\delta = \frac{E''}{E'} \tag{2.27}$$

Increase in $\tan\delta$ signifies the polymeric material dissipates more energy because it behaves more like a viscous liquid. The appearance of T_g reveal the softening of the network of polymer chains from their frozen glass-like state towards a rubber-like state with an increasing energy dissipation.

DMTA measurements were performed using a Tritec 2000 dynamic mechanical analyser (Triton Technology Ltd, UK). Two configurations were adopted to clamp the specimen, a single cantilever beam configuration for self-reinforced cellulose nanocomposites and all-cellulose hierarchical composites in shape of a rectangular coupon ($20 \times 3.5 \times 1.2$ mm^3).

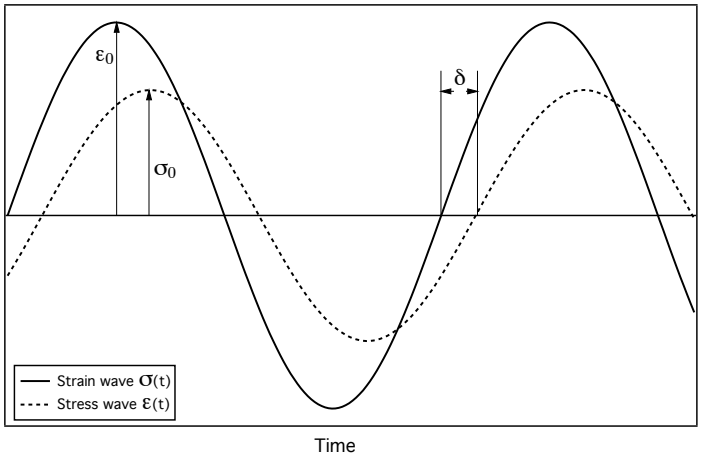


Figure 2.2: DMA principle, stress-strain relationship for linear viscoelastic material.

The latter was a tensile-tensile configuration used for thin films ($20 \times 10 \times 0.1$ mm^3) of hydrophobised BC nanofibrils reinforced PHB nanocomposites. For both configurations, the dynamic displacement applied was 0.05%. The temperature was increased from $35°C$ to $300°C$ at a heating rate of $5°C/min$ and an excitation frequency of 1 Hz for self-reinforced cellulose nanocomposites and all-cellulose hierarchical composites. Whereas, the temperature for BC nanofibrils reinforced biopolymer nanocomposites was increased from $-20°C$ to $150°C$ at a heating rate of $5°C/min$ and an excitation frequency of 1 Hz. All the tests were performed in inert nitrogen atmosphere.

2.11 Mechanical testing of tensile properties

The mechanical performance of self-reinforced cellulose nanocomposites, all-cellulose hierarchical composites and hydrophobised BC nanofibrils reinforced PHB nanocomposites was characterised by tensile testing to deduce both tensile strength and Young's modulus.

Tensile tests were conducted according to the standard BS EN ISO 527-3:1996 (gauge length: 20 mm) using an Instron (4502, Instron, UK) equipped with a 1 kN load cell. In addition, all-cellulose hierarchical composites were tested using the same Instron equipped with a 10 kN load cell. The test complied with ISO standard 527-2:1996 (gauge length: 10 mm). A cross-head speed of 1 mm/min was used for the various tensile tests. Tensile test coupons (around 1.2 mm thick) were cut to dog-bone shape using a Zwick cutter (Zwick

Roell AG, Germany) equipped with an appropriate cutter template. The cut coupons were pre-conditioned for 7 d at $20°C$ in a desiccator with 60% relative humidity (RH) achieved using a saturated sodium bromide solution. The tabulated values are averaged from at least 5 independent tests and the errors presented are standard errors.

The effect of BC coating of sisal by exposing them to the bacterial culture medium on bulk properties of modified fibres, as described in Chapter 4, was evaluated by single fibre tensile testing. The mechanical tests were performed on original fibres, NaOH washed sisal fibres and BC coated and NaOH washed sisal fibres. A TST350 tensile stress tester (Linkam Scientific Instrument, UK) was used for single fibre testing with a cross-head speed of 1 mm/min and gauge length of 20 mm. The tests were carried out according to ASTM 1557-03 with a minimum of 10 fibres for each sample. Prior to testing the specimen were conditioned at $20°C$ for 7 d in 60% RH, then a single fibre was glued onto a cardboard frame with cyanoacrylate adhesive, which was cut prior to testing.

Furthermore, the tensile properties of hydrophobised BC nanofibrils reinforced PHB nanocomposites tested using the former tensile stress tester with a cross-head speed of 1 mm/min. The tensile tests complied with ISO standard 527:1995. The dog-bone specimens of the nanocomposites were of type 5A with a gauge length of 20 mm, width of 4 mm and a thickness around 110 μm.

2.12 Scanning electron microscopy

The morphology of various produced cellulose-based materials was characterised using scanning electron microscopy (SEM) at an appropriate magnification. The SEM observations were performed using a field emission gun scanning electron microscope (FEGSEM) LEO Gemini 1525 with an acceleration voltage of 5-15 kV (Leo Electron Microscopy Ltd, Germany). Initially, specimen were placed on a double-sided carbon tape mounted onto an aluminium stub and subsequently coated. Certain specimen (*i.e.*, BC nanofibrils, chemically modified BC nanofibrils, bioinorganic nanohybrids) were chromium sputtered for 1 min with current of 75 mA, other (*i.e.*, self-reinforced cellulose nanocomposites and all-cellulose hierarchical composites) were gold sputtered coated for 2 min at 20 mA using a K550 sputter coater (Emitech Ltd, UK).

2.13 Dynamic vapour sorption

The moisture sorption behaviour of self-reinforced regenerated cellulose nanocomposites was evaluated using dynamic vapour sorption (DVS) with respect to change in degree of crystallinity of regenerated cellulose matrix. DVS measures the change of mass of a specimen as a function of time, temperature and level of RH generated in an enclosed chamber. DVS characterises the rate of moisture uptake by a specimen as well as its ultimate moisture content.

The cellulose specimens were dried in a vacuum oven at $80°C$ to a constant weight prior to testing. Specimen testing was carried using a DVS-1000 (Surface Measurement System Ltd, UK). The environmental chamber was regulated to $30°C$. A single step protocol was chosen. The specimen was first conditioned in-situ at 0% RH for 5 h. Afterwards, the internal microbalance was tared and the mass change recorded. The moisture sorption was then initiated by a step rise of RH from 0% to 95% RH during 45 h. The sorption dynamic was assessed by the rate of mass change. The final moisture content is defined as:.

$$M_{\%} = \frac{M_t - M_0}{M_0} \tag{2.28}$$

where M_t is the specimen mass (g) at any given time and M_0 the initial sample mass (g). The change of specimen mass was normalised as a function of the root square time.

2.14 Summary of analytical methods

The various analytical methods introduced in this chapter are summarised in the following Table 2.1.

Table 2.1: Summary of various analytical methods described in the present chapter.

Analytical method	Specimen	Properties investigated
OD_{600}	Suspension of bacteria cells	Growth kinetics of bacteria population
ATR-FTIR	BC nanofibrils; regenerated MCC & BC; chemically modified BC nanofibrils	Functional groups on BC; cellulose polymorphs & allomorphs; functionalisation of BC
UV-Vis	Suspension of Au NPs & CdTe QDs; BC-based bioinorganic nanohybrids	Surface plasmon resonance (SPR)
Particle sizing (DLS)	Suspension of Au NPs & CdTe QDs; BC-based bioinorganic nanohybrids	Particle diameter of Au NPs
XRD	BC nanofibrils; regenerated MCC & BC; chemically modified BC nanofibrils	Degree of crystallinity; crystal type; crystal size
BET (N_2 adsorption)	BC cryogel & regenerated BC cryogel microsphere	Sorption behaviour; BET surface area; pore size distribution
EA	BC; grafted BC	Fraction of CHNS elements
TGA	BC nanofibrils; regenerated MCC & BC; chemically modified BC nanofibrils	Thermal stability; weight loss; rate of degradation
DSC	PHB & BC/PHB nanocomposites	Glass transition, crystallisation & melting temperature; crystallinity
DMTA	Regenerated MCC nano- & composites; BC/PHB nanocomposites	Glass transition; storage modulus; damping $\tan\delta$
Tensile testing	Regenerated MCC nano- & composites; BC/PHB nanocomposites	Tensile strength; Young's modulus
SEM	All specimens	Morphology; Surface topography
DVS	Regenerate MCC nanocomposites	Moisture content; rate of sorption

3

Production of Bacterial Cellulose

3.1 Introduction

3.1.1 Aims and objectives

The aim of the work reported in this chapter was to increase the bacterial cellulose (BC) production by a cellulose-producing strain of bacteria namely, *Gluconobacter xylinus*, using an instrumented stirred-tank bioreactor. The motivation for the higher BC yield was to reduce both the number of fermentations needed and the cost associated to produce a stock of BC required for later studies as described in following chapters.

The objectives of the work reported in this chapter were:

- To characterise the effect of both static and agitated fermentation conditions on the physical properties of biosynthesised BC.
- To increase the yield of biosynthesised BC by addition of a stainless-steel mesh along the vessel wall and the stirring shaft, thus enhancing the internal area of the bioreactor vessel.
- To characterise the properties of biosynthesised BC using analytical methods introduced in Chapter 2 such as SEM, OD_{600}, XRD, ATR-FTIR and TGA.

The present chapter is composed of 7 parts: literature review, experimental methodology, characterisation of *Gluconobacter xylinus* and biosynthesised BC, X-ray diffraction of BC produced in different fermentation conditions, ATR-FTIR spectroscopy of biosynthesised BC, thermal degradation of biosynthesised BC and conclusions. The following sections review

the generalities on cellulose materials, the biosynthesis of BC by cellulose-producing bacteria strain, the different fermentation processes of *Gluconobacter xylinus* strain, the physical properties of biosynthesised BC and the applications of BC. Section 3.2 describes the methodology used to produced BC in static and agitated culture conditions. The BC production, the growth kinetics of bacteria population of *Gluconobacter xylinus* and the improvement of BC yield subsequent to modification of the bioreactor vessel are characterised in Section 3.3. Then, the XRD characterisation of BC produced in different culture conditions will be discussed in Section 3.4. In the subsequent Section 3.5, the characterisation of BC by ATR-FTIR spectroscopy is discussed. The thermal stability and degradation behaviour of BC are characterised in Section 3.6. At last conclusions are drawn in Section 3.7, which is followed by suggestion for future work in Section 3.8.

3.1.2 Sources of cellulose materials

Cellulose polymer chains consist of repeating D-glucopyranose rings connected to one another by $\beta(1 \rightarrow 4)$ glycosidic links. Every anhydroglucose unit (AGU) in cellulose is flipped at 180° with respect to its adjacent AGU, as seen in Figure 3.1 [26]. Cellulose is a semicrystalline homopolymer. Generally, native cellulose materials possess a high degree of crystallinity, with occurrence of a paracrystalline organisation [3]. Cellulose is intrinsically hydrophilic owing to an extensive amount of hydroxyl groups, *i.e.*, three accessible per AGU [51]. Various cellulose-derivatives are produced using a versatile range of chemistry owing to chirality of the cellulose structure.

In fact, cellulose biosynthesised by plants is arranged within the plant cell walls to form a hierarchically self-assembled structure, which is composed of water soluble polysaccharides, hemicelluloses, lignocellulose, pectin, wax and other organic matters [52]. Thus, the purity and composition of plant cellulose are a function of its source. The properties of cellulose vary with respect to its morphology such as fibre, microfibril, nanofibril down to an elementary fibril, respectively, each of the aforementioned having a building block composed of AGUs. In the plant kingdom, cellulose is the primary structural constituent, thus constituting between 15% to 99% of plant-dried matter [3].

Cellulose, naturally synthesised, occurs in different conformation of polymorphs, such as, cellulose type I and II, the former being in a parallel-chain morphology and the latter in an anti-parallel-chain morphology [3], as seen in Figure 3.2. Other polymorphs of cellulose were observed when cellulose was subjected to liquid ammonia treatment and high temperature,

thus forming cellulose type III and IV, respectively [53,54]. In the early 1980s, the allomorphic forms of native cellulose, cellulose I_α and I_β were revealed using IR spectroscopy and ^{13}C solid-state nuclear magnetic resonance (NMR), where I_α corresponded to a one-chain triclinic unit cell and I_β was defined by a two-chain monoclinic unit cell [55]. Indeed the crystal type I of native cellulose is a composite made of two distinct crystalline allomorphs, I_α and I_β [56,57]. The ratio of I_α and I_β found within cellulose material depends on its biological origin. When originating from primitive organism (bacteria, algae) the I_α component is dominant, whereas, the I_β component is dominant for higher plants, as part of secondary walls of cellulose type I [58].

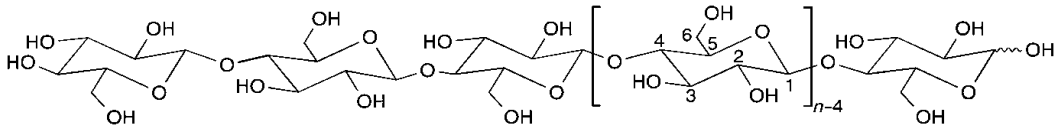


Figure 3.1: Molecular structure of cellulose (n=DP, degree of polymerisation) (reproduced from [2]).

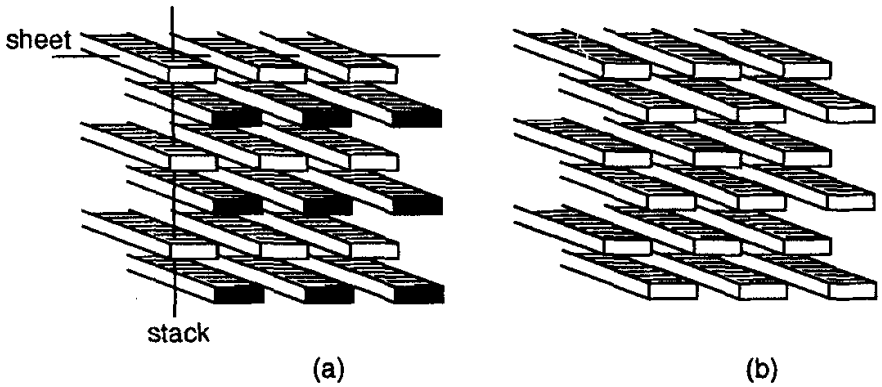


Figure 3.2: Schematic diagrams of (**a**) antiparallel orientation and (**b**) all-parallel orientation. All polymer chains within the same stack or sheet are parallel (reproduced from [3]).

3.1.3 Source of bacterial cellulose

Although, cellulose produced during plant photosynthesis accounts for most of cellulosic materials originating from biomass (Section 3.1), biosynthesis of cellulose is observed in other organisms. Biosynthesis of cellulose takes place also in a marine animal (Tunicate), fungi,

algae (*Valonia, Chaetamorpha*) and certain strains of bacteria (*Acetobacter, Acanthamoeba, and Achromobacter*)[22,59,60,61]. In recent years, cellulose-producing bacteria had received a strong interest as an alternative source of cellulose. An aerobic gram-negative strain of bacteria, namely *Acetobacter xylinum*, later reclassified as *Gluconobacter xylinus*[62] has been extensively studied and characterised owing to its ability to biosynthesise cellulose[63], as seen in Figure 3.3. The *Gluconobacter xylinus* strain has been isolated from various sources like, fruits, rotten-fruits, vegetables and environments such as juices, vinegar and alcoholic beverages[64]. Amongst 3000 bacteria strains screened for cellulose biosynthesis in agitated conditions, *Gluconobacter xylinus* subspecies BPR2001 isolated from cherry was by far the most efficient cellulose-producing microorganism[65]. Watanabe *et al.*[66] reported later, the breed of mutant *Gluconobacter xylinus* strain, namely BPR3001A, from their wild type parent BPR2001. This BPR3001A mutant in agitated cultivation was able to produce 65% more BC from a corn-steep liquor medium, while reducing by 83% the accumulation of acetan, a metabolic by-product, as compared to parent BPR2001.

Moreover, subspecies of cellulose-producing bacteria strain were selected by controlled mutation, genetic engineering and hybridisation, which exhibited a metabolic specificity or an ability to produce by-products or a greater tolerance to the composition of culture medium[67,68,69,70]. The development in *Gluconobacter xylinus* strains was attempted to improve the efficiency of the fermentation by increasing BC production with respect to the carbon source[71].

3.1.4 Biosynthesis of bacterial cellulose

In the literature, several studies described extensively the complex microbiologic machinery involved in controlling and regulating the biosynthesis of BC by *Gluconobacter xylinus*[72,73]. The biosynthesis of BC by *Gluconobacter xylinus* takes place in the plasma membrane of cells via a cellulose-synthesising complex (also referred as terminal complex) containing a specific enzyme, namely, cellulose synthase[74]. This enzyme is able to polymerise uridine diphosphate glucose (UDP glucose) produced by the metabolism of bacteria into single cellulose chains[69,75]. The terminal complex is located in nano-sized pores of 3.5 nm width aligned along cell side (approx. 50-80). Where these nano-sized pores containing terminal complexes (TC) are situated within the lipopolysaccharide membrane of bacteria, as seen in Figure 3.4[64,73]. Tokoh *et al.*[4] reported that the formation of BC ribbons by *Gluconobacter xylinus* occurred by 3 successive phases. The first one being the biosynthesis of sub-elementary BC

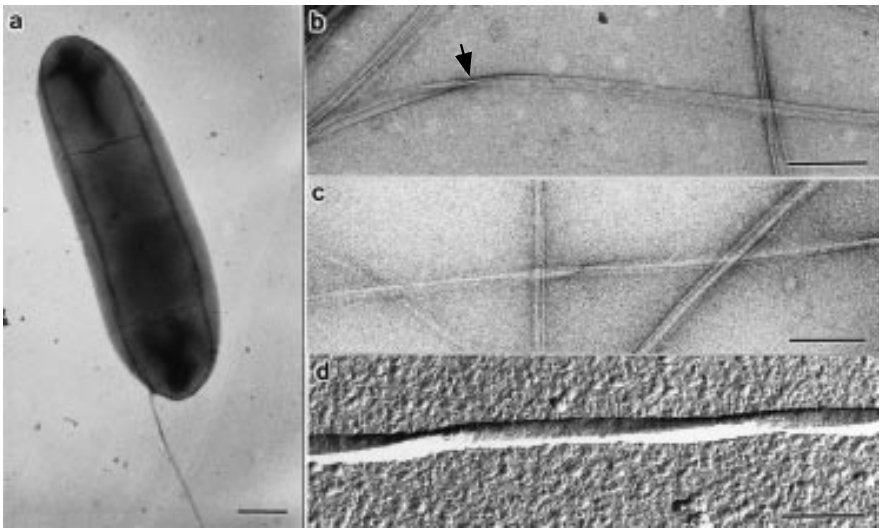


Figure 3.3: The cellulose and *Gluconobacter xylinus* cell in an H&S medium a.) A negatively stained cell producing a cellulose ribbon. The ribbon is formed parallel to the longitudinal axis of the cell. b.) Higher magnification of cellulose ribbons showing striations and twists (arrow). c.) A negatively stained cellulose ribbon prepared by rapid-freeze and substitution (RFS) method. d.) A shadowed cellulose ribbon. Scale bars: 0.5 (a) and 0.2 (b-d) μm. (reproduced from [4])

fibrils by TC, followed by aggregation of several sub-elementary BC fibrils forming microfibrils, followed by bundling of several microfibrils together into one ribbon.

The division of bacteria cells drives the rate of BC production, independently of carbon source used. A static culture experiment of *Gluconobacter xylinus* grown using succinate as a carbon source, showed that almost 50% of the succinate was utilised in BC biosynthesis after 24 h [76]. Under optimum conditions, cells of *Gluconobacter xylinus* achieved a rate of polymerisation of 200,000 glucose molecules per second [2,20]. In addition, an early study by Brown *et al.* [77] showed that BC ribbons elongated away from bacteria cell at a rate of 2 $\mu m \cdot min^{-1}$, from this observation an assimilation into cellulose of 470 attomole (amol) of glucose/ cell per hour was deduced.

In laboratory control experiment, Williams and Cannon [64] showed that extracellular BC synthesised by *Gluconobacter xylinus* promoted colonisation of a substrate (*i.e.*, apple slices) while preventing emergence of rival organisms competing for the same substrate. It is also assumed that a BC pellicle retains sufficient moisture to avoid drying of the colonised environment and provided shelter against UV irradiation, thus enhancing the viability of a *Gluconobacter xylinus* population [64,72].

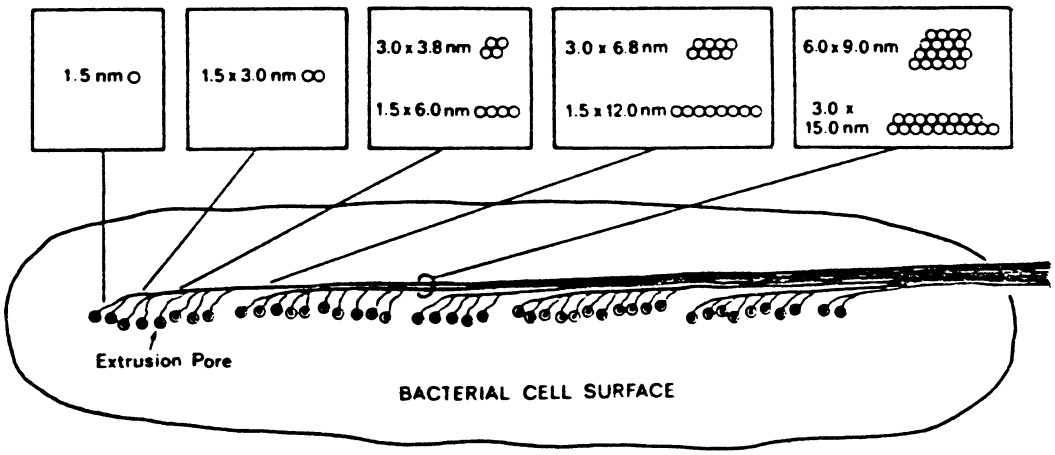


Figure 3.4: Generalised model of ribbon assembly in *Gluconobacter xylinus*, showing a possible mechanism of origin of microfibrils and separate fibrillar subunits within the ribbon. Shown in the boxes are possible packing arrangements of the 1.5-nm tactoidal aggregates (reproduced from [5]).

3.1.5 Fermentation process of *Gluconobacter xylinus* for biosynthesis of BC

Gluconobacter xylinus grows on various culture substrates. Under laboratory conditions, *Gluconobacter xylinus* and other cellulose-producing strains were cultured under static and agitated conditions and up-scaled to semi-industrial size bioreactors [78]. Static culture consists in inoculating aseptically a broth medium with a viable bacteria population and letting it grow statically for a certain cultivation time at a predefined temperature between 28° to 37° for thermotolerant *Gluconobacter xylinus* strain [79]. In this configuration, the bacteria produce a BC film at the air-liquid interface [80], where the thickness of BC film increases as a function of culture duration from a few micrometers to few centimetres [21,81], as exemplified in Figure 3.5a. On the other hand, agitated culture consist in the inoculation of a culture medium where the subsequent cultivation is carried out under a constant and controlled agitation, using an orbital shaker. The agitated culture condition enhances liquid-gas transfer leading to rapid growth of the bacteria population to the detriment of BC production. BC synthesised under agitated condition forms round balls in the broth instead of a well-organised film as in static culture [64], as exemplified in Figure 3.5b. Both aforementioned types of culture have a relatively low yield of BC since they are carried out in flasks with a restricted surface area. To improve BC production, cellulose-producing bacteria were cultured in an

instrumented bioreactor, as seen in Figure 3.6. However fermentation in bioreactor resulted in low yield of BC, although, oxygen and mass transfer were dramatically improved by mixing and agitation. When a *Gluconobacter xylinus* population was subjected to stress imposed by agitation in a bioreactor, it gave rise spontaneously to non-cellulose-producing mutants [64,72]. The mutants phenotypes throve from the excess of oxygen present in the culture medium. Moreover, the mutation undertaken was stable as long the culture medium remained agitated. Interestingly, if those mutant phenotypes were re-established into a static culture, they once again reverted to cellulose-producing bacteria. Furthermore, the BC accumulated during fermentation in the bioreactor increases the medium viscosity, thereby lowering the effectiveness of both mixing and aeration due to decrease in homogeneity of the culture medium [65].

Traditional culture medium, such as Hestrin and Schramm (H&S) medium [20], are composed of different carbon sources (glucose, fructose, sucrose, mannitol, arabitol), complex nitrogen (yeast extract), vitamin source (polypeptone) and other additives, those of which are costly and economically unsustainable at an industrial scale [82,83,84]. The cost of culture medium generally accounts for at least 30% of the total cost of fermentation. Therefore, cost-effective culture medium were investigated, such as, corn steep liquor (CSL) and molasses medium, by-products of corn wet-milling and the sugar industry, respectively [78,85].

Despite the fact that bacteria population of *Gluconobacter xylinus* cultured in agitated condition tended to mutate, thus significantly reducing BC production, the economical gain occurring from this fermentation process led to the development of strains of *Gluconobacter xylinus* more tolerant to stressing conditions and shearing inherent to agitated fermentation process, as discussed in Section 3.1.3. Meanwhile, bioreactor configurations were developed to tackle the requirements posed by culture of *Gluconobacter xylinus* strain in agitated conditions, such as an enhanced oxygen aeration through the culture medium for bacteria growth, reduction of shear forces to avoid mutation, as well as reasonable energy consumption [82]. Several configurations of bioreactors were reported in recent literature, such as a stirred tank bioreactor fitted with various type of impellers [86], a low-shear stress air-lifted bioreactor (steering-free), a spherical type bubble column bioreactor, a rotary disk bioreactor and a plastic composite support (PCS) biofilm reactor [78,82,87,88,89].

3.1.6 Properties of bacterial cellulose

BC is characterised by a high degree of crystallinity between 70% to 90% [23,90]. As much as 70% of its crystalline structure is composed of metastable cellulose type I_α (triclinic con-

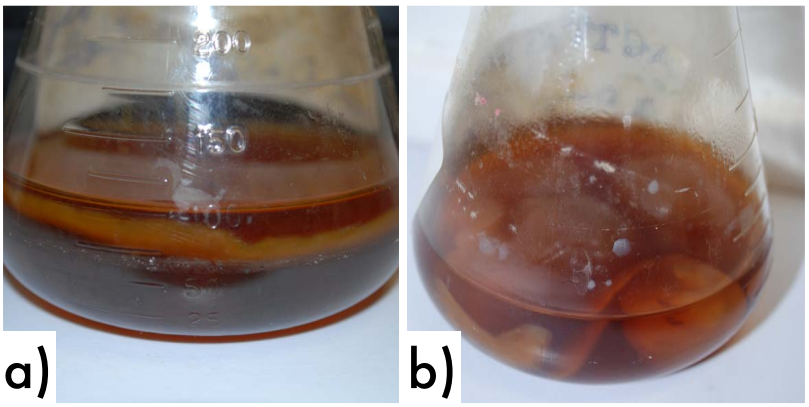


Figure 3.5: Shape of biosynthesised BC by *Gluconobacter xylinus* BPR2001 after 3 d of culture at 30°C under; a) static Erlenmeyer flask; b) agitated Erlenmeyer flask.

formation), compared to 30% for plant cellulose[65]. Furthermore, the weight-average degree of polymerisation ($D\bar{P}w$) of nitrated BC samples, which were nitrated in a solution of nitric acid/diphosphorous pentoxide was determined using a gel permeation chromatography (GPC) for static and agitated culture, where the $D\bar{P}w$ were 14400 and 10900, respectively[23]. In addition BC is insoluble in common organic solvents owing to its molecular configuration constituted of parallel and alignment arrangement of $\beta(1 \rightarrow 4)$ glycosidic AGU chain, so called cellulose type I[72]. The structural characteristics and features of BC nanofibrils are dependent on the bacterial strain producing it, the type of culture and composition of broth medium.

The dimension of BC nanofibrils varies from 1 to 25 nm in width, which corresponds to stacking of 10 to 250 AGU chains, thus forming highly regular intra- and interchain hydrogen bonds. The length of BC nanofibrils varies between 1 to 9 μm, which is equivalent to 2 000 to 18 000 AGU[72,91]. BC ribbons formed by aggregation of individual BC nanofibrils are approximately 100 nm wide and 3 to 8 nm thick[25]. Yamanaka *et al.*[92] reported the use of antibiotics and other chemical reagents added to the culture medium to change the morphology of bacteria cells of *Gluconobacter xylinus*, which in time synthesised wider BC ribbons having thus modified both the mode of aggregation and structural features of their biosynthesised BC nanofibrils. Single BC nanofibrils exhibits outstanding mechanical performance. Guhados *et al.*[93] calculated a Young's modulus of 78 GPa using atomic force microscopy (AFM) where the calculation was based on a clamped-beam model. However,

Tanaka *et al.*[94] reported for elementary of cellulose I_β a Young's modulus between 124 and 155 GPa, which was determined by molecular simulation.

The properties of BC depend on whether the BC tested was a swollen-gel (*i.e.*, pellicle) or a dried-film or else individual nanofibrils. Purified and subsequently dehydrated BC gel formed during static culture exhibits interesting in-plane mechanical properties. In fact, a Young's modulus of 30 GPa was measured for a BC film, which was heat-press dried after removal of cell debris by subsequent treatments with 0.5% NaClO and 5% NaOH solution, respectively[95]. Such outstanding performance arose from the extensive hydrogen bonding of BC nanofibrils and the inherent high degree of crystallinity of BC. However the swollen-gel possesses an out-of-plane elastic response when squeezed[24,25]. BC gel has an excellent H_2O holding capacity of nearly 100 times its own weight. The H_2O retention of BC gel was improved by addition of a small concentration of water-soluble polymers (WSP) to the H&S culture medium, such WSP included were carboxymethyl cellulose (CMC), methyl cellulose (MC), cyclodextrin, cationic starch or polyethylene glycol (PEG)[96,97].

3.1.7 Applications of bacterial cellulose

Since the early isolation of the *Acetobacter xylinus* strain by Hestrin and Schramm in 1954[21], BC biosynthesis by strain of cellulose-producing bacteria had received enormous attention from scientists keen to exploit its intrinsic properties[2]. The outstanding mechanical properties and biocompatibility of BC enable its use in a broad range of applications from paper products, biomedical devices, acoustic diaphragms, filtration membranes, electronic papers to nano- and composite materials[98,99,100,101].

BC paper was implemented successfully in to high fidelity loudspeakers and earphones in the mid-90's by Sony Corp., owing to high sonic velocity and low dynamic loss[25]. Recently, Czaja *et al.*[27,102] reviewed the potential use of films of never-dried BC in biomedical applications emphasising its excellent ex- and in-vivo biocompatibility and hemocompatibility, oxygen permeability and mechanical properties of BC. Moreover, the shaping and moulding of BC into versatile forms, such as membranes, films, hollow tubes was achieved during its biosynthesis by *Gluconobacter xylinus*[103]. BC was employed in preparation of various scaffolds for tissue engineering, tissue regeneration applications, owing to an excellent biocompatibility and mechanical performance[28,104]. BC has recently been used in engineering materials to produce both nano- and composite materials. Soykeabkaew *et al.*[105] reported the preparation of all-cellulose composites based on selective dissolution of BC nanofibrils

using a cellulose solvent. Juntaro *et al.*[106] developed hierarchical bio-based composites materials composed of bio-based polymers, natural fibres, onto which bacteria cells deposited in-situ BC in agitated culture, thus creating a BC coating. This procedure enabled a significant enhancement of fibre-matrix interfacial properties in composites[107]. A novel class of advanced functional materials was developed using BC nanofibrils, where BC nanofibrils were hybridised with various nanoparticles, such as silver, gold, titanium oxide to confer to a BC substrate, antimicrobial[108], glucose biosensing[109,110] and photocatalytic properties[111], respectively. Furthermore, BC is a promising biopolymer, which exhibits great potential for a wide range of applications such as biomedicine, biomaterials engineering, membranes and polymer nanocomposites[27,28,29].

3.2 Experimental

3.2.1 Materials

Freeze-dried bacteria of *Gluconobacter xylinus* BPR2001 (ATCC® 700178) strain were purchased from LGC Promochem Ltd. (Middlesex, UK). D-fructose, peptone, yeast-extract, sodium phosphate dibasic (Na_2HPO_4), citric acid, cellulase (Celluclast®), sodium hydroxide (NaOH) and nitric acid (assay 37%) (HNO_3) were purchased from Sigma-Aldrich (UK). Sodium citrate tribasic dihydrate ($Na_3C_6H_5O_7{\cdot}2H_2O$) was bought from Fluka (UK). Other reagents, hydrochloric acid (HCl), standard grade ethanol (EtOH) and acetone were obtained from VWR (UK). Ultra pure water produced by a NANOpure deionisation system (Barnsteadl Thermolyne, Dubuque, USA) with resistivity of 18.2 $M\Omega \cdot cm^{-1}$ was used for the preparation of the culture medium. All reagents were ACS grade and used without further purification, however those used to prepare the culture medium were cell culture-tested grade.

3.2.2 Cultivation of *Gluconobacter xylinus* bacteria

Growth medium based on Hestrin and Schramm[21] (H&S) recipe was modified by using D-fructose (5 wt./v.%) as carbon source instead of glucose, yeast extract (0.5 wt./v.%), peptone (0.5 wt./v.%), Na_2HPO_4 (0.27 wt./v.%) and citric acid (0.115 wt./v.%) with an appropriate volume of ultra pure H_2O, *i.e.*, 100 ml and 5 L, respectively.

Modified H&S culture medium were prepared in a beaker with an appropriate volume depending on the type of culture performed. Briefly, 100 ml of freshly prepared culture medium

was placed in a 250 ml Erlenmeyer flask for either static or agitated culture conditions. Alternatively, for culture in a bioreactor, 5 L of freshly prepared modified H&S culture medium was placed in a 7 L bioreactor vessel, Bioflo® 110 (New Brunswick Scientific, UK) equipped with a Rushton impeller. Prior to any bacteria inoculation the different culture medium were sterilised in an autoclave (LTE Scientific Ltd., UK) at 120°C for 20 min. Initially, freeze-dried bacteria of *Gluconobacter xylinus* were brought gently to ambient temperature and inoculated aseptically into a 250 ml Erlenmeyer flask containing 100 ml of modified H&S culture medium. The Erlenmeyer flask was placed onto an orbital shaker (Denley Orbital Mixer, UK) with an oscillation frequency of 110 rpm for 3 d in an environmental chamber set to 30°C. To detach bacteria cells from the BC pellicle formed, the Erlenmeyer flask was shaken vigorously for a short period of time both by hands and using a vortex shaker and then, left settling down. To maintain a viable bacteria population, every 3 d, 10 ml of broth containing bacteria was inoculated into a 250 ml Erlenmeyer flask containing 100 ml of fresh culture medium.

An appropriate number of 250 ml Erlenmeyer flasks containing 100 ml of culture medium were inoculated with 10 ml of a 3 d old pre-cultured broth (modified H&S) and then were stored accordingly for static or dynamic culture for a predefined cultivation time. In the case of culture using a bioreactor, 100 ml of a 3 d old pre-cultured broth was inoculated aseptically into the bioreactor vessel. Then, cultivation was carried out for 7 d at a stable temperature of 30°C with an agitation of 750 rpm, which was later increased to 900 rpm after 4 d which was necessary because of the increase of viscosity of culture medium[63,82]. Sterile airflow was supplied at a flow rate of 4 L/min through a high volume sterile filter with pore size of 0.2 μm. The pH of culture medium was continuously adjusted to pH 5.5 by addition of 4 N solution of either NaOH or HCl.

The growth of bacteria population of *Gluconobacter xylinus* was assessed by optical density measured at a wavelength of 600 nm (OD_{600}), as described in Section 2.1. To obtain a suspension of *Gluconobacter xylinus* cells without BC nanofibrils, a broth containing bacteria cells and BC produced was readily homogenised for 2 min. Then, 5 ml of the suspension was collected and placed in a 15 ml Falcon tube, prior to centrifugation at 4000 g for 5 min. The pellet composed of BC and bacteria cells was re-suspended into 3 ml of phosphate buffer solution (pH 5) containing 5 wt./v.% of cellulase. The suspension was gently stirred at 250 rpm at 50°C for 30 min to hydrolyse BC. Subsequently, an aliquot of cells suspension was placed

in a UV-transparent plastic cuvette prior to measuring its OD_{600} using a BioPhotometer (Eppendorf, UK).

BC pellicle produced from various culture conditions were collected and blended with additional dH_2O using a Waring laboratory blender (Torrington CT, USA). A centrifugation at 15,000 g for 15 min in Sorvall Legend RT^+ centrifuge (DJB Labcare Ltd, Buckinghamshire, UK) was performed to remove the excess of H_2O. The de-watered BC product was then re-suspended in 5 L of 0.1 N NaOH solution and stirred for 20 min at $80°C$ to lyse cells and dissolve debris. The NaOH treated BC was successively centrifuged and washed with dH_2O until it reached neutral pH. Furthermore, the never-dried BC was placed in either 50 ml falcon tube or 250 ml Nalgene® centrifuge bottle, prior to slow drying in a vacuum oven set at $60°C$ for its characterisation as presented in the present chapter. However, stock of never-dried BC was prepared using biosynthesised BC in bioreactor for later experiments described in following chapters 5, 6 & 7. In subsequent chapters, never-dried BC was further hydrolysed to constitute a stock of HCl hydrolysed never-dried BC. Hydrolysis of NaOH treated BC was performed as follows; 3.3 wt./v.% of never-dried NaOH-treated BC was placed in a 500 ml round bottom flask containing 300 ml of 5 N HCl solution and fitted with a condenser. Then the BC suspension in HCl solution was heated to $110°C$ for 20 min under reflux and vigourous stirring. The hydrolysed BC was successively centrifuged and re-suspended in 2.5 L of dH_2O and homogenised at 30,000 rpm for 2 min with a Polytron® PT 10/35 GT (Kinematica AG, Lucerne, Switzerland), the former operation was repeated until neutral pH was reached. At last, HCl hydrolysed BC was centrifuged at 15,000 g for 45 min and stored in fridge at $5°C$ until further usage.

3.2.3 Conditions for bacterial cellulose production

Static culture was carried out on bench-top located within a temperature-controlled environmental chamber. Agitated culture was carried out using an orbital shaker set to a predefined oscillation rate, which, itself was located within a temperature-controlled environmental chamber, as seen in Figure 3.6a. The bioreactor used in this study for cultivation of *Gluconobacter xylinus* is shown in Figure 3.6b in operating conditions. The instrumented-bioreactor was composed of 3 distinct parts, a chilling unit, a control unit and a stirred vessel, respectively. The chilling unit was continuously maintaining the cooling fluid at a constant temperature and circulated it in a closed-loop within a cooling-coil inside the bioreactor vessel. The control unit enabled input and adjustment of various parameters during

bacteria culture, such as agitation speed, air flow-rate, pH, temperature, sampling sequence and culture duration, respectively. The stirred-vessel was equipped with an agitation motor, measuring probes, a heating blanket and various tubing. The vessel was equipped with baffles, cooling-coil, air-sparger and stirring rod fitted with Rushton impellers.

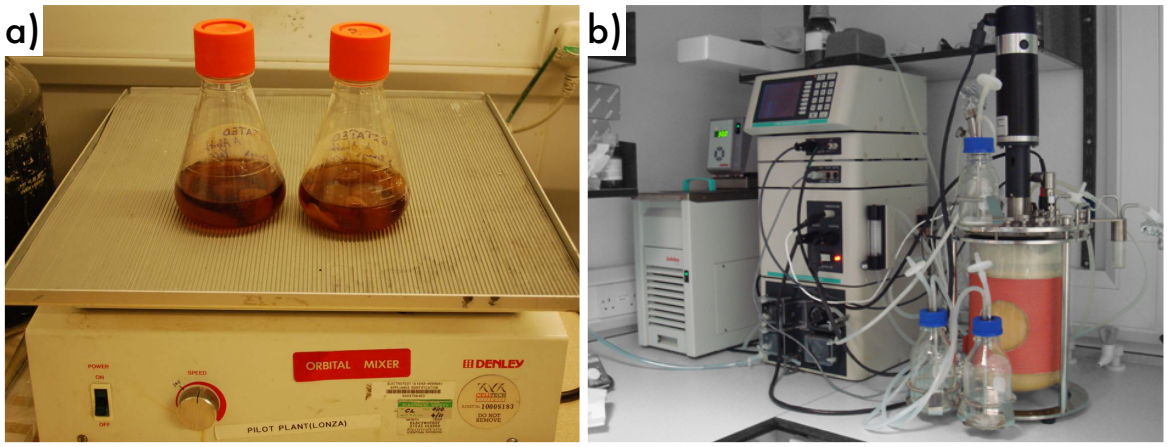


Figure 3.6: a) Photograph of Erlenmeyer flasks placed onto an orbital shaker in the case of agitated culture; b) Photograph of instrumented-bioreactor equipped with feedback control-loop.

3.3 Characterisation of *Gluconobacter xylinus* and biosynthesised BC

3.3.1 Biosynthesised bacterial cellulose

BC was biosynthesised by *Gluconobacter xylinus* strain using either a static culture or an agitated culture. SEM micrographs of dehydrated BC from static culture and containing *Gluconobacter xylinus* cells are shown in Figure 3.7 for both low and high magnification. The BC network is covered by randomly distributed *Gluconobacter xylinus* cells, where some of them had bundles of BC nanofibrils expelled from their membranes. At higher magnification, *Gluconobacter xylinus* cells appear slightly embedded into the surrounding BC network. The ball-like shape of bacteria cells resulted from the ambient dehydration of the BC pellicle with attached bacteria cells. Nonetheless, bacteria cells present generally more elongated cylinder-like shape when observed under SEM after freeze-drying of a BC pellicle, as reported by Iguchi *et al.*[25].

The morphology of BC nanofibrils after 7 d of static culture and NaOH treatment is shown is Figure 3.8. BC nanofibrils appear agglomerated to one another, thus forming a dense network, where extensive hydrogen bonds were formed during ambient drying as H_2O evaporated. However, the width of single BC nanofibril was between 50 to 60 nm, as measured from the SEM micrographs. The morphology of BC nanofibrils observed was in agreement with dimension usually reported in literature[25,72,91,92].

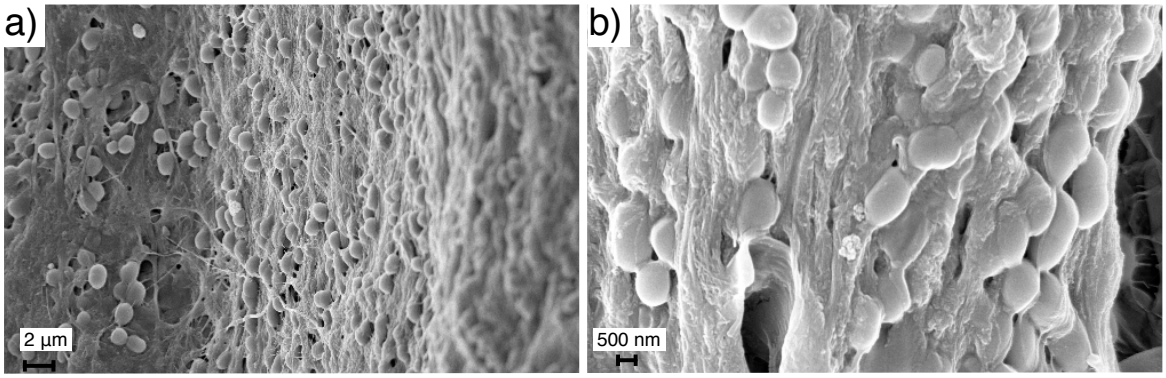


Figure 3.7: SEM micrographs of dried BC pellicle with attached *Gluconobacter xylinus* cells after 7 d of static culture.

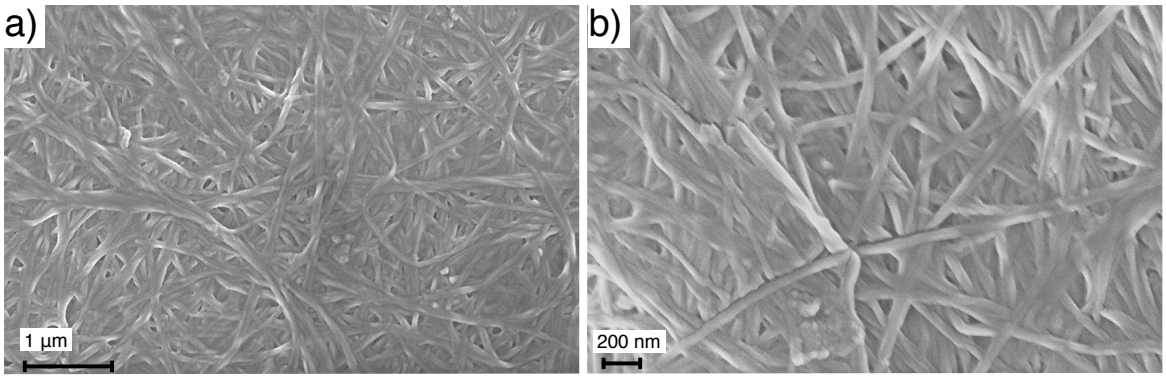


Figure 3.8: SEM micrographs of dehydrated BC nanofibrils after 7 d of static culture and subsequent treatment with 0.1 N NaOH to lyse *Gluconobacter xylinus* cells (Section 3.2.2).

3.3.2 BC productivity and growth of *Gluconobacter xylinus* population

BC productivity under agitated culture condition and growth of bacteria population of *Gluconobacter xylinus* were monitored using OD_{600} as shown in Figure 3.9. OD_{600} shows that bacteria population of *Gluconobacter xylinus* expanded rapidly for the initial 48 h (2 d) culture. During the exponential growth phase of the bacteria, the BC production increased slightly while remaining at a low level. Thereafter, the OD_{600} of bacteria in the broth culture increased only slightly, as bacteria population went into a stationary growth phase. Thus, BC production steeply rose after 72 h (3 d) until end of cultivation 4 d later, where, the BC yield reached nearly 2 g/L. The pH of the culture medium remained slightly acidic throughout cultivation. For the initial 96 h (4 d) of cultivation, the pH of the culture medium decreased steadily from 5.41 to 4.87, thus corresponding to the growth of the bacteria population. Beyond 96 h of cultivation, the pH increased slowly over the remaining culture time to 5.75, thus corresponding to both stationary phase of bacteria and intense BC production. Yang *et al.*[112] reported the profile of bacteria population of the *Gluconobacter xylinus* subspecies BRC5 in agitated culture using a CSL culture medium exhibited a 24 h lag phase, followed by exponential cell growth, where, thereafter a slow increase of the cells number was noticed until 120 h. The *Gluconobacter xylinus* BPR2001 studied here in agitated culture using a modified H&S culture medium, followed a growth profile of bacteria population similar to those reported in the literature for other cellulose-producing bacteria strains. The absence of a lag phase was attributed to utilisation of a 3 d old pre-cultured *Gluconobacter xylinus* BPR2001 to inoculate a fresh culture medium, thus enabling a rapid growth of bacteria.

3.3.3 Improvement of BC production using a bioreactor

The idea of increasing the area inside the bioreactor vessel came from the experimental observations of agitated fermentation of *Gluconobacter xylinus* bacteria, where a significant fraction of the biosynthesised BC was anchored around the stainless-steel components inside the bioreactor vessel, *i.e.*, baffles, cooling-coil, air-sparger and stirring-axe. Therefore, stainless-steel meshes were added along the internal wall of the bioreactor vessel and stirring shaft to increase the area where the biosynthesised BC can be anchored. Furthermore, the effect of the additional stainless-steel meshes in the bioreactor vessel on the yield of BC produced during agitated fermentation *Gluconobacter xylinus* bacteria was investigated.

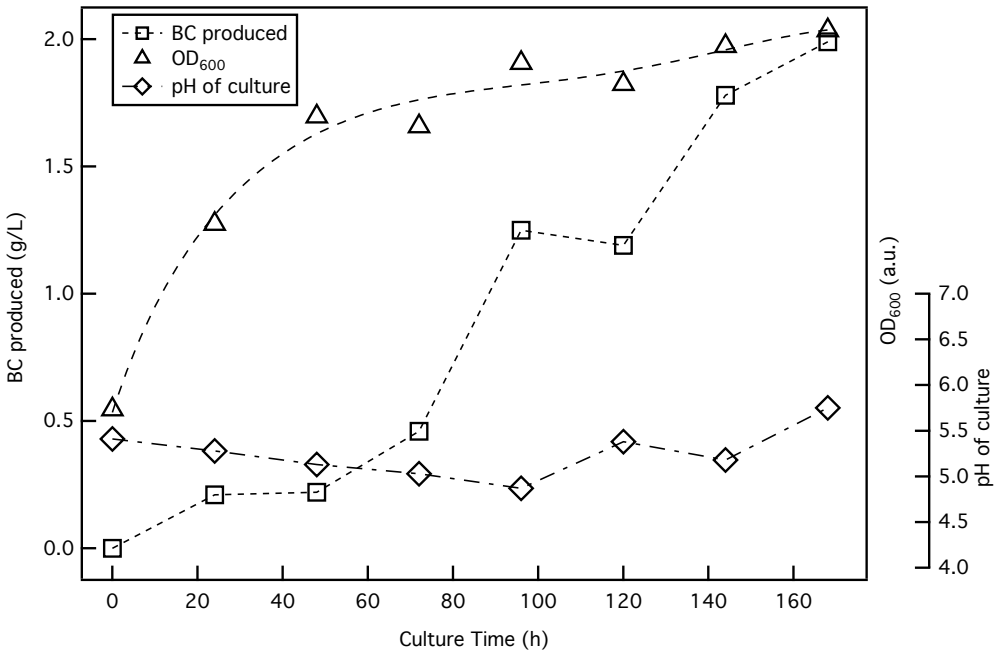


Figure 3.9: BC productivity, growth of *Gluconobacter xylinus* bacteria and variation of pH in the case of agitated culture in Erlenmeyer flasks using modified H&S culture medium.

Photographs of the internal configuration of the bioreactor vessel are shown in Figure 3.10 for both standard and enhanced configuration, respectively. The standard configuration refers to the configuration recommended by the manufacturer. Whereas, the modified configuration is composed of the standard components with the exception of two additional components. First, an open-ended cylindrical-shaped cage made from stainless-steel with a diameter of 110 mm and height of 30 mm. This cage is located on the impeller shaft and was positioned above the top impeller blade by sections of silicon tubing of various diameter forming stepped-stopper. In addition, the cage is able to rotate freely around the axis, therefore not driven during axis rotation. The other component placed along the internal wall of the bioreactor vessel is a rectangular mesh made from stainless-steel, with the following dimensions, 310 mm in length and 210 mm in height. The rectangular mesh is thus kept in place by the outward force exerted by semicircular baffles part, as shown in Figure 3.10.

The additional components enabled a significant increase in the BC production using the bioreactor, from 2.5 g/L produced using the standard configuration to 6.1 g/L yielded using the modified configuration, which resulted in more than two-fold improvement, as

summarised in Table 3.1. The gain in BC productivity was achieved by an extensive BC biosynthesis away from stainless-steel mesh supports. After 7 d of agitated culture, the stainless-steel mesh supports were covered with a thick layer of BC having the aspect of a rough surface aspect on one side and a smooth templated pattern of the squared-mesh on the other, which corresponded to the surface of the BC layer in contact with the agitated culture medium and the mesh support itself, respectively. The mechanism by which BC was anchored onto stainless-steel mesh supports has yet to be fully understood nor has it been reported in literature about cellulose-producing bacteria strains. Experimental observations suggested that *Gluconobacter xylinus* cells had a strong affinity toward the mesh supports possibly due to surface compatibility or flow stagnation along the leading edge of wire facing the agitated flow (radially generated), where BC nanofibrils are produced thus immobilising bacteria. Cheng *et al.*[88] reported that immobilisation of bacteria during cultivation in cell-recycle and hollow-fibre bioreactors resulted in enhanced BC production, owing to formation of biofilms. Moreover, BC began to aggregate onto stainless-steel mesh supports during the early stage of cultivation in bioreactor.

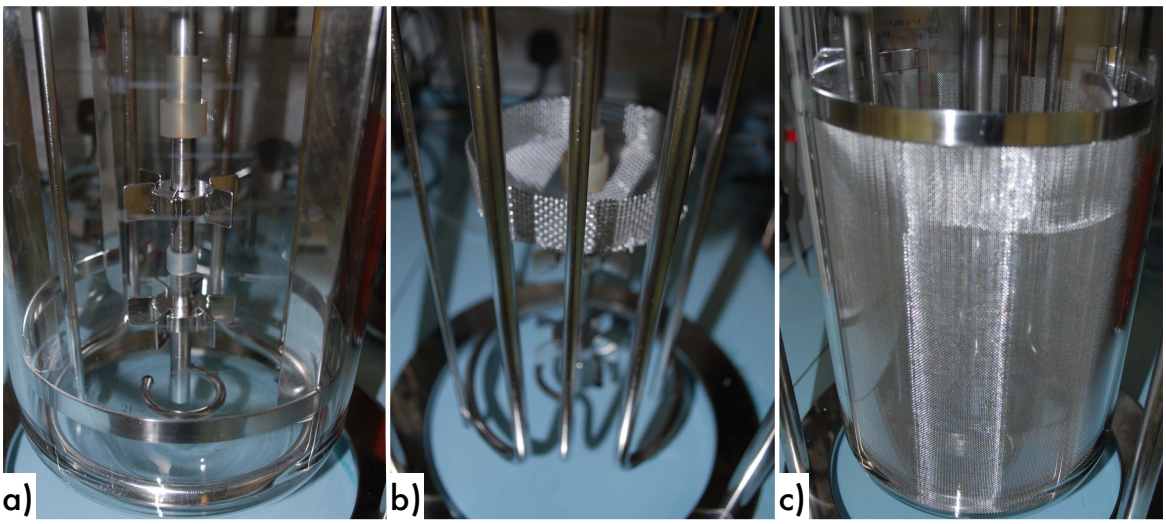


Figure 3.10: Photographs of bioreactor vessel with different internal configurations. a) standard configuration; b,c) modified configuration with additional stainless-steel meshes to create a greater surface area.

Table 3.1: Effects of internal configuration of stirred tank vessel on BC biosynthesis by *Gluconobacter xylinus* under agitated culture.

Configuration type	BC produced (g/L)
Standard	2.5 ± 0.6
Modified	6.1 ± 0.5

3.4 XRD characterisation of BC cultured in different culture conditions

The XRD diffractograms of BC produced in different culture conditions is presented in Figure 3.11. All specimens exhibit the typical diffractogram of cellulose type I, as expected from biosynthesised BC by *Gluconobacter xylinus* and also discussed in earlier Section 3.1.6. The diffraction planes, which correspond to [101], [10$\bar{1}$], [002] and [040] lattice were positioned at 2θ of 14.5°, 16.6°, 22.7° and 35°, respectively. The degree of crystallinity of BC, as determined by Segal's equation[36] (equation 2.9), is smaller for BC produced under agitated culture conditions (Table 3.2). For BC produced in static culture, the degree of crystallinity is as high as 95% and drops to 82% for BC produced in the bioreactor. Similarly, the size of BC crystals formed under static culture was larger than those formed in agitated culture conditions. The external stress exerted during agitated culture disturbed the crystallisation process of BC, and thus, the self-assembly mechanism taking place away from the membrane of the bacteria cells (Section 3.1.4). In an earlier study, Watanabe *et al.*[23] showed that the reduction of the degree of crystallinity and the size of BC crystals were strongly correlated with the culture conditions in which cellulose-producing bacteria were cultured. Despite of various culture conditions, BC specimen retained the characteristic of cellulose type I, as well as, a high degree of crystallinity although it decreased slightly in case of agitated culture conditions. Moreover, the reduction of both crystal size and degree of crystallinity of BC from agitated conditions were related to the variation in the ratio of cellulose allomorph I_α and I_β, as will be discussed in Section 3.5, later.

3.5 ATR-FTIR characterisation of biosynthesised BC

The superimposed ATR-FTIR spectra of BC produced in static, agitated Erlenmeyer flask and in a bioreactor are presented in Figure 3.12. A typical ATR-FTIR spectrum of BC

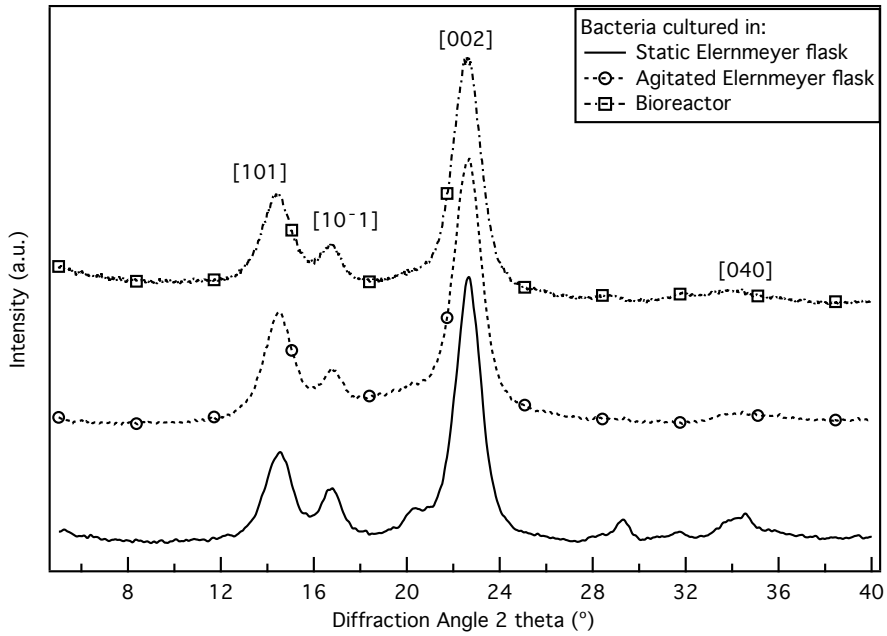


Figure 3.11: X-ray diffractogram of dried biosynthesised BC produced by *Gluconobacter xylinus* cultured in various conditions: static, agitated and in a bioreactor, respectively.

Table 3.2: Crystal size of lattice [101], [10$\bar{1}$] and [002], and degree of crystallinity of bacterial cellulose synthesised by *Gluconobacter xylinus* under various culture conditions.

Culture conditions	Crystallite size			Crystallinity
	[101] (nm)	[10$\bar{1}$] (nm)	[002] (nm)	(%)
Static Erlenmeyer	5.4	6.9	6.6	95.2
Agitated Erlenmeyer	5.5	6.6	6.2	89.6
Bioreactor	4.9	6.1	6.0	82.3

exhibits specific spectral bands at high wavenumbers and other within the fingerprint region of cellulose, between 1800 cm^{-1} and 900 cm^{-1}. Spectral band assignment to cellulose have been studied extensively and reported in comprehensive reviews [113,114]. Moreover, Table 3.3 summarised the main absorption bands and assignment for the ATR-FTIR spectra of bacterial cellulose. The band assigned to O-H stretching vibration of cellulose is identified between 3600 cm^{-1} and 3000 cm^{-1} [115]. Other functional groups contribute to this broad spectral region, they are related to inter-, intra-molecular hydrogen bonds, as well as, H-bonded OH groups, resulting from conformation and packing arrangements of cellulose chains [116]. The spectral band located at 2900 cm^{-1} is assigned to C-H stretching vibrations of BC (including -CH_2 and -CH_3) [117], whereas the spectral bands located at 1420, 1375, 1335 and 1278 cm^{-1}, are corresponding to the in-plane bending of the former C-H groups [114]. Furthermore, the band located at 3350 cm^{-1} indicates that BC has a conformation of cellulose type I [118], which is in agreement with XRD analysis in Section 3.4. Within the fingerprint region, the band at 1640 cm^{-1} is assigned to -OH bending of H_2O absorbed onto the BC network and also to -OH groups of BC itself [119]. Other peaks located at 900 cm^{-1} and 1160 cm^{-1} are assigned to C-O-C stretching of $\beta(1 \rightarrow 4)$ glycosidic link of BC [118,120]. The bands centred around at 1032 cm^{-1} and 1058 cm^{-1} are assigned to C-O stretching of secondary and primary alcohols, respectively, positioned on the AGU ring at C-3 and C-6 [116]. The most obvious change observed related to -OH stretching of BC produced under agitated culture conditions the peak intensity decreased as compared to spectrum of BC obtained in static culture, this variation in intensity revealed a reorganisation of hydrogen bonding in BC. This reorganisation was also an indication of transformation of cellulose crystal I_α to I_β [121]. Moreover, ATR-FTIR spectra presented herein for biosynthesised BC by *Gluconobacter xylinus* BPR2001 were very similar to those reported by Czaja *et al.* [90] for BC produced in static and agitated culture using a *Acetobacter xylinum* NQ5 strain.

As discussed in early section, cellulose allomorph I_α corresponds to a triclinic conformation of cellulose crystals, whereas, I_β relates to a monoclinic arrangement, which is thermodynamically more stable. The fraction of cellulose I_α and I_β was determined from ATR-FTIR spectra of BC by integrating of area associated to spectral bands located at 750 cm^{-1} and 710 cm^{-1}, respectively [122]. In addition, the band around 750 cm^{-1} was assigned to the CH_2 rocking mode of cellulose I_α [121]. The shoulder band around 3240 cm^{-1} was also assigned to cellulose I_α [121]. The change in the fraction of cellulose allomorph type I_α and I_β constituting the BC network is presented in Table 3.4 for different culture conditions. Under static conditions,

biosynthesised BC using a modified H&S medium is composed at 62% of cellulose I_α. However for both types of agitation, namely, agitated Erlenmeyer flask and in a bioreactor, the amount of cellulose I_α decreases with regards to its I_β counterpart. The analysis of cellulose crystal allomorphs formed during biosynthesis of BC by *Gluconobacter xylinus* showed that an agitated culture modified the fraction of cellulose I_α and I_β. The interference in crystallisation of BC nanofibrils, initiated by agitated culture conditions, resulted in formation of BC crystals of smaller size, which preferentially induced the formation of cellulose allomorph type I_β.

Table 3.3: Summary of main absorption bands and assignment for the ATR-FTIR spectra of bacterial cellulose.

Wavenumber (cm^{-1})	Band assignment	Reference
3600-3000	O-H stretching	[115]
2900	C-H stretching	[117]
1640	-OH bending (& absorbed H_2O)	[119]
1420, 1375, 1335, 1278	C-H in-plane bending	[114]
1160, 900	C-O-C stretching (glycosidic link)	[118,120]
1058, 1032	C-O stretching (at C-3 & C-6)	[116]
750	CH_2 rocking	[121]

Table 3.4: Fraction of cellulose allomorph I_α and I_β constituting the BC structure produced under various culture conditions.

BC produced in	I_α (%)	I_β (%)
Static Erlenmeyer flask	62	38
Agitated Erlenmeyer flask	61	39
Bioreactor	56	44

3.6 Thermal degradation of biosynthesised BC

The thermal degradation under inert N_2 atmosphere of biosynthesised BC by *Gluconobacter xylinus* strain in static, agitated culture and bioreactor are presented in Figure 3.13. The degradation profile is different for all BC specimens (Figure 3.13**I**). The degradation temper-

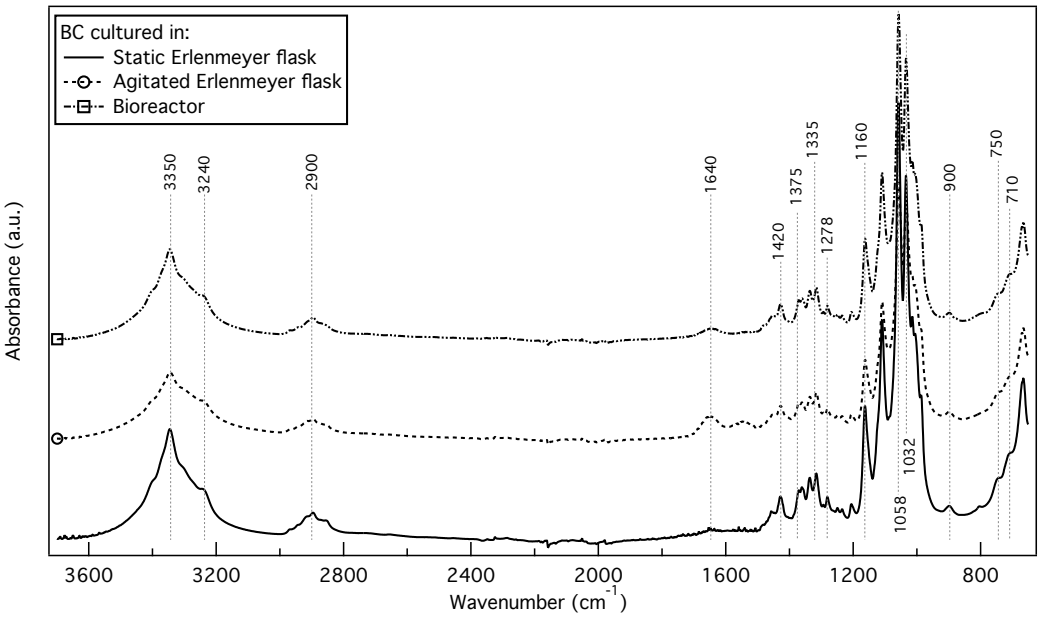


Figure 3.12: ATR-FTIR spectra of biosynthesised BC in various culture conditions namely, static, agitated and in a bioreactor.

ature of BC produced in agitated Erlenmeyer flask culture and in a bioreactor are $277°C$ and $276°C$, respectively, those are lower than the $309°C$ observed for BC produced in a static Erlenmeyer flask culture (Table 3.5). Such difference was attributed to both reduction of degree of crystallinity (Section 3.4) and different fraction of cellulose allomorphs for BC produced in agitated conditions. Although, the rate of BC degradation decreases from 1.84 to 1.50 wt.% $\cdot\, min^{-1}$ for static and agitated Erlenmeyer flask cultures, respectively. This drop is greater for BC produced in a bioreactor with value of 1.42 wt.% $\cdot\, min^{-1}$ (Table 3.5). On the other hand, the peak of degradation temperature shifts slightly from lower to higher temperature depending on the culture conditions (Figure 3.13**II**). The char yield was between 11% and 13% of initial weight of BC, showing that BC biosynthesis results in a high purity cellulose product. TGA of BC revealed that degradation kinetic and thermal stability were closely associated with the culture conditions and thus with the degree of crystallinity and ratio of crystal allomorph I_α and I_β present in BC specimen. Moreover, the thermal degradation profile of biosynthesis BC under various culture conditions was in strong agreement with thermal degradation of cotton textile fabric reported by Alongi *et al.*[123].

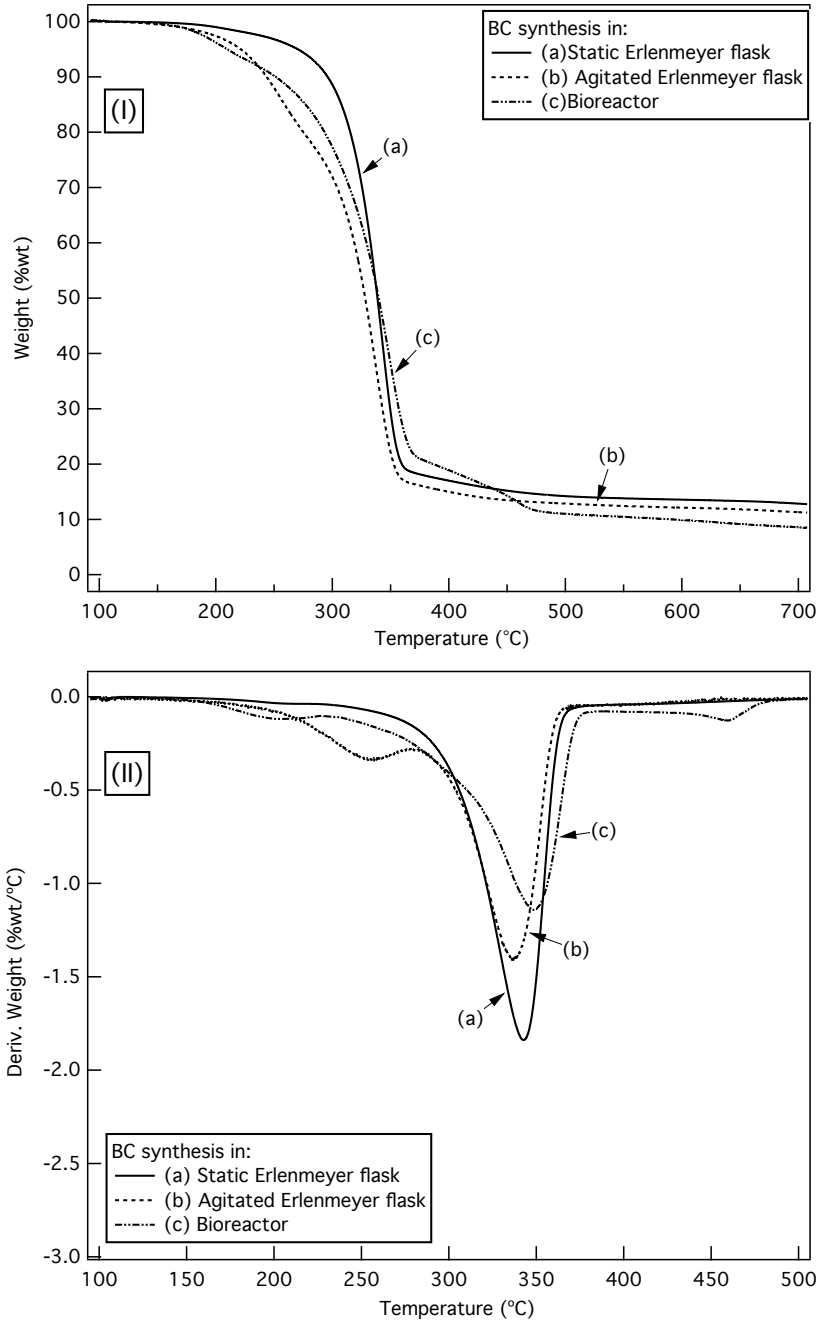


Figure 3.13: **I**) Thermal degradation in N_2 atmosphere of BC cultured in static, agitated Erlenmeyer flask and in a bioreactor. **II**) Derivative weight loss in N_2 atmosphere of BC synthesised in static, agitated Erlenmeyer flask and in a bioreactor.

Table 3.5: Onset degradation temperature, maximum degradation temperature, weight loss rate and char yield of the thermal degradation process in N_2 of BC synthesised under various culture conditions.

BC culture condition	Onset Temp. ($^\circ C$)	Degradation Temp. ($^\circ C$)	Wt. loss rate (-)($\% \cdot min^{-1}$)	Char Yield (% wt.)
Static culture	309	343	1.8	13
Agitated culture	277	338	1.5	13
Bioreactor culture	276	348	1.4	11

3.7 Conclusions

Fermentation of cellulose-producing strain, *Gluconobacter xylinus* BPR2001 was carried out using a modified H&S medium under various conditions, static Erlenmeyer flask, agitated Erlenmeyer flask and stirred-tank bioreactor. The modification of the bioreactor vessel by the addition of stainless-steel mesh (*i.e.*, support) increased significantly the BC production by twofold with respect to the standard configuration of bioreactor vessel. The increase of BC production was attributed to increased area inside the bioreactor vessel. Thus, the stainless-steel mesh acted as a support from which *Gluconobacter xylinus* cells were anchored while producing BC. The resulting BC pellicle was also attached onto the supporting mesh and then gradually thickened away from it. The morphology of biosynthesised BC nanofibrils by *Gluconobacter xylinus* strain was in agreement with the characteristics reported in literature. The biosynthesised BC by *Gluconobacter xylinus* possessed a high degree of crystallinity composed exclusively of cellulose polymorph type I. In addition, ATR-FTIR investigation revealed that the ratio of cellulose allomorph I_α to I_β composing the polymorph type I varied with different culture conditions. In fact the above ratio decreased when *Gluconobacter xylinus* strain was cultured in agitated conditions, which was attributed to shear forces introduced either by agitation or mixing thus affecting the self-assembly of BC nanofibrils from the bacteria membrane. On the other hand, the thermal degradation of BC produced under various culture condition showed that thermal stability was lower for BC biosynthesised in agitated culture, hence, correlating the decrease of degree of crystallinity, as observed in XRD analysis.

3.8 Future work

Future work should involve further improvement of BC production by an optimisation of the concentration of nutrients, dissolved oxygen and agitation of the culture medium based on the principles of design of experiments (DOE). The constant supply of fresh nutrients and removal of metabolic waste will favour an enhanced growth of *Gluconobacter xylinus* bacteria population, hence increasing the yield of biosynthesised BC. The internal configuration of the stainless-steel mesh support in the bioreactor vessel can be optimised in term of mixing and aeration of the culture medium. This will be achievable by further understanding of the flow behaviour throughout cultivation time, by exploring various stirrer type and configurations with variable mixing characteristics. Moreover, the surface area obtained by introduction of mesh supports in bioreactor vessel can be improved by introducing additional meshes arranged inwardly in a concentric-fashion, while ensuring appropriate mixing conditions inside the bioreactor vessel.

4

Self-Reinforced Cellulose Nanocomposites & Bacterial Cellulose Coated Sisal Fibres Reinforced Cellulose Composites †

4.1 Introduction

4.1.1 Aims and objectives

The aim of the work reported in this chapter was to produce all-cellulose nano- and composite materials using subsequent dissolution and regeneration of cellulose. Self-reinforced regenerated cellulose nanocomposites only consist of regenerated microcrystalline cellulose in which the reinforcing phase consist of cellulose crystals. Herein, the concept of hierarchical all-cellulose composites to be introduced is based on a combination of self-reinforced regenerated cellulose nanocomposites and natural (BC-coated) fibres, which constitute matrix and reinforcement, respectively.

This chapter is composed of 5 parts: literature review, experimental methodology, characterisation of self-reinforced regenerated cellulose nanocomposites, characterisation of hierarchical all-cellulose composites and conclusions. The following sections review the progress in the field of renewable composite materials, the development of all-cellulose nano- and

†This chapter is based on the paper: A. Abbott, A. Bismarck "Self-Reinforced Cellulose Nanocomposites" *Cellulose* **17** (2010) 779-791

composite materials, the various solvent systems able to dissolve cellulose, the properties of sisal fibres and the various strategies currently employed to enhance fibre-matrix interface adhesion, respectively. Section 4.2 describes the methodology used for dissolution and regeneration of microcrystalline cellulose and to produce all-cellulose nano- and composites materials. Moreover, the methodology employed to perform BC coating on sisal fibre based on fermentation of *Gluconobacter xylinus* in bioreactor introduced in previous Chapter 3 is also explained in section 4.2. The characterisation of self-reinforced regenerated cellulose nanocomposite materials and their properties are analysed and discussed in Section 4.3. Then, the characterisation of hierarchical all-cellulose composite materials and their properties will be discussed in Section 4.4. At last conclusions remarks on both self-reinforced regenerated cellulose nanocomposites and hierarchical all-cellulose composite materials will be drawn in Section 4.5, which are followed by suggestions for alternative regeneration procedure of cellulose and improved methodology to produce hierarchical all-cellulose composites.

4.1.2 Sustainable composite materials

Increasing environmental awareness, worldwide, has drawn a strong interest towards renewable materials[124,125]. To date commodity polymers derived from petroleum resources are in majority used for many applications (*e.g.*, packaging, consumer electronics, automobiles, *etc.*), although being non-degradable and remaining ubiquitously in nature long after the product end-of-life[126]. Thus, the use of renewable and sustainable polymeric materials is becoming societally beneficial and economically profitable[127,128].

Over the last decades, the automotive industry has been manufacturing parts for car interiors containing a variety of natural fibres embedded in synthetic matrices (polypropylene, polyester, polyurethane)[7,129], as opposed to glass fibres. Moreover, various composition of composites made of natural fibres and synthetic polymer matrices exhibited specific mechanical properties equivalent to those of glass fibre reinforced polymer (GFRP) composites[130,131,132,133]. Life cycle assessment of natural fibre reinforced synthetic polymer composites demonstrated a significantly lower environmental impact than conventional GFRP composites[134,135].

Alternatively, truly renewable composites were investigated, owing to their sustainability and potential biodegradability[7,136]. Renewable composites were made using various raw materials; natural fibres extracted from various types of plant, such as ramie, abaca, jute and flax[137,138,139]. On the other hand, several naturally occurring polymers were used

as matrices: cellulose acetate[140], cellulose acetate propionate (CAP)[141], cellulose acetate butyrate (CAB)[142], thermoplastic starch[143,144], natural polyester[145,146], soy resins[139] and polylactic acid (PLA)[147].

4.1.3 All-cellulose nanocomposites and composites

"All-cellulose nanocomposites and composites" are a class of materials obtained by (partial) dissolution and regeneration of cellulosic materials. Several approaches to manufacture all-cellulose composites have been described in the literature and will be summarised below. Partial dissolution of microcrystalline cellulose[148], beech pulp fibres[149], kraft pulp[150] in DMAc/LiCl cosolvent and subsequent regeneration was achieved to produce all-cellulose nanocomposites. Recently, cotton linter pulp was dissolved in an alkali/urea system and then regenerated in a H_2SO_4 bath to obtain films of regenerated cellulose[151]. The dissolution and regeneration procedure resulted in a regenerated cellulose material in which cellulose crystals reinforce an amorphous cellulose phase[152,153]. The use of a cellulose solution in the production of cellulosic fibres, membranes or films was already performed in the 1990's due to its ease of manufacturing[154]. All-cellulose composites have been produced by impregnating lignocellulosic fibres, such as sisal[150] and rice husk[155] with a cellulose solution, which was then regenerated to form the matrix, which was reinforced by partially dissolved fibrous cellulose. Furthermore, all-cellulose composites have been produced by selective dissolution of cellulose fibres and fibrils. A surface layer of a fibrous cellulose material was partially dissolved and regenerated to form the matrix of the composites, in which the reinforcement was provided by the undissolved core of the fibrous cellulose. The selective dissolution of filter paper, regenerated cellulose fibres, BC, pulp cellulose and microfibrillated cellulose was achieved in DMAc/LiCl cosolvent[105,156,157] or in Ionic liquid (IL), such as 1-butyl-3-methylimidazolium chloride[158,159]. More recently, the selective dissolution of filter paper was achieved by using a solvent system composed of a PEG/NaOH aqueous solution[160]. Another class of all-cellulose composites was manufactured by partial esterification of wood pulp. The produced cellulose ester behaved like a thermoplastic and allowed the pulp to be processed by compression moulding[161,162].

4.1.4 Dissolution of cellulose

Solvent resistance of cellulose necessitated development of harsh chemical procedures for its dissolution and modification. Consequently, the viscose process was developed to enable

the industrial use of cellulose materials and their modification[154]. However, over the past decades environmentally friendlier solvent systems were introduced for cellulose dissolution. Heinze and Koschella[6] reviewed different solvents for cellulose and categorised them into derivatizing systems and non-derivatizing ones, which referred to dissolution by covalent derivatization of cellulose and dissolution of cellulose by intermolecular interactions, respectively, as presented in Figure 4.1. Cellulose had been successfully dissolved by combining dimethylacetamide and lithium chloride (DMAc/LiCl) to form a non-derivative solvent system for cellulose[163,164,165]. Striegel[166] reviewed the dissolution models for cellulose based on DMAc/LiCl, which involved a number of complex interactions occurring between polar aprotic solvent/salt and cellulose chains. Even high molecular weight microcrystalline cellulose could be dissolved using the cosolvent at room temperature without affecting its chemical structure and molecular weight[61,166,167]. Later, amine oxide namely, N-methylmorpholine-N-oxide (NMMO) was introduced to dissolve cellulose, however this process required elevated processing temperatures which degraded cellulose[168,169]. Nonetheless, NMMO found industrial applications in spun cellulose fibre products namely, Tencel®, Lyocell® from Lenzing AG (Austria). Another type of regenerated cellulose fibre called Bocell™ [170] from Acordis (Netherlands) was also manufactured at a large scale. In recent years, Swatloski *et al.*[158] reported the use of IL to dissolve cellulose materials. ILs, so called "green" solvents, present significant advantages over other solvent systems due to their low environmental impact and ease of handling.

4.1.5 Properties of sisal fibres

Natural fibres are composed of various polymeric components, such as cellulose, lignin, hemicelluloses, pectins and waxes. Natural fibres are regarded as naturally occurring composites, where cellulose fibrils aligned along growth direction confer strength and stiffness to the fibre[7]. In cell walls of plants, hydrophilic hemicelluloses provide a support to cellulose fibrils. Both cellulose and hemicellulose are embedded into a hydrophobic lignin matrix, which acts as a binder for cellulose fibrils and stiffener for fibres[8]. Moreover, pectins, also called heteropolysaccarides, allow for flexibility of plants. Amongst the various types of fibres, a complex architecture is observed, where primary walls adjacent to one another grow concentrically around successive inwards layers of secondary walls that possess a lumen at their centre, as shown in Figure 4.2. Natural fibres are classified as a function of their sourcing into

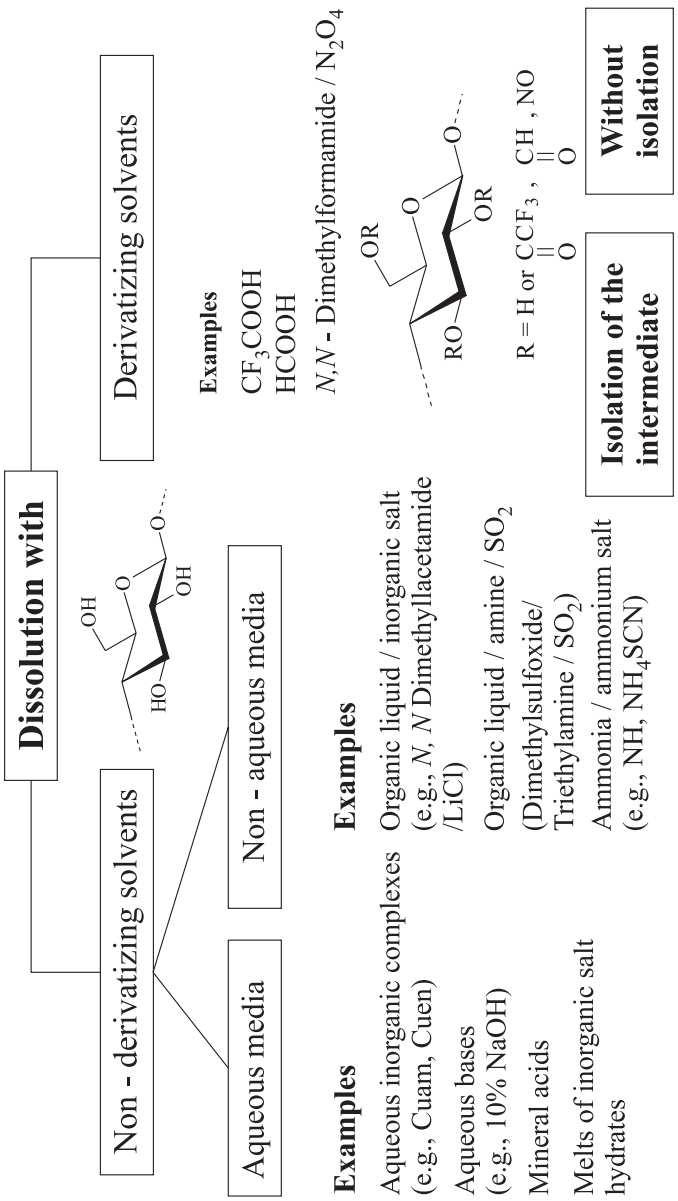


Figure 4.1: Classification of various cellulose solvents (reproduced from [6]).

leaf (*e.g.*, sisal), bast (*e.g.*, hemp, ramie and flax), seed, grass and fruit type (*e.g.*, coconut husk (coir)), respectively.

Increasingly, natural fibres are used as reinforcement in sustainable composite materials in construction and automotive industries[171,172,173]. Moreover *Agave Sisalana* is the fourth plant cultivated worldwide for engineering applications, which accounts for half of all textile fibres produced. Sisal fibres are also used in the production of ropes and twines for marine applications owing to its moisture resistance. Sisal fibres are extracted from the leaf of mature *Agave Sisalana* plants, which contains 3% to 4% of usable technical fibres and 90% of moisture with respect to weight of dried leaves[124]. Cellulose and lignin represent respectively 75% and 10% of the composition of sisal fibre. The mechanical properties of sisal fibres vary for tensile strength and Young's modulus between 530 to 630 MPa and 17 to 22 GPa, respectively, and are both a function of plant maturity[174]. Sisal fibres from 3 and 9 years old plants exhibit a tensile strength of 450 MPa and 600 MPa, respectively[175]. In fact, the tensile strength of sisal fibre increases with maturity of *Agave Sisalana* plant from which they are harvested. Diameters of sisal fibres are measured in the range of 100 to 300 μm[131].

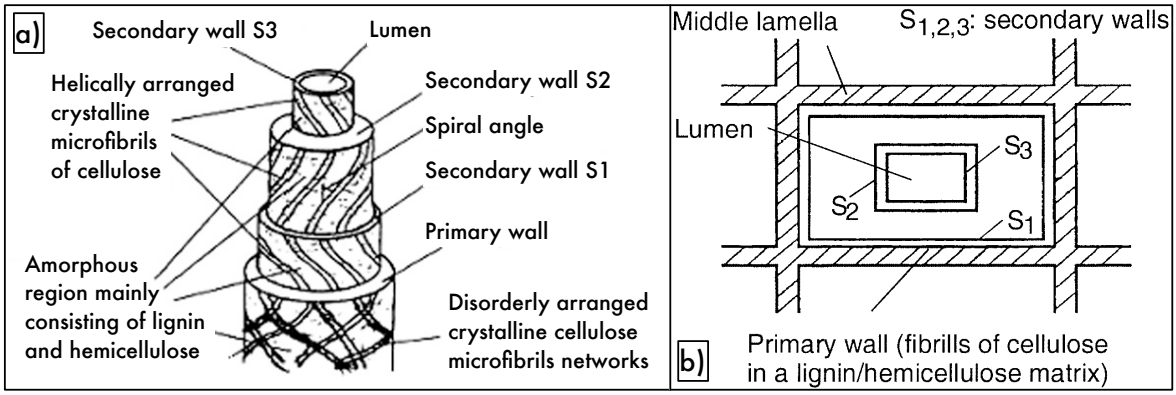


Figure 4.2: a) Structure of natural plant fibre (reproduced from[7]); b) Schematic of cross-section of a flax fibre (reproduced from[8])

4.1.6 Modification of natural fibre/matrix interface

In use, external loading applied to composite materials is transferred from polymer matrix to fibrous reinforcement across an interface. It is generally accepted, that mechanical performances of composite materials are in direct relation with the quality of their fibre/matrix

interface[176]. Different approaches were developed to modify the surfaces of natural fibres to enhance the fibre/matrix interface in renewable composite materials. Mercerisation was used to purify natural fibres by removing hemicelluloses, pectins and waxes from their surfaces. After NaOH treatment, the roughness of natural fibres was increased and enhanced interaction with thermoplastic matrices was observed[177,178]. Several reviews comprehensively reported different types of modification carried out on the surfaces of natural fibres to enhance compatibility with polymer matrices[179,180,181,182], *e.g.*, alkalisation, silanisation, acetylation, benzoylation, acrylation, maleated coupling, surface functionalisation with isocyanate moieties and graft polymerisation of monomers. However, the various chemical modifications performed on natural fibres required extensive use of both solvents and chemicals, which were potentially detrimental to the environment.

As an alternative, Baltazar *et al.*[183,184,185] developed a greener surface modification of natural fibres using an atmospheric air plasma treatment to enhance the affinity between various natural fibres and cellulose derivative matrix, such as CAB. Recently, Juntaro *et al.*[106,186] reported an innovative procedure to modify the surface of natural fibres based on cellulose-producing bacteria strain, which deposited during *in situ* fermentation a nano-sized layer of BC onto the surface of natural fibres. It was found that a BC coating on natural fibres enhanced the adhesion between biodegradable polymer matrices (*i.e.*, CAB) and BC-coated natural fibres.

4.2 Experimental

4.2.1 Materials

Microcrystalline cellulose (MCC) powder with a particle size of 20 μm purchased from Aldrich (Dorset, UK) was used as starting material for the production of all-cellulose nanocomposites. Cellulose dissolution was achieved using a cosolvent of N,N-dimethylacetamide (DMAc) (Aldrich, Dorset, UK) and LiCl (Fluka, Dorset, UK). Acetone and ethanol were purchased from VWR Ltd (Lutterworth, UK). Technical grade sisal fibres were kindly provided by Wigglesworth and Co Ltd. (London, UK). The fibres were harvested from mature *Agave Sisalana* plants grown in Kenya. Sisal fibres were washed thoroughly with deionised water, ethanol and acetone prior to use to remove impurities and soluble compounds from their surfaces. Deionised H_2O was produced using a NANOpure deionisation system (Barnstead

Thermolyne, Dubuque, USA). All the chemicals were used as received without further purification.

4.2.2 Preparation of self-reinforced cellulose nanocomposites

The dissolution of cellulose in DMAc/LiCl requires an activation step to make its inter- and intramolecular hydrogen bonds more accessible thus easing cellulose complexation by the DMAc/LiCl cosolvent [61,164]. 0.9 wt./v.% of MCC was activated at room temperature (RT) in 5 L of H_2O under continuous stirring for 24 h. Swollen MCC was solvent exchanged from H_2O to 5 L of ethanol then 5 L of acetone and at last to 2.5 L of DMAc, corresponding to 1.8 wt./v.% of MCC in DMAc. MCC was separated from each solvent by vacuum filtration using a fritted funnel (pore size type 3), the residue was manually broken up into small pieces and subsequently dispersed in a 5 L beaker containing the next solvent to be used. In each solvent the MCC suspension was vigorously stirred for 6 h. The cosolvent composed of 9 wt./v.% of LiCl in 100 ml DMAc was freshly prepared prior to using it for dissolution of MCC. Subsequently, after removal from pure DMAc, the DMAc swollen MCC equivalent to 9 wt./v.% of dried MCC was added to 100 ml of cosolvent. The cellulose dissolution was carried out in conical flask covered with an airtight seal using an overhead stirrer, allowing gentle shearing to be applied. To tailor the residual crystallinity of regenerated cellulose several cellulose dissolution times were chosen (2, 4, 12, 24 and 48 h). After the desired dissolution time the cellulose solution was poured into a 12 cm diameter petri dish and degassed in a desiccator for 1 h under continuous vacuum to remove entrapped air. Then, the MCC solution was placed overnight in a high flow rate fume cupboard to partially evaporate off some of the DMAc. The gel-like material formed after partial removal of DMAc was immersed in 20 L of distilled H_2O for 5 d to regenerate cellulose and extract the DMAC/LiCl cosolvent. The H_2O bath was continuously agitated and exchanged daily with fresh H_2O. The regenerated cellulose disks were dried in between brass plates measuring $25 \times 25\ cm^2$ under compression (4 MPa) at RT for 1 d. To further dry and keep regenerated cellulose disks flat, the compression load was doubled (8 MPa) and the disks placed into a vacuum oven at $30°C$ for 24 h under continuous suction. In addition, an amorphous as possible regenerated cellulose was prepared by dissolving only 1 wt./v.% of MCC in 100 ml of 9 wt./v.% of LiCl in DMAc for 48 h and then processed as previously described.

4.2.3 BC coating of sisal fibres using *Gluconobacter xylinus* bacteria

The BC coating of sisal fibres was carried in a fully instrumented bioreactor presented in Section 3.1.5 of the previous chapter. The BC coating procedure of sisal fibres was carried out in accordance with the procedure for the fermentation of *Gluconobacter xylinus* in the bioreactor described in Section 3.2.2. 50 g of thoroughly washed sisal fibres were introduced into the bioreactor vessel prior to autoclaving. Thereafter, inoculation and fermentation of *Gluconobacter xylinus* was carried out for 7 d at $30°C$. Subsequently, the BC-coated sisal fibres were suspended in 5 L of 0.1 N NaOH solution and stirred for 20 min at $80°C$ to lyse cells and dissolve debris. BC-coated sisal fibres were thoroughly washed with H_2O until neutral pH was reached.

4.2.4 Preparation of hierarchical all-cellulose composites

The preparation of hierarchical all-cellulose composites is schematically shown in Figure 4.3. Cellulose (MCC) was dissolved for 2, 4, 8, 12 and 24 h, respectively, according to the dissolution procedure described above. 40 wt./wt.% of either sisal fibres or BC-coated sisal fibres with respect to dissolved cellulose was homogeneously dispersed in freshly prepared cellulose solution and further stirred for 5 min. The viscous cellulose solution containing sisal fibres was transferred into a 15 cm petri dish and degassed in a desiccator for 1 h under continuous vacuum to remove entrapped air and then allowed to stand in fume cupboard overnight for gelation of the cellulose/sisal fibre system. The removal of DMAc/LiCl cosolvent and drying of regenerated cellulose/sisal fibre system were performed as previously mentioned above.

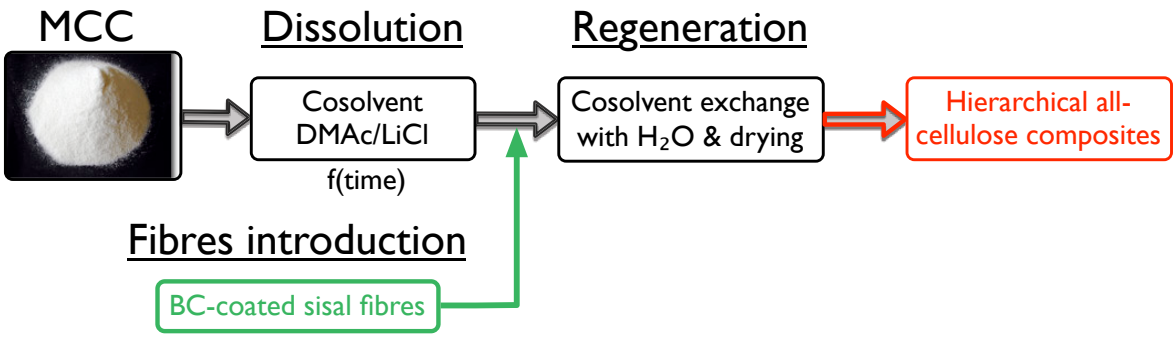


Figure 4.3: Schematic of preparation of hierarchical all-cellulose composites.

4.3 Characterisation of self-reinforced regenerated cellulose nanocomposites

4.3.1 Crystallinity evolution in self-reinforced regenerated cellulose nanocomposites

The XRD diffractograms of microcrystalline cellulose (MCC) and self-reinforced regenerated cellulose are shown in Figure 4.4. The XRD pattern of MCC powder was characteristic for native cellulose. Diffraction peaks of native cellulose are located at 2θ= 14°, 16°, 22° and 35° and correspond respectively to the [101], [10$\bar{1}$], [002] and [040] crystal lattices[23]. The diffractograms of self-reinforced regenerated cellulose specimens exhibit with increasing dissolution time, broader and flatter diffraction peaks (Figure 4.4). The characteristic peak of cellulose located at 2θ=22° corresponding to [002] lattice became broader with increasing dissolution time. Moreover, a small shift of the peak maximum of the [002] peak to lower values of 2θ denoted the presence of type II cellulose in the regenerated cellulose[148,187]. Also, the [101] and [10$\bar{1}$] peaks at 2θ= 14° and 16° progressively blurred with increasing dissolution time because of the decreasing cellulose crystallinity. MCC dissolution in DMAc/LiCl and regeneration produced different cellulose polymorphs: type I, type II cellulose and amorphous cellulose. Regeneration of cellulose in H_2O caused reorganisation and immobilisation of cellulose into type II and amorphous cellulose[188,189]. Both crystal configuration and morphology changed with increasing dissolution time. Increasing the dissolution time of MCC in DMAc/LiCl cosolvent significantly affected the crystallinity of the regenerated cellulose.

The evolution of the degree of crystallinity as determined using Segal's equation (Equation 2.9) as function of dissolution time is presented in Figure 4.5. The crystallinity of MCC as received was 72%; it dropped to 62% for cellulose regenerated after 4 h of dissolution and then further to 43% for cellulose which was regenerated after 24 h of dissolution. The degree of crystallinity for regenerated cellulose dropped steeply during the initial 10 h of dissolution and then plateaued with minor changes. From 24 h onwards, the degree of crystallinity of regenerated cellulose decreased only slightly, this was attributed to a saturation of the cosolvent system, which was unable to dissolve further cellulose crystals. It was observed, that reducing the initial concentration of MCC in the cosolvent from 8 wt./v.% to 1 wt./v.% significantly reduced the crystallinity of the cellulose regenerated from the cosolvent after 48 h of dissolution. Duchemin *et al.*[159] reported that the concentration of cellulose used

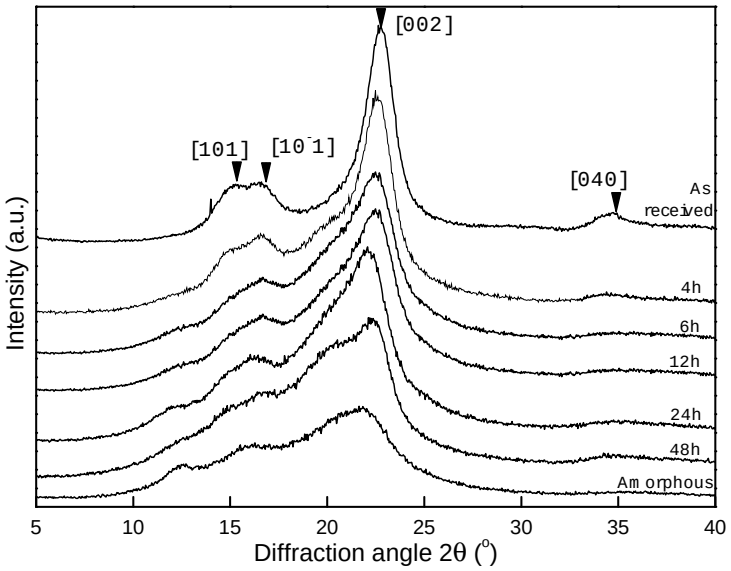


Figure 4.4: X-ray diffractogram of received microcrystalline cellulose powder and self-reinforced regenerated cellulose regenerated from DMAc/LiCl cosolvent after increasing dissolution times and amorphous regenerated cellulose obtained by dissolution of 1 wt./v.% of MCC in DMAc/LiCl for 48 h and subsequent regeneration.

for dissolution at a given dissolution time effects the degree of crystallinity of regenerated cellulose.

The initial crystal dimension in MCC as calculated using Scherrer's equation (Equation 2.10) was 39.5 nm as in Table 4.1 and Figure 4.5. As expected the crystal size of regenerated cellulose as a function of dissolution time was drastically reduced. As for the degree of crystallinity, the crystal size in regenerated cellulose decreases significantly and then levelled off beyond 24 h of dissolution.

The dissolution of swollen MCC proceeded initially by penetration of DMAc/LiCl co-solvent into the amorphous regions of MCC and then was followed by de-crystallisation of cellulose. The dissolution of cellulose crystals was achieved by disruption of extensive hydrogen bonds formed in lamellar arrangement of cellulose crystals [61,164] (see Section 3.1.3). The reduction of crystal size in DMAc/LiCl cosolvent during processing is explained by a layer by layer peeling of cellulose chains away from cellulose crystals as shown by the analysis of the WAXD observations of regenerated cellulose.

The type I cellulose crystals remaining within amorphous cellulose acted as (self-) re-

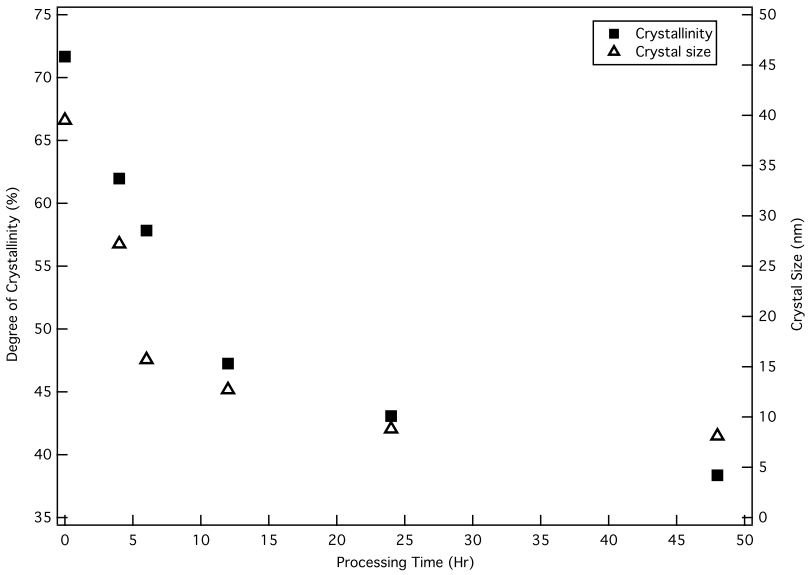


Figure 4.5: Degree of crystallinity as determined using Segal's equation and crystal size of self-reinforced regenerated cellulose as determined using the Scherrer's equation as a function of dissolution time of MCC in DMAc/LiCl cosolvent

Table 4.1: Degree of crystallinity, full width half maximum (FWHM) peak for [002] lattice and crystal size of self-reinforced regenerated cellulose as a function of dissolution time of MCC in DMAc/LiCl cosolvent.

Dissolution time (h)	Degree of crystallinity (%)	FWHM [002] peak (°)	Crystal size (nm)
*0	72.0	1.88	39.5
4	62.0	2.73	27.2
6	57.8	4.74	15.7
12	47.3	5.83	12.7
24	43.0	8.42	8.8
48	38.3	9.20	8.1
†48	26.6	-	-

* As received microcrystalline cellulose

† Regenerated cellulose prepared by dissolving 1 wt./v.% of MCC in 100 ml of 9 wt./v.% LiCl in DMAc for 48 h.

inforcement for regenerated cellulose; the amount of which was tailored by controlling the dissolution time of MCC. In addition, these reinforcing cellulose crystals were randomly distributed and orientated throughout the regenerated cellulose[148]. The self-reinforced cellulose nanocomposites made by MCC dissolution in DMAc/LiCl and subsequent regeneration, consisted of cellulose crystals of type I and type II, amorphous cellulose as well as paracrystalline cellulose[153]. The complex composition of regenerated cellulose limited the quantitative determination of the fraction of nano-reinforcement. However, the overall degree of crystallinity can be taken as a qualitative estimation of the amount of reinforcing phase of cellulose crystals in regenerated cellulose.

4.3.2 Investigation of the crystallinity of regenerated cellulose using ATR-FTIR spectroscopy

ATR-FTIR spectra of regenerated cellulose presented in Figure 4.6 were recorded on dried samples with different degrees of crystallinity as determined using Segal's equation. The dissolution of MCC and its subsequent regeneration led to changes in both degree of crystallinity and crystal organisation of regenerated cellulose (Figure 4.4). These changes were investigated by ATR-FTIR within a spectral region ranging from 1600 cm^{-1} to 600 cm^{-1}. The relation between degree of crystallinity obtained from XRD and ATR-FTIR is presented in Figure 4.7. The degree of crystallinity obtained from ATR-FTIR is defined by the absorbance of A_{1430}/A_{900} ratio. This ratio corresponds to the area under adsorption bands located at 1430 cm^{-1} and 900 cm^{-1}, which are assigned to CH_2 symmetrical bending and C-O-C stretching of the $\beta(1 \rightarrow 4)$ glycosidic link, respectively[114,190,191,192], as summarised in Table 4.2. For regenerated cellulose with a degree of crystallinity of 66% and 43%, the corresponding A_{1430}/A_{900} ratio are 1.61 and 1.24, respectively. The A_{1430}/A_{900} ratio decreases steadily with decreasing degree of crystallinity of regenerated cellulose obtained from XRD. However, the ratio for as received MCC is lower as compared to regenerated cellulose with a degree of crystallinity of 66%, which resulted from a variation of ATR-FTIR signal caused by the type of cellulosic material, one being a MCC the other a regenerated cellulose[191]. The A_{1430}/A_{900} ratio corresponding to ATR-FTIR degree of crystallinity of regenerated cellulose was in agreement with the change of degree of crystallinity observed from XRD; nonetheless, the A_{1430}/A_{900} ratio provides only an empirical value for the crystallinity of self-reinforced regenerated cellulose specimen.

The formation of regenerated cellulose required dissolution of MCC in DMAc/LiCl followed by regeneration; therefore, during this process cellulose crystals changed from type-I to the thermodynamically more stable type-II form [188,189]. The change of cellulose crystals within regenerated cellulose with respect to their degree of crystallinity is presented in Figure 4.8. The A_{1370}/A_{670} ratio expressed the relation between cellulose type-II and type-I, and is defined by the area under absorbance peaks 1370 cm^{-1} and 670 cm^{-1}, which are assigned to CH bending and C-OH out of plane bending of cellulose, respectively [193,194] (Table 4.2). The A_{1370}/A_{670} ratio for regenerated cellulose with degree of crystallinity of 66% and 26.6% increased from 2.63 to 3.1, respectively. Thus, the A_{1370}/A_{670} ratio increased with decreasing degree of crystallinity, which indicated the conversion of cellulose type-I into cellulose type-II during dissolution and regeneration of cellulose. Self-reinforced regenerated cellulose with a low degree of crystallinity had a higher content of cellulose type-II. Consequently, cellulose dissolution in DMAc/LiCl resulted in the modification of intra- and intermolecular H-bonds in regenerated cellulose as observed by ATR-FTIR spectroscopy.

Table 4.2: Summary of absorption bands and assignment for the ATR-FTIR spectra of regenerated cellulose.

Wavenumber (cm^{-1})	Band assignment	Reference
1430	CH_2 symmetrical bending	[114,190,191,192].
1370	CH bending	[193]
900	C-O-C stretching (glycosidic link)	[114,190,191,192].
670	C-OH out of plane bending	[194]

4.3.3 Thermal behaviour of self-reinforced regenerated cellulose nanocomposites

The weight loss of microcrystalline (MCC) and regenerated cellulose caused by thermal degradation in inert N_2 atmosphere is presented in Figure 4.9. In the case of MCC, the onset degradation temperature occurs around $280°C$ followed by thermal degradation occurring at $360°C$. The degradation behaviour of regenerated cellulose is significantly different to that of MCC, most importantly the degradation is initiated at lower temperatures. With decreasing degree of crystallinity of regenerated cellulose from 66% to 38% the onset degradation temperature shifts from $235°C$ to $220°C$; comparatively, these values are respectively $45°C$ to

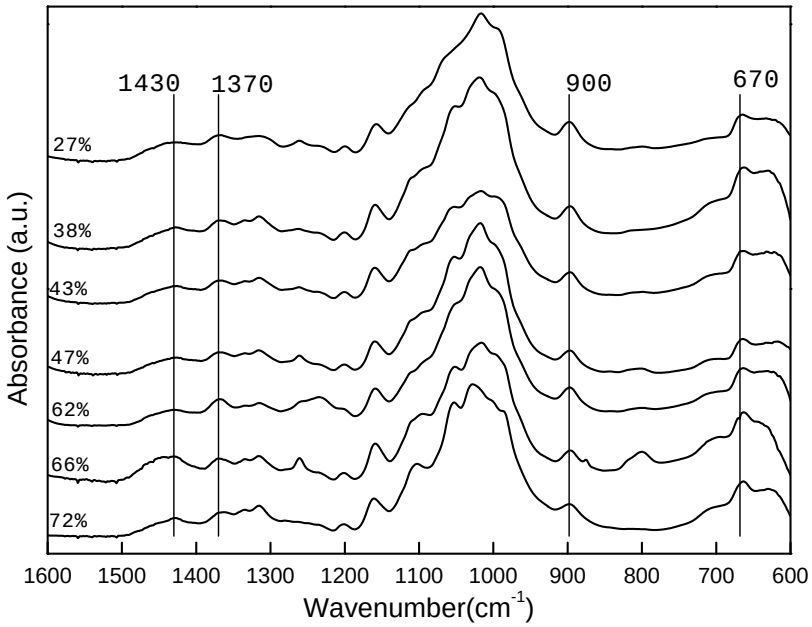


Figure 4.6: ATR-FTIR spectra of self-reinforced regenerated cellulose with different degree of crystallinity.

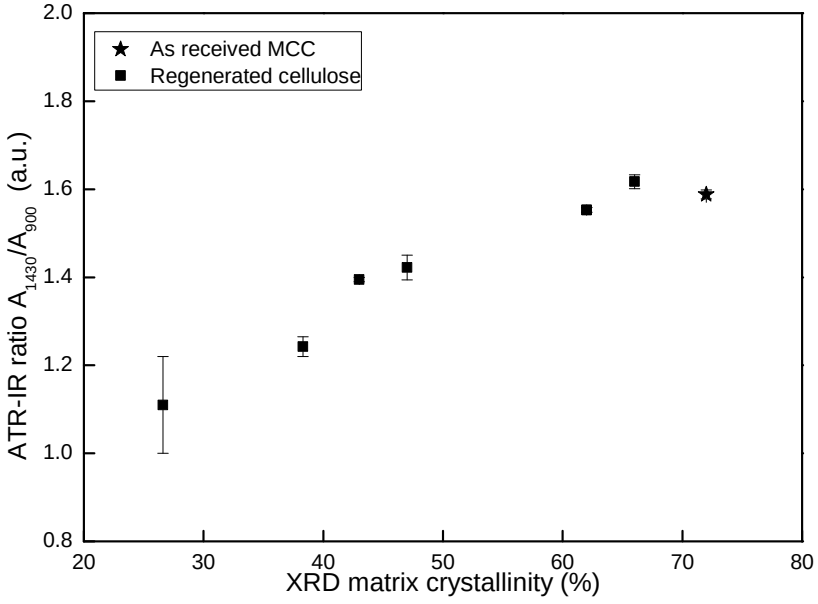


Figure 4.7: Change in degree of crystallinity of self-reinforced regenerated cellulose defined by ATR-FTIR A_{1430}/A_{900} ratio as a function of degree of crystallinity measured by XRD.

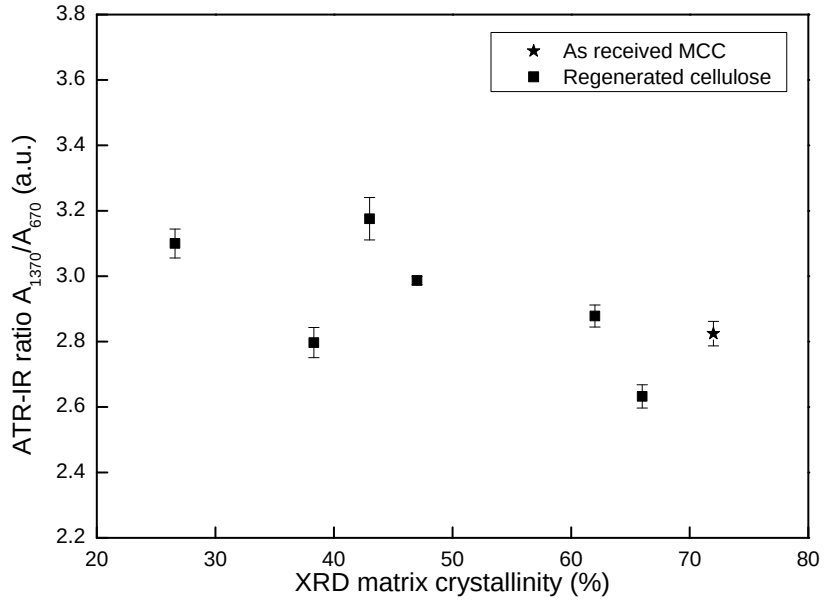


Figure 4.8: Modification of cellulose crystal polymorph type-I to type-II as characterised by ATR-FTIR A_{1370}/A_{670} ratio as a function of degree of crystallinity of self-reinforced regenerated cellulose.

$60°C$ lower than the onset degradation temperature observed for MCC (Table 4.3). Regeneration of cellulose leads to an increase of char formation at elevated temperatures compared to MCC. At $800°C$ the char yield of regenerated cellulose increased gradually from 7 wt.% to 32 wt.% for cellulose with a degree of crystallinity of 72% and 38%, respectively. The degradation rate varied significantly between MCC and regenerated cellulose (Table 4.3). A weight loss rate of 2.28 wt.%$\cdot min^{-1}$ was recorded for MCC, whereas for regenerated cellulose with degree of crystallinity of 66% it dropped to 1.29 wt.%$\cdot min^{-1}$. Interestingly a reduction of degree of crystallinity resulted in a degradation rate similar to that of MCC. Cellulose degradation was initiated by depolymerisation of cellulose to low molecular weight oligosaccharides and then occurred further by scission of D-glucopyranose [195]. Char formation was initiated by cross-linking and re-polymerisation of pyrolysis products of regenerated cellulose. During the degradation process, amorphous cellulose was initially attacked [196], thus, regenerated cellulose with a low degree of crystallinity exhibited a rapid degradation rate and an increase in char formation.

The activation energy (E_a) of the thermal degradation based on Broido's method (Equa-

tion 2.15) was determined for MCC and regenerated cellulose as function of the degree of crystallinity (Table 4.3). E_a for regenerated cellulose with a degree of crystallinity of 66% and 38% were 82.9 $kJ \cdot mol^{-1}$ and 110.6 $kJ \cdot mol^{-1}$, respectively. The regenerated cellulose specimen with low degree of crystallinity had a higher activation energy for degradation as compared to those with higher degree of crystallinity. In general, the lower the degree of crystallinity, the higher the activation energy for regenerated cellulose during degradation, this was related to the structural change in regenerated cellulose nanocomposite. Nevertheless, it was observed that the E_a determined for MCC (as received) was significantly greater than the E_a for regenerated cellulose, owing to the non-dissolved state of MCC.

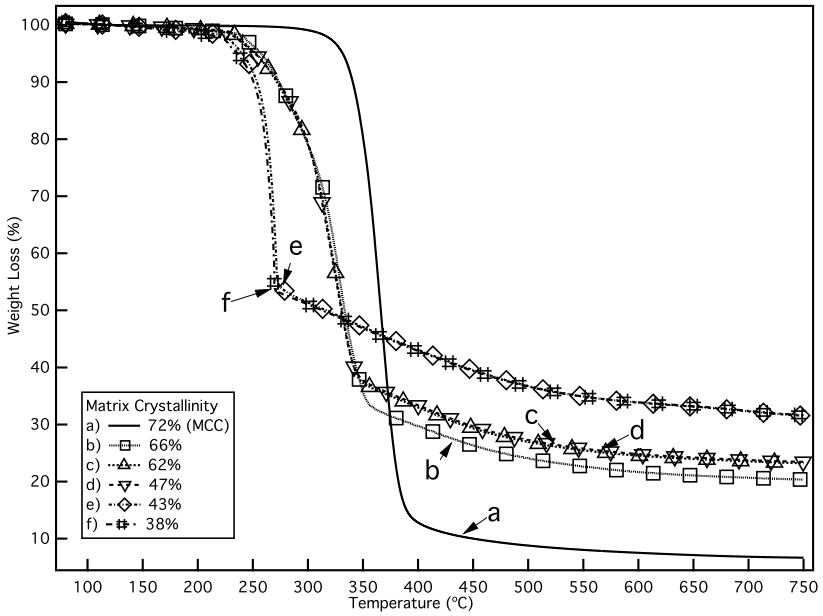


Figure 4.9: Weight loss due to thermal degradation in N_2 as a function of temperature of microcrystalline and self-reinforced regenerated cellulose as a function of degree of crystallinity.

4.3.4 Dynamic mechanical analysis of self-reinforced regenerated cellulose nanocomposites

The viscoelastic response of self-reinforced regenerated cellulose with respect to the degree of crystallinity is shown in Figure 4.10. The flexural storage modulus E' of regenerated cellulose decreases gradually from RT up to 230°C. A slight change in curve inflection is observed at this temperature for all specimens, which corresponds to the initial onset degradation of

Table 4.3: Onset degradation temperature, degradation temperature, weight loss rate, char yield and activation energy of the thermal degradation process in N_2 of self-reinforced regenerated cellulose with various degrees of crystallinity.

Crystallinity (%)	Onset Temp. (°C)	Degradat. Temp. (°C)	Wt. loss rate (-)($\% \cdot min^{-1}$)	Char Yield (wt.%)	E_a ($kJ \cdot mol^{-1}$)
72 *	280	360	2.28	6.7	192.6
66	235	318	1.29	20.4	82.9
62	236	323	1.28	23.3	81.6
47	231	307	1.43	23.5	96.5
43	220	261	2.26	31.5	113.6
38	220	258	2.31	31.7	110.6

* As received microcrystalline cellulose

regenerated cellulose (see Table 4.3). As the temperature increases a steep drop of the storage modulus is seen for regenerated cellulose with a degree of crystallinity of 66% and 38%; other specimen however maintained a higher storage modulus in comparison as the temperature rose. Subsequently, a significant drop in storage modulus is observed as regenerated cellulose specimens approach their degradation temperature.

At $30°C$, the storage modulus E' decreased from 12 GPa to 9 GPa with decreasing degree of crystallinity of regenerated cellulose specimen from 66% and 38%. Within self-reinforced regenerated cellulose, crystallites acted as hard nano-inclusions which locally provided reinforcement to the surrounding regenerated cellulose composed of paracrystalline and amorphous cellulose. The drop in stiffness was related to a reduction of number of crystallite within the self-reinforced regenerated cellulose. Upon reaching the onset degradation temperature, the regenerated cellulose rapidly lost its structural integrity induced by the degradation of both paracrystalline and amorphous cellulose.

4.3.5 Mechanical properties of self-reinforced regenerated cellulose nanocomposites

The mechanical properties of self-reinforced regenerated cellulose are presented in Figure 4.11. Both tensile strength and Young's modulus of regenerated cellulose decreased with decreasing degree of crystallinity. The ultimate tensile strength dropped gradually from 65 MPa to 35 MPa for a degree of crystallinity of 66% and 38%, respectively. The tensile modulus similarly

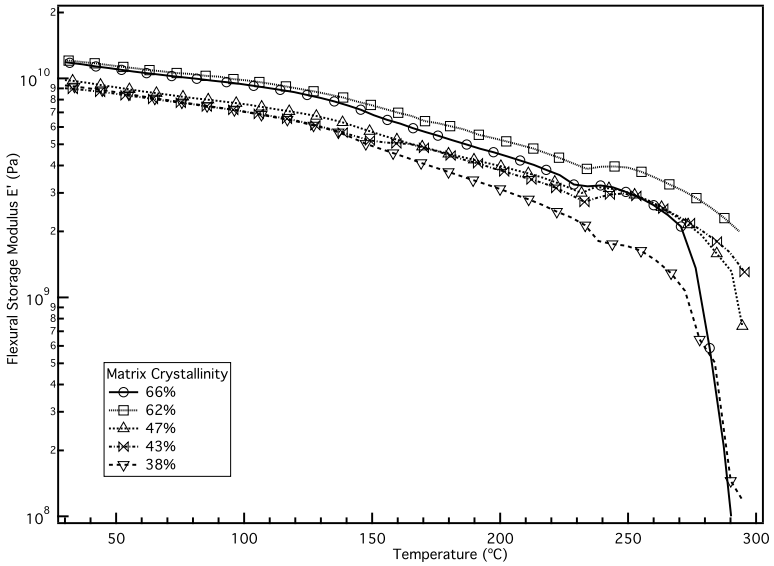


Figure 4.10: Change of flexural E' modulus of self-reinforced regenerated cellulose at different degree of crystallinity

decreased from 1.5 GPa to 0.7 GPa. The tensile performance of self-reinforced regenerated cellulose with degree of crystallinity of 47% and 62% were lower than values reported in the literature for dry cellulose films with a comparable degree of crystallinity; those films had a tensile strength ranging from 219 to 215 MPa and a modulus between 13 to 15 GPa[148].

Mechanical properties of all-cellulose nanocomposites reported in the literature varied widely depending on the manufacturing routes and source of cellulose materials used to prepare the specimen. Gindl *et al.*[148] reported a tensile strength of 243 MPa and Young's modulus of 13 GPa, respectively, for all-cellulose composites made by partial dissolution of MCC. Whereas, regenerated cellulose made from beech pulp exhibited a tensile strength and a modulus of 154 MPa and 12 GPa, respectively[149]. Nishino *et al.*[156] reported a tensile strength of 211 MPa and a modulus of 8 GPa, respectively, for all-cellulose composites made by selective dissolution of filter paper. It is worth mentioning that the test specimens in the referenced works had a thickness between 0.2-0.5 mm, while the specimen tested by the author had a thickness of 1-1.2 mm. Presumably, thin films of regenerated cellulose contained far fewer defects than specimen prepared by the author. Moreover, Nishino *et al.*[156] also reported a tensile strength of 50 MPa for the complete dissolution of filter paper 12 h of immersion in DMAc/LiCl thus similar to the values of specimen reported by the author

here. Recently, Duchemin *et al.*[159] dissolved 20 wt./v.% of MCC in DMAc/LiCl during 48 h followed by its regeneration. The resulting material had a degree of crystallinity of 77% and a tensile strength and Young's modulus of 106 MPa and 7.6 GPa, respectively, however the specimen thickness varied between 0.2 mm to 0.3 mm[159]. It appeared that mechanical performance of regenerated cellulose was significantly affected by its processing conditions and dissolution procedure.

Moreover, fully-dried specimens were characterised to assess the effect of the conditioning procedure on the mechanical properties of regenerated cellulose specimens. The mechanical performance of dried regenerated cellulose with a degree of crystallinity of 47% was 112 MPa and 3 GPa for tensile strength and Young's modulus, respectively. These values were comparable to those reported by Duchemin *et al.*[159]. Drying of regenerated cellulose specimen resulted in a significant enhancement of tensile properties by a factor of 2 as compared to specimen conditioned at 65% RH, thus confirming that H_2O acted as a plasticiser for cellulose by weakening hydrogen bonds between cellulose chains, which lowered the mechanical performance.

The work of fracture, defined as the area under stress-strain curves, is presented in Figure 4.12. The work of fracture was determined to be 6.7 J/m^2 and 14.5 J/m^2 for regenerated cellulose with a degree of crystallinity of 66% and 43%, respectively. An increase of the degree of crystallinity resulted in a decrease of the work of fracture, which corresponded to a brittle-type failure of regenerated cellulose. On the other hand, high work of fracture values were obtained for regenerated cellulose with a low degree of crystallinity, which corresponded to a ductile-type failure with plastic deformation taking place. A distinct drop in the work of fracture to 11.4 J/m^2 was observed for specimen with degree of crystallinity of 38%. This decrease was caused by a significant fraction of amorphous cellulose with respect to cellulose crystals as degree of crystallinity decreased. The decrease in the number and size of cellulose crystals affected their ability to act as reinforcement within the regenerated cellulose matrix. The control of crystal content and size in regenerated cellulose enables tailoring the failure behaviour from ductile to brittle.

4.3.6 SEM observation of fracture surfaces of self-reinforced of regenerated cellulose nanocomposites

The typical morphology of cryo-fractured surfaces of self-reinforced regenerated cellulose is shown in Figure 4.13. The fracture surfaces, shown in Figures 4.13a, 4.13c, were recorded

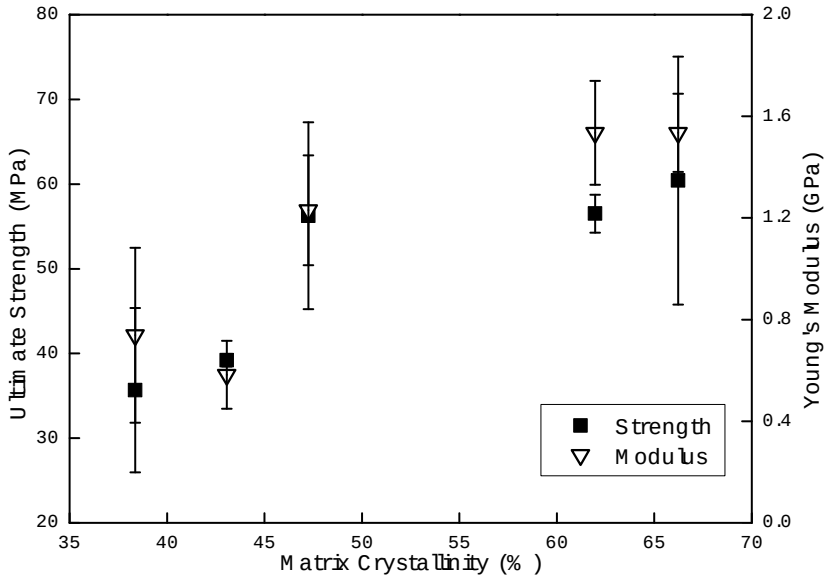


Figure 4.11: Ultimate tensile strength and Young's modulus of self-reinforced regenerated cellulose conditioned at 65% RH as a function of the degree of crystallinity.

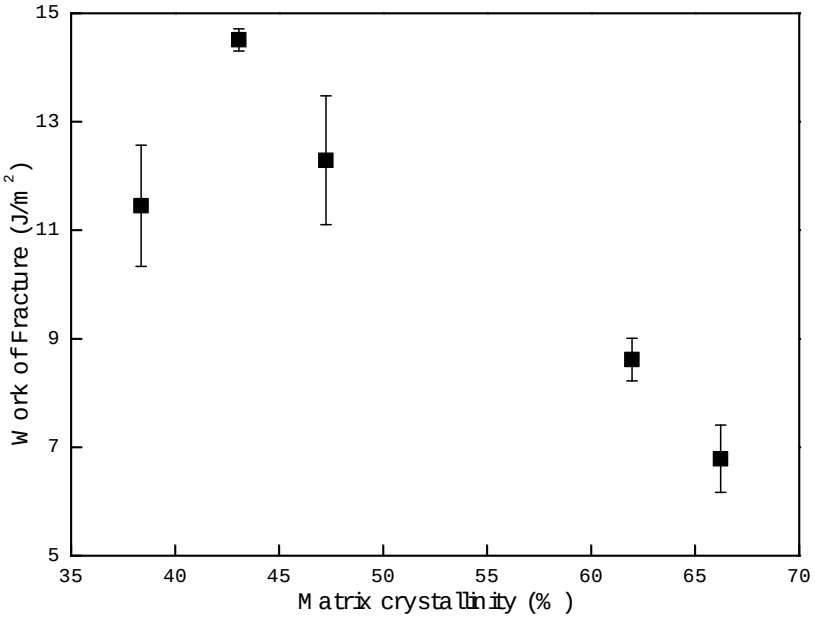


Figure 4.12: Work to fracture of self-reinforced regenerated cellulose tested in tensile mode with respect to degree of crystallinity.

at low magnification for regenerated cellulose containing 66% and 38% of crystallinity, respectively. For cellulose with high degree of crystallinity, the fracture surfaces exhibit an irregular pattern, with a lamellar-like structure present parallel to fracture plane. On the other hand a smoother surface with more uniform features is observed at degree of crystallinity of 38%. At high magnification, fracture surfaces for specimen with a crystallinity of 68% (Figure 4.13b) exhibit at a different length scale the in-plane lamellar structures as observed previously in Figure 4.13a. Specimen with 38% crystallinity (Figure 4.13d) have a different morphology than their high crystallinity counterpart, the fracture morphology can be described as smeared hill-valley. Figures 4.13a, 4.13b revealed a brittle-like fracture where sharp and distinct features were observed, moreover such brittle behaviour is in agreement with the calculated work of fracture (Figure 4.12). On the other hand, cryo-fractured regenerated cellulose specimen with a degree of crystallinity of 38% (Figure 4.13c, 4.13d) displayed a smooth fracture with less defined features more characteristic of a ductile failure behaviour. Different fracture mechanisms were observed for regenerated cellulose as a function of degree of crystallinity of specimen.

4.3.7 Moisture uptake behaviour of self-reinforced regenerated cellulose nanocomposites

The moisture sorption profile of regenerated cellulose specimens is shown in Figure 4.14 as a function of the square root of exposure time. The rate of moisture uptake as well as maximum moisture content, varied with the degree of crystallinity of regenerated cellulose. Moisture uptake of regenerated cellulose containing 66% and 38% crystallinity reaches 20.3% and 37.8% of their dried mass, respectively. Similarly as seen in Table 4.4, the rate of moisture uptake is strongly linked to crystallite and the amorphous phase ratio. The bulk organisation of regenerated cellulose influenced significantly the rate of moisture ingress into specimen as well as the maximum moisture content. Water molecules diffused faster into the amorphous phase of regenerated cellulose than in its crystalline phase, owing to a greater accessibility to binding sites. Hydrogen bonds in amorphous phase of cellulose were easily hydrated by H_2O molecules, thus inducing swelling of cellulose network.

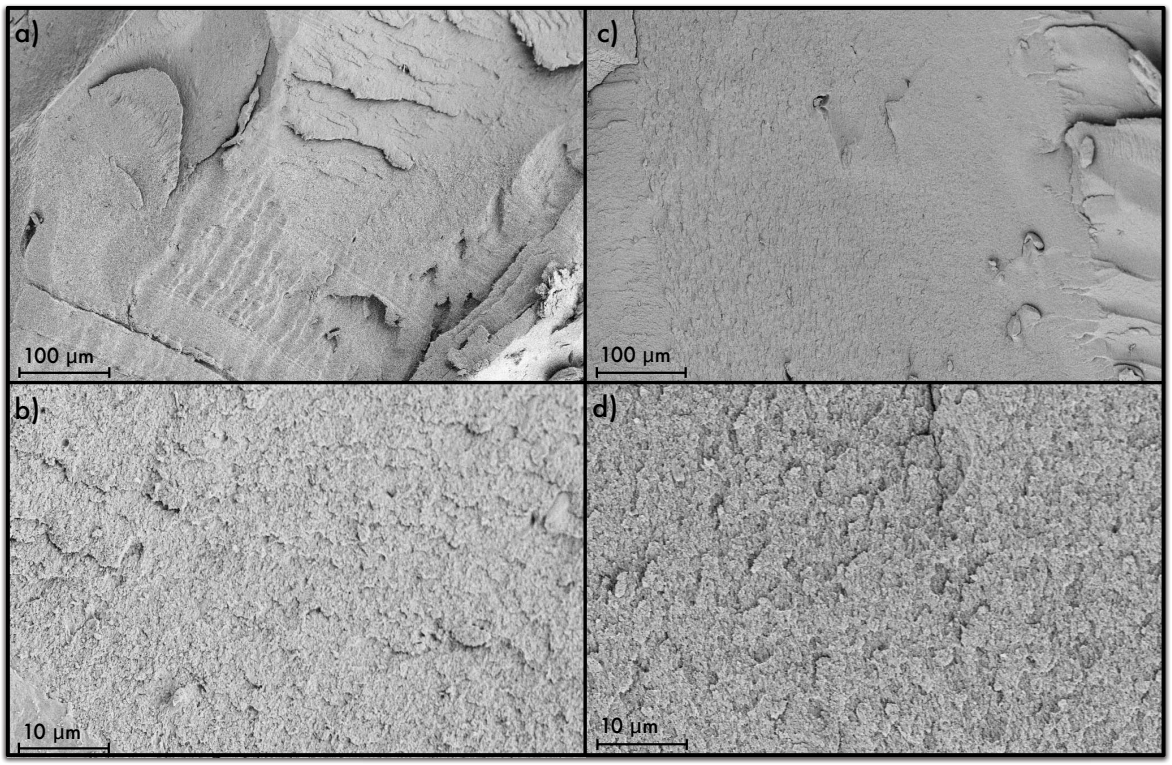


Figure 4.13: SEM micrographs of cryo-fractured surface of self-reinforced regenerated cellulose at different degree of crystallinity: 66% for a & b); 38% for c & d).

Table 4.4: Moisture uptake and content of self-reinforced regenerated cellulose exposed to 95% RH at $30°C$.

Cellulose degree of crystallinity (%)	Moisture uptake rate (wt.%/$\sqrt{sec}$)	Moisture content (wt.%)
66	0.217	20.3
62	0.230	20.7
47	0.381	30.7
43	0.378	33.9
38	0.515	37.8

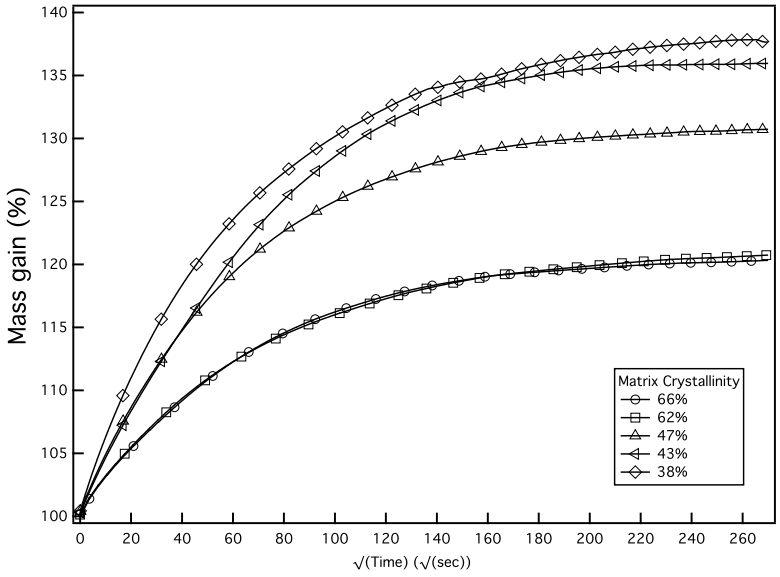


Figure 4.14: Moisture absorption profiles for self-reinforced regenerated cellulose at 95% RH for different degree of crystallinity.

4.4 Characterisation of hierarchical all-cellulose composites

To enhance the quality of the fibres-matrix interface in hierarchical all-cellulose composites, the surface of sisal fibres was coated by a dense layer of BC. Therefore, an improved adhesion between the BC-coated sisal fibres and the regenerated cellulose matrix was expected owing to their similar composition. Here, the effect of the BC-coated sisal fibres and the degree of crystallinity of the regenerated cellulose matrix (see Section 4.3) on the mechanical properties of the hierarchical all-cellulose composites are investigated.

4.4.1 Surface morphology of sisal fibres and BC-coated sisal fibres.

The typical surface morphology of sisal fibres and BC-coated sisal fibres is shown in Figure 4.15. BC-coated fibres reveal a different surface morphology as compared to the original one, where a layer of BC nanofibrils cover the fibre surface, thus introducing a rough topography. The nature and appearance of this BC layer is very similar to BC nanofibrils presented in Chapter 3 (see Figure 3.8) for standard fermentation of *Gluconobacter xylinus*. Moreover the presence of sisal fibres in the culture medium did not hinder BC biosynthesis by bacteria. The BC coating was strongly attached to the fibre surfaces during the fermentation and remained

persistent after NaOH treatment of fibres. Moreover, the interaction between fibre surface and BC nanofibrils was due to the numerous hydrogen bonds formed between the sisal fibres and the BC nanofibrils[107], which resulted in an excellent stability of the BC coating onto sisal fibres.

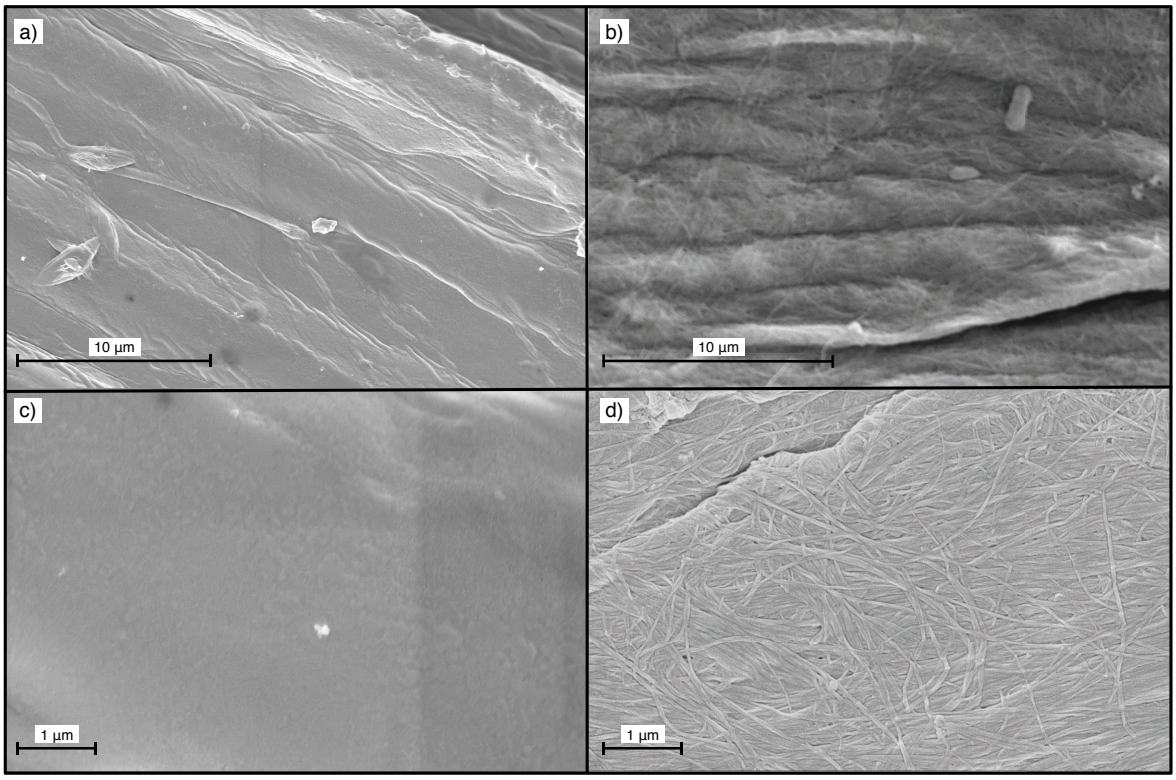


Figure 4.15: **a** & **c**) SEM micrograph of sisal fibres after autoclaving, soaking for 7 d in culture medium and after NaOH treatment; **b** & **d**) SEM micrograph of BC-coated sisal fibres, where the BC coating was obtained using the procedure described in Section 4.2.3.

4.4.2 XRD characterisation of sisal fibres and BC-coated sisal fibres

The XRD diffractograms of original sisal, NaOH treated sisal, BC-coated,& NaOH treated sisal and BC NaOH treated, respectively are shown in Figure 4.16. The diffractogram of NaOH treated BC nanofibrils was identical to the one described in the previous chapter (see Section 3.4). The diffractograms of both original and NaOH treated sisal fibres showed the presence of cellulose type I, with peaks located at 14°, 16°, 22° and 34° are assigned to the [101], [10$\bar{1}$], [002] and [040] crystal lattices, respectively. However, the peaks assigned to the

[101] and [10$\bar{1}$] lattice were merged owing to semi-crystalline nature of the sisal fibres[197]. The diffractogram of BC-coated sisal fibres revealed a slight shift of the [002] lattice towards a higher 2θ angle owing to the presence of a dense layer of BC. In addition, the diffraction peaks assigned to the [101] and [10$\bar{1}$] lattice of cellulose type I appeared more distinctively (*i.e.*, more dissociated from one another) for the BC-coated sisal fibres than for either original or NaOH treated sisal fibres. Therefore, the high degree of crystallinity of the BC coating strengthened the intensity of the diffraction peaks of BC-coated sisal fibres. The change in the degree of crystallinity (as determined by Segal's equation[36]) of the aforementioned fibres are summarised in Table 4.5. Interestingly, the BC coating procedure resulted in an increase of 12% of the crystal size of the [002] lattice and, similarly to a 10% gain in the degree of crystallinity of BC-coated sisal fibres as compared to original sisal fibres. The mild conditions used for NaOH treatment of the sisal fibres did not induce a drastic modification of the morphology of cellulose crystals nor did it significantly reduce the degree of crystallinity of the sisal fibres, as opposed to fibres treated with higher concentration of NaOH for several hours[197,198].

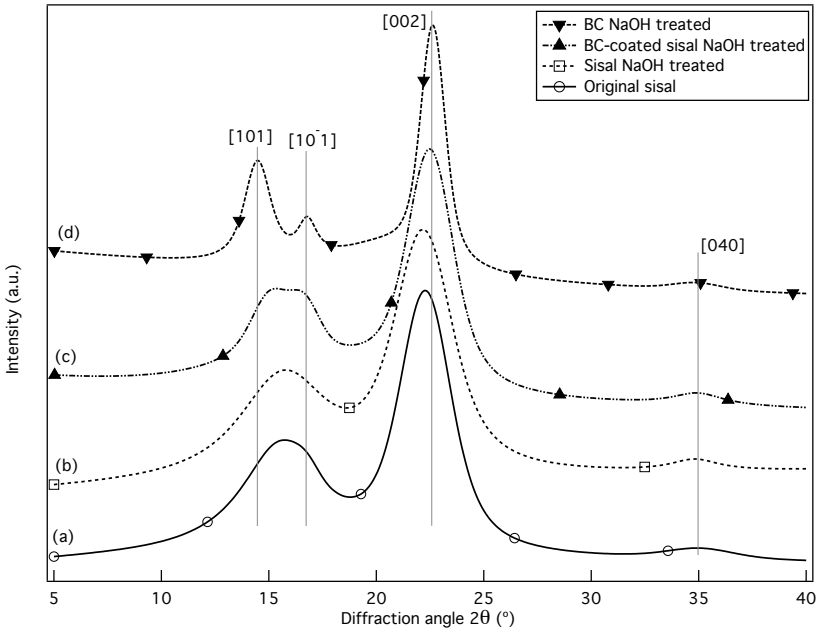


Figure 4.16: Effect of BC coating procedure on crystallinity of sisal fibres. (a) Original sisal; (b) NaOH treated sisal; (c) BC-coated and NaOH treated sisal; and (d) BC nanofibrils extracted from BC pellicle and NaOH treated.

Table 4.5: Evolution of the degree of crystallinity of sisal fibre after bacterial cellulose coating; full width half maximum (FWHM) peak for [002] lattice, crystal size and degree of crystallinity.

Specimen	[002] FWHM (°)	Crystal size (nm)	χ_{cr} (%)
Original sisal fibre	2.9	2.9	57.2
NaOH treated sisal fibre	3.2	2.7	55.2
BC-coated sisal fibre NaOH treated	2.6	3.3	64.6
BC NaOH treated	1.4	6.0	82.3

4.4.3 Mechanical properties of single (modified) sisal fibres

Tensile testing was carried out on single fibres to evaluate the change in bulk properties of sisal fibres, which underwent NaOH treatment and were coated with BC. The tensile properties are summarised in Table 4.6 for original sisal, sisal immersed into H&S medium without bacteria followed by NaOH treatment, BC-coated sisal and BC-coated and NaOH treated sisal fibres, respectively. The original sisal fibres exhibited a Young's modulus of 15 GPa, however it dropped steadily to 12 GPa for sisal fibres which underwent immersion in H&S medium followed by NaOH treatment and for both BC-coated sisal and BC-coated sisal followed by NaOH treatment. Therefore this drop accounted for a reduction of 20% of the Young's modulus. On the other hand, regardless of the treatments performed on the sisal fibres (*i.e.*, immersion in H&S medium, BC-coating or NaOH treatment), their tensile strength remained nearly constant. Indeed, the variations of the tensile strength between the different sisal fibres were confined within test errors. The tensile properties of sisal fibres tested herein were lower than the 15.5 GPa and 472 MPa reported elsewhere for the Young's modulus and tensile strength, respectively [199]. In addition, the scattering of the mechanical properties of plant fibres is inherent to the plant maturity, growth region, soil composition and harvesting technique, respectively [174,175].

4.4.4 Dynamic mechanical analysis of hierarchical all-cellulose composites

The viscoelastic response of hierarchical all-cellulose composites containing 40 wt./wt.% of sisal fibres is shown in Figure 4.17, as a function of the degree of crystallinity of the regenerated cellulose matrix and modification of surfaces of sisal fibres by coating it with BC. The flexural storage modulus E' of hierarchical all-cellulose composites gradually decreases with

Table 4.6: Young's modulus, tensile strength and strain of sisal fibres for immersion in culture medium, NaOH treatment and BC coating procedure.

Specimen	Young's modulus (GPA)	Strength (MPa)	Strain (%)
Original fibres	15.0 ± 1.2	342 ± 33	2.9 ± 0.1
Fibres in medium without bacteria	13.8 ± 1.8	352 ± 42	5.4 ± 1.0
BC-coated fibres	12.5 ± 1.0	324 ± 33	4.5 ± 0.4
BC-coated fibres NaOH treated	12.0 ± 0.9	310 ± 32	4.1 ± 0.5

increasing temperature, as described in earlier section for self-reinforced regenerated cellulose. For all specimen, the slope of E' curve steepens around $240°C$ which corresponds to onset degradation of the regenerated cellulose matrix determined from TGA. Nishino *et al.*[150] and Soykeabkaew *et al.*[157] both reported similarly the temperature dependence of the storage modulus E' for aligned lignocellulosic and regenerated cellulose fibre reinforced all-cellulose composites, respectively. Furthermore, the storage modulus E' measured at RT dropped with the decreasing degree of crystallinity of the regenerated cellulose matrix. The storage modulus E' measured for the original sisal and BC-coated sisal fibre reinforced regenerated cellulose matrix (66% crystallinity) were 3.4 GPa and 26 GPa, respectively. Indeed, the storage modulus E' at RT of hierarchical all-cellulose composites reinforced with BC-coated sisal fibres was higher than that of all-cellulose composites reinforced with non-coated sisal fibres and thus, independently of the degree of crystallinity of the regenerated cellulose matrix. The increase of storage modulus observed for the hierarchical all-cellulose composites reinforced with BC-coated sisal fibres was attributed to the improvement of the interfacial adhesion between fibres and matrix[155] due to the addition of a dense BC coating surrounding the sisal fibres, which rough surfaces also differed from the smooth surfaces of original sisal fibres mainly composed of lignin and hemicellulose[181,200].

4.4.5 Mechanical properties of hierarchical all-cellulose composites

The tensile strength and Young's modulus of hierarchical all-cellulose composites are presented in Figure 4.19 & 4.20, respectively, as a function of the degree of crystallinity of both regenerated cellulose matrix and type of sisal fibres used. Moreover, typical test coupons of hierarchical all-cellulose composites exhibiting a random distribution of short BC-coated sisal

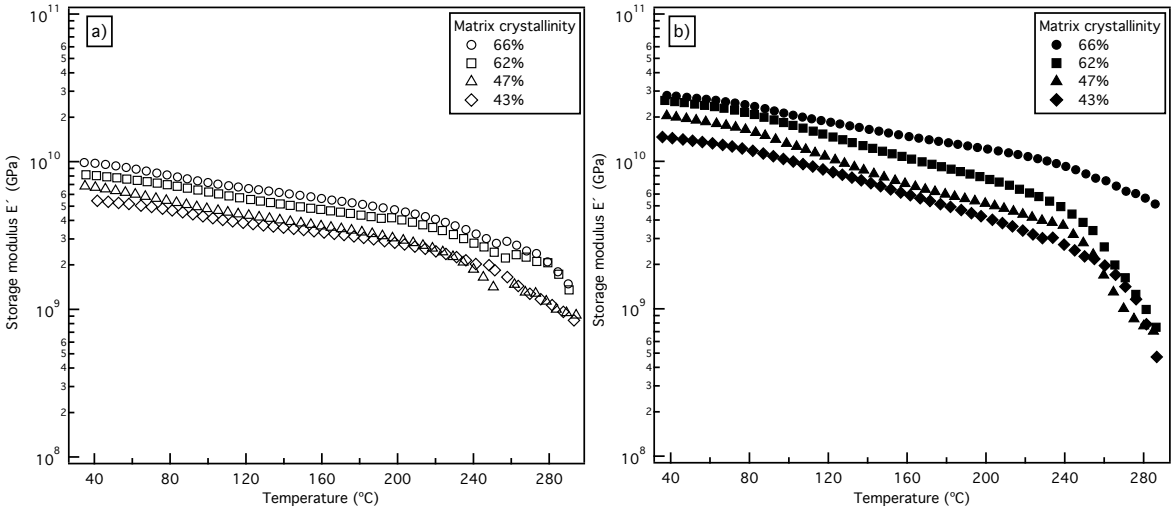


Figure 4.17: Change of flexural E' modulus of all-cellulose composites reinforced with: a) original sisal fibres; b) BC-coated sisal fibres.

fibres (fibre content 40 wt./wt.%) throughout the regenerated cellulose matrix are exemplified in Figure 4.18. The tensile strength of all-cellulose composites reinforced with original sisal fibres increased from 85 MPa to 133 MPa for increasing degree of crystallinity of the regenerated cellulose matrix from 38% to 67%, respectively (Figure 4.19). The Young's modulus of all-cellulose composites increased similarly with increasing degree of crystallinity of the regenerated cellulose matrix (Figure 4.20). In addition, all-cellulose composites reinforced with BC-coated sisal fibres exhibited higher mechanical properties than those of their counterparts reinforced with sisal fibres and thus, regardless of the degree of crystallinity of the regenerated cellulose matrix. Indeed, for a degree of crystallinity of 66%,the tensile strength and Young's modulus were 150 MPa and 4.4 GPa, respectively, which corresponded to an improvement of 12% for the tensile strength and of 15% for the Young's modulus comparatively to those of all-cellulose composites reinforced with sisal fibres for an identical fibre fraction (*i.e.*, 40 wt./wt.%) and assuming a similar randomisation of the sisal fibres throughout the regenerated cellulose matrix. Tensile properties of all-cellulose composites varied also as a function of the degree of crystallinity of the regenerated cellulose matrix, such behaviour was likewise observed for pure self-reinforced regenerated cellulose as discussed earlier (see Section 4.3.5). Gindl *et al.*[149] reported for all-cellulose composites reinforced by pulp fibres (80 v./v.%) value of 154 MPa and 12 GPa for tensile strength and Young's modulus, respec-

tively. Those compared favourably with the mechanical properties of all-cellulose composites presented herein, although the composites had a lower Young's moduli than those reported by Gindl *et al.*[149]. The mechanical properties of the hierarchical all-cellulose composites reinforced with BC-coated sisal fibres were improved comparatively to those of all-cellulose composites reinforced with sisal fibres. This enhancement was attributed to the presence of a BC coating of the surface of sisal fibres, which resulted in to a pure cellulose-cellulose interaction (*i.e.*, BC-regenerated cellulose). Therefore, BC-coated sisal exhibited a greater affinity for the regenerated cellulose matrix owing to its pure cellulose composition, whereas, the surfaces of sisal fibres possessed a cuticular layer containing pectins and waxes[201,202].

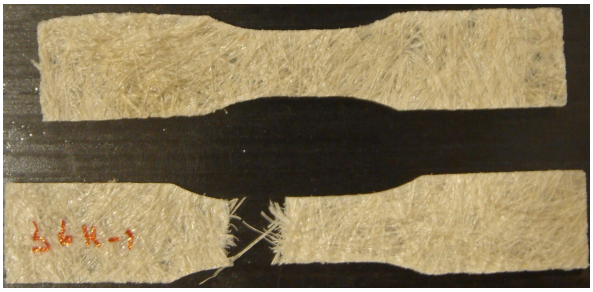


Figure 4.18: Photograph of typical tensile test coupons of hierarchical all-cellulose composite reinforced with BC-coated sisal fibres with a fibre fraction of 40 wt./wt.%: top, before testing; bottom, after testing.

4.4.6 SEM observation of fracture surfaces of hierarchical all-cellulose composites

The morphology of cryo-fractured surfaces of sisal fibres and BC-coated sisal fibre reinforced all-cellulose composites are shown in Figure 4.21**a**&**b**, respectively. In the case of sisal fibre reinforced all-cellulose composites, a clear gap was visible at the fibre-matrix interface (see arrows Figure 4.21**a**), which resulted from the shrinkage of the regenerated cellulose matrix away from the surface of sisal fibre during its drying. Therefore, the formation of a gap at the fibre-matrix interface resulted from the poor affinity between the surfaces of sisal fibres and the regenerated cellulose gel. Nonetheless, this observation was different from that reported by Nishino *et al.*[150]. They made unidirectional ramie fibre reinforced all-cellulose composites, which exhibited a perfect interface created by the partial dissolution of the surface of ramie fibres. This discrepancy was attributed to the unicellular cell structure of ramie fibres, which

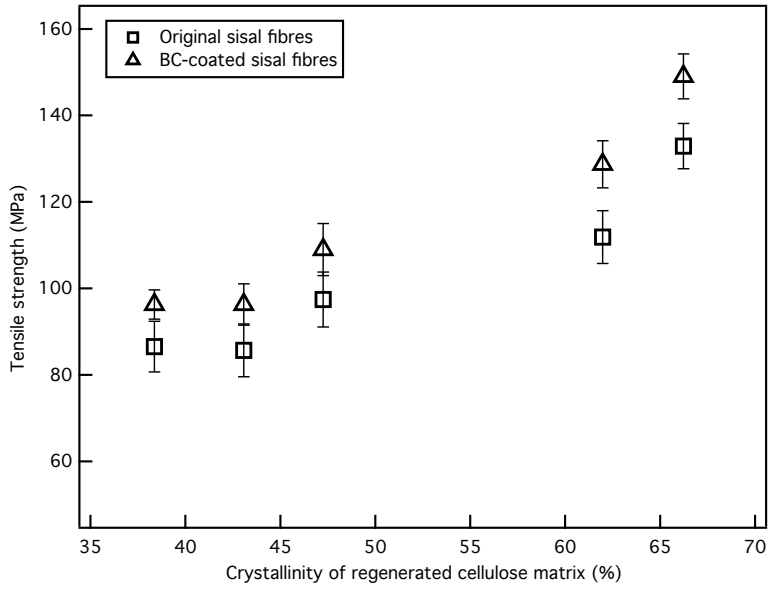


Figure 4.19: Tensile strength of all-cellulose composites as a function of degree of crystallinity of regenerated cellulose matrix and sisal fibre reinforcement (40 wt./wt.%).

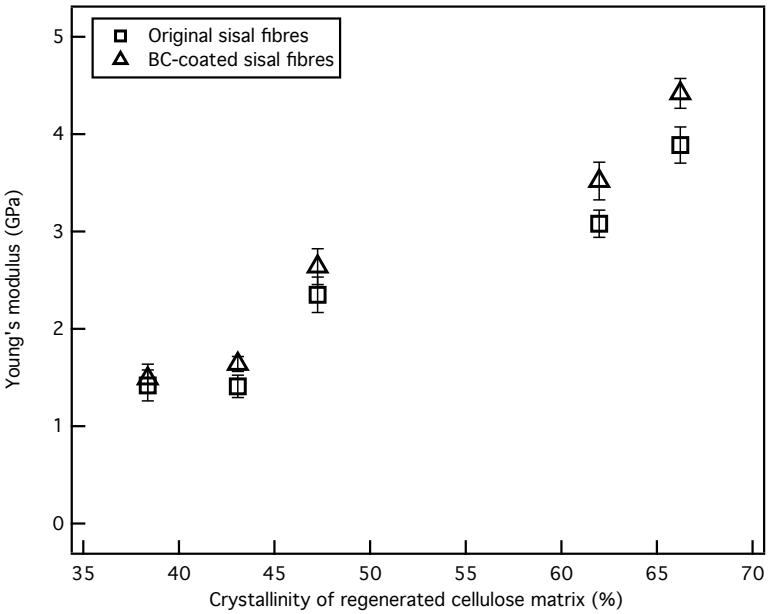


Figure 4.20: Young's modulus of all-cellulose composites as a function of degree of crystallinity of regenerated cellulose matrix and sisal fibre reinforcement (40 wt./wt.%).

exhibited both a high degree of crystallinity (82%) and a high cellulose content (86%)[203]. Comparatively, the structure of sisal fibres was composed of 134 cells[204], which exhibited a moderate degree of crystallinity of 57% and a cellulose content of 75%[205]. Therefore, the difference in structure and composition between the ramie and sisal fibres resulted in different interactions, *i.e.*, lower affinity between surfaces of sisal fibres and the DMAc/LiCl cosolvent contained in the regenerated cellulose gel, thus resulting in the formation of the gap observed earlier.

However, in the case of BC-coated sisal fibre reinforced all-cellulose composites, the regenerated cellulose matrix adhered to the fibres, thus revealing a fused interface (see arrows Figure 4.21**b**). In fact, the layer of BC formed on the surface of BC-coated sisal fibres acted as a coupling intermediate between the fibre and the regenerated cellulose matrix, while being strongly attached to the surface of the sisal fibre. BC-coated sisal fibre was covered by pure and highly crystalline BC, which was more resistant to dissolution but interacted favourably with the regenerated cellulose matrix, which was also pure cellulose. The presence of the BC coating on the surface of sisal significantly diminished the retraction of the regenerated cellulose matrix away from the fibre during drying because of the enhanced affinity at the fibre-matrix interface. Moreover, the streamline patterns which appeared in the cross-section and the apparent porosity, as seen in Figure 4.21**a**&**b**, were inherent to the processing of the all-cellulose composites. Furthermore, these artifacts, *i.e.*, streamlines, were also observed by Duchemin *et al.*[159,206] for the preparation of all-cellulose composites.

4.5 Conclusions

Self-reinforced regenerated cellulose nanocomposites were produced by dissolution of microcrystalline cellulose in dimethylacetamide/LiCl cosolvent and subsequent regeneration. Both dissolution procedure and dissolution time affected the physical, chemical and mechanical properties of the resulting self-reinforced regenerated cellulose nanocomposites. A strong correlation was established between overall reduction of degree of crystallinity of the regenerated cellulose and the increase of the processing time, which consequently reduced significantly the mechanical performances of the nanocomposites. The change in cellulose crystal allomorph from type-I to type-II following cellulose regeneration showed the effect of processing conditions on structural arrangement of cellulose crystals. Similarly, the thermal properties

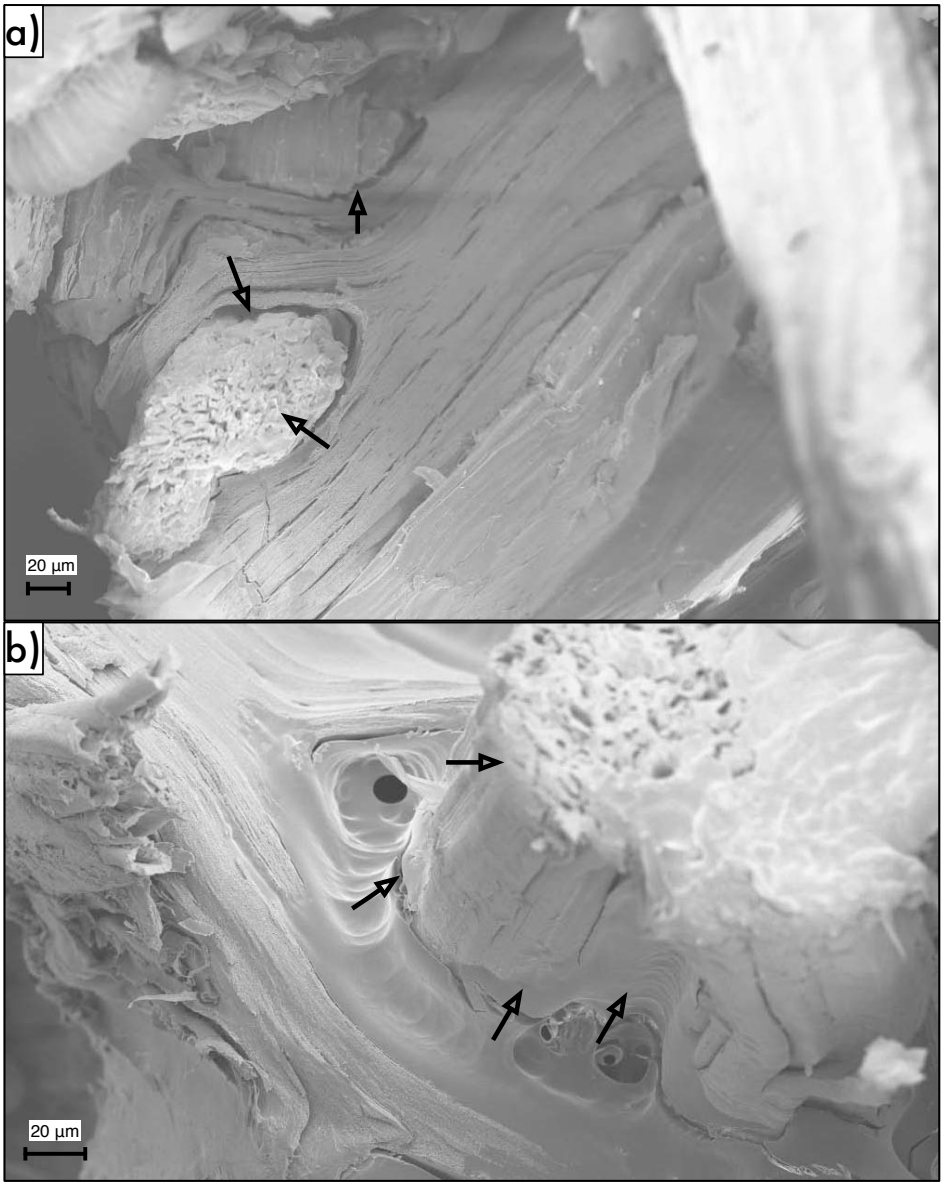


Figure 4.21: Typical SEM micrograph of a fracture surface of all-cellulose cellulose composites reinforced with: **a**, sisal fibres and **b**, BC-coated sisal fibres (fibre fraction of 40 wt./wt.%).

of regenerated cellulose were affected by the ratio of crystallite and amorphous phases distributed throughout the regenerated cellulose nanocomposite, where with decreasing degree of crystallinity the thermal degradation shifted towards lower temperature and led to an increase of the char yield. Change of the degree of crystallinity resulted in modification of both mechanical performance and failure behaviour of self-reinforced cellulose nanocomposites. Moisture uptake behaviour of regenerated cellulose nanocomposites changed with the degree of crystallinity, both moisture uptake rate and content increased with lowering of the degree of crystallinity. In fact, the properties of regenerated cellulose investigated were strongly related to its crystallinity content. Therefore by controlling the processing time of cellulose in solution, a range of properties of regenerated cellulose can be adjusted, which resulted in tailored mechanical response.

All-cellulose hierarchical composites were produced by combining self-reinforced regenerated cellulose and randomly distributed sisal fibres to form respectively the matrix and reinforcement of the all-cellulose composites. To enhance the mechanical performance, the surface of sisal fibres was modified by depositing BC by cellulose-producing bacteria strain *Gluconobacter xylinus* (see Chapter 3), which formed a dense BC coating on the surface of sisal fibres. Moreover, the use of BC-coated sisal fibres (40 wt./wt.%) in the preparation of hierarchical all-cellulose composites resulted in an improved quality of the fibre-matrix interface, as compared to their counterparts reinforced with sisal fibres. The effect of this improved interface was reflected in the higher dynamic mechanical and mechanical properties of the BC-coated sisal fibres reinforced all-cellulose composites reinforced as compared to those of their counterparts reinforced with sisal fibres.

4.6 Future work

Furthermore, the properties of the hierarchical all-cellulose composites can be improved by controlling the processing parameters such as the gelation time of the cellulose solution and the ageing of the cellulose gel. Another approach to regenerate the cellulose matrix would consist to use H_2O vapour to induce the progressive regeneration of the cellulose gel instead of its direct immersion in a H_2O bath. An alternative processing route for the hierarchical all-cellulose composites would consist in the infusion of a randomly distributed mat of BC-coated sisal fibres by a cellulose solution using a resin infusion under flexible tooling (RIFT) technique, which would maintain an effective randomisation of sisal fibres and ensure their

controlled impregnation. Thereafter, the bagged "pre-impregnate" would be subjected to moisture under a controlled relative humidity (RH), thus enabling the gelation and regeneration of the cellulose solution to obtain all-cellulose composites.

5

Regenerated Bacterial Cellulose Cryogels: Microsphere Templating and Morphology of Porous Structure

5.1 Introduction

5.1.1 Aims and objectives

The aims of the work reported in this chapter were to present the concept of highly porous cryogel microspheres consisting of the dissolution of bacterial cellulose (BC) nanofibrils in DMAc/LiCl cosolvent then templating into a microsphere shape of the BC solution followed by the regeneration of BC solution in H_20 and subsequently freeze-drying of regenerated BC microsphere to form a highly porous cryogel structure.

The objectives of the work reported in this chapter were:

- To produce highly porous cryogel microspheres and tailor the processing methodology.
- To investigate the effect of dissolution time on the formation and templating of the regenerated BC cryogel microspheres.
- To characterise the morphology of the porous network and BET surface area of the regenerated BC cryogel microspheres.

- To assess the thermal degradation behaviour and characterise to crystal structure of regenerated BC cryogel microspheres.

The present chapter is composed of 4 parts: literature review, experimental methodology, characterisation of BC cryogels and regenerated BC microspheres and conclusions. The following sections review different types of inorganic and organic porous materials, the main techniques used to produce porous materials, the different types and the properties of porous materials (*i.e.*, aerogel, cryogel and xerogel), the various methodology used to prepare cellulose-based porous materials and the usefulness of porous microsphere-shaped materials in different applications. Section 5.2 describes the methodology used to prepare highly porous cryogel microspheres composed of regenerated BC. The characterisation of highly porous cryogel microspheres and their properties are described and discussed in Section 5.3. The final Section 5.4 with the conclusions on the work presented, which is followed by suggestions for future work.

5.1.2 Introduction to highly porous materials

By definition, "an **Aerogel** is a solid material of extremely low density, produced by removing the liquid component from a conventional gel" according to the New Oxford American Dictionary. In 1931, Kistler pioneered the preparation of silica (SiO_2) aerogels, in which the continuous liquid phase of a gel was substituted by a gas phase resulting in high porosity[207]. SiO_2 aerogels are characterised by a low apparent density ranging from 0.004 g/cm^3 to 0.500 g/cm^3 (for comparison, the density of air is 0.00129 g/cm^3) and a very high pore volume (porosity) between 80 % to 99.8 %[208]. Aerogels provide an interesting combination of properties such as: high transparency close to glass, low thermal conductivity equivalent to expanded foams such as polystyrene and polyurethane and good sound attenuation[9,208]. Moreover, the irregular pore structure (caused by cross linking, aggregation and agglomeration of particles) and pore interconnectivity of aerogels account for their high specific surface area, ranging from 100 m^2/g to 1600 m^2/g[208]. Aerogel materials have been prepared from a wide variety of inorganic oxides beside SiO_2 such as: alumina (Al_2O_3), ferric oxide (Fe_2O_3), nickel oxide (NiO), tin oxide (SnO_2), tungsten oxide (WO_2)[9,209]. Other inorganic aerogels produced by sol-gel processes using novel precursor materials such as: carbon nanotubes (CNT)[210], colloidal metallic nanoparticles[211] and colloidal quantum dots (QD)[212,213,214] were recently reported .

In 1932, Kistler successfully prepared organic-based aerogels composed of cellulose, nitrocellulose, gelatin, agar and egg albumin respectively by removing H_2O from a gel precursor [209]. Different types of organic aerogels obtained by the sol-gel process were later developed based on resorcinol/formaldehyde (RF) systems, on which interconnected colloidal-like particles with diameters of 10 nm was formed by aqueous polycondensation of resorcinol with formaldehyde [215,216]. However, researchers investigated alternatives to RF systems by preparing aerogels using polyisocyanate precursors. Polyisocyanate-based aerogels produced were highly cross linked and made from different precursors such as: polyurethanes, polyureas, polyurethone imines or polyisocyanurates [217,218]. These polyisocyanate-based aerogels exhibited a lower thermal conductivity than standard polyurethane foams because of their nanostructure. The polyisocyanate-based aerogel have higher specific mechanical properties than equivalent monolithic SiO_2 aerogels because of the larger size of their elementary particles, thus producing the interpenetrating network [218].

Recently, biodegradable cellulose derivatives, like cellulose acetate butyrate (CAB) have been used as sol precursor for the preparation of cellulose-based aerogels [219]. The monolithic of cellulose aerogel was composed of both a nano-structured solid and a nano-porous network, which accounted for the large pore volume. Mine *et al.* [220] reported the preparation of cryogels composed of guar gum, a hydrocolloid polysaccharide, as precursor and a molten ionic liquid, namely 1-butyl-3-methylimidazolium chloride (BMIMCl), as liquid phase. A tight network structure of guar gum was obtained, which contributed towards good mechanical performances.

5.1.3 Various preparation routes to highly porous aerogel-like materials

In general, aerogels are prepared by the so called sol-gel process using molecular precursors. This process takes place at temperatures below $100°C$ in which the sol often consisting of a colloidal suspension of inorganic nano- or micro-particles (see Figure 5.1a) is subjected to different chemical treatments (hydrolysis, polymerisation) aiming to cross link the suspension of particles to form a gel [221,222]. The gel structure is created by an interpenetrated and continuous network of solid particles forming pores of different sizes filled with the liquid phase from the initial sol (see Figure 5.1b).

To obtain a porous structure from a wet gel, the liquid phase has to be removed. Thus, the method used to remove the liquid phase has a great influence on both final structure and

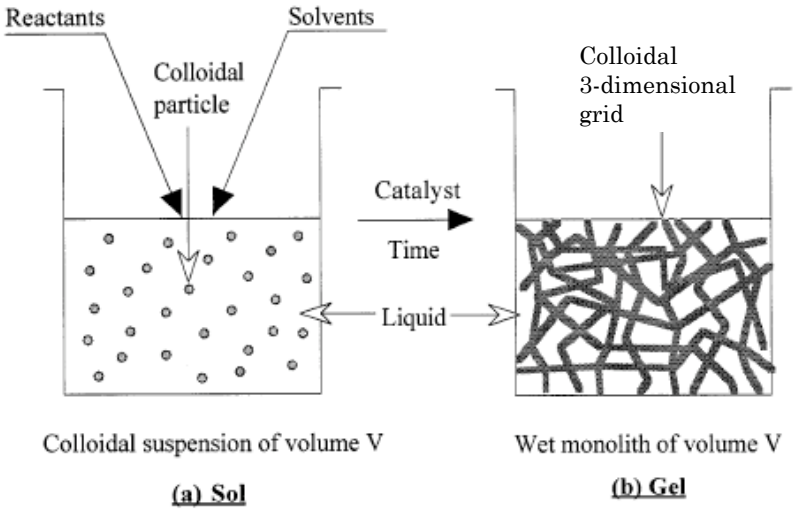


Figure 5.1: Description of the sol-gel process by Pajonk: (a) sol; (b) gel[9].

physical characteristics of the dried gel. Here, the different types of gels are listed according to their mode of preparation.

- A xerogel is produced by simply evaporating the liquid phase at low temperature under controlled drying. However, to avoid gel fragmentation and cracking, a slow rate of evaporation is required to avoid the collapse of meso- and macro-pores and thus, the overall gel shrinkage. Pore collapse is caused by an increase in capillary forces when the liquid phase is removed from the pores and the surface tension of the liquid used[223].

- An aerogel is obtained when the liquid phase of gel is removed under supercritical conditions (by application of critical temperature or/and pressure). The generation of supercritical conditions enables an instantaneous phase transformation from liquid to gas without the presence of an intermediate liquid-vapour phase. Furthermore, the development of surface tension or capillary forces within pores is prevented under supercritical conditions, which drastically limit shrinkage of aerogels as compared to xerogel. Thus, supercritical drying of gels in an autoclave produces a highly porous structure while preserving the initial morphology of the gel network.

  Barnes *et al.*[224] reported a new methodology to synthesise aerogels using 1-ethyl-3-methylimidazolium bis[(trifluoromethyl)sulfonyl] amide, a ionic liquid (IL), as solvent

and tetramethylorthosilicate (TMOS) as sol-gel precursor. The advantage of this technique was the substitution of supercritical drying process with instead, a soxhlet extraction in acetonitrile after the formation of the gel. It was shown from N_2 adsorption and SAXS measurements that the aerogel synthesised in IL was comparable with aerogels synthesised by conventional protocols.

- A cryogel is produced by freeze-drying a frozen aqueous gel. Thus, sublimating the frozen liquid phase in the gel to H_2O vapour under high-vacuum. The highly porous cryogel retains its structural integrity upon drying [225].

5.1.4 Applications of aerogels

After the discovery of SiO_2 aerogels in 1931, Monsanto initiated the industrial production of milled silica aerogels in the 1950s for use as paint thickener and thermal insulant. The production was however stopped within a few years for economical reasons. Nevertheless, in 1970, a new application of SiO_2 aerogel was found in Cerenkov detectors [226] in the shape of tile; later the optical and thermal properties enabled their use in luminescent solar concentrators [223]. A notable use of aerogels for aerospace applications was introduced by NASA; the first one consisting in using SiO_2 aerogel to entrap cosmic dust particles in its structure and another one for thermal shielding of the Mars exploration module [226]. In a review on aerogel applications, Hrubesh *et al.* [16] categorised different properties exhibited by aerogels and linked their features to potential types of applications (Table 5.1).

Since, the industrialisation of aerogels, their insulation capabilities whether thermal or acoustic remained a major aspect for the use of aerogels in engineering applications [227], for instance in super-insulating window glazing [9]. The recent preparation of organic aerogels made from different polysaccharides, such as alginate [228,229,230], bacterial cellulose [10], chitin [231], chitosan [232,233,234], starch [235] is likely to expand the range of applications for this type of porous material from tissue engineering, drug delivery, catalyst supports (catalysis) for wastewater (removal of SDBS surfactant) treatment.

5.1.5 Cellulose-based porous materials: state of the art

Although cellulose is regarded as a sustainable resource, there have been far fewer reports on cellulose-based aerogels than their inorganic counterparts. An initial attempt by Kistler [209] to produce aerogel from cellulose materials was not pursued further at the time. In the early

Table 5.1: Identification of aerogel properties and features, and associated potential applications[16].

Property	Features	Applications
· thermal conductivity	· best insulating solid · transparent · high temperature · lightweight	· architectural and appliance insulation, portable coolers, transport vehicles, pipes, cryogenic, skylights · space vehicles and probes, casting molds
· density/porosity	· lightest synthetic solid · homogeneous · high specific surf. area · multiple compositions	· catalysts, sorbers, sensors, fuel storage, ion exchange · targets for ICF, X-ray lasers
· optical	· low refractive index solid · transparent · multiple compositions	· Cherenkov detectors, lightweight optics, lightguides, special effect optics
· acoustic	· lowest sound speed	· impedance matchers for transducers, range finders, speakers
· mechanical	· elastic · lightweight	· energy absorber, hypervelocity particle trap
· electrical	· lowest dielectric constant · high dielectric strength · high surface area	· dielectrics for ICs, spacers for vacuum electrodes, vacuum display spacers, capacitors

1970s, Weatherwax and Caulfield[236,237] investigated the formation of a porous dry paper aerogel by critical-point drying[238] of EtOH-swollen cellulose paper . Later on, formaldehyde cross linked cellulose aerogels were prepared using a similar drying technique[239]. These paper-like aerogels had a specific surface of 145-159 m^2/g as determined by N_2 adsorption.

5.1.5.1 Cellulose aerogels

Cellulose aerogels have been subsequently prepared from different sources such as eucalyptus beech[240], bleached sulfite softwood cellulose pulp[241], microfibrillated cellulose fibres[242] , cellulose fibres[243], Whatman CF11 fibrous cellulose particles[244] and cotton wool[245]. The preparation of cellulose aerogels consisted in the dissolution and regeneration of cellulose to obtain a gel of regenerated cellulose[246]. Other approaches consisted in the direct drying of a cellulose gel (aqueous gel) by freeze-drying[241,242] or (alcogel) by supercritical CO_2 ($scCO_2$) drying[245], where the cellulose was not degraded by chemical or physical modifications .

Jin *et al.*[244] prepared a cellulose solution in calcium thiocyanate tetrahydrate ($Ca(SCN)_2 \cdot 4H_2O$) followed by the formation of $Ca(SCN)_2$-cellulose gel at $80°C$. The $Ca(SCN)_2$-cellulose gel was regenerated in a methanol bath and further rinsed with H_2O to remove salt prior to freeze-drying. Jin *et al.* showed that the properties of their cellulose gels were

dependant on the cellulose concentration as well as the freeze-drying methodology applied, which allowed to tailor the specific surface area from 70 m^2/g to 190 m^2/g[244]. In 2008, Hoepfner *et al.*[243] reported results based on methodology used by Jin *et al.*[244] to prepare cellulose aerogels from salt hydrate melts, where the porous structure was obtained by $scCO_2$ drying. It was shown that cellulose gels produced by $scCO_2$ drying exhibited apparent densities ranging from 0.01 g/cm^3 to 0.06 g/cm^3 and higher specific surface areas of up to 250 m^2/g compared to the results reported by Jin *et al.*[244]. Recently, Heath & Thielemans[245] produced a cellulose aerogel with a density of 0.078 g/cm^3 and a specific surface area as high as 602 m^2/g; one of the highest reported to date for cellulose-based aerogels. Their cellulose aerogel was directly obtained from $scCO_2$ drying of a stable hydrogen-bonded cellulose gel obtained from a suspension of ultrasonicated percolated cellulose nanowhiskers.

5.1.5.2 Aerogels made from cellulose derivatives

Aerogels were also produced using different cellulose derivatives as precursors, namely cellulose acetate (CA) and cellulose acetate butyrate (CAB)[219,247]. To increase the mechanical stability and toughness of aerogels, solutions of cellulose derivatives have been cross linked with isocyanates. For example, solution of cellulose acetate (CA) in acetone was cross linked by polyisocyanate catalysed by a tin-based organometallic complex. This approach was successfully used in the preparation of cellulose aerogels using a sol-gel process with various gelation times, the aerogel was finally obtained by $scCO_2$ drying[219]. The properties of these aerogels were a function of the concentration of precursors and their molecular weight. The specific surface area and density varied between 140-250 m^2 and 0.25-0.85 g/cm^3, respectively. Moreover the thermal conductivity of 0.030 $W/m{\cdot}K$ of the CA aerogel was comparable to that of insulating monolithic silica xerogel 0.020 $W/m{\cdot}K$[248].

5.1.5.3 Bacterial cellulose aerogel

In the recent literature, the only reports on the preparation of BC-based aerogels were by Maeda *et al.*[249] and Liebner *et al.*[10], respectively. A BC aerogel was obtained from a BC pellicle formed by the gram-negative bacterium *Gluconobacter Xylinum* under static fermentation[10]. The as-produced gel was purified and solvent exchanged to EtOH. The EtOH swollen BC pellicles were directly dried with $scCO_2$ at $40°C$ and 100 bar, resulting in an aerogel with a porosity exceeding 99%[249]. BC aerogel has a hierarchical internal structure as seen in Figure 5.2 with a density ranging between 0.006 to 0.008 g/cm^3 and

specific surface area of 200 m^2/g as determined by N_2 adsorption at $77°K$ as compared to a density and specific surface area of 0.12 g/cm^3 and up to 1000 m^2/g, respectively for a typical SiO-based aerogel[227]). Overall, the densities of BC-based aerogels are lower than their cellulose-based counter parts as discussed in previous sections.

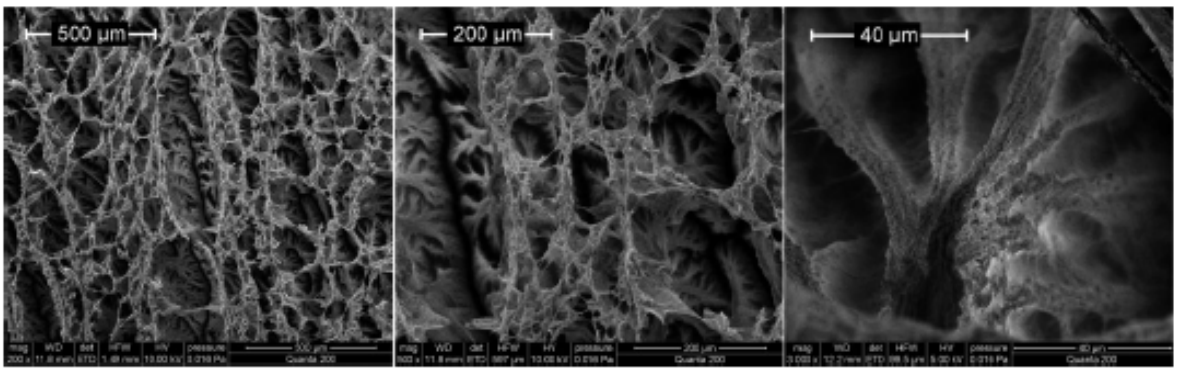


Figure 5.2: Scanning electron microscopy micrograph at various magnifications (x200, x500, x3 000; from left to right) of a $scCO_2$ dried aerogel from bacterial cellulose[10].

5.1.6 Manufacturing routes to highly porous cellulose materials

As mentioned in the previous section the preparation of cellulose aerogels or cryogels often required its prior dissolution using various solvents. In Chapter 4 (Section 4.1.4), a short review on dissolution of cellulose materials summarised different routes explored to obtain so-called all-cellulose (nano-) composites materials.

5.1.6.1 Preparation of cellulose precursors for aerogels

The production of cellulose-based aerogels necessitates the preparation of a cellulose gel, whether such gel contains a dissolved cellulose or a percolated network of high aspect-ratio cellulose nano-whiskers or fibrils (Section 5.1.5). The literature contains a few examples of cellulose aerogels produced from a gel made of a physically interconnected network of cellulose (nano-)fibrils in H_2O[10,242,245,249,250]. However, the rest of cellulose-based aerogels reported were produced by the gelation of cellulose (or derivatives) solutions. To obtain cellulose aerogel-like materials different type of cellulose solvents have been applied.

Cellulose cryogel (so called "Aerocellulose") was prepared by Duchemin *et al.*[246] by dissolving microcrystalline cellulose (MCC) in LiCl and N, N-dimethylacetamide (DMAc)

cosolvent at ambient conditions . The cryogel properties were a function of the initial cellulose concentration in LiCl/DMAc cosolvent as well as the regeneration conditions.

A hydrated calcium thiocyanate melt was successfully used to dissolve cellulose materials with a degree of polymerisation (DP) ranging from 180 for MCC to 1620 for cotton linters[251]. Cellulose with concentration ranging from 0.5 wt.% to 3 wt.% in the solution could be dissolved at temperatures between $110°C$ and $140°C$ to obtain either an aerogel or cryogel[243].

The industrial Lyocell process was used to dissolve cellulose to obtain an aerogel precursor. In this process, the solvent is a tertiary amine oxide N-methylmorpholine-N-oxide (NMMO)-H_2O mixture, which enables the dissolution of cellulose at temperatures below $100°C$ in concentration of cellulose ranging from 0.5 wt.% to 13 wt.%[240,252].

Recently, a cellulose solution was prepared in NaOH-H_2O mixture with a NaOH concentration varying between 7 wt.% to 12 wt.%. The dissolution of cellulose took place at $-6°C$ and a cellulose concentration of 5 wt.% could be achieved[253].

An emerging class of "green" solvents called ionic liquids (ILs) can also be employed to dissolve cellulose readily to provide a precursor in the preparation of cellulose cryogel. Deng *et al.*[254] reported the use of an IL composed of 1-butyl-3-methylimidazolium chloride (BMIMCl) salt to dissolve MCC with a DP of 196, with BMIMCl salt molten and equilibrated at $130°C$.

5.1.7 Potential applications of porous microspheres

In the last three decades, polymeric microspheres have attracted considerable attention from various fields such as nanotechnology, bioengineering, drug delivery system (DDS), regenerative medicine, owing to versatile preparation routes, tailorable properties and surface chemistry reactivity[255,256,257]. The microsphere sizes range from the nano- to micrometer in diameter, moreover the internal pore architecture can be tailored to the end-use applications, *e.g*, DDS or cell culture carrier[258]. Polymeric microspheres have been prepared using interfacial polymerisation, in situ polymerisation, interfacial precipitation as well as adapted electrospinning and electrospraying[259,260]. The control of processing parameters such as solution concentration, solvent, viscosity, influenced the formation of closed- or open-cell structure of porous microsphere, which enabled the encapsulation of various compounds[260,261]. Molvinger *et al.*[234] produced hybrid microspheres composed of chitosan and silica nanoparticles for wastewater treatment applications. Mesoporous bioactive materials

in form of composite microspheres and containing bioactive glasses or silica/calcium oxide were used as hemostatic agent, DDS and bone tissue regeneration, owing to their compatibility and dispersability in bone cement, as well as ability to form stable suspension [262,263]. Magnetic cellulose microspheres (MCMS) were employed to remove metal ions from aqueous solution. Recently, Tang *et al.*[264] reported the used of MCMS for immunomagnetic capture of *Salmonella* bacteria, owing to antibody absorption to MCMS hence conferring high biological specific affinity and absorption capability to MCMS.

5.2 Experimental

5.2.1 Materials

BC was synthesised and treated with NaOH to lyse cells and remove debris as described in Chapter 3. The dissolution of BC was achieved using a cosolvent composed of N,N-dimethylacetamide (DMAc) (Aldrich, Dorset, UK) and LiCl (Fluka, Dorset, UK). Solvent exchange of BC nanofibrils was performed using acetone, ethanol (both from VWR Ltd, Lutterworth, UK) and deionised H_2O produced using a NANOpure deionisation system (Barnstead Thermolyne, Dubuque, USA). All the chemicals were used as received without further purification.

5.2.2 Preparation of regenerated BC cryogel microspheres

To enable dissolution of BC in DMAc/LiCl cosolvent, activation of BC nanofibrils was performed by successive solvent exchange from H_2O to EtOH, then acetone and at last DMAc. Briefly, 40 g of BC (with a dry mass equivalent to 4 g) biosynthesised by *Gluconobacter Xylinus* BPR2001, as described in Chapter 3 (Section 3.2.2), was suspended in 600 ml of EtOH in a 1.5 L beaker and homogenised for 5 min at 30,000 rpm using a Polytron PT 1035GT homogenizer (Kinematica, CH). The resulting suspension was transferred into 12 Falcon tubes from Fisherbrand® (Fisher, UK) with a 50 mL capacity and then centrifuged at 15,000 g for 45 min. The solvent exchange procedure was repeated twice for each solvent. At last, swollen BC in DMAc was weighed on aluminium foil to their desired concentrations with respect to the cosolvent. Prior to dissolution, the cosolvent composed of 8 wt./v.% of LiCl (4 g) in 50 mL of DMAc was prepared in inert atmosphere by sparging N_2 to remove moisture from the cosolvent solution. Subsequently, BC solutions were prepared by adding 2.5 g or 5 g of swollen BC in DMAc to 50 mL of cosolvent, which corresponded to a (dried

equivalent) concentration of 0.5 wt./v.% and 1 wt./v.%, respectively. To ease dissolution of BC in cosolvent, the swollen BC in DMAc were initially homogenised in the cosolvent at 30 000 rpm for 2 min, which resulted in a relatively viscous suspension of not yet dissolved BC in DMAc/LiCl. Then, dissolution of BC was pursued at $55°C$ at a stirring speed of 500 rpm in a 100 mL ISO bottle fitted with a rubber septum of the appropriate diameter. Throughout the dissolution an inert atmosphere was maintained by sparging N_2 through the BC solution to remove entrapped air that was introduced by the prior homogenisation step. To tailor the morphology of regenerated BC cryogel microspheres, several dissolution times were chosen (1, 2, 4 and 24 h). After the desired dissolution time, the BC solution was loaded into a 10 mL glass syringe, which was then equipped with a 28 G blunt tip stainless steel needle. To initiate and maintain a constant dripping of the viscous BC solution into liquid N_2 bath, a mass of 500 g was applied to the needle plunger. The drops of BC solution were collected in a 100 μm metal sieve placed in a polystyrene box filled with liquid N_2 (Figure 5.3). After 10 min of immersion in liquid N_2, the frozen regenerated BC (rBC) microspheres were transferred into a 5 L beaker containing 4.8 L of dH_2O to both seize the outer spherical shape and initiate regeneration of BC gel microspheres. The regenerated BC gel microspheres were subjected to a low shear with an agitation of 200 rpm for 48 h using a 60 mm long triangular stirrer bar during regeneration of BC, thus preventing distortion and elongation of regenerated BC gel microspheres. Subsequently, the regenerated BC microspheres were collected using the 100 μm metal sieve and then transferred to 50 mL Falcon tubes filled with 30 mL of dH_2O. The Falcon tubes were closed and immersed into liquid N_2 for a rapid quench-freezing of H_2O prior to freeze-drying of regenerated BC gel microspheres for 72 h.

The resultant regenerated BC cryogel microspheres obtained were characterised as follows. On the other hand, freeze-dried specimen of BC (referred in following Sections as: Freeze-dried BC) was produced directly from BC stock prepared in Section 3.2, as previously described . A suspension of 2.5 g (0.5 wt./v.%) of BC stock in 10 ml of dH_2O was prepared by homogenisation and then transferred to a 50 ml Falcon. To ensure freeze-quenching of BC/dH_2O suspension, the closed Falcon tube was immersed into liquid N_2 for 10 min, prior to freeze-drying for 72 h, as previously described.

5.2.3 Schematic of preparation of regenerated BC cryogel microspheres

The procedure used to shape BC microsphere is presented in Figure 5.3. The formation of regenerated BC (rBC) cryogel microspheres consisted in seizing the outer shape of a drop

of BC solution in liquid N_2. The large temperature difference between BC solution ($328°K$) and liquid N_2 ($77°K$) resulted in an abrupt phase change of BC solution from liquid to solid. During this rapid freezing, both vitrification and levitation took place simultaneously. Vitrification of BC solution arose from the hindrance of DMAc crystal formation. Whereas, the Leidenfrost effect generated levitation of BC microspheres, which was induced by formation of N_2 vapour phase surrounding the microspheres of BC solution; this vapour was generated from boiling of liquid N_2 while absorbing heat from immersed microspheres[265]. When equilibrium was reached, the frozen and vitrified microspheres sank beneath the liquid N_2 surface. The regeneration of BC microspheres was achieved by their immersion into the non-solvent H_2O. The direct contact between the frozen microspheres of BC solution with H_2O resulted in the rapid regeneration of BC on the microsphere surface, which progressed inwards to its centre. As the quality of DMAc/LiCl cosolvent decreased progressively with its solvent exchange against polar H_2O, precipitation (coagulation) of the dissolved BC took place until complete regeneration of BC microsphere occurred.

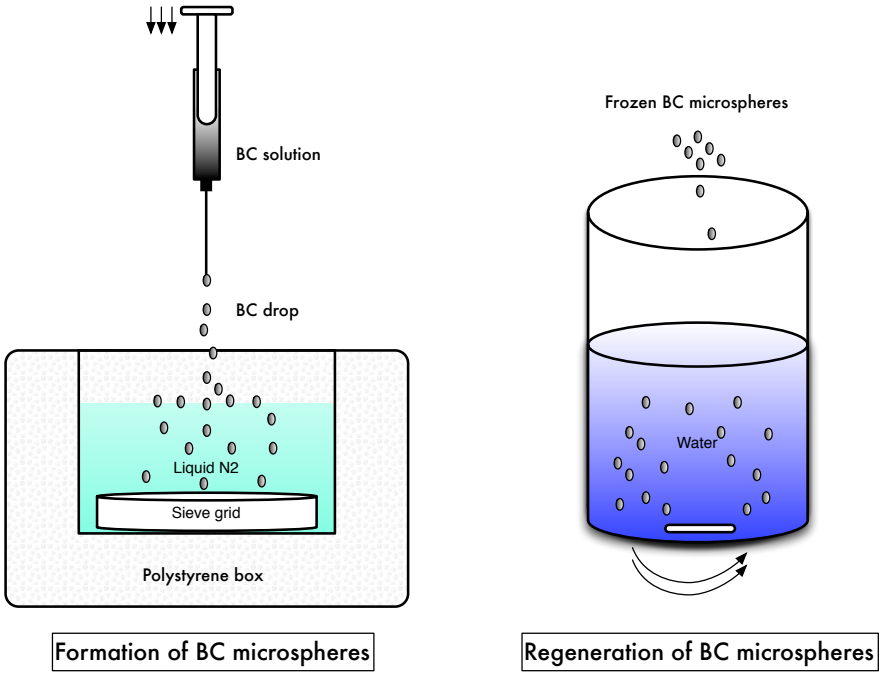


Figure 5.3: Schematic setup for preparation of regenerated BC cryogel microspheres.

5.3 Characterisation of BC cryogels and regenerated BC microspheres

5.3.1 X-ray diffraction of regenerated BC cryogel microspheres

Typical XRD diffractogram of freeze-dried BC and regenerated BC (rBC) cryogel microspheres are presented in Figure 5.4 as a function of dissolution times in DMAc/LiCl and concentration of BC. The diffractogram of freeze-dried BC exhibits a typical pattern of cellulose type I similar to the one presented by Czaja *et al.*[90] for BC. As described previously in Chapter 3, the different peaks observed in Figure 5.4 at 2θ equal: 14.5°, 16.6°, 22.7° and 35° were assigned to diffraction plane [101], [10$\bar{1}$], [002] and [040], respectively. After partial dissolution of BC in DMAc/LiCl cosolvent, diffractogram of rBC cryogel microsphere retained the overall profile of cellulose type I. Furthermore, the peak position of [002] lattice stayed nearly constant (oscillating between 22.6° & 22.8°), as summarised in Table 5.2. The shape of the [002] peak[266] ascertained that no distinguishable transformation to cellulose type II occurred due to highly crystalline nature of BC nanofibrils and processing conditions used in the present study. The freeze-dried BC possess a degree of crystallinity of 90%, whereas rBC cryogel microspheres with BC concentration of 2.5 wt.% and 5 wt.% have a value of 78% and 88%, respectively (Table 5.2). The crystallite size and degree of crystallinity of rBC cryogels after 1 h of dissolution compare favourably with the freeze-dried BC one. The drop of degree of crystallinity accounts for at most 11% when comparing specimen with different BC concentration (2.5 wt.% and 5 wt./v.%) and dissolution time ranging from 1 h to 4 h. After 1 h of dissolution, the crystallite size of [002] lattice varied from 7 nm to 6.7 nm for BC concentration of 2.5 wt.% and 5 wt.%, respectively as compared to the 6.4 nm for freeze-dried BC. The processing parameters used in the preparation of rBC cryogel microspheres resulted in the partial dissolution of BC nanofibrils. Therefore, the morphology and type of cellulose crystals in rBC cryogel microspheres were marginally modified by the dissolution and regeneration procedure, as will be presented in SEM observation in later section. Nonetheless, rBC exhibited a small drop in their degree of crystallinity with increasing dissolution time to up 4 h for either BC concentration. Which was attributed to dissolution of BC in DMAc/LiCl cosolvent as discussed in Chapter 4. It is worth noticing that change in the degree of crystallinity and crystallite size of rBC cryogel microspheres was observed independently of BC concentration dissolved in DMAc/LiCl cosolvent. Recently, Soykeabkaew *et al.*[105] reported a significant increase of amorphous phase to the detriment of the crystallinity of rBC after 1 h of static

immersion in DMAc/LiCl cosolvent (8 wt./v.%). Soykeabkaew *et al.* reported a rapid reduction of crystallite size of BC in the case of a selective surface dissolution of BC. However, in the present investigation, the decrease in degree of crystallinity after 4 h of dissolution (under dynamics conditions) are nonetheless less than those reported by Soykeabkaew *et al.*[105] after 1 h, such discrepancy can be attributed to BC concentration in the membrane-like film as well as the morphology of BC nanofibrils resulting from a static fermentation .

An increase of dissolution time to 24 h results to a complete dissolution of BC nanofibrils for a BC concentration of 2.5 wt.%. Thus, it enabled preparation of rBC cryogel microspheres composed mainly of amorphous rBC nanofibrils, as seen in Figure 5.4. This lost in degree of crystallinity is accompanied by a shift of peak [002] lattice to $2\theta = 20°$ and by the disappearance of peaks assigned to [101] and [$10\bar{1}$] lattices, respectively. The preparation of fully amorphous rBC cryogel microspheres led to the formation of a porous structure, which differed significantly from the one formed by rBC nanofibrils with higher degree of crystallinity, as will be discussed in Section 5.3.5.

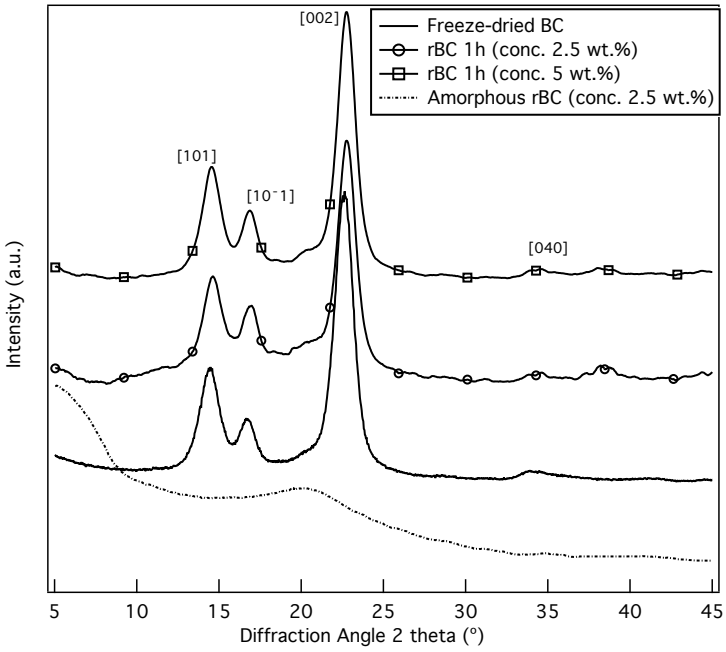


Figure 5.4: X-ray diffractogram of freeze-dried BC, amorphous regenerated BC and regenerated BC cryogel microsphere at BC concentration of 2.5 wt.% and 5 wt.% for 1 h of dissolution in DMAc/LiCl.

Table 5.2: Degree of crystallinity, BC concentration, crystal size and peak location for [002] lattice of BC cryogels and rBC cryogel microspheres as a function of dissolution time of BC in DMAc/LiCl cosolvent.

Dissol. time	BC conc.	Crystallite size			[002] location	Crystallinity
		[101]	[10$\bar{1}$]	[002]		
(h)	(wt.%)	(nm)	(nm)	(nm)	(°)	(%)
*	2.5	5.6	7.0	6.4	22.6	90.5
1	2.5	5.4	7.3	7.0	22.8	78
2	2.5	7.0	6.8	5.9	22.7	84
4	2.5	5.9	7.3	6.9	22.7	67
24 †	2.5	n/a	n/a	n/a	20.3	n/a
1	5	6.1	7.3	6.7	22.8	88
2	5	6.1	7.8	6.7	22.8	79
4	5	5.8	7.1	6.9	22.8	76

*Freeze-dried BC.

† Fully amorphous rBC cryogel microspheres.

5.3.2 ATR-FTIR spectroscopy of regenerated BC cryogel microspheres

ATR-FTIR spectra of freeze-dried BC and regenerated BC cryogel recorded at various dissolution time and BC concentration are presented in Figure 5.5 with a spectral region ranging from 3700 cm^{-1} to 2700 cm^{-1} and from 1700 cm^{-1} to 600 cm^{-1}. The spectra of freeze-dried BC specimen resembles closely to those presented by Shirk *et al.*[267] and Czaja *et al.*[90], the spectral assignment of the different peaks was detailed earlier in Chapter 3 (Table 3.3). In the case of rBC cryogel microspheres, the intensity and resolution of the peak assigned to -OH stretching at 3350 cm^{-1} decreases with increasing dissolution time in DMAc/LiCl cosolvent. While the peak assigned to C-O-C stretching of the $\beta(1 \rightarrow 4)$ glycosidic ring at 900 cm^{-1} sharpen and strengthen with increasing dissolution time. Based on IR investigations discussed in Chapter 4, the peak increase at 900 cm^{-1} for rBC cryogel microspheres was associated with a reduction in degree of crystallinity, which complied with XRD measurements in previous section. The ATR-FTIR spectra of rBC cryogel microspheres varied in a similar fashion as a function of dissolution time and independently to their BC concentration.

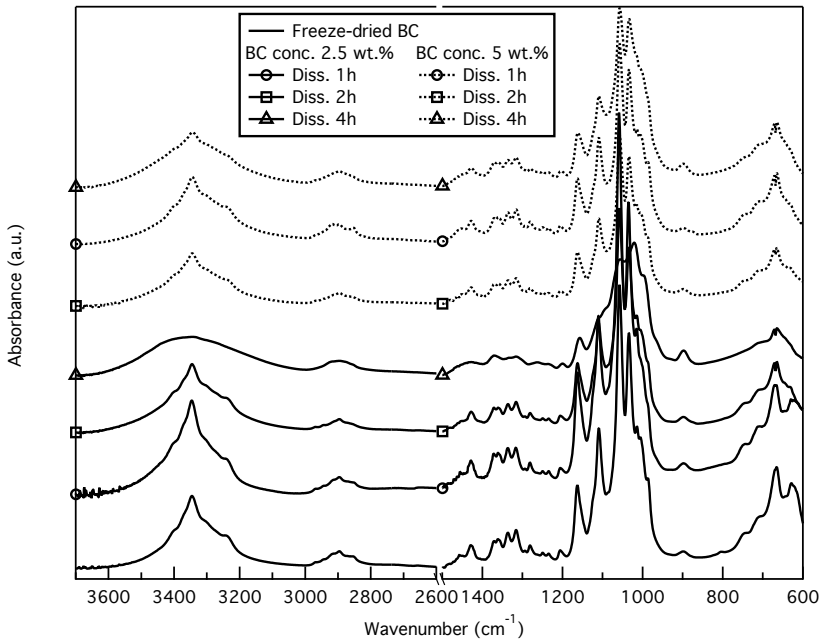


Figure 5.5: ATR-FTIR spectra of freeze-dried BC and regenerated BC cryogel microspheres at various dissolution time and BC concentration of 2.5 wt.% and 5 wt.%.

5.3.3 Thermal degradation of regenerated BC porous microspheres

The weight loss of freeze-dried BC and rBC cryogel microspheres caused by thermal degradation in inert N_2 atmosphere is presented in Figure 5.6. In the case of freeze-dried BC, the degradation profile in N_2 atmosphere resembles the one reported by Barud *et al.*[108] for BC membrane with an onset degradation temperature of $276°C$ and a thermal degradation of $348°C$. The onset degradation of rBC cryogel microsphere are shifted after 1 h of dissolution to $286°C$ and $272°C$ for BC concentration of 2.5 wt.% and 5 wt.%, respectively. An increasing dissolution time shifted the onset degradation temperature to higher values some exceeding the reference specimen of freeze-dried BC, as shown in Table 5.3, the degradation temperature underwent similar shifting independently of BC concentration. The degradation behaviour of the rBC cryogel microspheres with various BC concentration is different to that of freeze-dried BC, with a steeper slope of degradation, rBC cryogel exhibits a rate of degradation higher than its freeze-dried counterpart, as seen in Figure 5.6II. For the amorphous rBC cryogel, both onset and degradation temperature shift to higher temperature than all other specimens, as if amorphous rBC was thermally more stable, thus requiring higher

temperature to start it degradation (Table 5.3). As previously remarked in Chapter 4, the (partial) dissolution step and subsequent dissolution modified the morphology of BC nanofibrils by altering the BC crystal as well as the degree of crystallinity, thus promoting a different degradation kinetic in inert N_2 atmosphere.

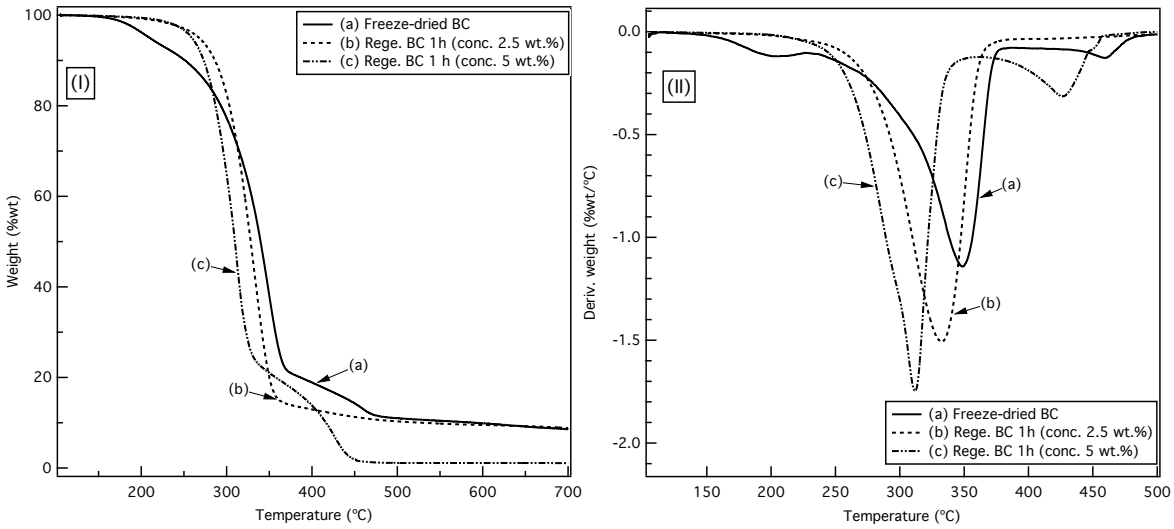


Figure 5.6: I) Thermal degradation of freeze-dried BC and regenerated BC cryogel microspheres in N_2 atmosphere for BC concentration of 2.5 wt.%/ and 5 wt.%. **II**) Derivative weight loss of freeze-dried BC and regenerated BC cryogel microspheres in N_2 atmosphere for BC concentration of 2.5 wt.%/ and 5 wt.%.

5.3.4 Nitrogen sorption isotherm for regenerated BC cryogel microspheres

The porous properties of rBC cryogel microspheres were investigated using N_2 adsorption-desorption isotherms at 77 K to determine specific pore volume, average pore diameter, specific surface area. The N_2 adsorption-desorption isotherm of typical BC cryogel and rBC cryogel microsphere is shown in Figure 5.7I.

The freeze-dried BC (curve a) exhibits a high volume of isotherm adsorbed, nearly 700 cm^3/g compare to the 250 cm^3/g of rBC cryogel (curve b & c). Such difference was attributed to the unaltered nature and aspect of BC nanofibrils in the freeze-dried BC whereas rBC underwent dissolution in DMAc/LiCl and subsequent regeneration in H_20. For low relative pressure (below 0.2 unit), the isotherm profile of both freeze-dried BC and rBC cryogel show a type I isotherm characteristic of the adsorption of micropores (less than 5 nm) according

Table 5.3: Onset degradation temperature, degradation temperature, weight loss rate and char yield of the thermal degradation process in N_2 of freeze-dried BC and regenerated BC with various dissolution time and BC concentration

Dissol. time (h)	BC conc. (wt. %)	Onset Temp. (°C)	Degradat. Temp. (°C)	Wt. loss rate (-)($\%.min^{-1}$)	Char Yield (wt. %)
*	2.5	276.4	348.4	1.42	11.3
1	2.5	286.4	332.4	1.50	8.7
2	2.5	262.5	291.7	1.36	2.3
4	2.5	307.0	340.7	1.50	10.7
24†	2.5	310.4	354.2	1.82	0.10
1	5	272.1	311.2	1.74	1.0
2	5	268.6	296.4	1.69	1.7
4	5	302.9	323.4	1.60	6.2

*Freeze-dried BC prepared from NaOH treated BC.

† Fully amorphous regenerated BC cryogel microsphere.

to I.U.P.A.C. presented in Chapter 2. At higher relative pressure, freeze-dried BC (0.6 unit to 1 unit) and rBC cryogel (0.7 unit to 1 unit) adsorb a significant volume of isotherm in their fibrillar porous network. Thus, the sorption profile of porous cellulose specimen correspond to an isotherm of type IV according to I.U.P.A.C., which describes the characteristic slit-shaped pore structure of BC and rBC cryogels. Furthermore, the hysteresis loop formed during N_2 desorption at high relative pressure relates to a state of condensation of pore fluid (N_2) within non-rigid aggregates of pores in the structure of freeze-dried BC and rBC cryogels, respectively. The pore size distribution of freeze-dried BC and rBC cryogels calculated according to BJH (Equation 2.13) is presented in Figure 5.7II. The measured pores have a broad distribution ranging from mesopores (2-50 nm) to macropores (50 nm to 200 nm). BC and rBC cryogels are mainly composed of mesopores with a mean pore diameter of 17.7 nm and 31.4 nm, respectively (Table 5.4). Markedly on Figure 5.7II, freeze-dried BC has a greater pore volume than rBC cryogel microsphere, which was attributed to use of unaltered BC nanofibrils. However, preparation of rBC cryogel with BC concentration of 2.5 wt.% and 5 wt.% had only a minor effect on their respective pore size distribution and overall pore volume.

The porous properties of freeze-dried BC and rBC cryogel microsphere are summarised

in Table 5.4 for various dissolution time and BC concentration. As previously described, the freeze-dried BC properties outperformed those of rBC cryogel microspheres. In fact, the specific (BET) surface area (Equation 2.12) of BC cryogel with 240 m^2/g was nearly twice as much the value of all the specimen. The value for specific surface area compared favourably with the 200 m^2/g reached by Liebner *et al.*[10] for BC aerogel obtained by $scCO_2$ drying of BC alcogel. But was lower than the 600 m^2/g, recently reported by Heath and Thielemans[245] for cellulose aerogel prepared using nanowhiskers precursor. The specific surface area of rBC cryogel microspheres is a function of dissolution time in DMAc/LiCl and degree of crystallinity of BC, these parameters controlled the stiffness and malleability of BC nanofibrils. The specific surface area of rBC cryogel (conc. 2.5 wt.%) decreases by 24% from 99 m^2/g to 75 m^2/g for dissolution time of 1 h and 4 h, respectively. However, amorphous rBC cryogel (conc. 2.5 wt.%) obtained after 24 h of dissolution exhibits a specific surface area of 123 m^2/g. The gain in specific surface area in this case was attributed to the lost of crystallinity of BC nanofibrils, thus able to generate a different pore structure and organisation, as will be presented in following section. Interestingly with a BC concentration of 5 wt.%, the variation in specific surface area undergoes more drastic changes including a near 50% drop after 2 h of dissolution followed by an increase to 115 m^2/g for 4 h as compared to the initial 90 m^2/g. From the data in Table 5.4, two correlations were drawn between increasing dissolution time and lowering of average pore diameter and another between decreasing specific pore volume and reduction of specific surface area for rBC cryogel microsphere specimen. The rBC cryogel microsphere prepared had a specific surface area ranging from 99 m^2/g to 123 m^2/g for crystalline and amorphous rBC network, respectively. The value of specific surface area reported in literature for dissolved and regenerated cellulose-based aerogel were in similar order of magnitude. For instance, Deng *et al.*[254] reported value of 186 m^2/g (IL & $scCO_2$ drying) for nanoporous cellulose foam, Hoepfner *et al.*[243] a value of 160 m^2/g (NMMO & freeze-drying) for nanofibrillar cellulose aerogel and Gavillon and Budtova[252] a value of 200 m^2/g (NaOH & $scCO_2$ drying) for highly porous aerocellulose.

5.3.5 SEM observation of regenerated BC cryogel microspheres

SEM micrographs of surface of rBC cryogel microspheres presented in Figure 5.8 reveal the open-porous surface, which also appears rough at low magnification. The porous structure of rBC cryogel microspheres is composed at its surface of distinct and visible pores but also

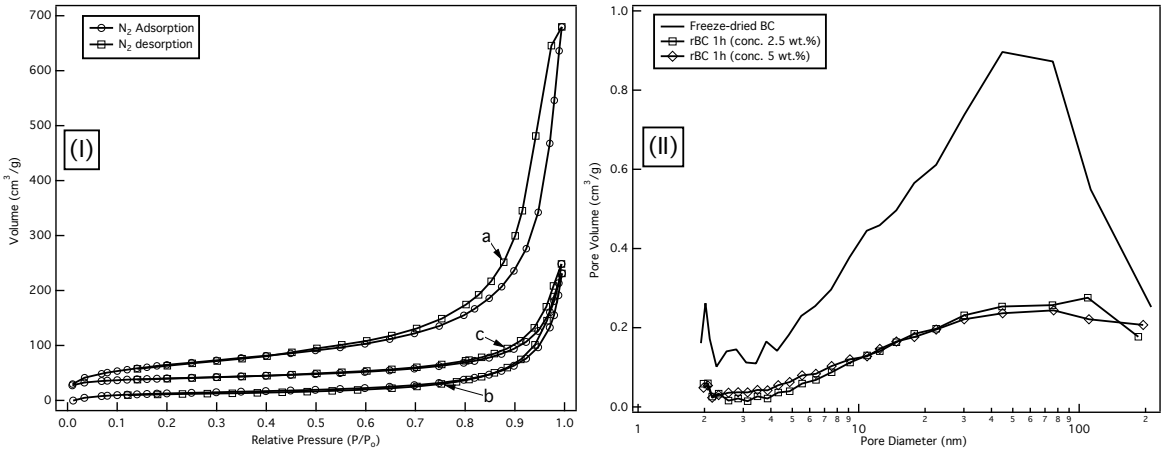


Figure 5.7: I) N_2 adsorptiondesorption at 77K for Freeze-dried BC (a), rBC cryogel microspheres with a BC concentration of 2.5 wt.% (b) and 5 wt.% (c). **II**) BJH pore size distribution (N_2 adsorption) obtained for freeze-dried BC and rBC cryogel microspheres.

Table 5.4: Average pore diameter, specific pore volume and specific (BET) surface area determined by N_2 sorption measurements at 77 K for freeze-dried BC cryogel and rBC cryogel microspheres at various dissolution time in DMAc/LiCl and BC concentration.

Dissolution time (h)	BC conc. (%wt.)	Average pore dia. (nm)	Spec. pore vol. (cm^3/g)	Spec. surface area (m^2/g)
†	2.5	17.8	0.72	240.5
1	2.5	25.2	0.23	99.3
2	2.5	31.4	0.20	90.4
4	2.5	13.5	0.13	75.4
24*	2.5	14.5	0.26	123.5
1	5	20.0	0.22	90.3
2	5	25.5	0.14	55.2
4	5	14.1	0.23	115.3

† Freeze-dried BC

* Fully amorphous rBC cryogel microspheres.

of bundles of BC nanofibrils rendering a fibrous aspect (micrographs a & b). A high magnification (micrographs c & d) resolves the porous hierarchical structure, which is composed of dense aggregates of BC nanofibrils, forming a film-like structure and a less dense local network of BC nanofibrils, forming pseudo-like pores. The hierarchical structure of rBC cryogel microsphere resulted in apparition of macroscopic open pores with broad size distribution, but, also in formation of both micropores and mesopores throughout the structure, as described in Section 5.3.4.

The modification of surface morphology of rBC cryogel microspheres with respect to dissolution time of BC in DMAc/LiCl is presented in Figure 5.9. The surface of rBC cryogel microspheres appear rugged with visible irregularities inherent of their preparation methodology. Furthermore, the surface roughness of microspheres comprises the presence of macro-size pores observable under low magnification, as seen in Figure 5.8(a, c & e). It is worth noticing that BC concentration did not contribute, significantly, to neither apparition nor alteration of the surface features of rBC cryogel microspheres. Interestingly, the surface of rBC cryogel microsphere tends to smooth itself with increasing dissolution time with formation of a continuous apparent outer layer. The densification of surface of microspheres resulted from fusing of BC nanofibrils followed by their adjacent aggregation from one another (see Figure 5.9; b, d & f). Evidences of a progressive fusion of BC nanofibrils were also reported for increasing immersion time of BC membrane in DAMc/LiCl cosolvent to obtain selective partial dissolution of BC nanofibrils[105]. Similarly, Deng *et al.*[254] observed this behaviour for microcrystalline cellulose dissolved in ILs followed by regeneration in H_2O and subsequent $scCO_2$ drying. Observations of cross-section of rBC cryogel microspheres reveal that the porous structure remained of nano- and fibrillar nature, with sporadic macro-size pores distributed throughout the rBC nanofibril network, as seen in Figure 5.9(inserts). Recently, Hu *et al.*[268] reported the formation of sphere-like BC particles directly produced by an *Gluconobacter Xylinus* JCM9730 strain. The BC spheres exhibited a dense outer layer of BC nanofibrils, where the inner shell was composed of hierarchical arrangement of interlayers of dense aggregates of BC and fibrillar network of BC nanofibrils.

The surface and cross-section of amorphous rBC cryogel microspheres are shown in Figure 5.10. The surface of microsphere is similar to the one previously described for Figure 5.9, where both irregularities and ruggedness appeared. Nonetheless, a relatively dense and continuous layer was formed from an extensive fusion of rBC nanofibrils. The cross-section distinctly reveals the presence of a cohesive rBC outer-layer, which is covering an underlying

network of macro-size pores converging inwardly to the microsphere centre. The surface of macro-size pores formed is composed of a relatively smooth thin wall of rBC, which is covered with a hexagonal-like patterns of rBC nanofibril bundles stacked on top of one another in clusters, as seen in Figure 5.11. In fact, increasing the dissolution time resulted in formation of denser surfaces throughout rBC cryogel microsphere by fusion and aggregation of rBC nanofibrils. Distinct porous structures were achieved depending on the residual degree of crystallinity of the rBC; a high degree of crystallinity yielded a very fibrillar rBC network with presence of film-like aggregates whereas a low degree of crystallinity resulted in formation of dense rBC surface by fusion and aggregation, as seen in Figure 5.9 and Figure 5.10, respectively.

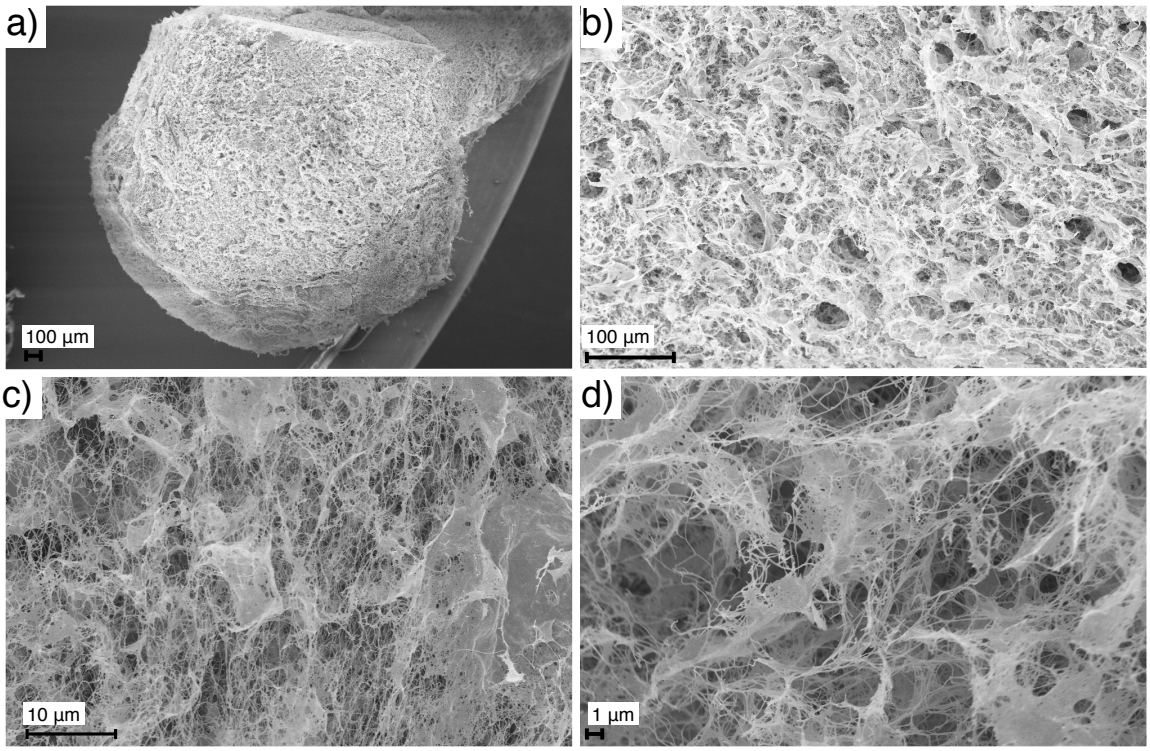


Figure 5.8: SEM micrographs at various magnifications of surface of rBC cryogel microspheres with a BC concentration of 2.5 wt.% after 1 h of dissolution in DMAc/LiCl. With **a**) x100; **b**) x500; **c**) x5K and **d**) x10K.

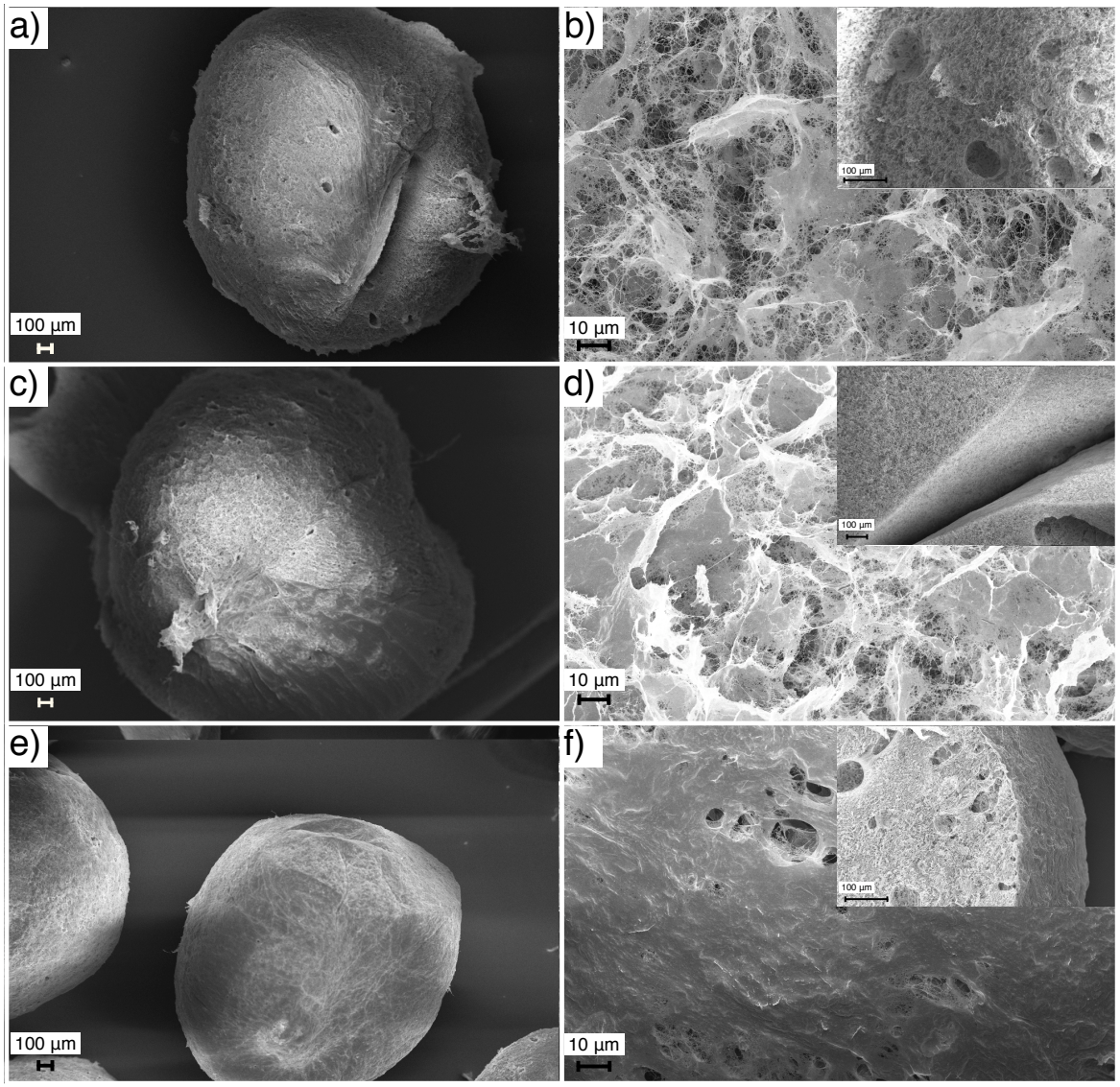


Figure 5.9: SEM micrographs at various magnifications (x100 and x2K; from left to right) of surface and cross-section (inserts) of rBC cryogel microspheres with a BC concentration of 5 wt.% for different dissolution time in DMAc/LiCl. With: **a** & **b**) for 1h; **c** & **d**) for 2 h and **e** & **f**) for 4 h, respectively.

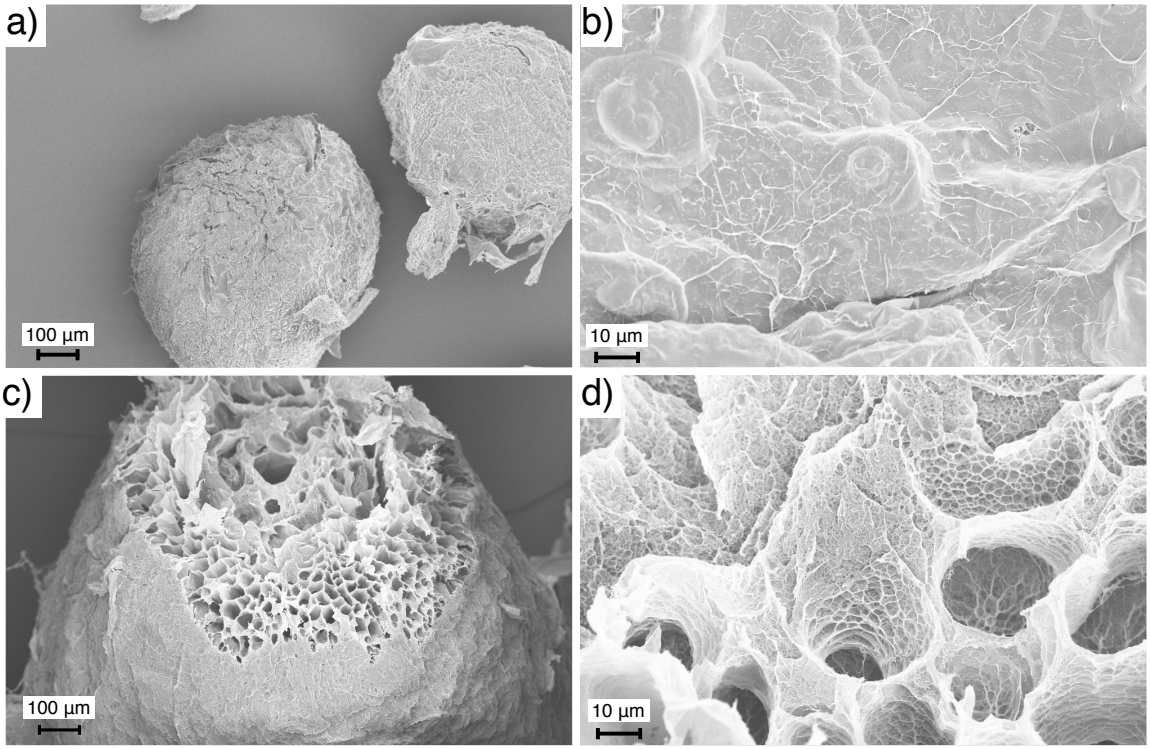


Figure 5.10: SEM micrographs at various magnifications (x250 and x2.5K; from left to right) of both surface and cross-section of amorphous rBC cryogel microsphere with a BC concentration of 2.5 wt.% after 24 h of dissolution in DMAc/LiCl.

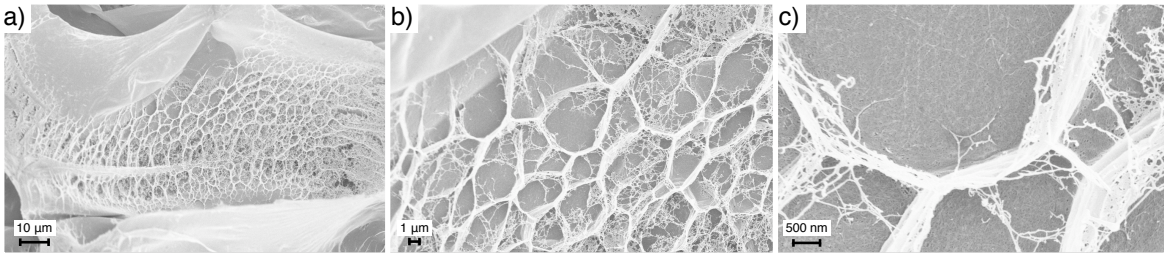


Figure 5.11: SEM micrographs at various magnifications (x2.5K, x10K and x50k; from left to right) of a pore cross-section of amorphous rBC cryogel microsphere with a BC concentration of 2.5 wt.% after 24 h of dissolution in DMAc/LiCl.

5.4 Conclusions

The development of regenerated bacterial cellulose (rBC) cryogel microspheres was achieved. BC nanofibrils were dissolved in DMAc/LiCl cosolvent followed by outer shape seizure in liquid N_2, then regeneration in H_2O followed by a freeze-drying step. The structure and properties of the rBC cryogel microspheres produced were influenced by the processing parameters applied. The degree of crystallinity of rBC decreased with increasing dissolution time, independently of the initial BC concentration. The reduction of thermal stability of rBC was linked to reducing degree of crystallinity, which was in term dictated by the dissolution time in DMAc/LiCl cosolvent. The BET surface area for the rBC cryogel microspheres varied from 123 m^2/g to 55 m^2/g for various dissolution time in DAMc/LiCl cosolvent. The SEM observation revealed the correlation between surface layer and internal hierarchical structure with respect to dissolution in DMAc/LiCl. Interestingly, the structure of fully amorphous rBC cryogel microsphere specimen presented significant difference compared to the specimen with a certain degree of crystallinity. A dense and continuous layer was formed at the surface of amorphous rBC cryogel microsphere. Moreover, the cross-section observation revealed the formation of macro-size pore composed of thin wall and covered with hexagonal-like pattern, whereas a nano- and fibrillar structure was observed for specimen having various degree of crystallinity.

5.5 Future work

The intrinsic properties of the rBC cryogel microspheres produced, such as, high specific surface area, fibrillar porous network, extensive availability of hydroxyl groups and maintenance of spherical shape can be potentially interesting for several applications. The rBC cryogel microspheres could be used as cell culture carrier in zero-gravity culture condition in bioreactor for cells expansion. The readily accessible hydroxyl groups could be used to functionalise the rBC cryogel microspheres by introducing various functionalities such as carboxyl, amines or thioether moieties. Moreover, the rBC cryogel microspheres could be used as drug delivery systems, where active drugs would be loaded using super-saturation precipitation techniques, widely used in the pharmaceutical industry, followed by the application of sealing coating.

The size of the rBC cryogel microsphere produced limit their range of applications. Therefore, an improved processing route would be needed to enable the formation of smaller BC drops prior to their shape seizure owing to the high viscosity of the BC solution. Therefore,

instead of a needle, the use of an atomising nozzle (or similar spray-drying technique) pointing downwards to a recipient filled with liquid N_2 would create smaller drops, hence reducing significantly the size of rBC cryogel microsphere formed.

6

Bacterial Cellulose-based Bioinorganic Nanohybrids

6.1 Introduction

6.1.1 Aims and objectives

The aim of the work reported in this chapter was to synthesise thioether-functionalised bacterial cellulose (BC) nanofibrils using a so-called "grafting from" approach; radicals were created on the surface of BC by cerium oxidation and subsequently free radical grafting polymerisation (FRGP) of thioether containing monomer was initiated from the surfaces of BC nanofibrils in an aqueous system. Another aim was to produce functional BC-based bioinorganic nanohybrid materials by chemisorption of gold nanoparticles (Au NPs) or semiconductor cadmium-telluride (CdTe) quantum dots (QDs) onto thioether-functionalised BC nanofibrils to introduce optical properties, *i.e.*, surface plasmon resonance and photoluminescence.

The objectives of the work reported in this chapter were to characterise the effect of the FGRP reaction on the chemical composition and physical properties of then thioether-functionalised BC nanofibrils. The properties of thioether-functionalised BC nanofibrils were characterised using the analytical methods introduced in Chapter 2, such as XRD, ATR-FTIR, elemental analysis (EA), TGA and SEM. The optical properties of the functional bioinorganic nanohybrid materials were also characterised. The photoluminescence of CdTe QDs functionalised bioinorganic nanohybrids dispersed in polymer matrix was assessed by UV irradiation.

This chapter is composed of 7 parts: literature review, experimental methodology, characterisation of thioether-functionalised BC nanofibrils (MTEMA-g-BC), characterisation of Au NPs chemisorbed MTEMA-g-BC nanohybrids (MTEMA-g-BC-Au), characterisation of CdTe QDs chemisorbed MTEMA-g-BC nanohybrids (MTEMA-g-BC-CdTe), observation of photoluminescence of polymer films containing MTEMA-g-BC-CdTe nanohybrids and conclusions. The following section reviews the progress in the emerging field of bioinorganic nanohybrid materials, the various bioinorganic nanohybrid systems developed and in particular those containing NPs of different nature. The state of the art on polysaccharide-based bioinorganic nanohybrids is described, followed by a presentation of applications of bioinorganic nanohybrid materials. Section 6.2 describes the methodology used to synthesise thioether-functionalised BC nanofibrils (MTEMA-g-BC), bioinorganic nanohybrids based on MTEMA-g-BC nanofibrils and chemisorption of either Au NPs or CdTe QDs, as well as the preparation of photoluminescent nanocomposite polymer films containing MTEMA-g-BC-CdTe nanohybrids. The result of the characterisation of MTEMA-g-BC nanofibrils and their properties are described and discussed in Section 6.3. Then, the characterisation of MTEMA-g-BC-Au and MTEMA-g-BC-CdTe nanohybrids and their properties will be discussed in Section 6.4 and Section 6.5, respectively. In the subsequent Section 6.6 the photoluminescence of nanocomposite polymer films containing MTEMA-g-BC-CdTe nanohybrids will be described. The final section is the conclusion which is followed by suggestion for further improvement in the preparation of BC-based bioinorganic nanohybrids.

The motivation for the research presented thereafter was to investigate the covalent grafting of a thioether functional (SCH_3) monomer from the surface of BC nanofibrils using a "grafting from" approach and to assess the ability of SCH_3 groups to form strong bond with noble metallic NPs and semiconductor QDs. Therefore, to demonstrate the preparation of functional bioinorganic nanohybrids composed of thioether-functionalised BC (MTEMA-g-BC) nanofibrils by chemisorption of Au NPs and CdTe QDs. In addition, the development of these BC-based bioinorganic nanohybrids exemplified the versatility of BC biosynthesised by *Gluconobacter xylinus* and its propensity to be used in the production of advanced functional nanomaterials for sensing or biomedical applications.

6.1.2 Introduction to (bio)organic-inorganic materials

The last two decades have witnessed the development of (bio)organic-inorganic hybrid materials or so-called "functional hybrid materials", which are forecasted to play a key role in

the upcoming surge of advanced functional nanomaterials employed in electronic, biomedical, catalytic applications[11]. Organic-inorganic hybrid materials were made by combination of both organic and inorganic components, which resulted in creation or/and enhancement of new functionalities and properties, such as electrical, electromagnetic, thermal, optical, owing to the synergistic interaction of both components used, while retaining the inherent properties of the substrate[269]. Recently, Sanchez *et al.*[270] classified organic-inorganic hybrid materials as a function of the nature of interactions at their interface. In the first one, the interface adhesion between organic and inorganic components was maintained by weak intermolecular forces like, van der Waals, hydrogen or iono-covalent bonds. In the other one, however, strong bonds formed across the interface such as, covalent or ionic bonds ensured the adhesion.

The development of functional hybrid nano- materials combining inorganic, organic or/and biological compounds opens the way to innovative concepts such as, biomimetics[139,271], biomineralisation[272], multiscale hierarchical structuring[273,274], which exploit and bond together the chemical, optical, physical properties of the individual constituents[270]. Due to the rapid expansion and growth in the development of inorganic-organic materials, an exhaustive overview of this research area was not feasible in the present review, several reviews reported elsewhere[269,274,275,276,277] aimed to survey the development organic-inorganic materials in different research fields such as, optics, electronics, membranes, protective coatings, catalysts, sensors and biology. Therefore, to narrow the scope of this review, the author restricted the survey to recent literature on **bioinorganic hybrid** materials with an emphasis on those composed of an organic substrate originating from polysaccharides and inorganic NPs ranging from metal oxides, metals or minerals.

6.1.3 Routes to organic-inorganic hybrid materials

Over the years, it was established that the bottom-up self-assembly approach in the construction of organic-inorganic hybrid materials presented significant advantages, such as well-defined nanostructures, morphology and tailored properties[11]. Therefore various strategies were developed to produce organic-inorganic hybrid materials[278,279]. The soft chemistry-based route, *i.e.*, sol-gel chemistry, introduced in the eighties remains the most widely used[280] (see Figure 6.1) owing to its versatility and the possibility to combine various types of organic precursors with a wide range of inorganic components (i.e., minerals, metallic oxides, metals, chalcogenides)[278,281]. Organic-inorganic hybrid materials were prepared by the

intercalation within the mesoporous network (2D or 3D) of an inorganic host, also referred as nanobuilding blocks (NBBs), of various organic components. These were immobilised within the NNB structure via weak intermolecular forces (Figure 6.1). Furthermore, the surfaces of NBBs were chemically functionalised with a wide range of reactive functional groups[282,283]. Organic-inorganic hybrid materials were prepared by grafting functionalisation between organic and inorganic components to introduce or enhance functional properties of either components (Figure 6.1). Moreover, organic-inorganic hybrid materials with tailored structural and functional properties were prepared by a combination of the aforementioned routes. Therefore, complex hybrid structures were achieved such as, precise templating of surface features, formation of nanoaggregates or control over the mesostructure of the hybrid network[284,285].

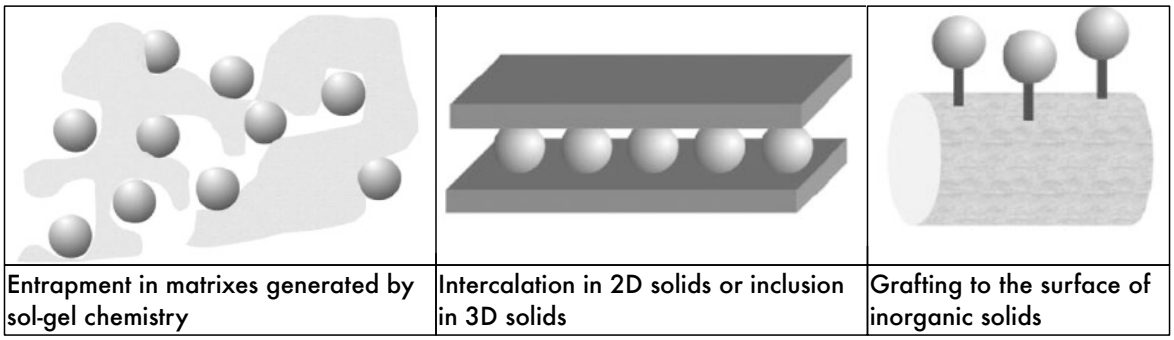


Figure 6.1: Schematic of the synthetic routes for the development of organic-inorganic hybrid materials (reproduced from reference[11]).

6.1.4 Cellulose-based bioinorganic hybrid materials: state of the art

In recent years, cellulose and its derivative have been used for the preparation of functional bioinorganic (nano-) hybrid materials, where various type of polysaccharides (*i.e.*, polymer or particle) were supporting and immobilising a wide variety of NPs using different approaches[286]. In recent literature on bioinorganic hybrid materials, reports of organic substrates originating from, cellulose (whiskers, nanofibres)[286,287], BC (membranes, nanofibrils)[288,289], regenerated cellulose[290,291], cellulose derivatives[292,293,294,295,296,297,298,299] and chitosan[300,301,302] were found. Some of these examples were summarised in Table 6.1. The variety of organic substrates revealed the versatility of polysaccharides for the preparation of hybrid materials, which was attributed to a diversity of shape, aspect ratio, as well as, the

ease of functionalisation using well documented wet chemistry. Similarly, the use of a wide variety of inorganic NPs including, minerals, metallic oxides, metals and semiconductor QDs to introduce new functionality to the polysaccharide substrates has been reported (Table 6.1).

In the late eighties, Rajeshwar and Kaneko[303] were already reporting both the preparation and usage of bioinorganic hybrid materials as luminescent probes to study electron-transfer phenomena. The simple method of preparation, still performed nowadays, of these bioinorganic hybrids, consisted in soaking cellulose paper in a $CdCl_2$ salt solution followed by immersion in $Na_2S{\cdot}9H_2O$ solution to form CdS QDs. The cellulose acted as a host for the embedded CdS QDs.

Over the last decade, cellulose originating from plants whether in fibres[304], pulp[305] or whiskers[306] was mainly as the organic component for the preparation of bioinorganic hybrids on which NPs were either immobilised or self-assembled[287]. The immobilisation procedure consisted of *in situ* chemical reduction of metal ions in solution in the presence of a cellulose host[306,307]. The hydroxyl groups on the cellulose surfaces formed cellulose/metal ion complexes by coordination[108] and acted as anchors and nucleation sites to reduced NPs[308]. Shin *et al.*[306] reported the immobilisation of Au-Ag alloy on cellulose whiskers by *in situ* coreduction in a $AgNO_3/HAuCl_4$ solution by sodium borohydride ($NaBH_4$) in the presence of suspended cellulose whiskers, thus enabling stabilisation of NPs. The resulting cellulose/Au-Ag alloy NP bioinorganic hybrids exhibited a well defined surface plasmon resonance (SPR) band, moreover, the initial morphology and crystallinity of cellulose whiskers was maintained. Similarly, using wood pulp fibres and $AgNO_3$ salt solution followed by reduction in $NaBH_4$ solution Zhu *et al.*[308] prepared bioinorganic hybrids exhibiting antimicrobial properties, which effectively inhibited the growth of *Escherichia Coli*. Lately, this approach was also employed by Chen *et al.*[309] for the *in situ* growth of silica NPs onto cotton fabrics. The silica NPs were synthesised via sol-gel chemistry based on hydrolysis and polycondensation of a silane precursor (methyltrimethoxysilane) in a basic aqueous solution in the presence of the cotton fabric. Then, the resulting cellulose/silica bioinorganic hybrids were coated with a fluoropolymer, which resulted into bioinorganic hybrids with both a nanoscaled roughness and superhydrophobic properties. Moreover, the versatility of this approach was further demonstrated by He *et al.*[304] during *in situ* reduction of a metal precursor solution in the presence of porous cellulose template. In fact, He *et al.*[304] prepared bioinorganic hybrids by anchoring Au, Ag, Pt or Pd NPs into a cellulose (filter paper) substrate, these hybrids

presented a SPR band characteristic of the metallic NPs. He *et al.* suggested that the combination of nanopores on the surfaces of porous cellulose and high density of OH groups constituted nanoreactors essential for NPs synthesis and immobilisation, where metal ions were coordinated with OH groups via ion-dipole interactions. Contrary to the aforementioned reports[304,306,308,309], Padalkar *et al.*[310] highlighted the fact that a rather low coverage of NPs on cellulose or a random deposition of NPs in porous cellulose was achieved owing to the low surface charge of cellulose. To tackle this problem, Padalkar *et al.*[310] proposed instead, a modified reductive deposition procedure of metallic NPs (Au, Pt & Cu) onto surfaces of cellulose nanocrystals by addition of cationic surfactant namely, cetyltrimethylammonium bromide (CTAB). In fact, CTAB acted both as a NPs stabiliser[311,312] and a means to position metallic NPs along surface of cellulose nanocrystals.

Recently, Benaissi *et al.*[313] presented an innovative approach based-on a $scCO_2/H_2O$ system to synthesise Pt NPs from H_2PtCl_6 metal salt in the presence of suspended cellulose nanofibrils. Under supercritical conditions, cellulose nanofibrils enabled the direct reduction of the platinum species to Pt NPs without further addition of a reducing reagent. Marques *et al.*[314] reported the preparation of cellulose/TiO_2 bioinorganic nanohybrids to enhance brightness and opacity of paper (handsheet). These cellulose/TiO_2 hybrids were produced by hydrolysis of titanyl sulphate ($TiOSO_4 \cdot xH_2SO_4 \cdot xH_2O$) in an acidic medium in the presence of cellulose fibres (*i.e.*, bleached kraft pulp). Moreover, an identical procedure was used by Sun *et al.*[111] for the preparation of bacterial cellulose (BC)/TiO_2 bioinorganic hybrids for photocatalytic purposes.

However, the use of semiconductor QDs in the preparation of cellulose-based bioinorganic hybrids required either chemical or physical modification of cellulose surfaces prior to QDs immobilisation onto them to ensure stable photoluminescent properties of QDs[287,297,315]. In that respect, Hwang *et al.*[297] produced cellulose/CdS hybrids, where *in situ* synthesised CdS QDs were immobilised and stabilised within the dendrons of a dendrimerised cellulose template. A 3^{rd} generation isocyanate-based dendron was grafted from the C_6 position of AGU of cellulose, which resulted in the formation of dendrimerised cellulose. To label and visualise the planar face of cellulose crystals extracted from *Valonia* plant, Xu *et al.*[315] developed a labelling strategy to bind histidine-capped (CdSe)ZnS QDs to the planar face of cellulose crystals via a carbohydrate binding modules (CBMs) probes[316], the CBMs specifically bind to the crystalline face of cellulose crystals. The (CdSe)ZnS QDs formed a conjugate with the CBM-bound-cellulose complexes, which resulted in a cellulose/CBM/QD bioinorganic

hybrid. This formation of a conjugate was reported by Zhang[317] for the preparation of a bacterial cellulose/CBM/QD bioinorganic hybrids. Niu *et al.*[287] reported the fabrication a hierarchical luminescent cellulose/QDs bioinorganic hybrid using CdSe QD and titania pre-coated cellulose nanofibres. The cellulose substrate was initially coated with titania layer using a sol-gel process followed by adsorption of a layer of stearic acid (SA), which enabled the self-assembly of trioctylphosphine oxide/1-hexadecylamine (TOPO/HDA) capped CdSe QDs. In that case, the CdSe QDs were self-assembled to titania/SA-coated cellulose nanofibrils by mean of hydrophobic interactions between TOPO/HDA ligands of CdSe precursor and the SA molecules. Therefore, the bioinorganic hybrid structure was composed of cellulose/titania/SA/(CdSe/SA) and possessed luminescent properties.

In recent years, the growing interest received by biosynthesised bacterial cellulose (BC) has promoted its use in the preparation of BC-based Au[109,110], Ag[108,289,318,319,320], SiO_2[288], TiO_2[111,321] NPs and CdS[298] QDs bioinorganic hybrids.

Currently, the preparation of bioinorganic hybrids composed of BC nanofibrils (or membranes) and metallic NPs was based on the chemical reduction of metal salt solution in the presence of BC using a reducing reagent, as described earlier for other cellulose substrates. Wang *et al.*[110] and Zhang *et al.*[109] prepared BC/Au bioinorganic hybrids using poly(ethyleneimine) (PEI) polyelectrolyte to coat BC nanofibrils prior to the *in situ* reduction of $AuCl_4^-$ ions to Au NPs onto BC nanofibrils. In that case, the PEI layer acted both as a linking molecule and a reducing agent during reduction reaction and stabilisation of Au NPs onto surfaces of BC nanofibrils. Generally, to prepare BC/Ag bioinorganic hybrids, a never-dried or dried BC membrane was immersed into (or impregnated with) a Ag^+ ion solution, then different reducing agents were used for the formation of Ag NPs. For instance, Maneerung *et al.*[289] employed $NaBH_4$ as reducing reagent, whereas Barud *et al.*[108] reduced Ag^+ by hydrolytic decomposition of Ag-triethanolamine (TEA) complexes. Hu *et al.*[318] used a NaCl solution as reducing reagent. Santa-Maria *et al.*[320] demonstrated the combined use of a reducing reagent (hydrazine, hydroxylamine or ascorbic acid) and a colloidal protector (gelatin or polyvinylpyrrolidone), which enabled to tailor the size of Ag NPs and their degree of coalescence in the BC membrane. A different approach to produce BC/Ag hybrids was developed by Ifuku *et al.*[319], which consisted in a 2,2,6,6-tetramethylpiperidine-1-oxyradical (TEMPO)-mediated oxidation of C_6 primary hydroxyl groups to introduce carboxylate (COO^-) groups on the surfaces of BC nanofibrils. The TEMPO-oxidised BC (BC-COO^-Na^+) acted as a reaction template where ion-exchange from Na^+ to Ag^+ cations took place to form BC-COO^-Ag^+

complexes. Subsequently, the Ag NPs were synthesised during a thermal reduction ($100°C$) reaction of Ag^+, thus resulting in stabilisation and immobilisation of Ag NPs on surface of BC nanofibrils. Li *et al.*[298] reported the preparation of BC/CdS bioinorganic hybrids by reduction of Cd^{2+} cations solution by Na_2S in the presence of BC nanofibrils, where the CdS QDs were anchored to BC nanofibrils via strong intermolecular interactions with OH groups, which also enabled the stabilisation of CdS QDs.

Cellulose bioinorganic hybrid materials were also produced by dissolution of cellulose in aqueous solution of LiOH/urea[322], NaOH/urea[290,311,323,324] or N-methylmorpholine-N-oxide/dimethyl sulfoxide (NMMO/DMSO)[291] followed by a subsequent regeneration of cellulose hydrogel. In some cases, the NP precursors were also dissolved in the solvent used (reaction medium) to carry out the dissolution of cellulose, thus allowing for an intimate mixing between NP precursors (ions) and the cellulose network[291,323,324]. Or alternatively, a cellulose hydrogel was immersed in a NP precursor solution for its thorough impregnation with metal ions[290,311,322]. After regeneration of the cellulose network, the entrapped metal ions precursors were chemical reduced *in situ* by their corresponding reducing reagents. As a result, the regenerated cellulose formed an organic matrix in which well dispersed NPs or QDs of various types such as, Au[291,311], Ag[311], Pt[311] NPs, TiO_2[322] NPs, mineral NPs, Fe_3O_4[290] NPs and CdSe/ZnS[323], CdS[303,324] QDs were embedded.

6.1.5 Applications of bioinorganic hybrid materials

To date bioinorganic hybrid materials are of particular interest for applications ranging from optics, electronics, ionics, mechanics, energy, environment, biology, medicine for example as membranes and separation devices, functional smart coatings, fuel and solar cells, catalysts or sensors[279]. Owing to the versatile nature of polysaccharide-based organic component, various shapes and conformations of bioinorganic hybrid materials were produced ranging from films, porous or fibrillar structures (Table 6.1). In addition, polysaccharide-based components are relatively cheap, renewable, abundantly available in a variety of forms and readily modifiable by various chemistries[310]. The functionality[290] acquired by polysaccharide-based bioinorganic hybrid materials was mainly a result of the inherent properties (chemical, magnetic, thermal or electronic) of their inorganic components, thus defining accordingly a range of potential biomedical[326,327], electronic[328], catalytic[329] applications. For instance, cellulose-based bioinorganic Pd and Cu hybrids were used for catalytic applications[286]. Those containing Ag NPs were exploited to inhibit bacterial growth because of the

Table 6.1: Sampling of the composition of various types of bioinorganic hybrid materials as a function of their composition and shape of organic component and nature of inorganic NPs and corresponding references.

Organic substrate	Hybrid processing	Shape/state of subst.	Inorganic NPs	Application/functionality	Refs.
Cellulose (nanofibres)	Self-assembly	Sheet	CdSe	Photoluminescence	[287]
(Nanocrystallites)	Deposition	Colloidal	Pd	Catalytic hydrogenation	[286]
(Nanofibrils)	*In situ* synthesis in $scCO_2$	Suspension	Pt	Nanomaterial synthesis	[313]
(Cellulose fabric)	Sol-gel /X-linking	Film (fabric)	SiO_2	Thermal stability	[325]
BC	*In situ* synthesis of NPs /embedding	Membrane	SiO_2	Tunable photoluminescence	[288]
	Impregnation with Ag^+ /*in situ* reduction	Membrane	Ag	Wound dressing with antimicrobial properties	[289]
Regenerated cellulose (viscose rayon)	Dissolution /spin-coating	Film	Au	Electrical conductivity	[291]
	Dissolution /*in situ* reduction of Fe^+	Film	Fe_3O_4	Superparamagnetic	[290]
	Dissolution /*in situ* precipitation of QDs	Film	CdS	Optic, electronic & biology, photoluminescence	[324]
Cellulose nitrate	Pickering emulsion	Film	ZnO	Superhydrophobic coating	[294]
Cellulose triacetate	Dispersion /solvent-casting	Film	CdSe/ZnS	Paper making & photoluminescence	[323]
Chitosan	Sol-gel	Microsphere	ZrO_2, TiO_2, Al_2O_3	Catalyst adsorption and metal remediation	[300]
	NBBs self-assembly	Film	MTM	Fire retardancy & biomimetic	[302]
	Dissolution/*in situ* reduction	Film	Au	Optical & surface-enhanced raman	[291]

antibacterial properties of Ag[304,330] or to introduce antimicrobial activity in wound dressing[331]. Au NP polysaccharide-based bioinorganic hybrids were developed for biosensors to detect hydrogen peroxide (H_2O_2), glucose or as probes for the immobilisation of diverse enzymes[109,110]. Whereas, QDs were used in polysaccharide-based bioinorganic hybrids for their fluorescent properties, which could be useful in bioanalysis, *i.e.*, the diagnosis of antibodies[296], biological labelling probes[315,317] or fluoroimmunoassay applications[323].

6.2 Experimental

6.2.1 Materials

Never-dried and HCl hydrolysed BC nanofibrils were obtained as described in Chapter 3. 2-(methylthio)ethyl methacrylate (MTEMA), gold (III) chlorite trihydrate ($HAuCl_4 \cdot 3H_2O$), trisodium citrate dihydrate ($Na_3C_6H_5O_7 \cdot 2H_2O$) cadmium perchlorate hydrate ($Cd(ClO_4)_2 \cdot xH_2O$), thioglycolic acid, sodium hydroxide (NaOH), tetrahydrofuran (THF), dichloromethane (DCM), nitric acid (assay 37%) (HNO_3) and sulfuric acid (assay 98%) (H_2SO_4) were purchased from Sigma-Aldrich (UK). Cerium (IV) ammonium nitrate (CAN) was bought from Fluka (UK). Aluminium telluride (assay 99.9%) (Al_2Te_3) was purchased from ABSCO Materials (Suffolk, UK). Poly(3-hydroxybutyrate-co-3-hydroxyhexanoate) (PHBHHx) with 4.7 mol% of hydroxyhexanoate (HHx) comonomer and a molecular weight (Mw) of 549 kDa was kindly supply by Meredian Inc. (Georgia, USA) and facilitated by Dr Isao Noda research fellow at Procter & Gamble Co. (OH, USA). The other reagents, standard grade ethanol and acetone were obtained from VWR (UK). All reagents were ACS grade and used without further purification. Deionised H_2O was produced using a NANOpure deionisation system (Barnstead Thermolyne, Dubuque, USA).

6.2.2 Preparation of 2-(methylthio)ethyl methacrylate (MTEMA) grafted BC nanofibrils

The functionalisation of never-dried BC nanofibrils was performed by a "grafting from" approach. The free radical grafting polymerisation (FRGP) of MTEMA from BC nanofibrils was carried out in an acidic aqueous reaction medium[332]. Typically, 2.5 g of BC nanofibrils (250 mg dry-weight equiv.) was placed in a 250 ml 3-neck round bottom flask fitted with a reflux condenser and containing 100 ml of 0.1 M HNO_3 and homogenised at 30,000 rpm for 1 min. Then, the 3-neck round bottom flask was immersed into an oil bath with a temperature

set to $50°C$. The FRGP reaction was carried out in N_2 atmosphere. The suspension of BC was initially stirred for 1 h at 250 rpm. Subsequently, the stirring speed was adjusted to 500 rpm, then 1 mmol or 2.5 mmol of CAN corresponding to either 0.6 g or 1.4 g was added to the suspension of BC as a function of the oxidation desired. Approximately 1 min after the addition of CAN into the BC suspension, MTEMA was injected drop-wise into the reaction medium, the concentration of MTEMA was arbitrarily chosen to be 1, 5 and 10 mmol, which corresponded to a volume of 0.15, 0.77 and 1.54 ml, respectively. The FRGP of MTEMA from BC nanofibrils was carried out for 2 hr, then an excess of EtOH was added to terminate the reaction. The MTEMA grafted BC (MTEMA-g-BC) was solvent exchanged by successive centrifugations at 15 000 g for 15 min and homogenisations at 30 000 rpm for 2 min in EtOH, acetone, THF and back to H_2O, subsequently. This procedure was repeated 3 times for each solvent to ensure removal of unreacted MTEMA monomer.

6.2.3 Schematic of free radical grafting polymerisation of MTEMA from BC nanofibrils

The steps taking place during FRGP of MTEMA from BC nanofibrils are described in Figure 6.2. The FRGP reaction consisted of two phases. The first one was the radical initiation; a Ce^{4+} complex formed with hydroxyl groups at C_2 position, which promoted the oxidation reaction of AGU and the formation of C=O groups[332,333]. The oxidation reaction resulted in the cleavage of AGU between C_2-C_3 bond with the subsequent formation of a free radical site at the C_2 position. During the oxidation, a free radical was formed at the C_2 position, Ce^{4+} was reduced to Ce^{3+} and H^+ (proton) was released (Figure 6.2a). During the oxidation reaction of cellulose, ceric ions (Ce^{4+}) were consumed in the formation of reactive free radical at cellulose sites. The second one followed the initiation reaction, where the highly reactive free radical formed reacted with the methacrylate moiety of MTEMA by the free radical propagation and formation of MTEMA chains. Arthur *et al.*[334] reported that during FRGP reaction the initial free radical formed on the cellulose backbone was retained on the end of the growing chain of polymer composed of monomer units. The FRGP produced multiple sort chains of poy(MTEMA) who were anchored to accessible AGU rings of BC nanofibrils (Figure 6.2b).

Recent studies using CAN mediated redox initiation of various monomers (*e.g.*, acrylonitrile, methylmethacrylate, acrylamide) from different cellulose substrates (e.g., carboxymethyl

cellulose, fibres, cotton, pulp) unravelled the reaction mechanism of FRGP [335,336], which has been adapted for FRGR of MTEMA-g-BC nanofibrils, herein, as follows:

$$Radical\ formation: \quad \mathbf{BC}-OH + Ce^{4+} \xrightarrow{k} \underset{Radical}{\mathbf{BC}^{\bullet}} + Ce^{3+} + H^{+} \tag{6.1}$$

$$Initiation: \quad \mathbf{BC}^{\bullet} + MTEMA \xrightarrow{k_i} \mathbf{BC}-MTEMA^{\bullet} \tag{6.2}$$

$$Propagation: \quad \mathbf{BC}-MTEMA^{\bullet} + MTEMA \xrightarrow{k_p} \mathbf{BC}-MTEMA_n^{\bullet} \tag{6.3}$$

$$Termination: \quad \mathbf{BC}-(MTEMA)_n-MTEMA^{\bullet} +^{\bullet} MTEMA-(MTEMA)_m-\mathbf{BC} \xrightarrow{k_t} \mathbf{BC}-(MTEMA)_{n+m}-\mathbf{BC} \tag{6.4}$$

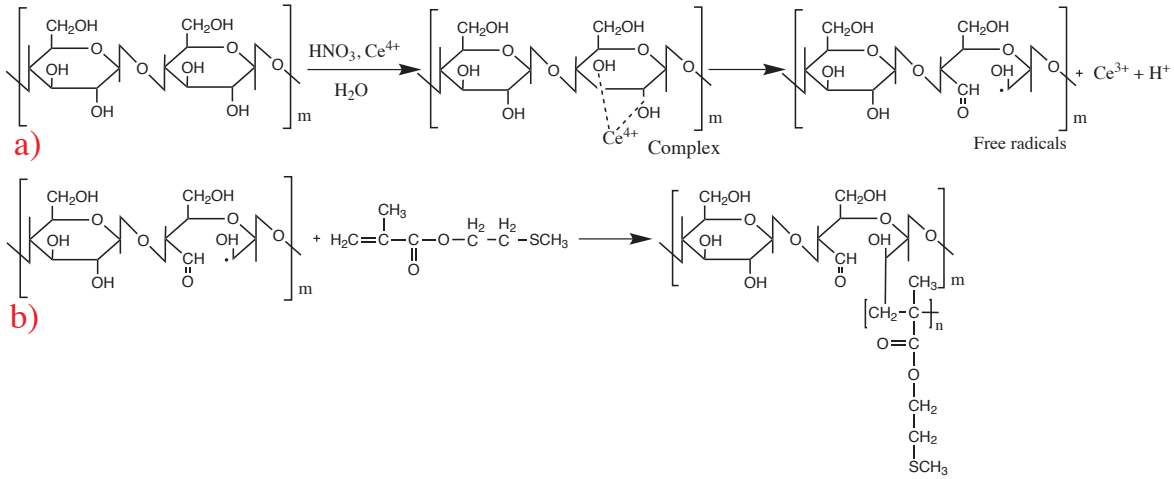


Figure 6.2: Schematic of free radical grafting from BC polymerisation reaction of 2−(methylthio) ethyl methacrylate. **a**) Initiation phase and free radical formation; **b**) propagation phase.

6.2.4 Synthesis of Au nanoparticles and preparation of MTEMA-g-BC-Au nanohybrids

Au nanoparticles (Au NPs) were synthesised based on a modified Turkevich procedure [337] using $HAuCl_4{\cdot}H_2O$ salt precursor in aqueous medium. Typically, 16.7 mg (1 mmol) of $HAuCl_4 \cdot H_2O$ salt was dissolved at RT ($22°C$) in a 100 ml 3-neck round bottom flask containing 45 ml of dH_2O and subsequently heated to $100°C$ under reflux for 1 h under N_2. Then, 0.5 g (43 mg

dry-weight equiv.) of MTEMA-g-BC nanofibrils was added to the $HAuCl_4 \cdot H_2O$ solution and homogenised at 30,000 rpm for 2 min under N_2 flow. Thereafter, the 3-neck round bottom flask was promptly re-immersed into the oil bath. The nucleation of AuNPs was initiated by drop-wise injection of 5 ml of a 1 wt./v.% $Na_3C_6H_5O_7 \cdot 2H_2O$ solution to the suspension. The thermal growth of Au NPs and their seeding onto MTEMA-g-BC nanofibrils was carried out for 1 h. Then, freshly synthesised MTEMA-g-BC-Au nanohybrids and Au colloid resulting from excess of Au NPs were separated by sedimentation of MTEMA-g-BC-Au nanohybrids for 1 h, subsequently the colloidal suspension of Au NPs constituting the supernatant was extracted using a syringe. MTEMA-g-BC-Au nanohybrids were re-suspended and dispersed in 100 ml of H_2O using a 50 W ultrasonic probe (UP50H, Hielscher Ultrasonics GmbH, Berlin, Germany) with an intermittent pulse mode for 5 min to remove loosely attached Au NPs prior to centrifugation at 3 000 g for 5 min. This operation was repeated 6 times until the supernatant obtained was clear. MTEMA-g-BC-Au nanohybrids were solvent exchanged into EtOH by successive centrifugation and homogenisation procedures as described earlier.

The preparation of MTEMA-g-BC-Au nanohybrids proceeded as schematically shown in Figure 6.3 and was in accordance with the aforementioned experimental procedure. Initially, never-dried MTEMA-g-BC nanofibrils (Figure 6.3**a**) were dispersed in a aqueous solution of gold (III) chlorite trihydrate salt ($HAuCl_4 \cdot H_2O$). To enable the formation of Au NPs and their growth, Au^{3+} ions were reduced to Au^{+} form using trisodium citrate[338] (Figure 6.3**b**), followed a rapid aggregation of Au^{+} to form via a self-nucleation process, Au nuclei, which themselves coalesced into bigger Au NPs[339] (Figure 6.3**c**). The Au nuclei or/and Au NPs formed in the vicinity of MTEMA-g-BC nanofibrils were anchored to the pendant thioether moiety (SCH_3) of the polyMTEMA chains. Therefore, thioether moiety of MTEMA-g-BC nanofibrils acted as seed for further growth of Au nuclei or/and Au NPs to their final size until complete consumption of the precursor species (Figure 6.3**c**). After separation and thorough removal of colloidal suspension of Au NPs from the reaction medium, MTEMA-g-BC-Au nanohybrids were isolated (Figure 6.3**d**). These nanohybrids consisted of MTEMA-g-BC nanofibrils, which acted as an immobilisation substrate for Au NPs, where the thermally grown Au NPs were immobilised *in situ* during their synthesis by chemisorption to the thioether moiety of polyMTEMA chains. The self-assembly of Au NPs to MTEMA by chemisorption in the case of MTEMA-g-BC-Au nanohybrids was explained by the propensity of thioether-containing molecules to form spontaneously a strong interaction with metal surfaces[340]. Similarly, Lenk *et al.*[341] reported the synthesis of poly(methyl-co-2-(methylthio)ethyl)methacrylate

(PMMA-co-MTEMA) copolymer and its subsequent chemisorption from solution onto an Au substrate, which resulted in the formation of self-assembly of highly-ordered monolayers of copolymer. Thereafter, Marra *et al.*[342] prepared by free radical polymerisation a terpolymer composed of MTEMA, 2-hydroxyethyl acrylate and 3-acryloyl-3-oxapropyl-3-(N,N-dioctadecylcarbamoyl)propionate repeating units, where the thioether-containing MTEMA units were bound (chemisorbed) to a Au-coated silicon wafer. The terpolymer was used for the preparation of unilamellar vesicles in a membrane for blood-contacting applications. Recently, Menzel *et al.*[343] reported a solvent-free methodology for the functionalisation of carbon nanotubes (CNTs) by which MTEMA-grafted CNTs (MTEMA-g-CNT)s were synthesised. In that case, the thioether moiety (SCH_3) enabled the binding of Au NPs from a colloidal suspension to characterise the distribution of grafting sites on CNT surfaces. It worth noticing that both Lenk *et al.*[341] and Marra *et al.*[342] had employed MTEMA to introduce thioether moieties (SCH_3) into the backbone of various copolymer they synthesised to enable readily the chemisorption onto an Au surface. The work of these authors justified the choice to use MTEMA for the synthesis of MTEMA-g-BC-Au nanohybrids.

6.2.5 Synthesis of CdTe quantum dots and preparation of MTEMA-g-BC-CdTe nanohybrids

CdTe quantum dots (QDs) were synthesised in aqueous media following the recipe developed by Gaponik *et al.*[344,345] from a $Cd(ClO_4)_2{\cdot}xH_2O$ precursor and hydrogen telluride (H_2Te) gas. Briefly, a total of 158 mg (0.685 mmol) of $Cd(ClO_4)_2{\cdot}xH_2O$ was dissolved at RT ($22°C$) in a 100 ml 3-neck round bottom flask containing 30 ml of dH_2O and then 0.123 ml (1.78 mmol) of thioglycolic acid was added under continuous stirring. The pH of the resulting transparent solution was adjusted to pH 11 by dropwise addition of a 2 M solution of NaOH. The solution was deaerated prior to QD synthesis via continuous sparging with Ar. Subsequently, H_2Te gas was generated by the chemical decomposition of Al_2Te_3 in the presence of H_2SO_4 (Equation 6.5). Typically, 50 mg (0.114 mmol) of Al_2Te_3 was placed in a 50 ml 3-neck round bottom flask fitted with septums. A needle supplying Ar, used as carrier gas, was inserted into one of the septums to create the gas inlet. Another septum was fitted with a bent long needle connecting the two round bottom flasks, which enabled the outlet gas (Ar+H_2Te) to pass through the solution of $Cd(ClO_4)_2$ contained in the initial round bottom flask. Then, to produce H_2Te, 20 ml of 0.5 M H_2SO_4 was injected dropwise into the round bottom flask containing the Al_2Te_3 via the middle septum using a syringe equipped with a needle. The

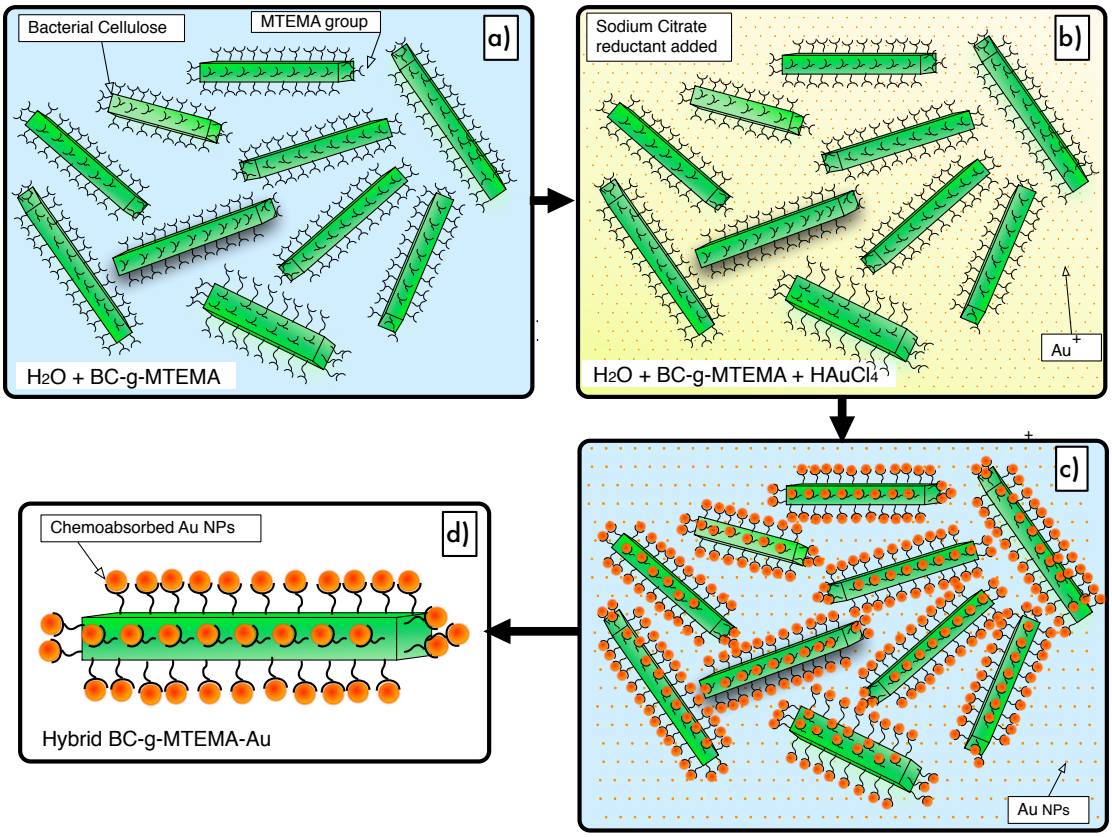


Figure 6.3: Schematic of preparation of MTEMA-g-BC-Au nanohybrids obtained by *in situ* immobilisation of Au NPs during Au NPs synthesis in the presence of MTEMA-g-BC nanofibrils. **a**) aqueous suspension of MTEMA-g-BC; **b**) nucleation step of Au NPs by reduction of Au^{3+} to Au^{+} by addition of $Na_3C_6H_5O_7{\cdot}2H_2O$; **c**) thermal growth of Au NPs in presence of MTEMA-g-BC and **d**) formation of MTEMA-g-BC-Au nanohybrid by chemisorption of Au NPs to MTEMA-g-BC nanofibrils.

formation of CdTe QD precursors was initiated by reaction of H_2Te and Cd thiolate complex (Cd-SR complex) (Equation 6.6). The nucleation and growth of CdTe QDs proceeded for various times by refluxing at $110°C$ in open air with a condenser attached (Equation 6.7). To tailor the electronic transition of CdTe QDs various refluxing times were investigated (10 min, 20 min, 30 min, 1 h, 2 h and 3 h).

MTEMA-g-BC-CdTe nanohybrids were obtained by partial ligand exchange with thioether moieties between CdTe QDs and MTEMA-g-BC nanofibrils following the precipitation of CdTe QDs from a colloidal suspension onto MTEMA-g-BC nanofibrils suspended in acetone. Briefly, 100 mg (10 mg dry-weight equiv.) of MTEMA-g-BC prepared as previously described was suspended in 15 ml Falcon tubes containing 10 ml of acetone. Then, a specific volume (0.1 ml, 0.5 ml, 1 ml and 2 ml) of freshly synthesised CdTe QDs colloids thermally grown for 2 h was added dropwise into the MTEMA-g-BC suspension, while an ultrasonic probe was used to ensure a good dispersion MTEMA-g-BC nanofibrils and an efficient deposition of CdTe QDs. The MTEMA-g-BC-CdTe nanohybrids thus formed were centrifuged and re-suspended in acetone by means of an ultrasonic probe. Subsequently, MTEMA-g-BC-CdTe nanohybrids in acetone were solvent exchanged to either EtOH or DCM according to the procedure described earlier in this section.

Extra care was required in the handling of both CdTe QDs colloids and suspension of MTEMA-g-BC-CdTe nanohybrids. There is limited knowledge available at present on health risks of exposure to Cd-based QDs[346].

$$Al_2Te_3 + 3H_2SO_4 \longrightarrow 3H_2Te \uparrow + Al_2(SO_4)_3 \tag{6.5}$$

$$Cd(ClO_4)_2 + H_2Te \xrightarrow{HS-R} Cd-(SR)_xTe_y + 2HClO_4 \tag{6.6}$$

$$Cd-(SR)_xTe_y \xrightarrow{110°C} CdTe \tag{6.7}$$

The preparation of nanohybrids composed of MTEMA-g-BC and CdTe QDs according to experimental procedure is described in Figure 6.4. Freshly synthesised CdTe QDs were added drop-wise to a suspension of MTEMA-g-BC nanofibrils in acetone subjected to an ultrasonic excitation, resulting in the deposition of the CdTe QDs onto MTEMA-g-BC nanofibrils. The ligand transfer of thioglycolic acid capped CdTe QDs to the thioether moieties of MTEMA-g-BC was performed in acetone and eased by ultrasonication. Similarly, Rogach *et al.*[345]

reported a 90% efficiency of ligand transfer of CdTe QDs stabilised by thioglycolic acid to long-chain thiol (1-dodecanethiol) in the presence of acetone.

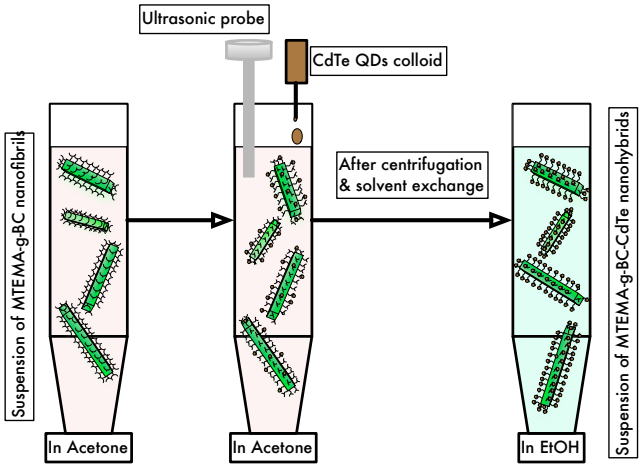


Figure 6.4: Schematic of preparation of MTEMA-g-BC-CdTe nanohybrids obtained by transfer of CdTe QDs to MTEMA-g-BC via ligand exchange in acetone between thioglycolic acid and thioether moieties.

6.2.6 Preparation of photoluminescent nanocomposites containing MTEMA-g-BC-CdTe nanohybrids

Fluorescent nanocomposite films were prepared by solution-casting of poly(3-hydroxybutyrate-co-3-hydroxyhexanoate) (PHBHHx) solution in which MTEMA-g-BC-CdTe nanohybrids were thoroughly dispersed. A 5 wt./v.% PHBHHx solution was prepared by dissolving 2.5 g of PHBHHx at RT ($22°C$) in 50 ml of DCM under gentle stirring overnight. Subsequently, 100 mg (10 mg dry-weight equiv.) of MTEMA-g-BC-CdTe nanohybrids, which corresponded to a 4 wt./wt.% (with respect to PHBHHx) in DCM was added to a 10 ml glass beaker containing 5 ml of PHBHHx solution. The suspension was homogenised for 20 s at 30,000 rpm to thoroughly disperse the MTEMA-g-BC-CdTe nanohybrid within the solution. The suspension of MTEMA-g-BC-CdTe in PHBHHx solution was stirred in a sealed beaker at 500 rpm for a further 8 h. To cast a film, the suspension was poured into a 50 mm diameter glass Petri dish and left covered under ambient conditions for 24 h for the solvent to evaporate. Finally, a transparent film with a thickness of 300 μm was peeled off from the glass surface.

6.3 Characterisation of MTEMA-g-BC Nanofibrils

6.3.1 Evolution of X-ray diffraction of cerium (IV) oxidised BC nanofibrils

XRD diffractogram of HCl hydrolysed BC nanofibrils (prepared as described in Chapter 3), CAN oxidised BC nanofibrils and CAN crystalline powder are presented in Figure 6.5. The diffraction of HCl hydrolysed BC nanofibrils revealed the characteristic pattern of cellulose type I, as described in previous chapters. The XRD diffractogram of CAN oxidised BC nanofibrils was different than the one of HCl hydrolysed BC nanofibrils. Two additional peaks appeared from these diffractograms and are located at 2θ equal 28° and 33°, respectively. The modification of XRD diffractogram of CAN oxidised BC nanofibrils was solely attributed to the oxidation reaction carried out using various concentrations of CAN. The FWHM of peak located at 2θ 28° broadened by 7.6% with increasing the concentration of CAN from 1 mmol to 2.5 mmol, respectively. The [040] crystal lattice visible in the diffractogram HCl hydrolysed BC was superimposed by the appearance of the new peaks of CAN oxidised BC nanofibrils. Interestingly, the overall diffraction pattern of BC nanofibrils was not significantly altered beside the appearance of two new peaks following the oxidation reaction, as seen in Table 6.2. However, the degree of crystallinity of CAN oxidised BC nanofibrils dropped significantly from 91% for HCl hydrolysed BC nanofibrils with values of 79% and 73% for a concentration of CAN of 1 mmol and 2.5 mmol, respectively (see Table 6.2).

As far as the author could research the literature on FRGP reaction initiated by oxidation of AGU of polysaccharides using CAN, no one did investigate the evolution of crystallinity for highly crystalline cellulose materials or the effect of the CAN oxidation reaction on the crystallographic structure of cellulose nano- or/and microfibrils. Only Stenstad *et al.*[347] reported the FRGP of glycidyl methacrylate from microfibrillated cellulose (MFC), however, these authors emphasised the chemical modification resulting from the FRGP reaction rather than the evolution of crystallographic structure of MFC. Canche-Escamilla *et al.*[348] reported that lignocellulosic fibres subjected to oxidation reaction initiated by CAN exhibited a reduction of their molecular weight owing to the rupture of AGU main chains. Recently, Radhakumary *et al.*[349] reported the FRGP of poly(ethylene glycol monomethacrylate) (PEGm) from chitosan using CAN. The XRD diffractogram of PEGm-g-chitosan revealed the presence of additional diffraction peak located at $2\theta = 27°$, which was attributed according to Radhakumary *et al.* to the formation of pendant chains of PEGm away from chitosan backbone.

In the present case, the modification of the crystallographic arrangement of the CAN oxidised BC nanofibrils, which consisted into the apparition of new diffraction peaks (*i.e.*, $2\theta = 28°$& $33°$), was attributed to the strong adsorption of CAN (*i.e.*, Ce^{4+}) with the CAN oxidised BC nanofibrils. The adsorption of CAN also resulted in a significant increase of the char residue of CAN oxidised BC nanofibrils after thermal degradation owing to the presence of the inorganic associated CAN, as discussed in later Section 6.3.5.

6.3.2 Evolution of X-ray diffraction of MTEMA-g-BC nanofibrils

The evolution of XRD of MTEMA-g-BC nanofibrils is presented in Figure 6.6 as a function of concentration of MTEMA and CAN, respectively. The XRD of MTEMA-g-BC nanofibrils varied with respect to the concentration of CAN employed to initiate FRGP of 2-(methylthio)ethyl methacrylate from the surface of BC nanofibrils (Section 6.2.3). For a concentration of CAN of 1 mmol, the XRD of MTEMA-g-BC nanofibrils showed some differences compared to HCl hydrolysed BC nanofibrils; the amorphous phase peak at 2θ around 18° increased and the new diffraction peaks, as mentioned previously, appeared. Increasing the concentration of MTEMA from 1 mmol to 10 mmol led to a decrease of the degree of crystallinity of MTEMA-g-BC nanofibrils from 92% to 81% (Table 6.2). However the determination of crystal size of [101], [10$\bar{1}$] and [002] lattices of BC using a pseudo-Voigt function to fit the various peaks [266] showed that, their size was marginally altered by grafting of MTEMA, when a concentration of CAN of 1 mmol was used. Thus, the reduction of the degree of crystallinity was attributed to the increase of the amorphous phase, which resulted from the grafting of MTEMA. In comparison to CAN oxidised BC nanofibrils, the additional diffraction peaks located at $2\theta = 28°$ and 33°, respectively, appeared less prominent and broader than in Figure 6.5. Nonetheless, the overall diffraction pattern of MTEMA-g-BC nanofibrils exhibited the characteristics of cellulose crystal type I and also remained very similar to those of HCl hydrolysed BC nanofibrils.

For a concentration of CAN of 5 mmol, the XRD of MTEMA-g-BC nanofibrils showed significant differences to those obtained when a concentration of CAN of only 1 mmol was used. The morphology of [101], [10$\bar{1}$] crystal lattices of MTEMA-g-BC became steadily more blurry as the [002] crystal lattice was decreasing in intensity with increasing concentration of MTEMA. Furthermore, a higher concentration of CAN (2.5 mmol) used to initiate the FRGP of MTEMA from BC nanofibrils led to reemergence of the prominent diffraction peak located 2θ equal 28°, as discussed earlier for CAN oxidised BC nanofibrils (Figure 6.5). The

intensity of the additional peak located at 2θ equal 28° increased with increasing concentration of MTEMA. In addition, a drastic reduction of the degree of crystallinity of MTEMA-g-BC nanofibrils from 88% to 33% was observed for the corresponding increase of the concentration of MTEMA from 1 mmol to 10 mmol (Table 6.2) which accounted mainly to the contribution of amorphous phase originating from grafted polyMTEMA anchored to the BC backbone. The deconvolution of individual diffraction peaks using a pseudo-Voigt function revealed minor fluctuations of crystallite size of [101], [$10\bar{1}$] and [002] lattice (Table 6.2), however, there was a significant contribution from a broad peak assigned to the amorphous phase, which affected the degree of crystallinity of MTEMA-g-BC nanofibrils.

Based on Radhakumary *et al.*'s[349] observation, the intensity of the diffraction peak of chitosan located at $2\theta = 20°$ and assigned to the [001] and [100] lattices decreased owing to a change in crystalline structure of chitosan induced by FRGP initiated by CAN oxidation. Wan *et al.*[350] reported that the degree of crystallinity of bamboo fibres grafted with methyl methacrylate (MMA) decreased because of the increase of the amorphous phase of the material by the graft polymer. Wang *et al.*[351] described similarly the reduction of the degree of crystallinity for chitosan grafted with copolymers composed of poly(p-dioxanone). Also Kaith *et al.*[352] observed the diminution of degree of crystallinity of poly(MMA)-g-flax. Therefore, the concentration of both CAN and MTEMA significantly affected the degree of crystallinity of MTEMA-g-BC nanofibrils. Interestingly at a low concentration of CAN the crystallographic pattern of MTEMA-g-BC was quite similar to the one of HCl hydrolysed BC nanofibrils. Whereas a higher concentration of CAN resulted in significant alteration of crystallographic pattern of BC with the presence of an additional diffraction peak as well as an increase of amorphous phase. As expected, the degree of crystallinity of MTEMA-g-BC (CAN conc. of 5 mmol) dropped steadily with an increase concentration of MTEMA. The reduction in the degree of crystallinity was attributed to FRGP of polyMTEMA chains from BC nanofibrils, which created a disordered network of polyMTEMA chains of various length around the nanofibrils.

6.3.3 ATR-FTIR spectroscopy of MTEMA-g-BC nanofibrils

The ATR-FTIR spectra of HCl hydrolysed BC and BC nanofibrils oxidised with a CAN concentration of 1 mmol and 2.5 mmol, respectively, are presented in Figure 6.7. The ATR-FTIR spectra of HCl hydrolysed BC exhibited similar features as compared to non-hydrolysed BC nanofibrils described in earlier Chapter 3, the ATR-FTIR spectra were also in agreement with

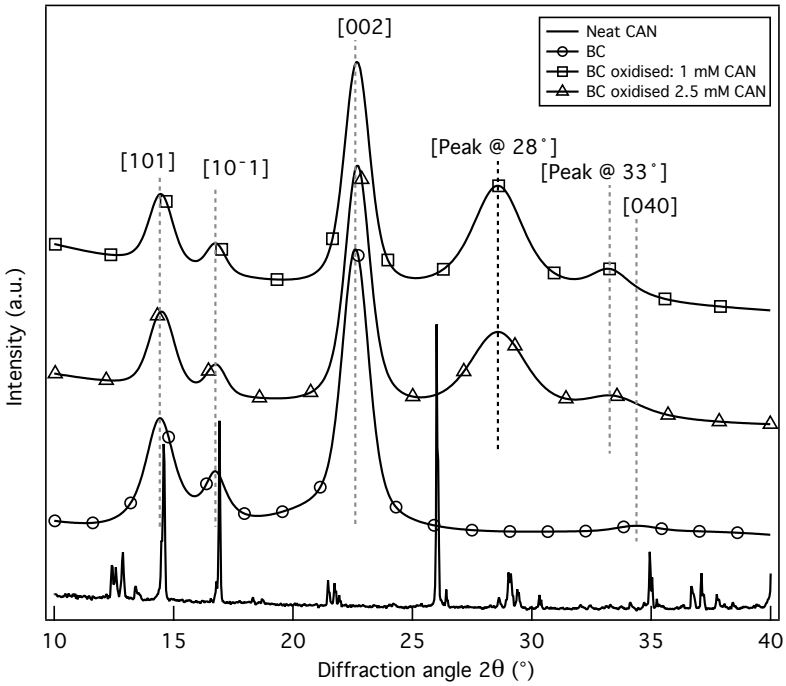


Figure 6.5: X-ray diffractograms of HCl hydrolysed BC and CAN oxidised BC nanofibrils.

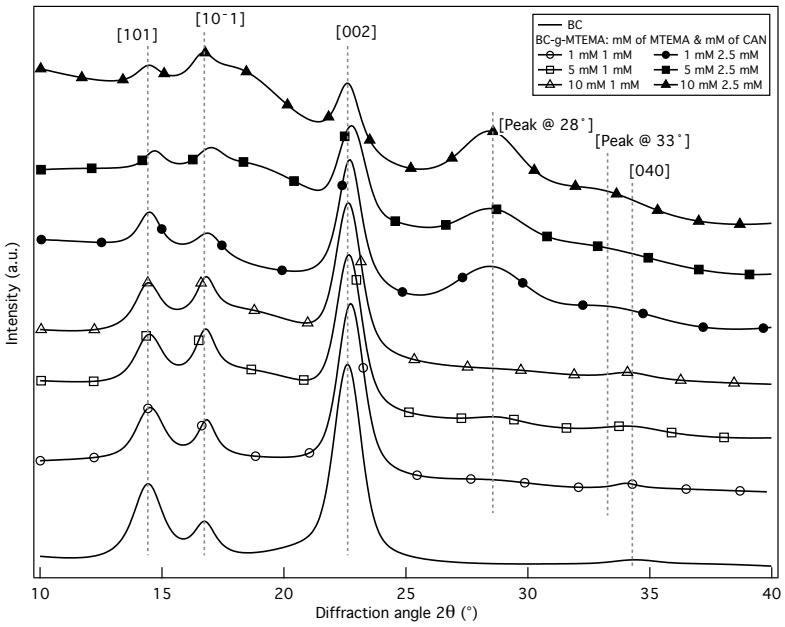


Figure 6.6: X-ray diffractograms of HCl hydrolysed BC and MTEMA-g-BC nanofibrils at various concentration of MTEMA & CAN).

Table 6.2: Crystal size of [101], [10$\bar{1}$] and [002] lattice determined using using Scherrer's equation (see Chapter 2); peak location for [002] lattice and degree of crystallinity for BC, CAN oxidised BC and MTEMA-g-BC nanofibrils, respectively, as a function of concentration of CAN and MTEMA.

Sample	CAN	MTETMA	Crystallite size			Location	Crystallinity
			[101]	[10$\bar{1}$]	[002]	[002]	
	(mM)	(mM)	(nm)	(nm)	(nm)	(°)	(%)
BC *			5.4	7.0	6.5	22.6	91.0
BC oxidised †	1		6.7	7.9	5.2	22.7	79.0
BC oxidised †	2.5		6.4	8.6	6.8	22.7	73.7
MTEMA-g-BC	1	1	6.1	9.0	6.8	22.9	92.1
	1	5	6.0	8.2	6.9	22.7	82.5
	1	10	6.4	8.6	7.0	22.7	81.1
MTEMA-g-BC	2.5	1	7.4	8.3	7.4	22.1	88.2
	2.5	5	7.1	8.1	6.8	22.8	67.2
	2.5	10	7.6	7.7	6.6	22.6	33.4

*HCl hydrolysed BC nanofibrils; † CAN oxidised BC nanofibrils.

those reported in the literature elsewhere[353]. Interestingly, ATR-FTIR spectra of CAN oxidised BC nanofibrils resolved two additional IR peaks located resolved at 1260 cm^{-1} and 800 cm^{-1}, respectively, which were assigned to -C-O- stretching[354] and the AGU ring breathing mode[355] (Table 6.3). The emergence of peaks at 1260 cm^{-1} and 800 cm^{-1} revealed that AGU chains (cellulose) of BC were subjected to an inter- and intramolecular rearrangement resulting from the oxidation reaction using CAN as compared to HCl hydrolysed BC nanofibrils. Arthur *et al.*[356] reported that CAN oxidation effected the morphology as well as physical and chemical properties of cellulose. Oxidative depolymerisation and random cleavage of cellulose chains initiated by free radicals entrapped within highly ordered region of cellulose network were also observed during CAN oxidation of cellulose type I[356] using electron spin resonance (ESR) spectroscopy.

The ATR-FTIR spectra of MTEMA-g-BC nanofibrils are presented in Figure 6.8 as a function of the conditions of the FRGP reaction. As FRGP was carried out in an acidic suspension of BC nanofibrils, methacrylate functional groups were covalently associated to the very reactive radicals generated by CAN oxidation on the BC backbone (Figure 6.2). For both concentrations of CAN, 1 mmol and 2.5 mmol, respectively, and with a concentration of

MTEMA ranging from 1 mmol to 10 mmol, a gradual increase in intensity of the absorption bands located at 1727 cm^{-1} was observed. This latter band was assigned to carbonyl group (C=O) constituting the methacrylic group of the polyMTEMA chains, as seen in Figure 6.2. The IR absorption resulting from C=O intensified with increasing concentration of MTEMA used, but was independent of the concentration of CAN. The absorption band associated to methylthiol (SCH_3) functional group of the polyMTEMA chains was resolved from ATR-FTIR spectra measured for MTEMA-g-BC nanofibrils and summarised in Table 6.3. Comparison between BC and MTEMA-g-BC specimen in the spectral region 3000-2800 cm^{-1} showed the emergence of absorption bands at 2917 cm^{-1} and 1148 cm^{-1}, which were assigned to asymmetric CH_3 stretching of SCH_3 functional group and CH_3 symmetric vibration, respectively[357]. The relative intensity of absorption bands at 2917 cm^{-1} and 1148 cm^{-1} became more pronounced with the increasing concentration of MTEMA used during FRGP reaction. In addition, a spectral band assigned to S-C stretching vibrations was resolved at 750 cm^{-1}. The intensity of this band increased also with increasing concentration of MTEMA. Furthermore, the intensity of spectral band located at 3350 cm^{-1}, which was assigned to OH group decreased with increasing concentration of MTEMA. Similarly, Neira *et al.*[354] showed a decrease in the intensity of band assigned to OH groups located at 3420 cm^{-1} with respect to increase of reaction duration for FRGP of acrylic acid from microcrystalline cellulose. Conclusive evidence of FRGP of MTEMA from BC nanofibrils were obtained by ATR-FTIR spectroscopic, where, the IR absorbance of carbonyl groups and methylthio functional groups of MTEMA-g-BC nanofibrils were resolved.

Table 6.3: Summary of main absorption bands and assignment for the ATR-FTIR spectra of CAN oxidised BC and MTEMA-g-BC.

Wavenumber (cm^{-1})	Band assignment	Reference
3420	O-H stretching	[354]
2917	asymmetric CH_3 stretching (SCH_3 of polyMTEMA)	[357]
1727	Carbonyl group (C=O)	[357]
1260	-C-O- stretching	[354]
1148	CH_3 symmetric vibration (SCH_3 of polyMTEMA)	[357]
800	AGU ring breathing mode	[355]
750	S-C stretching (SCH_3 of polyMTEMA)	[357]

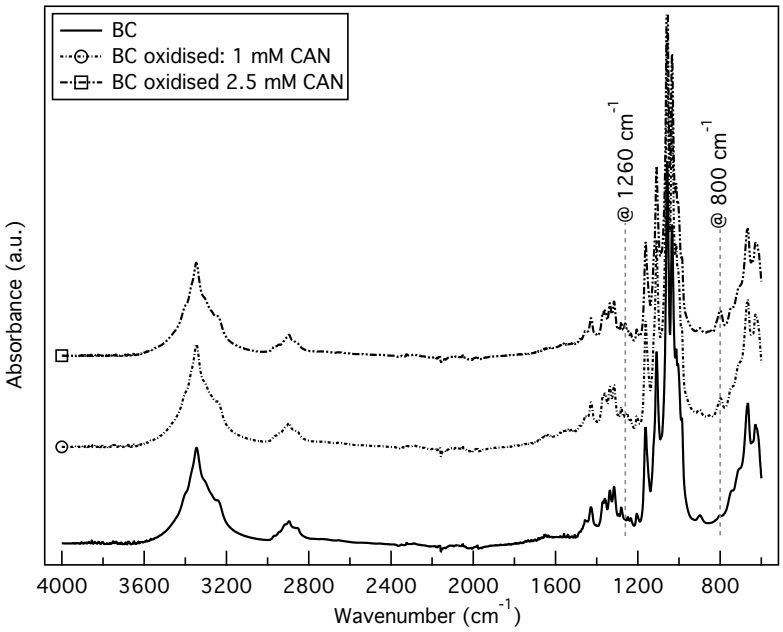


Figure 6.7: ATR-FTIR spectra HCl hydrolysed BC and CAN oxidised BC nanofibrils as a function of concentration of CAN.

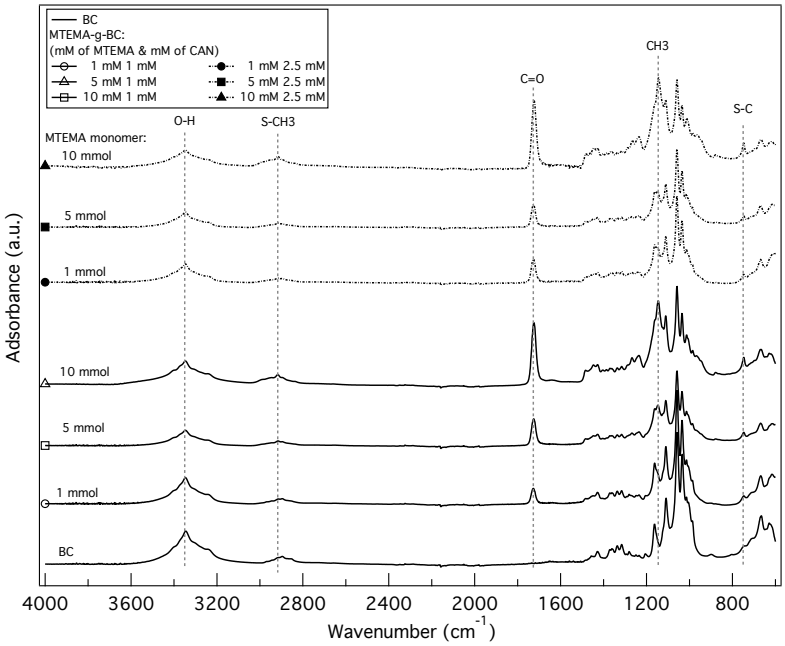


Figure 6.8: ATR-FTIR spectra of HCl hydrolysed BC and MTEMA-g-BC nanofibrils at various concentrations of MTEMA and CAN.

6.3.4 Elemental analysis of MTEMA-g-BC nanofibrils

The elemental analysis (EA) of BC, CAN oxidised BC and MTEMA-g-BC nanofibrils is presented in Table 6.4 as a function of concentration of CAN and MTEMA. During EA, the elemental composition of the various specimen were decomposed in %C, %H, %O and %S. The elemental weight fraction of HCl hydrolysed BC nanofibrils was in agreement with the chemical composition of AGU, where %C, %H, %O account for 44.55%, 6.11% and 49.34%, respectively. Similarly, Yoon *et al.*[358] reported an elemental weight decomposition BC, where %C, %H, %O accounted for 43.57% 6.30% and 50.13%, respectively.

However, the EA of CAN oxidised BC nanofibrils revealed significant difference compared to the HCl hydrolysed BC nanofibrils. Indeed, the weight fraction of %C decreased to 32% and 34% for a corresponding concentration of CAN of 1 mmol and 2.5 mmol, respectively, as compared to 44% of %C measured from HCl hydrolysed BC nanofibrils. On the other hand the weight fraction of %O of CAN oxidised BC nanofibrils increased accordingly based on the depletion of the elemental fraction of %C. The reduction elemental fraction of %C of CAN oxidised BC nanofibrils occurred due to depolymerisation and scission of cellulose chains by free radicals when subjected to CAN oxidation, as was discussed in the earlier section.

The EA of MTEMA-g-BC nanofibrils complied with the previously described ATR-FTIR measurements, thus corroborating the effective FRGP of MTEMA from the BC backbone. In fact, the elemental composition of MTEMA-g-BC revealed the substantial increase of the sulphur content (%S), which was anticipated from the effective grafting of MTEMA from BC nanofibrils. EA clearly suggested that the weight fraction of %S associated to thioether moiety increased with increasing concentration of MTEMA, as seen in Table 6.4. The increase of the weight fraction of %C with increasing concentration of MTEMA suggested the formation of pendant polyMTEMA chains from the BC backbone. Navarro *et al.*[359] and Nayak *et al.*[360] reported an increase of elemental fraction of %C after FRGP reaction of glycidyl methacrylate and acrylamide monomers from cellulose and guar gum, respectively, compared to polysaccharide not subjected to FRGP reaction. The increase of elemental fraction of %C also corresponded to an augmentation of concentration of monomer used during the FRGP reaction.

Table 6.4: Elemental weight composition for HCl hydrolysed BC, CAN oxidised BC and MTEMA-g-BC nanofibrils as a function of concentration of CAN and MTEMA as determined by elemental analysis.

			Elemental fraction			
Samples	CAN conc. (mM)	MTEMA conc. (mM)	%C	%H	%O	%S
BC *			44.55	6.11	49.34	
BC oxidised †	1		32.52	2.76	64.72	
	2.5		34.79	5.10	60.11	
MTEMA-g-BC	1	1	48.34	6.06	38.17	7.43
	1	5	51.34	7.39	32.02	9.25
	1	10	52.56	7.50	27.98	11.96
MTEMA-g-BC	2.5	1	43.99	4.66	46.63	4.72
	2.5	5	52.83	7.68	32.55	6.94
	2.5	10	45.68	6.78	31.85	15.69

*HCl hydrolysed BC nanofibrils; † CAN oxidised BC nanofibrils.

6.3.5 Thermal degradation behaviour of MTEMA-g-BC nanofibrils

The thermal degradation behaviour in inert N_2 atmosphere of HCl hydrolysed BC and CAN oxidised BC nanofibrils is presented in Figure 6.9 as a function of concentration of CAN. The profile of thermal degradation of HCl hydrolysed BC was steeper than the degradation profile of non-hydrolysed BC biosynthesised under static and agitated conditions, as presented in Chapter 3. The onset and degradation temperature of HCl hydrolysed BC were $304°C$ and $316°C$, respectively, the weight loss rate was 4.95 wt.$\% \cdot min^{-1}$, as summarised in Table 6.5. Comparatively, CAN oxidised BC nanofibrils were less thermally stable than HCl hydrolysed BC. In fact, CAN oxidised BC nanofibrils had an onset and degradation temperature of $260°C$ and $261°C$, respectively, for a concentration of CAN of 1 mmol, for a higher concentration of 2.5 mmol the thermal degradation behaviour remained very similar (Table 6.5). Interestingly, the rate of thermal degradation of CAN oxidised BC was 7.17 wt.$\% \cdot min^{-1}$ (1 mmol of CAN), which was 31% higher than that of HCl hydrolysed BC nanofibrils. The variation of thermal degradation behaviour of CAN oxidised BC as compared to HCl hydrolysed BC nanofibrils was attributed to the modification of the chemical composition by oxidative depolymerisation, as observed earlier for EA. Therefore, the oxidation reaction of BC nanofibrils using various concentrations of CAN affected the structure and chemical integrity of CAN oxidised BC

nanofibrils, thus resulting in a decrease of the thermal stability.

The thermal degradation behaviour in inert N_2 atmosphere of MTEMA-g-BC nanofibrils is presented in Figure 6.10 as a function of the concentration of CAN and MTEMA . The profile of the thermal degradation of MTEMA-g-BC nanofibrils differed from the one of HCl hydrolysed BC nanofibrils by a shift of degradation temperature to a higher value and a significant reduction of the weight loss rate, which were both attributed to effective grafting of polyMTEMA chains from the BC backbone, as shown in Figure 6.10.

At a fixed concentration of CAN (1 mmol), the onset degradation temperature and weight loss rate of MTEMA-g-BC nanofibrils decreased substantially with an increasing concentration of MTEMA, as summarised in Table 6.5. Moreover, at a higher concentration of CAN (2.5 mmol) the MTEMA-g-BC nanofibrils exhibited a lower onset degradation temperature and weight loss rate with an increasing concentration of MTEMA (Table 6.5). On the other hand, the thermal degradation of MTEMA-g-BC nanofibrils shifted towards higher values for an increasing concentration of MTEMA (Table 6.5).

Varma *et al.*[361] and Littunen *et al.*[362] reported that the concentration of reagents (CAN and monomer) in FRGP of cellulose as well as the duration of the reaction influence the molecular weight of the grafted polymer. Therefore, the increase of the thermal stability of MTEMA-g-BC nanofibrils was attributed to the synergistic effect between the increasing molecular weight of grafted polyMTEMA chains from BC nanofibrils with increasing of concentration of MTEMA.

6.3.6 SEM observation of MTEMA-g-BC nanofibrils

SEM micrographs of HCl hydrolysed BC, CAN oxidised BC and MTEMA-g-BC nanofibrils are presented in Figure 6.11. The morphology of HCl hydrolysed BC nanofibrils was comparable to those of non-hydrolysed BC described in Chapter 3. Observation of HCl hydrolysed BC nanofibrils at low magnification revealed the formation of BC bundles, which appeared irregular. At a higher resolution, individual BC nanofibrils were identified clearly. In the case of CAN oxidised BC nanofibrils, their morphology appeared smoother than that of HCl hydrolysed BC.

Interestingly CAN oxidised nanofibrils observed under both a high and low magnification exhibited a distinct feature, which appeared like sprinkled spherical shapes along the various nanofibrils. These artifacts observed from the CAN oxidised BC nanofibrils were consequent to the presence of CAN associated onto the CAN oxidised BC nanofibrils, as it was discussed

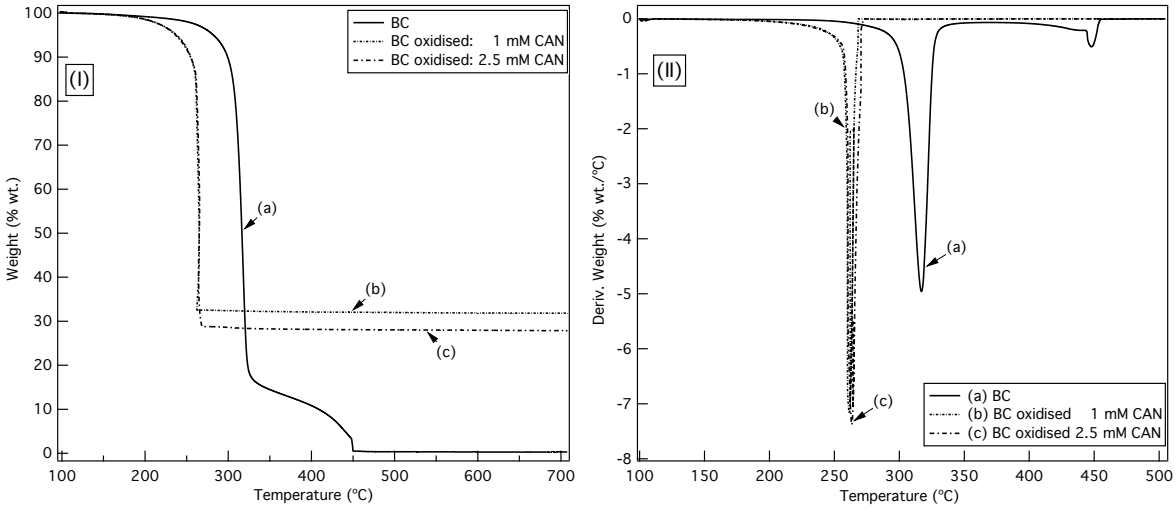


Figure 6.9: **I**) Thermal degradation behaviour of HCl hydrolysed BC and CAN oxidised BC nanofibrils (CAN conc. 1 & 2.5 mmol) in N_2 atmosphere. **II**) Derivative weight loss of HCl hydrolysed BC and CAN oxidised BC nanofibrils (CAN conc. 1 & 2.5 mmol) in N_2 atmosphere.

Table 6.5: Onset degradation temperature, degradation temperature, weight loss rate and char yield of the thermal degradation in N_2 atmosphere of BC, CAN oxidised BC and MTEMA-g-BC nanofibrils with various concentrations of CAN and MTEMA.

Sample	CAN (mM)	MTEMA (mM)	Onset Temp. ($^\circ C$)	Degrad. Temp. ($^\circ C$)	Wt. loss rate (-)($\%.min^{-1}$)	Char (wt.%)
BC *			304.4	316.8	4.95	0.3
BC oxidised †	1		260.8	261.2	7.17	31.8
BC oxidised †	2.5		262.7	263.4	7.38	27.9
MTEMA-g-BC	1	1	292.5	346.2	1.36	7.9
	1	5	207.8	351.6	0.98	5.6
	1	10	215.1	353	1.03	3.6
MTEMA-g-BC	2.5	1	230.4	347.6	0.98	19
	2.5	5	225.9	337	0.75	12.7
	2.5	10	212.8	341.9	0.60	10

*HCl hydrolysed BC nanofibrils; † CAN oxidised BC nanofibrils.

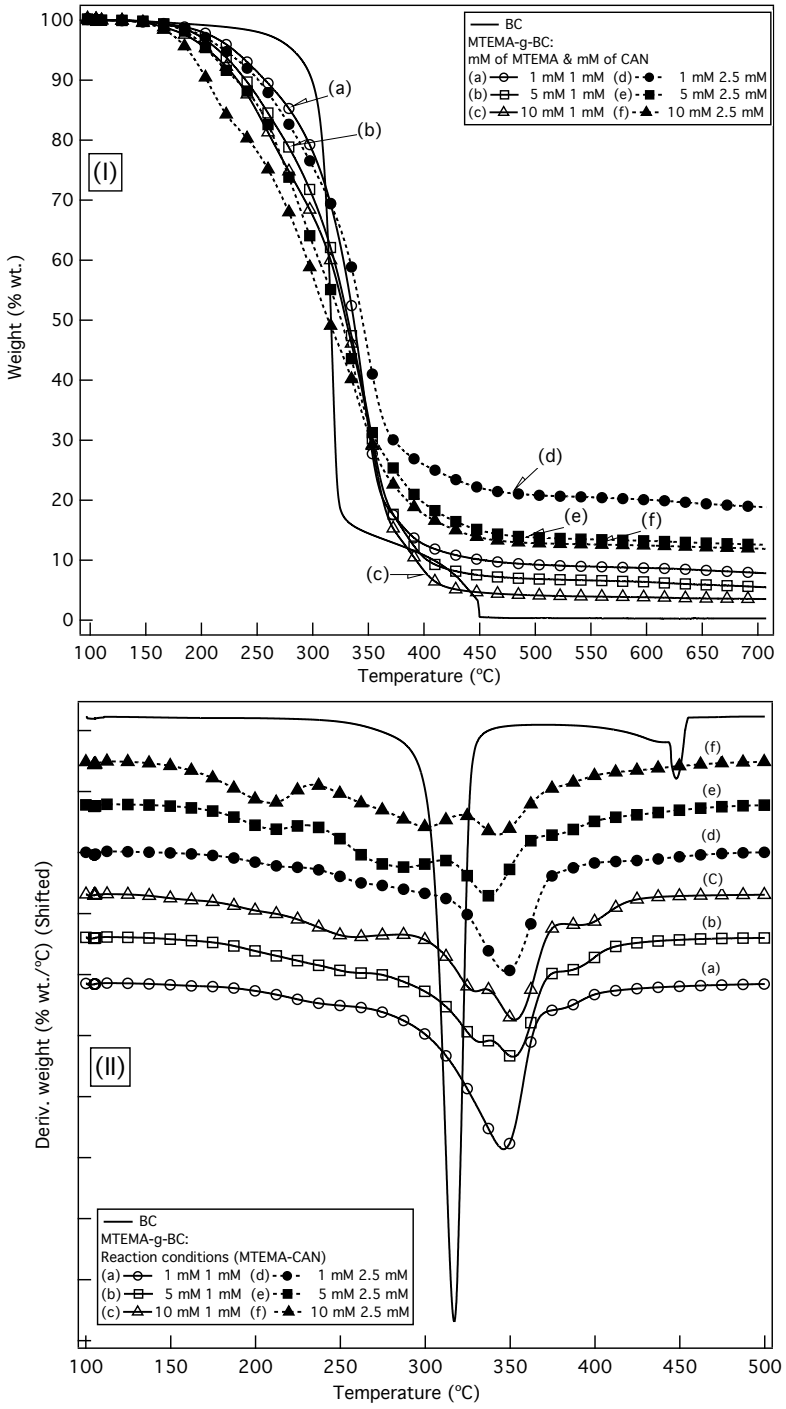


Figure 6.10: I) Thermogravimetric analysis of HCl hydrolysed BC and MTEMA-g-BC nanofibrils at various concentrations of MTEMA: 1, 5 and 10 mmol & CAN: 1 and 2.5 mmol in N_2 atmosphere. **II**) Derivative weight loss of HCl hydrolysed BC and MTEMA-g-BC nanofibrils at various concentrations of MTEMA: 1, 5 and 10 mmol & CAN: 1 and 2.5 mmol) in N_2 atmosphere.

earlier from the XRD measurements. Indeed, these artifacts (*i.e.*, CAN) had certainly been the cause of the apparition of new diffraction peak located at $2\theta = 28°$ and 33°, respectively (Figure 6.5).

In SEM micrograph under low magnification, MTEMA-g-BC nanofibrils appeared loosely fused with a smeared aspect, which was very distinct to HCl hydrolysed BC nanofibrils. When the resolution was increased, MTEMA-g-BC nanofibrils were less distinguishable from one another. The surface of MTEMA-g-BC nanofibrils was altered comparatively to HCl hydrolysed BC, this was attributed to the effective grafting of polyMTEMA chains away from the BC backbone as described earlier in the ATR-FTIR analysis section. Similarly, the surface morphology of MMA grafted bamboo fibres using CAN redox initiation revealed an uneven and rough surface, which resulted from FRGP of MMA [350].

6.4 Characterisation of MTEMA-g-BC-Au Nanohybrids

In this section, the characterisation of never-dried MTEMA-g-BC-Au nanohybrids will be discussed. The MTEMA-g-BC-Au nanohybrids presented herein were obtained using MTEMA-g-BC nanofibrils, which were synthesised by FRGP reaction using various concentrations of MTEMA (*i.e.*, 1, 5 & 10 mml) and CAN (*i.e.*, 1 & 2.5 mmol), respectively, as described previously in Section 6.2.2. Furthermore, the *i.e.* chemisorption of Au NPs onto MTEMA-g-BC nanofibrils was performed as described in earlier Section 6.2.4.

6.4.1 UV-Vis spectroscopy of MTEMA-g-BC-Au nanohybrids

The UV-Vis spectra of thermally grown Au NPs in the presence of MTEMA-g-BC nanofibrils and MTEMA-g-BC-Au nanohybrids are presented in Figure 6.12**I** and 6.12**II**, respectively. The UV-Vis spectra of colloidal suspension of Au NPs obtained, which were separated from the excess Au NPs thermally grown *in situ* in the presence of MTEMA-g-BC nanofibrils (as described in Section6.2.4) revealed the typical absorbance peak for Au NPs located between 522 nm and 533 nm, as seen in Table 6.6. The morphology of UV-Vis absorbance peaks for Au NPs (Figure 6.12**I**) were differed to those of MTEMA-g-BC nanofibrils employed during *in situ* thermal growth of Au NPs. As discussed in the earlier section, the characteristics (*i.e*, surface chemistry, morphology and crystallography) of MTEMA-g-BC nanofibrils were a function of the concentration of the reactants (MTEMA and CAN) used for FRGP. Indeed, the UV-Vis spectrum of Au NPs exhibited a broad and blurred absorbance peak for

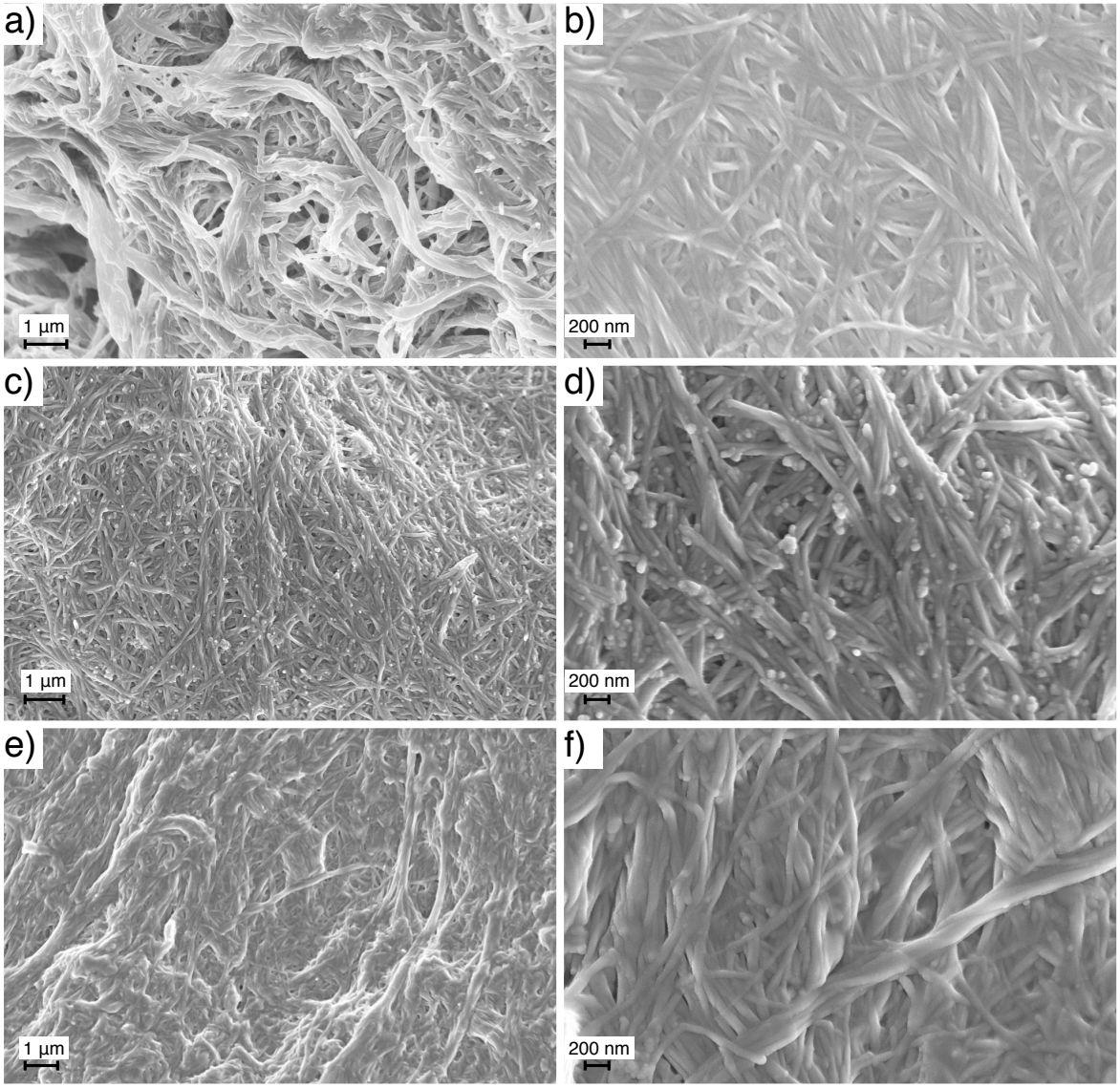


Figure 6.11: SEM micrographs of: **a**, **b**) HCl hydrolysed BC nanofibrils, as prepared in Chapter 3; **c**, **d**) BC nanofibrils oxidised with CAN conc. of 2.5 mmol and **e**, **f**) MTEMA-g-BC nanofibrils after FRGP (MTEMA with conc. of 10 mmol and CAN with conc. of 2.5).

thermally grown Au NPs with the presence of MTEMA-g-BC nanofibrils synthesised using a concentration of CAN of 1 mmol and a concentration of MTEMA of either 1 mmol, 5 mmol or 10 mmol, respectively. However, the UV-Vis spectrum of Au NPs was narrower and more pronounced for the cases, where, Au NPs were thermally grown in the presence of MTEMA-g-BC nanofibrils synthesised using a concentration of CAN of 2.5 mmol and a concentration of MTEMA of either 1 mmol, 5 mmol or 10 mmol, respectively. Interestingly, thermally grown colloidal suspension of Au NPs in the presence of MTEMA-g-BC nanofibrils synthesised with a concentration of MTEMA of 5 mmol and CAN of 2.5 mmol (filled squares) presented an atypical peak morphology as compared to other specimens thermally grown in the presence of MTEMA-g-BC nanofibrils synthesised using also a concentration of CAN of 2.5 mmol. The absorbance peak resolved by UV-Vis spectroscopy corresponded to the surface plasmon resonance (SPR) oscillation of the Au NPs constituting the colloidal suspension. Despite the presence of MTEMA-g-BC nanofibrils during the thermal growth of Au NPs, the resulting NPs exhibited the characteristic optical behaviour attributed to Au colloids. Similarly, Creighton *et al.*[363] and Grabar *et al.*[364] located the peak of SPR of Au colloid at 525 nm and 520 nm, respectively. Moreover, the dynamic light scattering (DLS) measurements revealed the aggregation in colloidal suspension of Au NPs to sizes ranging from 100 nm to 183 nm (Table 6.6), these values were in agreement with the 190 nm reported by Oh *et al.*[365] for the preparation of poly(ethylene glycol) ligand stabilised Au NPs. The stability of Au NPs was dependant on the concentration of trisodium citrate used as reducing agent and/or electrostatic capping ligand causing a negative surface charge of the surface of Au NPs, thus introducing a repulsive interparticle interaction amongst neighbouring NPs[366]. Therefore, an incomplete surface coverage of Au NPs by trisodium citrate composed of trivalent citrate ions[367,368] resulted in the formation of Au NPs aggregates resulting in coarsening[369].

The UV-Vis spectra of MTEMA-g-BC-Au nanohybrids are presented in Figure 6.12**II** as a function of the concentration of reagents used for FRGP. The morphology of the SPR absorbance peak of MTEMA-g-BC-Au nanohybrids appeared relatively flat and broad as compared to SPR absorbance peak of Au NPs (Figure 6.12**I**). As expected the UV-Vis spectra of MTEMA-g-BC nanofibrils were relatively flat and did not exhibit any clear absorbance peaks. However, the location of SPR absorbance peak shifted from 529 nm to 561 nm for MTEMA-g-BC-Au obtained from MTEMA-g-BC when synthesised using a concentration of CAN and MTEMA monomer of either 2.5 mmol and 1 mmol or 1 mmol and 1 mmol, respectively (see Table 6.6). The broad SPR absorbance peak of MTEMA-g-BC-Au revealed the

state of aggregation of Au NPs on the surface of MTEMA-g-BC substrate. Similarly, Rouhana *et al.*[366] observed the broadening of the SPR absorbance peak for colloidal suspension containing aggregated Au NPs, Rouhana *et al.* also noticed a shift of SPR absorbance peak to higher wavelength (red shift), which reflected the presence of aggregates of Au NPs. Kim *et al.*[368] observed a change of both morphology and location of the SPR absorbance peak of colloidal suspension of Au NPs, which resulted from interparticle aggregation of Au NPs initiated by addition of benzyl mercaptan after a stable colloidal suspension of Au NPs was formed. Interestingly, Liao *et al.*[370] also reported the resolution of an additional long wavelength component in UV-Vis spectra of Au NPs, which were aggregated linearly in EtOH, as compared to isolated and dispersed Au NPs. The broadening of the SPR absorbance peak of Au NPs was associated with the resonant modes of the SPR, *i.e.* longitudinal and transversal components, resulting from the linear aggregation of Au NPs. The UV-Vis spectra of MTEMA-g-BC-Au nanohybrids discussed herein were in agreement with results reported by Grabar *et al.*[364] regarding the formation and self-assembly of Au colloid monolayers onto surface of polymer-coated substrates, which were formed by condensation of functionalised alkoxysilanes. Recently, Zhang *et al.*[109] reported the preparation of bioinorganic nanohybrids composed of non-hydrolysed BC nanofibres and Au NPs. To immobilise Au NPS onto BC, Zhang *et al.* deposited onto BC nanofibres a layer of poly(ethyleneimine) (PEI), which was an amine-riched cationic polyelectrolyte. PEI attached to BC nanofibres via hydrogen bonding between hydroxyl (-OH) groups of BC and amine (-NH_3) groups of PEI. Subsequently, free protonated amine groups conjugated with $AuCl_4$ via electrostatic attraction, which enabled anchoring of Au NPs. The resulting UV-Vis spectra of AuBC nanocomposites measured by Zhang *et al.*[109] presented similar characteristics to those described here (Figure 6.12**II**), which consisted in a broad SPR absorbance peak and shifted towards a higher wavelength (red-shift) induced by plasmon coupling between closely spaced Au NPs[370,371] as was earlier reported by Zhang *et al.*[372] for UV-Vis spectra of Au-NPs/silica-nanofibre hybrid nanostructures.

The colour of MTEMA-g-BC-Au nanohybrids, MTEMA-g-BC nanofibrils and Au colloids is shown in Figure 6.13. The various nuances of red colour of MTEMA-g-BC-Au nanohybrids were attributed to the presence of Au NPs (and aggregates) chemisorbed onto the substrate of MTEMA-g-BC nanofibrils. The optical properties of MTEMA-g-BC-Au nanohybrids resulted from the combination of multiple factors, such as the absorption and scattering of visible light, which was influenced by the size of both individual Au NPs and aggregates. In

addition, the surface properties of the substrate, such as the density of thioether moieties along the surface of MTEMA-g-BC nanofibrils influenced the chemisorption of Au NPs as well as their aggregates formation, thus modifying the optical characteristics of the nanohybrids. Moreover, the suspension of MTEMA-g-BC-Au nanohybrids in EtOH using an ultrasonic probe emphasised the strong polymer-NPs interaction, which resulted from the chemisorption of Au NPs onto the thioether moiety (SCH_3) of MTEMA-g-BC nanofibrils. According to Rouhana *et al.*[366], this was explained by the greater affinity of thiols towards the surface of Au NPs, as compared to the weakly adsorbed trisodium citrate which was therefore displaced. Furthermore, MTEMA-g-BC-Au nanohybrids retained their structural integrity during ultrasonic excitation since no noticeable transfer of Au NPs into the medium was observed.

Table 6.6: SPR absorbance peak of colloidal suspensions of Au NPs and aqueous suspensions of MTEMA-g-BC-Au nanohybrids; aggregate sizes of Au NPs in colloidal suspensions measured by dynamic light scattering (DSL).

CAN (mM)	MTEMA (mM)	Sample	SPR (λ_{max}, nm)	Dia. (DSL) (nm)	Sample	SPR (λ_{max}, nm)
1	1	Au NPs*	524	183.7	MTEMA-g-BC-Au	561
1	5		524	132.1		543
1	10		526	175.4		541
2.5	1		522	126.1		529
2.5	5		524	150.5		533
2.5	10		533	100.9		541

* For colloidal suspensions of Au NPs non-chemisorbed to the thioether moieties (SCH_3) of polyMTEMA chains during thermal growth in the presence of MTEMA-g-BC nanofibrils.

6.4.2 SEM of MTEMA-g-BC-Au nanohybrids

The surface morphology of BC-MTEMA-Au nanohybrids is shown in Figure 6.14 for MTEMA-g-BC nanofibrils synthesised with a concentration of MTEMA of 1 mmol and a concentration of CAN of 2.5 mmol. When compared to the smooth surface of MTEMA-g-BC nanofibrils (Figure 6.11), the SEM micrographs indicated that the surface of MTEMA-g-BC-Au nanohybrids was covered by aggregates (clusters) of Au NPs. The aggregates of Au NPs were com-

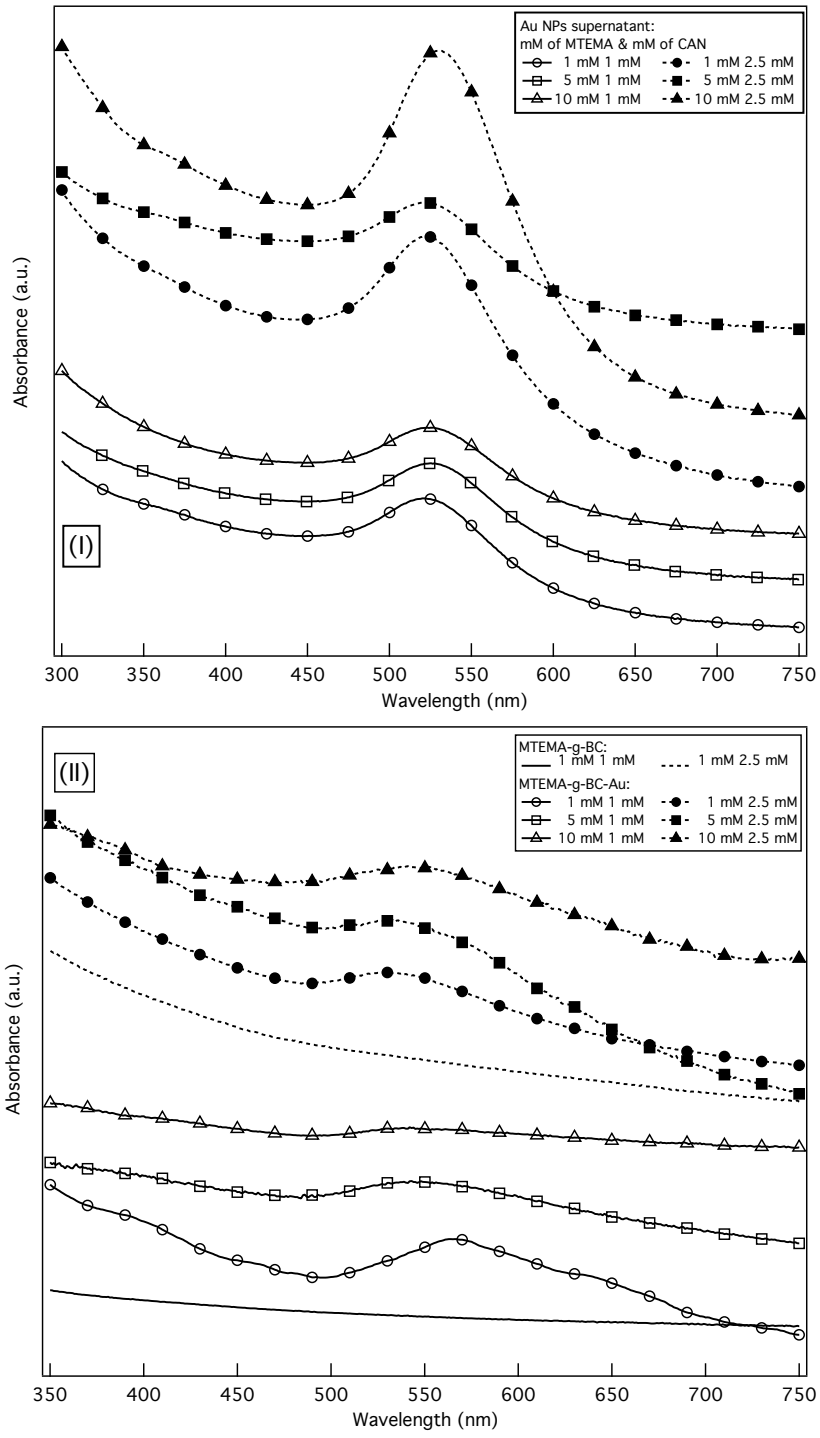


Figure 6.12: I) UV-Vis absorption of colloidal suspensions of Au NPs non-chemisorbed to the thioether moieties (SCH_3) of polyMTEMA chains during the thermal growth of Au NPs in the presence of MTEMA-g-BC nanofibrils. **II**) UV-Vis absorption of MTEMA-g-BC-Au nanohybrids prepared *in situ* by thermal growth of Au NPs in the presence of MTEMA-g-BC nanofibrils synthesised using different concentrations of MTEMA and CAN.

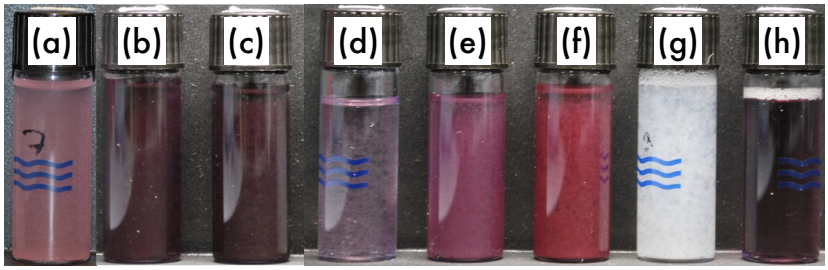


Figure 6.13: Photograph of MTEMA-g-BC-Au nanohybrids suspended in EtOH (conc. of 0.1 wt./v.%), where the red colour reflected the presence of Au NPs chemisorbed to thioether moieties of polyMTEMA chains of MTEMA-g-BC nanofibrils. MTEMA-g-BC-Au nanohybrids prepared with MTEMA-g-BC nanofibrils synthesised using various concentrations of MTEMA and CAN: **a**) 1 mmol & 1 mmol; **b**) 5 mmol & 1 mmol; **c**) 10 mmol & 1 mmol; **d**) 1 mmol & 2.5 mmol; **e**) 5 mmol & 2.5 mmol; **f**) 10 mmol & 2.5 mmol. **g**) MTEMA-g-BC nanofibrils synthesised using a concentration of MTEMA of 10 mmol and a concentration of CAN of 2.5 mmol, respectively. **h**) pure Au colloid.

posed of several NPs and were located along the MTEMA-g-BC nanofibrils. However, the spacing between aggregate of Au NPs was uneven, which suggested a heterogeneous disposition of suitable anchoring sites for Au^{3+} ions at the surface of MTEMA-g-BC nanofibrils prior to the reduction of Au NPs.

Recently Padalkar *et al.*[310] reported the decoration surface of tunicate cellulose nanocrystals (CNCs) with Au NPs using cetyltrimethylammonium bromide (CTAB), a cationic surfactant, which enabled both stabilisation and immobilisation of Au NPs onto surface of CNCs. Observation of these BC/CTAB/Au hybrids showed that Au NPs formed agglomerates, which were spaced along the CNCs.

6.5 Characterisation of MTEMA-g-BC-CdTe Nanohybrids

In this section, the UV-Vis spectroscopy and SEM characterisation of MTEMA-g-BC-CdTe nanohybrids will be discussed. The MTEMA-g-BC-CdTe nanohybrids presented here were produced using MTEMA-g-BC nanofibrils, which were synthesised by FRGP using a concentration of MTEMA and CAN of 10 mmol and 2.5 mmol, respectively, as described previously in Section 6.2.2. Furthermore, the deposition of CdTe QDs by ligand transfer *in situ* to MTEMA-g-BC nanofibrils was performed as described earlier in Section 6.2.5.

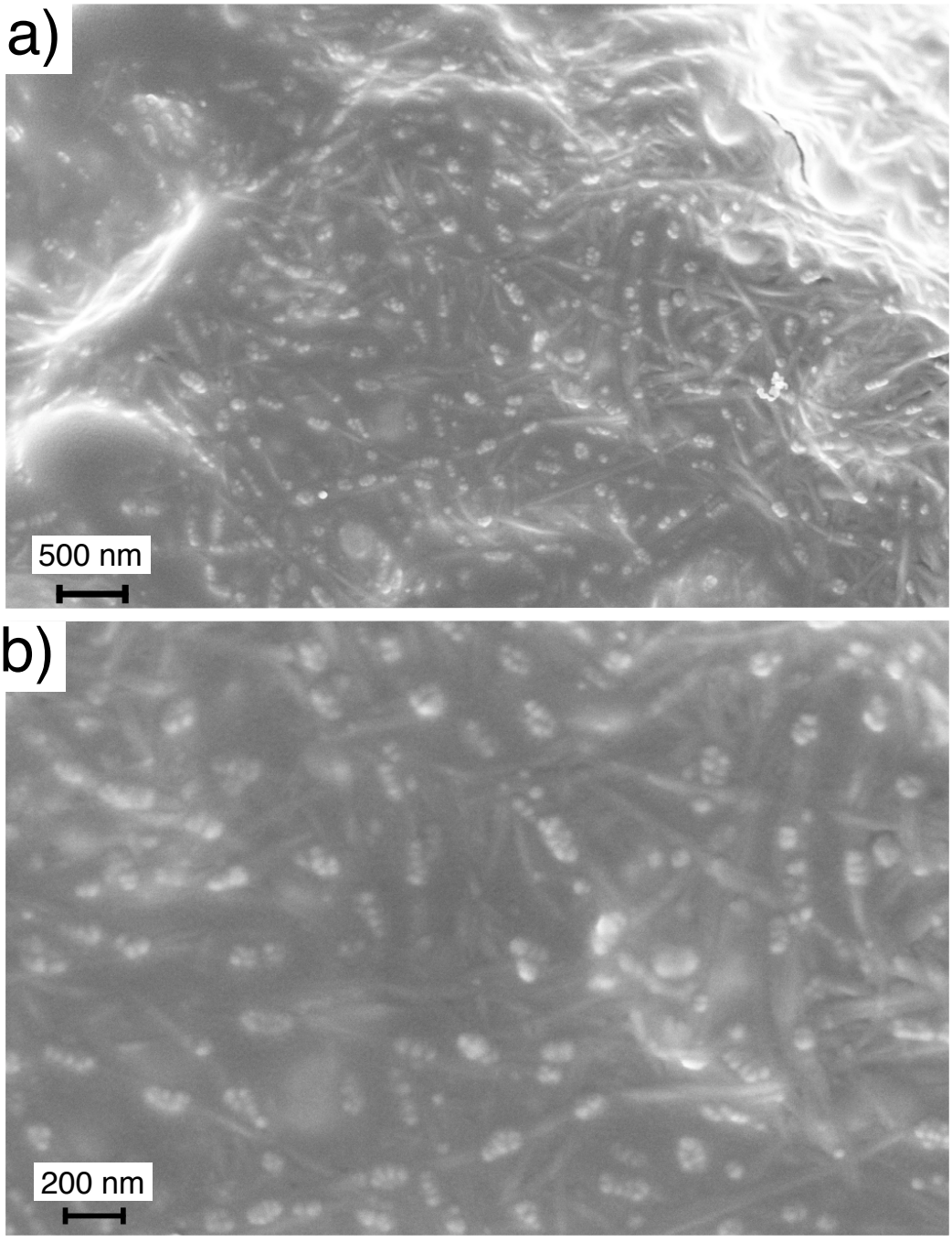


Figure 6.14: SEM micrographs of MTEMA-g-BC-Au nanohybrid at various magnifications: **a**) x75k; **b**) x100k. MTEMA-g-BC synthesised using a concentration of MTEMA of 1 mmol and CAN of 2.5 mmol.

6.5.1 UV-Vis spectroscopy of CdTe quantum dots

The UV-Vis spectra of CdTe QD colloids as function of refluxing time are presented in Figure 6.15**I**. The UV-Vis spectra of CdTe QD colloids remained similar with increasing reflux time. However, a significant red shift of the absorption peak was observed; the location of SPR absorbance peak was 475 nm for a reflux duration of 10 min and shifts to 550 nm for 1 h, as seen in Table 6.7. Therefore, the shift of SPR absorbance peak indicated the evolution of the optical and photoluminescent properties of CdTe QDs with respect to their refluxing time. The shift to longer wavelengths indicated an increase of size and a narrowing of the size distribution of QDs, which resulted in an enhancement of the optical and photoluminescent transitions [344].

Observation of CdTe QD colloids under daylight revealed a change of colour from yellowish, passing through orange to reddish with increasing refluxing time (Figure 6.15**II**). However, under UV irradiation (λ= 365 nm), the CdTe QD colloids exhibited photoluminescence with colours from green to red with increasing refluxing time (Figure 6.15**III**). The variation of photoluminescence colour emitted by CdTe QDs denoted the growth in size of the DQs, which was linked to their optical and photoluminescent properties.

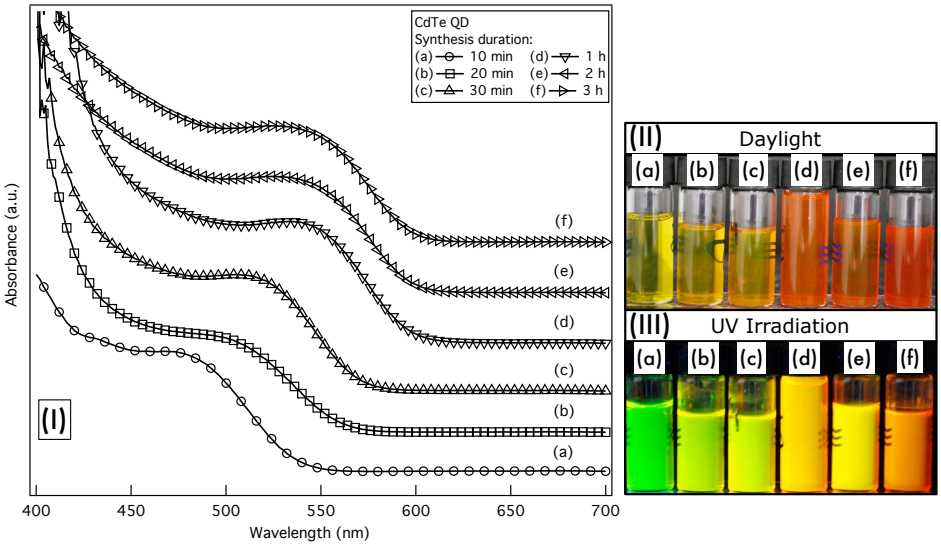


Figure 6.15: **I**) UV-Vis absorption of CdTe QD colloids as a function of refluxing time. **II**) Photograph of CdTe QDs colloid visualised under daylight. **III**) Photograph of CdTe QDs colloid visualised under UV irradiation. Refluxing time: (a) 10 min; (b) 20 min; (c) 30 min; (d) 60 min; (e) 120 min; (f) 180 min.

Table 6.7: SPR absorbance peak (UV-Vis spectroscopy) of CdTe QD colloids as a function of refluxing time.

Sample	Refluxing time (min)	SPR (λ_{max}, nm)
CdTe QDs colloid	10	475
	20	490
	30	505
	60	533
	120	545
	180	550

6.5.2 UV-Vis of MTEMA-g-BC-CdTe nanohybrids

The UV-Vis spectra of MTEMA-g-BC-CdTe nanohybrids are presented in Figure 6.16**I** as a function of concentration (wt./wt.%) CdTe QD deposited onto MTEMA-g-BC nanofibrils and immobilised during ligand transfer. The shape of absorbance peaks of MTEMA-g-BC-CdTe nanohybrids changed substantially with increasing concentration of CdTe QDs added. Indeed, the SPR absorbance peak appears flattened and broadened for low concentrations of CdTe QDs and was well defined and much narrower for higher concentrations of CdTe QDs (Figure 6.16**I**). The location of the peak maximum of SPR peaks of MTEMA-g-BC-CdTe nanohybrids varied between 557 nm and 608 nm for a concentration of 11.6 wt./wt.% and 37.1 wt./wt.%, respectively (Table 6.8). The peak maximum of SPR peaks shifted to higher wavelength with increasing concentration of CdTe QDs. Comparatively, the UV-Vis spectra of MTEMA-g-BC nanofibrils remained relatively smooth and flat. The UV-Vis spectra of MTEMA-g-BC-CdTe nanohybrids differ from those of CdTe QD colloids (2 h of refluxing time) with respect to the shape of the absorbance peak. The precipitation and immobilisation of CdTe QDs onto MTEMA-g-BC nanofibrils modified the SPR properties of MTEMA-g-BC-CdTe nanohybrids. The immobilisation of CdTe QDs onto the MTEMA-g-BC substrate altered their optical properties and their contribution to the functional nanohybrids, as seen when comparing Figure 6.15 and Figure 6.16**I**, respectively. Similarly, Hwang *et al.*[297] reported the preparation of photoluminescent hybrids composed of regioselective dendritic functionalised cellulose and cadmium sulphide (CdS) QDs, where the CdS QDs were stabilised within an isocyanate-based dendritic structure, which was covalently anchored to

cellulose backbone. The resulting CdS/cellulose nanohybrids presented a characteristic SPR absorbance peak located at 325 nm, as compared to 515 nm for CdS QDs alone. These CdS/cellulose nanohybrids also exhibited photoluminescence when irradiated with UV light. Recently, Niu *et al.*[287] prepared luminescent cellulose films by immobilising CdSe QDs onto cellulose nanofibres, which had been subsequently coated by titania and stearic acid (SA) to impart hydrophobic interactions between the alkyl chain of the surface ligands (capping molecules) of CdSe QDs and SA. The resulting cellulose/titania/SA/(CdSe/SA) composite films exhibited a SPR absorption band at 500 nm (UV-Vis measurements), as well as a stable green fluorescence whose intensity increased with increasing density of CdSe QDs deposited onto the cellulose substrate.

Figure 6.16**II** shows a suspension of MTEMA-g-BC-CdTe nanohybrids under daylight. A reddish colour emerges with increasing concentration of CdTe QDs immobilised onto the MTEMA-g-BC substrate (samples: b, c, d, e), which tends to the colour of CdTe QD colloids (sample: a). The intensification of colour of MTEMA-g-BC-CdTe nanohybrids corroborates the higher density of CdTe QDs and their effective immobilisation onto MTEMA-g-BC nanofibrils in accordance with the procedure described in Section 6.2.5. The same suspension of MTEMA-g-BC-CdTe nanohybrids was observed under UV irradiation (Figure 6.16**III**). The photoluminescence emitted from MTEMA-g-BC-CdTe nanohybrids revealed the preservation of the electronic properties of CdTe QDs after their immobilisation onto the MTEMA-g-BC substrate. Similarly the size selective precipitation procedure of CdTe QDs performed by Gaponik *et al.*[344] showed that the optical properties of QDs did not change either. However, the colour of the photoluminescence emitted from MTEMA-g-BC-CdTe nanohybrids (sample: b, c, d, e) is different to that of the corresponding CdTe QD colloids (sample: a). This difference of colour resulted from a preferential deposition of CdTe QDs onto MTEMA-g-BC within a certain size distribution, whereas, the other ones remained suspended and were subsequently removed during purification steps. Gaponik *et al.*[344] reported that size selective precipitation of CdTe QDs in a non-solvent induced the gradual precipitation of the largest QDs with a narrow size distribution.

6.5.3 SEM of MTEMA-g-BC-CdTe nanohybrids

The surface morphology of MTEMA-g-BC-CdTe nanohybrids is shown in Figure 6.17. Immobilised CdTe QDs are clearly identified along the MTEMA-g-BC nanofibrils. The CdTe QDs were spread along the MTEMA-g-BC substrate in a sporadic fashion. The spacing

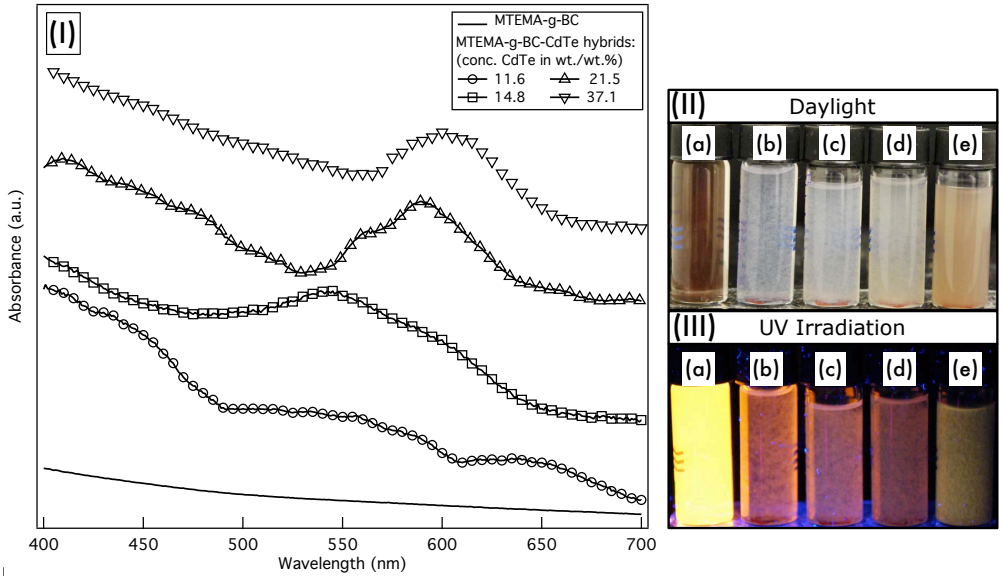


Figure 6.16: **I**) UV-Vis absorption of MTEMA-g-BC-CdTe nanohybrid nanofibrils with increasing concentration of CdTe QDs. **II**) Photograph of MTEMA-g-BC-CdTe nanohybrids (0.1 wt./v.%) suspensions in EtOH visualised under daylight. **III**) Photograph of MTEMA-g-BC-CdTe nanohybrids (0.1 wt./v.%) suspension in EtOH visualised under UV irradiation. The corresponding concentration of CdTe QDs in MTEMA-g-BC-CdTe nanohybrids: (a) CdTe QDs only; (b) 11.6 wt./wt.%; (c) 14.8 wt./wt.%; (d) 21.5 wt./wt.%; (e) 37.1 wt./wt.%.

Table 6.8: SPR absorbance peak (UV-Vis spectroscopy) of MTEMA-g-BC-CdTe nanohybrids (0.1 wt./v.%) in suspension as a function of concentration of CdTe QDs.

Sample	Conc. of CdTe QDs (wt./wt.%*)	SPR (λ_{max}, nm)
MTEMA-g-BC-CdTe	11.6	557
	14.8	548
	21.5	589
	37.1	608

* Concentration of CdTe QDs chemisorbed on the thioether moieties (SCH_3) of the MTEMA-g-BC nanofibrils as determined with respect to the weight of MTEMA-g-BC-CdTe nanohybrids.

among CdTe QDs was certainly dictated by the accessibility of thioether moieties along the MTEMA-g-BC nanofibrils.

Recently, Li *et al.*[298] reported the *in situ* synthesis of CdS QDs within BC membranes. SEM micrographs revealed the immobilisation of CdS QDs within the BC network. However, the coverage of BC nanofibrils by CdS QDs was limited, which resulted in a low density of QDs with respect to surface area of BC nanofibrils. Whereas, the MTEMA-g-BC-CdTe nanohybrids described here exhibited a high density of CdTe QDs immobilised along MTEMA-g-BC nanofibrils, as compared to CdS/BC nanohybrids described by Li *et al.*[298].

6.6 Observation of photoluminescent nanocomposite films containing MTEMA-g-BC-CdTe nanohybrids

This section describes the photoluminescent properties of MTEMA-g-BC-CdTe nanohybrids and PHBHHX/MTEMA-g-BC-CdTe nanocomposite films under UV irradiation as function of the concentration of CdTe QDs immobilised onto the MTEMA-g-BC substrates (*i.e.*, 11.6, 14.8, 21.5, 37.1 wt./wt.%) as discussed in earlier section.

A suspension of MTEMA-g-BC-CdTe nanohybrids (1 wt./v.%) in DCM as function of the concentration of CdTe QDs immobilised onto MTEMA-g-BC nanofibrils is shown in Figure 6.18. The MTEMA-g-BC-CdTe nanohybrids appeared well dispersed in DCM after ultrasonication. As seen in Figure 6.18**II**, the suspension of MTEMA-g-BC-CdTe nanohybrids in DCM exhibited a red colour photoluminescence when irradiated using a UV lamp. The photoluminescent properties of MTEMA-g-BC-CdTe originating from QDs were preserved in DCM, thus exemplifying the physical and chemical stability of the nanohybrid materials. Furthermore, the PHBHHx nanocomposites films containing MTEMA-g-BC-CdTe nanohybrids (4 wt./wt.% with respect to PHBHHx polymer) were optically active and emitted a red photoluminescence (Figure 6.19). The intensity of the photoluminescence of the nanocomposite films increased gradually with increasing concentration of CdTe QDs immobilised onto the MTEMA-g-BC nanofibrils (*i.e.*, 11.6, 14.8, 21.5, 37.1 wt./wt.%), thus for a constant concentration of MTEMA-g-BC-CdTe nanohybrids (*i.e.* 4 wt./wt.%) dispersed in the PHBHHx matrix. Furthermore, the MTEMA-g-BC-CdTe nanohybrids appeared well dispersed throughout the nanocomposite films, which resulted in the nanocomposite films being semi-translucent since incident light was not scattered by the presence of aggregates of MTEMA-g-BC-CdTe nanohybrids throughout the matrix. Indeed, visual observations showed that

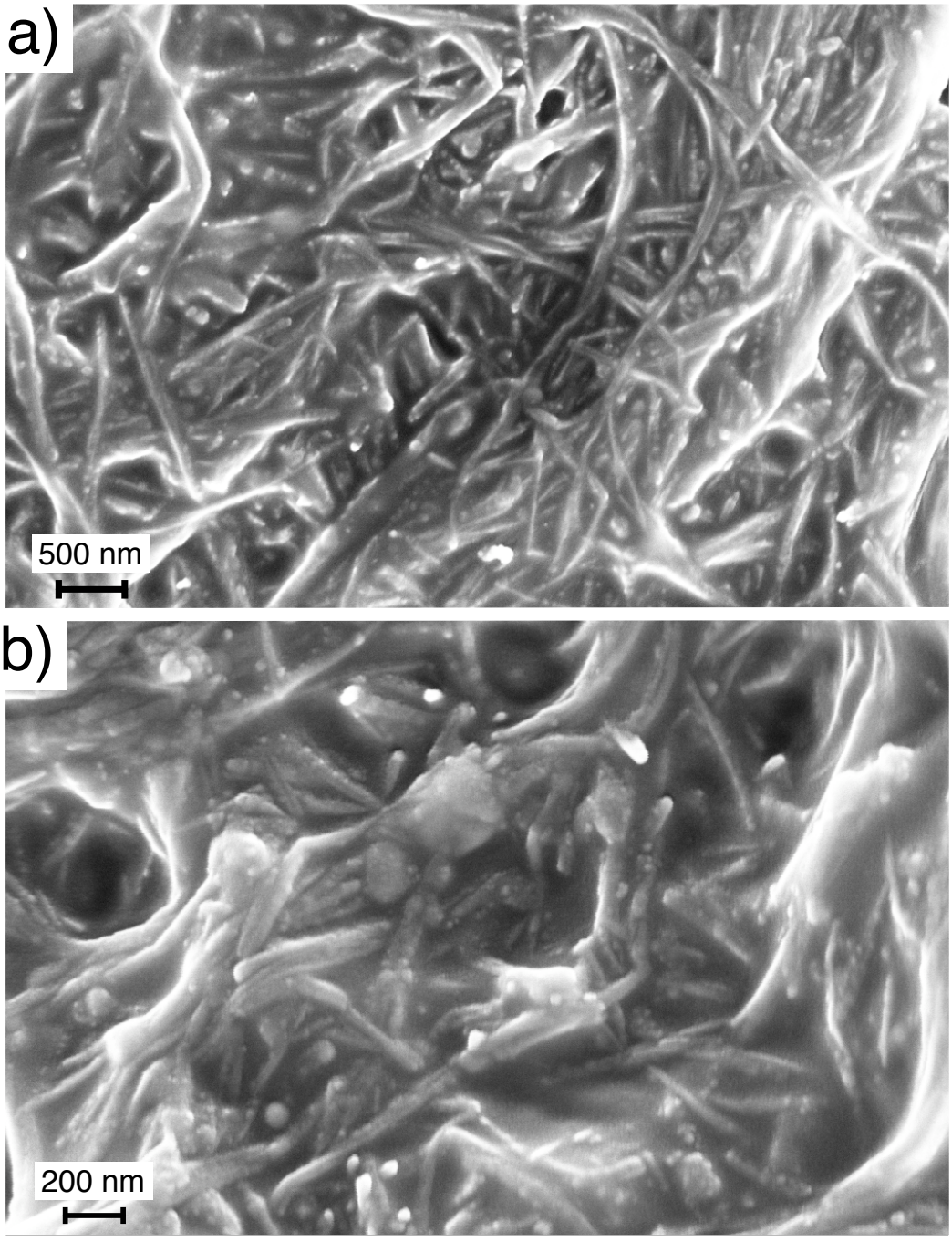


Figure 6.17: SEM micrographs of MTEMA-g-BC-CdTe nanohybrids at a magnification of x75k; **a**) and x100k; **b**)

the MTEMA-g-BC-CdTe nanohybrids retained their optical and photoluminescent properties when suspended in DCM or embedded in the polymer matrix to form nanocomposites films exhibiting photoluminescence. During the preparation of the nanocomposite films, the CdTe QDs remained strongly anchored to the MTEMA-g-BC nanofibrils.

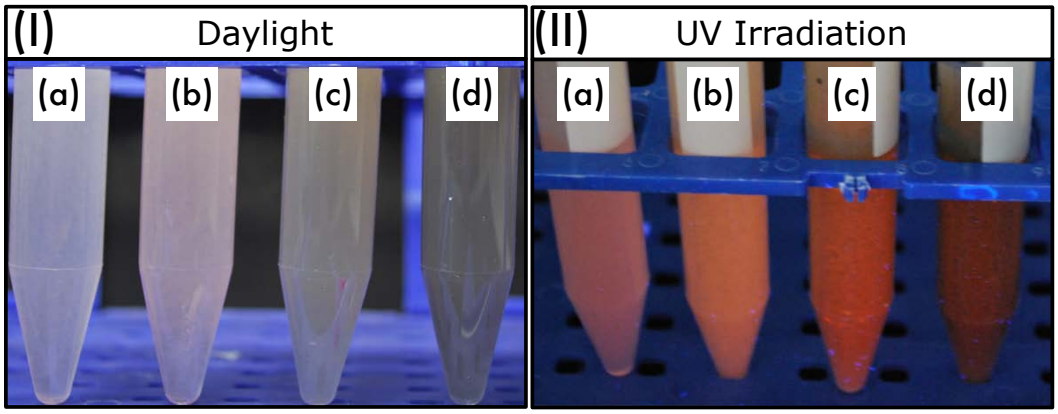


Figure 6.18: Photographs of suspensions of MTEMA-g-BC-CdTe nanohybrids (1 wt./v.%) in DCM: **I**) under daylight & **II**) under UV irradiation. The corresponding concentration of CdTe QDs immobilised on MTEMA-g-BC substrates were: (a) 11.6 wt./wt.%; (b) 14.8 wt./wt.%; (c) 21.5 wt./wt.%; (d) 37.1 wt./wt.%.

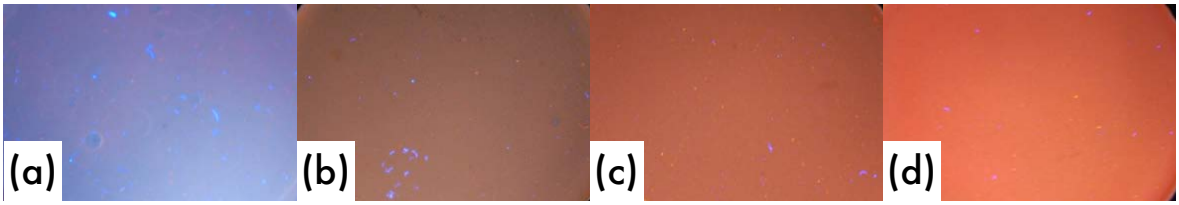


Figure 6.19: Photographs of PHBHHX nanocomposite films containing MTEMA-g-BC-CdTe nanohybrids (4 wt./wt.%) under UV irradiation. The corresponding concentration of CdTe QDs immobilised onto MTEMA-g-BC substrates were: (a) 11.6 wt./wt.%; (b) 14.8 wt./wt.%; (c) 21.5 wt./wt.%; (d) 37.1 wt./wt.%.

6.7 Conclusions

A novel and innovative approach to functionalise BC nanofibrils with thioether moieties in an aqueous reaction medium under mild reaction conditions was presented in this chapter.

BC nanofibrils were functionalised by FRGP of 2-(methylthio) ethyl methacrylate initiated by radicals generated on the BC backbone using CAN to form MTEMA-g-BC nanofibrils. Variation of concentration of reagents, namely, MTEMA and CAN modified the degree of crystallinity, chemical composition, thermal stability and morphology of the MTEMA-g-BC nanofibrils. Increasing the concentration of reagents resulted in a gradual increase of the grafting density of polyMTEMA chains, as deduced from the increasing intensity of the IR absorption band assigned to carboxyl groups and greater elemental fraction of sulphur present in the thioether moiety. Consequently, these changes in the chemical composition were characteristic for an effective FRGP reaction. They were also accompanied by significant alteration of the XRD diffractogram of MTEMA-g-BC nanofibrils with the appearance of a diffraction peak located at $2\theta = 28°$, which was cause by the association of CAN with BC. Similarly, the thermal stability and degradation of MTEMA-g-BC nanofibrils were notably modified as compared to either BC nanofibrils alone or CAN oxidised BC nanofibrils. In addition, the morphology of MTEMA-g-BC nanofibrils observed by SEM showed that the surface of MTEMA-g-BC nanofibrils was altered comparatively to HCl hydrolysed BC; this was also attributed to the effective grafting of polyMTEMA chains away from the BC nanofibrils

Subsequently, bioinorganic nanohybrids composed of MTEMA-g-BC nanofibrils as organic component and either Au NPs or CdTe QDs as inorganic component were produced. MTEMA-g-BC-Au nanohybrids were obtained by *in situ* reduction of Au salt solution to elemental Au NPs in the presence of MTEMA-g-BC nanofibrils. In that case the Au NPs were immobilised and stabilised onto surfaces of MTEMA-g-BC nanofibrils via chemisorption between Au NPs and the pendant thioether moieties (SCH_3) of the polyMTEMA chains grafted from BC nanofibrils MTEMA-g-BC-Au nanohybrids exhibited a characteristic SPR band, whose location corresponded to the one characteristic of colloidal suspension of Au NPs. When a suspension of MTEMA-g-BC-Au nanohybrids was subjected to intense and localised ultrasonic excitation, the chemisorbed Au NPs remained strongly anchored to the substrate. MTEMA-g-BC-CdTe nanohybrids were themselves produced by immobilisation of CdTe QDs onto surfaces of MTEMA-g-BC nanofibrils by their precipitation from suspension followed by ligand transfer between the thioglycolic acid capped CdTe QDs and the thioether moieties of MTEMA-g-BC nanofibrils. The resulting MTEMA-g-BC-CdTe nanohybrids exhibited an SPR band and emitted photoluminescence when irradiated with UV light, which resulted from a successful immobilisation and stabilisation of CdTe QDs onto the substrate. Interestingly, when MTEMA-g-BC-CdTe nanohybrids were suspended in dichloromethane

prior to dispersion in a polymeric matrix, their photoluminescence properties were still preserved, which accounted for an effective ligand transfer of thioglycolic acid capped CdTe QDs to the thioether moieties (SCH_3) of MTEMA-g-BC nanofibrils.

6.8 Future work

The future work should initially attempt to clarify the emergence of additional diffraction peak after CAN oxidation, as observed from XRD diffractograms of either CAN oxidised BC or MTEMA-g-BC nanofibrils. For MTEMA-g-BC-Au nanohybrids, there is a great potential to increase the surface coverage of Au NPs onto MTEMA-g-BC nanofibrils to establish electrical conductivity by close-packing of nanoparticles along the BC substrate for sensing and optoelectronics applications. This could be achieved by fine tuning of the reaction conditions to allow for higher density of thioether moieties on the BC backbone, which should result in a higher Au NPs loading. Electrical conductivity of MTEMA-g-BC-Au nanohybrids would be introduced by subsequently depositing Au NPs via a layer-by-layer procedure using an appropriate polyelectrolyte composition or specific bi-/trifunctional thiol linker [373] to bridge Au NPs with one another, thus forming a surrounding shell anchored to MTEMA-g-BC-Au nanohybrids by chemisorption. For MTEMA-g-BC-CdTe nanohybrids, it should be possible to control the photoluminescent properties and emission of MTEMA-g-BC-CdTe nanohybrids by using various sizes of QDs. The preparation of nanocomposite films composed of a conductive polymer matrix and tailored colour of photoluminescence-emitting MTEMA-g-BC-CdTe nanohybrids nanofillers could be achievable, which might be of interest for optoelectronic applications.

7

Bacterial-Based Nanocomposites: Hydrophobised Bacterial Cellulose Nanofibril Reinforced Poly−3−Hydroxybutyrate

7.1 Introduction

7.1.1 Aims and objectives

The aim of the work reported in this chapter was to synthesise hydrophobised bacterial cellulose (BC) nanofibrils using a "grafting from" approach; radicals were created on the surfaces of BC by a cerium oxidation and subsequently the free radical grafting polymerisation (FRGP) of a hydrophobic caprolactone-based macromonomer was carried out from the surfaces of BC nanofibrils in an aqueous medium. Another aim was to produce an entirely bacterial-based nanocomposites composed of biodegradable poly-3-hydroxybutyrate (PHB) biopolymer matrix and hydrophobised BC nanofibrils by solution-casting technique.

The objectives of the work reported in this chapter were:

- To investigate the implications of FGRP reaction on the chemical composition and physical properties of hydrophobised BC nanofibrils as function of the concentration of reagents and the duration of the FRGP reaction.

- To characterise the degree of hydrophobicity of hydrophobised BC nanofibrils attained after FRGP reaction using contact angle measurements.
- To assess the thermal properties and mechanical performance of hydrophobised BC nanofibril reinforced PHB nanocomposites as a function of the nanofiller content (*i.e.*, wt.%) and the degree of hydrophobicity of hydrophobised BC nanofibrils reinforcing the PHB matrix.

The present chapter is composed of 5 parts: literature review, experimental methodology, characterisation of hydrophobised BC nanofibrils (PCLMA-g-BC), characterisation of PCLMA-g-BC nanofibril reinforced PHB (PCLMA-g-BC/PHB) nanocomposites and conclusions. The following sections review the various types of nanocomposite systems reinforced with cellulosic nanofillers, the recent reports on BC-based nanocomposites, the different approaches and chemistries employed to functionalised cellulosic materials and the microbiological aspects and the properties of biosynthesised biopolymers namely, polyhydroxyalkanoates. Section 7.2 describes the methodology used to synthesise hydrophobised BC (PCLMA-g-BC) nanofibrils and to manufacture PCLMA-g-BC/PHB nanocomposites by solution-casting. The properties of PCLMA-g-BC nanofibrils are analysed and discussed in Section 7.3. Then, the thermal characterisation and mechanical properties of the PCLMA-g-BC/PHB nanocomposites will be discussed in Section 7.4. The final Section 7.5 with the conclusions on the work presented, which is followed by suggestions for future work and application development.

The motivation for the hydrophobicity of BC nanofibrils via FRGP reaction was to achieve both the dispersion and steric stabilisation of a hydrophobised BC nanofibrils in apolar solvents. Subsequently, to prepare nanocomposites composed of hydrophobic PHB matrix reinforced with hydrophobised BC nanofibrils and demonstrate to the effective reinforcement of the PHB matrix.

7.1.2 Introduction to renewable-based nanocomposites reinforced with cellulosic nanofillers

According to the International Union of Pure and Applied Chemistry (I.U.P.A.C.)[374], a nanocomposite is defined as a material in which at least one type of phase domain is a continuous phase and another phase has at least one dimension of the order of nanometers. Similarly, Schadler *et al.*[375] defined the polymer nanocomposites as polymer matrix composites in which the nanofillers are less than 100 nm in at least one dimension.

Herein, the nanocomposites refer to thermoplastic polymers reinforced with nanosized polysaccharide−based nanofillers having a high aspect ratio, which form a percolated network within the matrix, thus leading to an enhancement of the mechanical properties of these nanocomposites [29].

As early as 1995, Favier *et al.* [376] were the first to report the preparation of polymer nanocomposites reinforced with cellulose whiskers (from *Microcosmus fulcatus* tunicate), which exhibited superior shear modulus below and above the glass transition temperature of the polymer latexes matrices as compared to neat polymer latexes films owing to the attainment of the percolation threshold by the cellulose whiskers in the matrix. Since, there has been considerable advancements made in the preparation and development of nanocomposite systems making the use of a wide variety of polysaccharide-based nanofillers to reinforce polymer matrices such as starch crystals [377,378], cellulose whiskers [379], cellulose crystals [380], cellulose microfibrils [381] and bacterial cellulose [382]. Moreover, the growing environmental awareness has promoted the extensive use of biodegradable or/and renewable polymers to procure the matrices of cellulose-based nanocomposites such as natural rubber [380], starch [383,384], poly(lactide acid) [385,386,387,388] and poly(3-hydroxybutyrate) [389,390,391,392]. Nonetheless, synthetic polymers (*i.e.*, petroleum-derived) has remained significantly utilised over the years in the production of cellulose-based polymer nanocomposites, thus ranging from poly(styrene-co-butyl acrylate) latex [376,379], poly(ethylene glycol) [393], polyaniline [394] and poly(p-phenylene ethynylene) [394], polyvinyl alcohol [395] to poly(caprolactone) [381,396].

Recently, comprehensive reviews by Eichhorn *et al.* [18,397], Hubbe *et al.* [398], Samir *et al.* [29] and Siro *et al.* [19] have surveyed the various aspects of the production of cellulose-based nanocomposites. These included the preparation (by chemical and mechanical treatment) and characterisation (SEM, TEM, atomic force microscopy) of cellulosic nanofillers as well as the characterisation of cellulose-based nanocomposites (mechanical, optical and barrier properties) and also the surface modification of the cellulosic nanofillers for their dispersion in apolar solvents and hydrophobic polymer matrices. It is worth noticing that the production of cellulose-based nanocomposites mainly relied on the solution-casting technique according to the literature reporting on the subject [18,19,29,397,398]. Moreover, the prerequisite for this technique was the thorough dispersion of the cellulose-based nanofillers in the hydrophobic polymer solution, which was a critical step in the production of cellulose-based nanocomposites with enhanced physical properties (*i.e.*, mechanical, optical and barrier), thus requiring

the prior functionalisation of the surfaces of the cellulosic nanofillers by various means, as discussed in later Section 7.1.4.

7.1.3 Bacterial−based nanocomposite materials: state of the art

Comparatively to the nanocomposite systems previously discussed (Section 7.1.2), the literature on BC reinforced polymer nanocomposites is limited. The first nanocomposite materials reinforced with BC were reported by Gindl and Keckes[142], where the nanocomposites were prepared by the infusion of a pellicle of BC with a cellulose acetate butyrate (CAB) solution in acetone and followed by an atmospheric drying. Owing to the preservation of the pristine BC network during their production, these nanocomposites (32%v. of BC) exhibited a tensile strength and Young's modulus of 129 MPa and 5.8 GPa. These tensile properties were somewhat inferior to the tensile strength of 256 MPa and Young's modulus of 17 GPa reported by Yamanaka *et al.*[24] for a dried sheet of pure BC. Nakagaito *et al.*[99] prepared BC pellicle reinforced phenol-formaldehyde (PF) resin nanocomposites. High bending strength and bending Young's modulus of 400 MPa and 28 GPa, respectively, were achieved owing the planar orientation of the BC network obtained through the stacking and compression-moulding of the BC pellicles into sheets. Furthermore, Yano *et al.*[399] produced optically transparent (90% transmittance) BC-based (70%wt. of BC) nanocomposites using either acrylic or epoxy or PF resin to impregnated dried BC sheets. For these nanocomposites, Yano *et al.*[399] reported a tensile strength and Young's modulus of 325 MPa and 21 GPa, respectively. Similar, transparent BC-based nanocomposites have also been produced by Nogi *et al.*[400,401] by impregnation of BC pellicles with thermosetting resins. Trovatti *et al.*[402] prepared BC/acrylic nanocomposites (10%wt. of BC) by casting of water-based suspensions of homogeneously dispersed BC nanofibrils in acrylic copolymer emulsions (butyl acrylate and methyl methacrylate).

Moreover, hydrophilic thermoplastic matrices have been used in the preparation of BC reinforced nanocomposites. In fact, Cai *et al.*[403] produced BC reinforced poly(ethylene glycol) (PEG) nanocomposites, where BC pellicles were immersed in an aqueous PEG solution, which resulted in BC/PEG nanocomposites with a tensile strength and a Young's modulus of 96 MPa and 4.1 GPa, respectively. In the other hand, Brown *et al.*[404]obtained similar BC/poly(ethylene oxide) (PEO) nanocomposites by inserting the water-soluble PEO *in situ* during BC biosynthesis. Then, the BC/PEO pellicles were thoroughly washed to eliminate

the culture media and byproducts and followed by compression-moulding at room temperature.

Recently, the preparation of BC reinforced starch nanocomposites have been reported by Grande *et al.*[405], Martins *et al.*[406], Wan *et al.*[407] and Woehl[408]. However, these BC/starch nanocomposites were produced in various ways, *e.g.*, from a "bottom up" approach where BC was biosynthesised in the presence of swollen starch granules (90%v. of BC)[405], via a solution impregnation of BC pellicles with a starch/glycerin solution (22%wt. of BC)[407], or by aqueous solution-casting and drying of a suspension of enzymatically hydrolysed BC nanofibrils in a starch/glycerin solution (2.5%wt. of BC)[408] or by homogeneous pre-mixing of non-hydrolysed BC nanofibrils with starch/glycerin followed by mixing-compounding procedure (using a Brabender mixer) and injection moulding step (5%wt. of BC)[406].

To date, only Fernandes *et al.*[409] had reported the preparation of BC/chitosan nanocomposites. Fernandes *et al.* prepared the BC/chitosan nanocomposites by casting an aqueous suspension of chitosan containing a homogeneous dispersion of non-hydrolysed BC nanofibrils (up to 40%wt. of BC). These resulting nanocomposites exhibited a transmittance of 80% (between 400-700 nm) with a tensile strength and Young's modulus around 85 MPa and 3.5 GPa, respectively.

In the other hand, BC-based nanocomposites have been produced using hydrophobic thermoplastic matrices such as poly(L-lactic acid) (PLLA) and poly(3-hydroxybutyrate) (PHB). Kim *et al.*[410] and Quero *et al.*[411] prepared transparent BC reinforced PLLA matrix nanocomposites via immersion of BC sheet into a PLLA solution in chloroform followed by ambient drying and by compression-moulding of a BC sheet in between amorphous PLLA films (18%wt. of BC), respectively. Kim *et al.*[410] reported a tensile strength and Young's modulus of 54 MPa and 2.7 GPa, respectively, whereas, Quero *et al.*[411] revealed instead values of 115 MPa and 4 GPa, accordingly. To date, only Lee *et al.*[386] and Tome *et al.*[412] have described the preparation of BC/PLLA nanocomposites using non-hydrolysed BC nanofibrils, which underwent a chemical modification (hydrophobicity) of their surfaces namely, esterification reaction (using acetic, hexanoic and dodecanoic acid) and acetylation reaction (using acetic anhydride), respectively. While the processing routes were significantly different including thermally induced phase separation (TIPS), twin-screw micro-extrusion, pelletisation and compression-moulding for Lee *et al.*[386] and melt-compounding and injection moulding for Tome *et al.*[412], the tensile strength and Young's modulus were respectively, 68 MPa and 2 GPa (5%wt. of BC) for the former authors and 80 MPa and 5 GPa (6%wt. of BC) for the latter

ones. Interestingly, the use of poly(3-hydroxybutyrate) (PHB) and PHB copolymer matrices in the preparation of cellulose-based reinforced PHB nanocomposites have only been described in the last three years[389,390,392], thus accrediting for the very recent interest towards PHB biopolymers. Indeed, Zhijiang *et al.*[392] prepared transparent BC/PHB nanocomposites (around 80% transmittance) by solution impregnation of a BC pellicle (50%wt. of BC) with a PHB solution in chloroform, the resulting tensile strength and Young's modulus were 42 MPa and 2.6 GPa, respectively.

Moreover, it is worth noticing that most of the reports on BC-based nanocomposites described the use of a BC pellicle in which the respective polymer matrices (*i.e.*, CAB, PF, acrylic, epoxy, PEO, PEG, starch, PLLA and PHB) penetrated into either a dried or never-dried BC network prior to some sort of consolidation techniques (*i.e.*, drying, hot-pressing, compression-moulding). Whereas, fewer reports dealt with (non-)hydrolysed BC nanofibrils, which were dispersed in a polymer solution[386,402,406,408,409,412].

7.1.4 Surface hydrophobicity of cellulose-based materials: state of the art

In the development of novel cellulose-based reinforced polymers nanocomposites and strive for improving their mechanical performances, there has been a strong impetus to functionalise the surfaces of various types of cellulose-based reinforcements to ensure the appropriate nanofiller-matrix interactions and their thorough dispersion within the hydrophobic polymer matrices. Recently, Habibi *et al.*[413] reviewed the different chemical modifications attempted on the highly polar surfaces (hydroxyl groups)[414] of cellulose-based reinforcements ranging from noncovalent surface modification (by surfactant adsorption or polymer coating), esterification, etherification, oxidation, silylation to recently, polymer grafting. Furthermore, the esterification, etherification, oxidation and silylation reactions applied onto the surfaces of cellulosic materials have been discussed in-depth elsewhere[415,416,417,418,419,420], as exemplified in Figure 7.1.

In recent years, there has been a significant development in the grafting polymerisation reactions using cellulosic substrates such as whiskers[421], microfibrils[422] and filter paper[421,422] as well as other polysaccharides-based macromolecules[12,423]. In most cases, the grafting polymerisation of organic monomer like $L-$lactic acid[424] or synthetic monomers such as $\epsilon-$caprolactone[425] and methacrylate-based ones[426,427] "to or from" the cellulose backbone aimed at functionalising the surfaces of these cellulosic materials with hydrophobic moieties by taking advantage of the inherent reactivity of the anhydroglucose units (AGU)

of the cellulose backbone[416]. The graft copolymerisation of cellulose consisted into the creation of polymerised branches (*i.e.*, grafts) from various monomer precursors, which were grafted "to or from" the cellulose backbone by means of free radical polymerisation (FRGP) or ring opening polymerisation or living radical polymerisation reaction[51]. Moreover, a comprehensive review by Roy *et al.*[51] illustrated the different methods employed to synthesise grafted copolymers of cellulose via "grafting-to" or "grafting-from" approaches, respectively, as exemplified in Figure 7.2. In a "grafting-to" approach, the graft copolymers of cellulose were synthesised using a pre-synthesised and end-functionalised polymer chain, which reacted with the AGU of cellulose backbone using a coupling agent[13,413]. However, this approach resulted in a low grafting density of the grafted copolymer since the grafting reaction was constrained by a steric hindrance mechanism occurring with the neighboring already grafted polymer chains. Whereas, in a "grafting-from" approach, the graft copolymers of cellulose were synthesised from *in situ* surface-initiated polymerisation, where the activated sites of the cellulose-initiator (*i.e.*, macroinitiator) started the graft polymerisation reaction with the monomers present in the reaction medium, thus resulting in a higher grafting density and enabled to tailor the chain length of the grafted polymers[13,413].

7.1.5 Bacterial−synthesised biopolymers: polyhydroxyalkanoates as advanced materials

Polyhydroxyalkanoates (PHAs) biopolymers are a class of biodegradable linear polyesters, which are gaining attention since already employed in commercial applications ranging from biodegradable commodity products (*i.e.*, bottles, packaging) to regenerative medicine (*i.e.*, cardiovascular stents, bioabsorbable sutures, prosthetic devices)[428]. PHAs are composed of 3, 4, 5, and 6-hydroxyalkanoic acids, as exemplified in Figure 7.3**a**. Moreover, PHAs are categorised as a function of the number of carbon atoms forming the backbone of PHA monomers, short length PHA between C3 to C5, medium length PHA between C6 to C14 and long chain length higher the C14, respectively[429]. Recently, Rai *et al.*[14] and Chanprateep *et al.*[430] had reviewed comprehensively the different composition and structure of PHAs polymers and copolymers, as well as their intrinsic properties.

Poly(3-hydroxybutyrate) (PHB) was first isolated from aerobic spore-forming *Bacillus* in 1923 by Maurice Lemoigne at the Institut Pasteur under the name of "lipide$-\beta-$ hydroxybutyrique"[431,432] (Figure 7.3**b**). The PHB biopolymer is biosynthesised within the cell membrane (*i.e.*, cytoplasm) of a variety of microorganisms[391] (*Pseudomonas, Bacillus,*

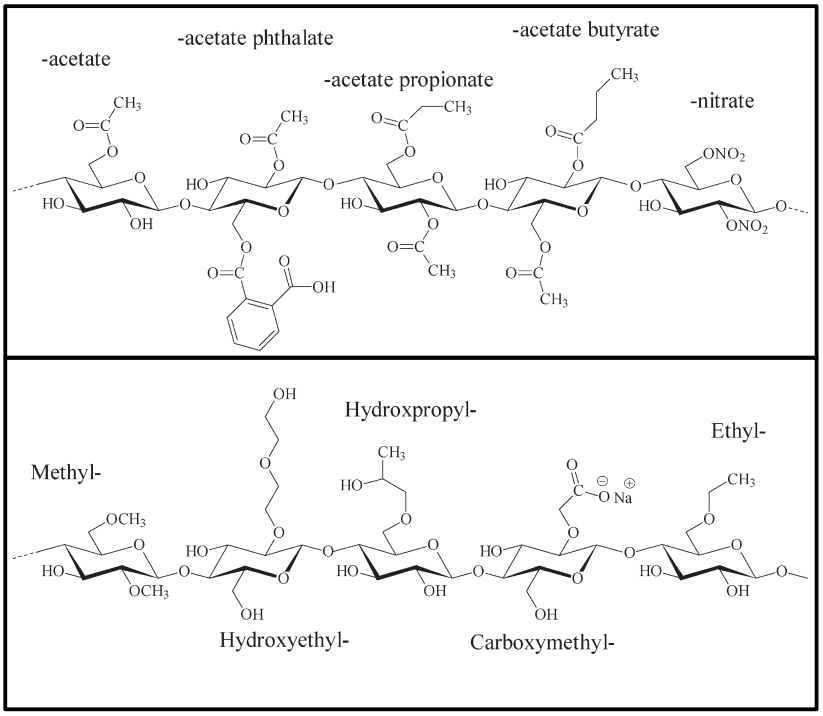


Figure 7.1: Schematic presentation of functionalisation of polysaccharide backbone by esterification reactions (top) and etherification reactions (bottom) (reproduced from [12]).

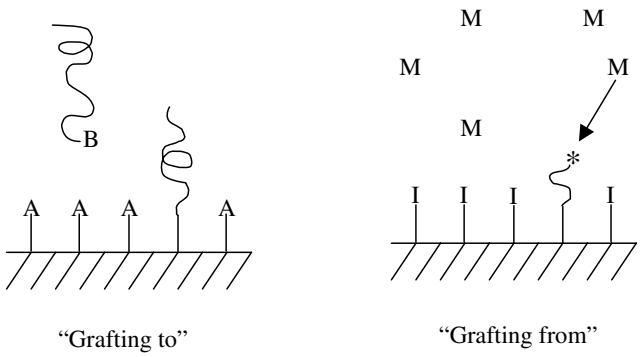


Figure 7.2: Preparation of polymer brushes by "grafting-to" and "grafting-from" (reproduced from [13]).

Ralstonia, Aeromonas, Rhodobacter)[433] and marine prokaryotes (bacteria and archaea)[434]. PHA-producing microorganisms accumulate PHB granules of various nature and molecular weight, which constitute between 80% to 90% of the total dry cell weight[14,434], as seen in Figure 7.3**c**. The production of PHA by the microorganisms was initiated from different environmental stress conditions (*i.e.*, nutritional constraints, nutrient rarefaction)[435] or/and using nutrients such as sugars, lipids, alkanes, alkenes and alkanoic acids[436]. Therefore, the microorganisms synthesised intracellularly granules of PHB or PHB copolymers with respect to the monomer contained in the culture medium[437]. Several fermentation strategies were developed to enhance the yield of PHAs with respect to dry cell weight in a cost-efficient manner such as nutrient feeding strategy, optimisation of culture medium, continuous feeding strategy, mixed or co-culture systems[435,438,439]. Moreover, the PHB granules are accumulated by the microorganisms as a carbon storage compounds, which could at a later time be re-assimilated into the metabolic pathway these microorganisms during intercellular depolymerisation to 3-hydroxybutyric acid[440,441].

In recent years, there has been a growing interest in the *in vitro* synthesis and production of PHAs via enzyme-catalytic routes, which enabled control of the monomer composition and molecular weight of the synthesised PHAs, as well as a greater flexibility on the range of monomeric subunits used in the reaction system for their synthesis[442].

The key property of PHA biopolymers is their readily biodegradation under both aerobic and anaerobic conditions as well as biocompatibility, *in vivo*[443] and *in vitro*[444]. Moreover the rate of degradation, the physical properties (*i.e.*, melting and glass transition temperatures) and mechanical properties of PHA biopolymers were dependent on their monomer composition, chemical structure and molecular weight[14,391]. Nonetheless, PHB is most common biological polyester and exhibits a relatively high degree of crystallinity between 50% to 80%[15]. However, it has also been renown for its brittleness, which was the result of the formation during crystallisation of large scale cracks within the PHB spherulites[15], thus hindering its wide application in materials science.

7.2 Experimental

7.2.1 Materials

Never-dried HCl hydrolysed BC nanofibrils were produced as described in Chapter 3. Caprolactone 2−(methacryloyloxy)ethyl ester (PCLMA), dichloromethane (DCM), tetrahydrofu-

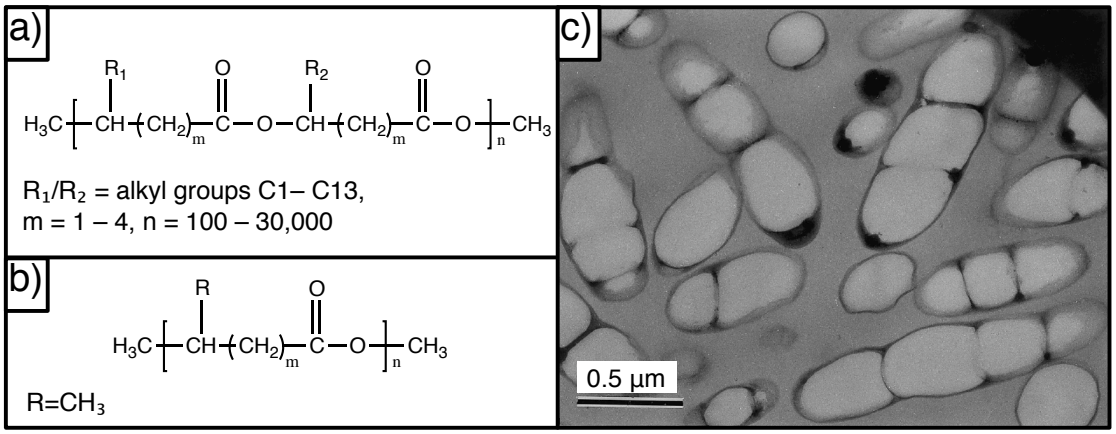


Figure 7.3: **a**) General structure of polyhydroxyalkanoates (adapted from [14]); **b**) Structure of poly(3-hydroxybutyrate); **c**) transmission electron micrograph of thin sections of recombinant *R. eutropha* PHB24 cells containing large amounts (90% of the dry cell weight) of P(3HB-co-5 mol% 3HHx) (reproduced from [15]).

ran (THF), toluene, nitric acid (assay 37%) (HNO_3), aluminium oxide (activated, basic, Brockmann I) and aluminium oxide (activated, neutral, Brockmann I) were purchased from Sigma-Aldrich (UK) and cerium (IV) ammonium nitrate (CAN) purchased from Fluka (UK). Poly(3-hydroxybutyrate) (PHB) biopolymer with a molecular weight (Mw) of 460 kDa was purchased from Biomer (Krailling, Germany). The other reagents, standard grade ethanol and acetone were purchased from VWR (UK). All reagents were ACS grade and used without further purification except for caprolactone 2-(methacryloyloxy)ethyl ester. Deionised H_2O was produced using a NANOpure deionisation system (Barnstead Thermolyne, Dubuque, USA).

7.2.2 Preparation of polycaprolactone 2−(methacryloyloxy)ethyl ester grafted BC nanofibrils

The hydrophobicity of never-dried BC nanofibrils was performed by a "grafting from" approach. The free radical grafting polymerisation (FRGP) of PCLMA from BC nanofibrils was carried out in an acidic aqueous reaction medium, as described in Chapter 6. Briefly, 2.5 g of never-dried BC nanofibrils (250 mg dry-weight equiv.) were placed in a 250 ml 3-neck round bottom flask fitted with a reflux condenser and containing 100 ml of 0.1 M HNO_3 solution, which was homogenised at 30,000 rpm for 1 min. The FRGP reaction was carried

out in N_2 atmosphere at a temperature of $50°C$. Initially the suspension of BC nanofibrils was stirred for 1 h at 250 rpm. Subsequently, the stirring speed was increased to 500 rpm, then 1 mmol (0.6 g) of CAN was added to the suspension to initiate oxidation and therefore radical formation on BC nanofibrils. Approximately 1 min after the start of the BC oxidation began, a concentration of either 1 mmol or 5 mmol of PCLMA macromonomer was injected drop-wise into the reaction medium. Prior to its usage, PCLMA was purified by 2 consecutive filtrations through a basic/neutral alumina column to remove the inhibitor, 2-methylhydroquinone. To tailor the grafting density of PCLMA on BC nanofibrils, FRGP reaction was carried out for 15 min, 30 min, 60 min and 120 min, respectively. After this time an excess of EtOH was added to terminate the reaction. The resulting PCLMA-g-BC nanofibrils were solvent exchanged from H_2O to DCM by successive centrifugations at 15,000 g for 30 min and homogenisations at 30,000 rpm for 2 min in first EtOH, then THF, toluene and DCM, subsequently. This procedure was repeated 2 times for each solvent to ensure a complete removal of unreacted PCLMA as well as physically adsorbed chains of PCLMA homopolymer from the surfaces of BC nanofibrils.

7.2.3 Schematic of free radical grafting polymerisation of PCLMA from BC nanofibrils

The chemical reactions taking place during FRGP of PCLMA from BC nanofibrils were identical to those described previously in Chapter 6 for a different monomer (2-(methylthio)ethyl methacrylate). The initiation by free radical formation generated on BC and subsequently propagation of the macromonomer, is presented in Figure 7.4.

7.2.4 Preparation of PCLMA−g−BC nanofibril reinforced PHB nanocomposites

Bacterial-based nanocomposite films were prepared by solution-casting of PHB solutions in which various concentration of PCLMA-g-BC nanofibrils were thoroughly dispersed. Briefly, a 5 wt.%/v. PHB solution in 10 ml of DCM was prepared by gentle stirring of 0.5 g of PHB at $55°C$. Subsequently, 2.5%, 5%, 10% or 17% of dried equivalent PCLMA-g-BC nanofibrils, which corresponded to 139 mg, 278 mg, 556 mg and 946 mg, respectively of never-dried PCLMA-g-BC nanofibrils, were added to 10 ml of PHB solution. The dispersion of PCLMA-g-BC nanofibrils in PHB solution was achieved initially by a homogenisation at 2,500 rpm for 1 min to break up aggregates of PCLMA-g-BC nanofibrils, which was then followed by a gentle

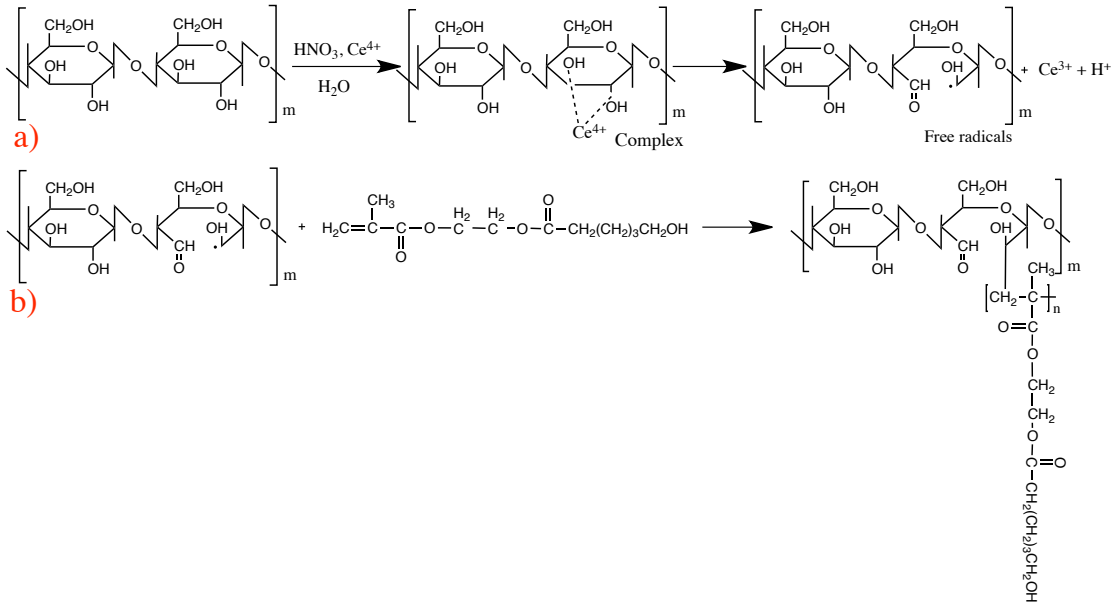


Figure 7.4: Schematic of free radical grafting polymerisation reaction of polycaprolactone 2-(methacryloyloxy) ethyl ester macromonomer from BC nanofibrils. **a**) Initiation phase and free radical formation; **b**) grafting and propagation phase of monomer.

stirring for a further 8 h in a tight sealed glass vessel. To cast bacterial-based nanocomposite films, the PHB/PCLMA-g-BC suspension was poured into a 50 mm diameter glass Petri dish and left covered under ambient conditions for 24 h to let the solvent evaporate. Thereafter, the nanocomposite films were carefully peeled off from the glass surface.

7.2.5 Schematic of preparation of PCLMA-g-BC/PHB nanocomposites

The preparation of bacterial-based nanocomposites is schematically shown in Figure 7.5. Initially, an aqueous suspension of HCl hydrolysed BC nanofibrils (Figure 7.5**a**) was grafted with PCLMA, as described in above section. It was observed that hydrophobised PCLMA-g-BC nanofibrils were flocculating and sedimented during the reaction in the medium when the agitation was stopped (Figure 7.5**b**). Then PCLMA-g-BC nanofibrils were solvent exchanged to DCM (CH_2Cl_2) by the centrifugation/re-dispersion procedure. When suspended in DCM, PCLMA-g-BC nanofibrils were sterically stabilised by the grafted chains of hydrophobic PCLMA (Figure 7.5**c**). Thereafter, PCLMA-g-BC nanofibrils were dispersed thoroughly into a PHB solution prior to solution-casting (Figure 7.5**d**). The PCLMA-g-BC nanofibril

reinforced PHB nanocomposites were translucent indicating a good dispersion of the nano-reinforcement within the biopolymer matrix. Steric stabilisation enabled by the grafting of hydrophobic chains of PCLMA allowed for dispersion of PCLMA-g-BC nanofibrils in various polar and apolar solvents. For instance Araki *et al.*[445] demonstrated the steric stabilisation of cellulose whiskers by grafting poly(ethylene glycol) (PEG) chains to their surfaces using a carboxylation-amidation procedure. Araki *et al.* showed that freeze-dried PEG-grafted cellulose whiskers redispersed in water or chloroform by shaking and sonication. Using an alkaline epoxide ring-opening strategy, Kloser and Gray[446] prepared aqueous suspensions of poly(ethylene oxide) (PEO)-grafted cellulose whiskers, which were sterically stabilised by PEO chains. Heux *et al.*[447] prepared stable suspensions of cellulose whiskers in apolar solvent using surfactant as stabilising agents. The surfactants being adsorbed onto surfaces of cellulose whiskers enabled homogeneous dispersion in various apolar solvents and polymer solutions. Indeed, the dispersion of cellulosic nano-reinforcements in apolar solvents, subsequent to chemical modification of their surfaces enabled at a later stage, their dispersion within apolar polymeric solutions[448,449,450].

7.3 Characterisation of PCLMA−g−BC nanofibrils

As has been discussed in previous Chapter 6 for FRGP of 2-(methylthio)ethyl methacrylate from BC backbone, the synthesised MTEMA-g-BC nanofibrils exhibited significant changes in their crystallographic arrangement, chemical composition and thermal degradation compared to pristine BC nanofibrils. In the following sections regarding the characterisation of PCLMA-g-BC nanofibrils synthesised by FRGP reaction themselves, the author will not reiterate the in-depth discussion made in the previous Chapter 6.

7.3.1 Crystallinity evolution of PCLMA−g−BC nanofibrils

The evolution of the XRD diffractograms of PCLMA-g-BC nanofibrils is presented in Figure 7.6 as a function of duration of FRGP reaction and concentration of PCLMA used during grafting. For a concentration of PCLMA of 1 mmol, the XRD diffractograms of PCLMA-g-BC nanofibrils revealed the characteristic pattern of cellulose type I with an additional diffraction peak located at $2\theta = 28°$. The intensity of the additional peak at 28° intensified with an increase of the duration of FRGP reaction, meanwhile a gradual decrease of degree of crystallinity of the PCLMA-g-BC nanofibrils was observed (Table 7.1). Despite the additional

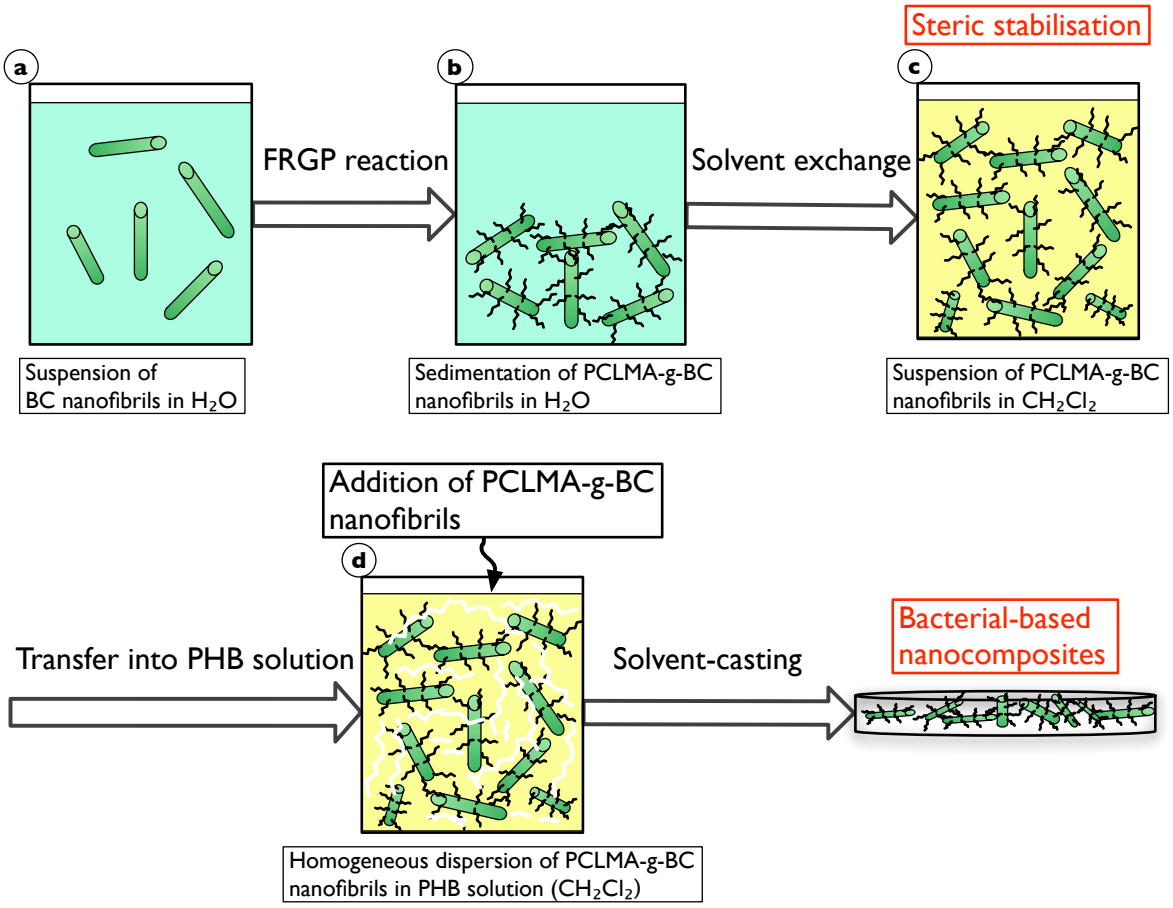


Figure 7.5: Schematic of preparation of PCLMA-g-BC nanofibril reinforced PHB nanocomposite films. **a**) Aqueous suspension of BC nanofibrils; **b**) sedimentation of PCLMA-g-BC nanofibrils in H_2O; **c**) dispersion of PCLMA-g-BC nanofibrils in DCM and **d**) dispersion of PCLMA-g-BC nanofibrils in PHB solution prior to solution-casting.

diffraction peak, the location and crystal sizes of the [101], [10$\bar{1}$] and [002] lattices showed a marginal variation with respect to both concentration of PCLMA and duration of FRPG reaction, as seen in Table 7.1.

For a concentration of PCLMA of 5 mmol, more drastic changes were observed in the XRD diffractograms of PCLMA-g-BC nanofibrils. In fact, the [101] and [10$\bar{1}$] lattices at 2θ equal 14° and 16°, respectively, were blurred with increasing duration of the FRGP reaction. Moreover, the appearance of a broad peak attributed to the amorphous phase (*i.e.*, brush-like chains of PCLMA) around 2θ equal 18° seemed to hamper the peak intensity of the [101] and [10$\bar{1}$] lattices, respectively. Interestingly, at higher concentration of PCLMA the additional peak located at $2\theta = 28°$ was less pronounced than at a lower concentration of PCLMA. It was worth noting that the crystal size and the location of the [002] lattice remained unchanged comparatively to HCl hydrolysed BC nanofibrils (Table 7.1), although from the XRD diffractograms their intensity decreases with increasing duration of the FRGP reaction (Figure 7.6).

Table 7.1: Crystal size of [101], [10$\bar{1}$] and [002] lattice; peak location for [002] lattice and degree of crystallinity for PCLMA-g-BC nanofibrils, respectively, as a function of concentration of PCLMA and duration of the FRGP reaction for a fixed concentration of CAN of 1 mmol.

Samples	PCLMA conc. (mM)	FRGP duration (min)	Crystallite size [101] (nm)	[10$\bar{1}$] (nm)	[002] (nm)	Location [002] (°)	Crystallinity (%)
BC *			5.4	7.0	6.5	22.6	91.0
PCLMA†	1	15	5.0	8.5	7.1	22.6	88.3
-g-BC	1	30	4.9	9.2	7.1	22.9	87.0
	1	60	6.4	9.4	7.0	22.8	83.3
	1	120	4.8	7.5	6.9	22.8	66.8
PCLMA†	5	15	n/a	n/a	7.1	23.0	n/a
-g-BC	5	30	n/a	n/a	7.3	23.1	n/a
	5	60	6.2	8.4	7.2	22.9	n/a
	5	120	6.2	14.9	7.8	22.8	n/a

*HCl hydrolysed BC nanofibrils; † Fixed concentration of CAN of 1 mmol for FRGP reaction of PCLMA.

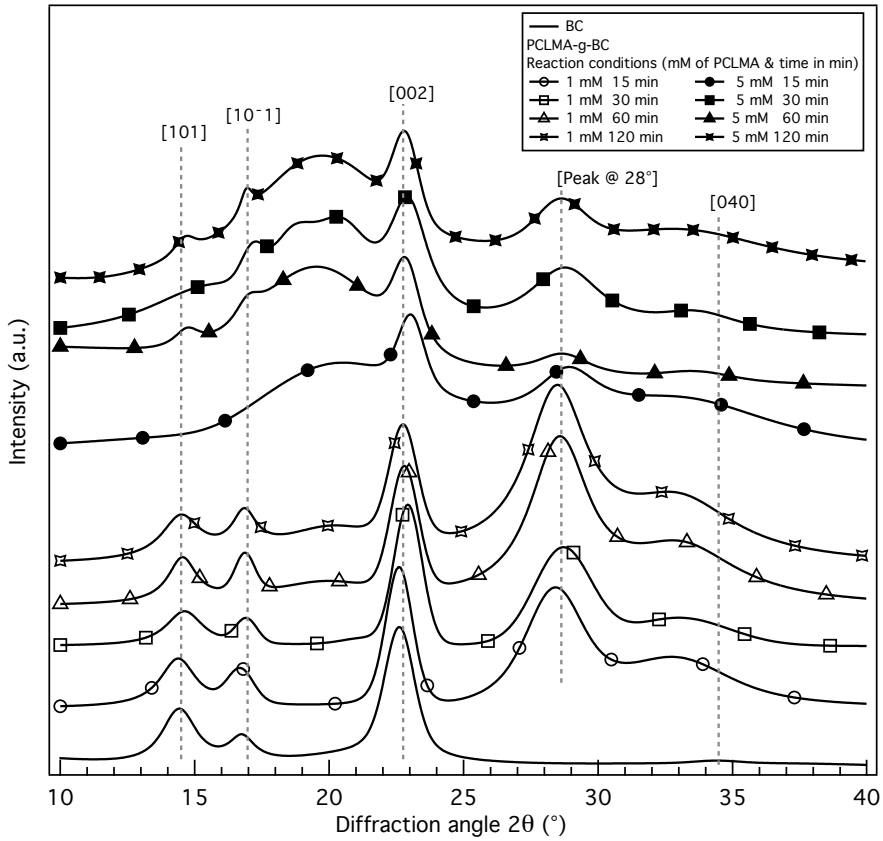


Figure 7.6: X-ray diffractograms of HCl hydrolysed BC and PCLMA-g-BC nanofibrils for various concentration of PCLMA and duration of FRGP reaction. (At a fixed concentration of CAN of 1 mmol).

7.3.2 ATR-FTIR spectroscopy of PCLMA−g−BC nanofibrils

The IR spectra of PCLMA-g-BC nanofibrils are presented in Figure 7.7 as a function of duration of FRGP reaction and concentration of PCLMA employed. The spectra of hydrophobised PCLMA-g-BC exhibited a spectral peak located at 1727 cm^{-1} assigned to the stretching vibration of carbonyl groups constituting the methacrylic group of the polymerised chains of PCLMA, as seen in Figure 7.4. Moreover, the intensity of the spectral peak located at 1727 cm^{-1} gradually increased for either an increase of the duration of FRGP reaction or an increase of the concentration of PCLMA, which suggested that the density of PCLMA chains grafted from the BC backbone was controllable, thus tailoring of the degree of hydrophobicity of PCLMA-g-BC nanofibrils, as discussed in the later Section 7.3.5.

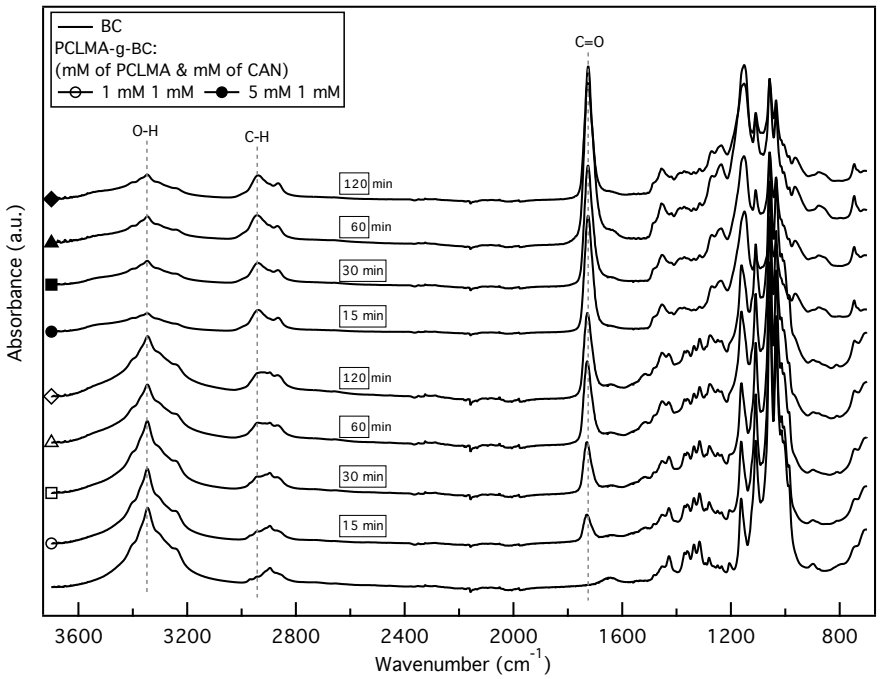


Figure 7.7: ATR-FTIR spectra of HCl hydrolysed BC and PCLMA-g-BC nanofibrils produced using increasing concentration of PCLMA and duration of FRGP reaction (Fixed concentration of CAN of 1 mmol).

Table 7.2: Elemental weight decomposition for HCl hydrolysed BC and PCLMA-g-BC nanofibrils as a function of concentration of PCLMA macromonomer and duration of FRGP reaction using EA.

Samples	PCLMA conc. (mM)	FRGP duration (min)	Elemental fraction %C	%H	%O
BC *			44.55	6.11	49.34
PCLMA-g-BC†	1	15	39.65	4.95	55.39
	1	30	42.05	5.13	52.81
	1	60	40.48	4.34	55.17
	1	120	40.09	4.38	55.53
PCLMA-g-BC†	5	15	50.77	7.11	42.11
	5	30	51.81	7.07	41.11
	5	60	55.24	6.98	37.78
	5	120	54.04	7.65	38.30

*HCl hydrolysed BC nanofibrils; † Fixed concentration of CAN of 1 mmol for FRGP reaction of PCLMA.

7.3.3 Elemental analysis of PCLMA−g−BC nanofibrils

The elemental analysis (EA) of HCl hydrolysed BC and PCLMA-g-BC nanofibrils is presented in Table 7.2 as a function of the duration of FRGP reaction and concentration of PCLMA used. Surprisingly, the elemental weight composition of the PCLMA-g-BC nanofibrils synthesised using a concentration of PCLMA macromonomer of 1 mmol exhibited a decrease of the elemental weight fraction of %C and %H, respectively, compared to the pristine BC nanofibrils. However, this drop suggested that the BC nanofibrils were subjected to depolymerisation and scission of their AGU chains, as it was observed in the previous Chapter 6 for CAN oxidised BC nanofibrils (see Table 6.4). Nonetheless, the elemental weight fraction of %C and %H, respectively, augmented with respect to an increase of the duration of FRGP reaction, thus demonstrating an effective grafting of PCLMA chains from the BC backbone. On the other hand, the PCLMA-g-BC nanofibrils synthesised using a concentration of PCLMA macromonomer of 5 mmol exhibited, as expected a substantial increase in the elemental weight fraction of %C and %H, respectively, which corresponded to an increase of grafting density of PCLMA chains from the BC backbone.

7.3.4 Thermal degradation of PCLMA−g−BC nanofibrils

The thermal degradation under inert N_2 atmosphere of the PCLMA-g-BC nanofibrils is presented in Figure 7.8 as a function of the duration of FRGP reaction and the concentration of PCLMA used. The profile of thermal degradation of the PCLMA-g-BC nanofibrils was in agreement with the one described in previous Chapter 6 for the MTEMA-g-BC nanofibrils (see Table 6.5). The residual char content of PCLMA-g-BC nanofibrils was higher than HCl hydrolysed BC nanofibril and increased with both the concentration of PCLMA (*i.e.* 1 mmol and 5 mmol) used during grafting and increasing duration of the reaction. Indeed, the FRGP of PCLMA from BC backbone drastically impacted the overall degradation behaviour of the PCLMA-g-BC nanofibrils, this was irrespective of the conditions of FRGP reaction used. Generally, an increase of either concentration of PCLMA or duration of the FRGP reaction resulted both, in a lower onset of the degradation and in the reduction of the rate of degradation, while the maximum degradation temperature reached higher value comparatively to HCl hydrolysed BC nanofibrils, as seen in Table 7.8.

Table 7.3: Onset degradation temperature, degradation temperature, weight loss rate and char yield of the thermal degradation process in N_2 atmosphere of PCLMA-g-BC nanofibrils as a function of concentration of PCLMA and duration of FRGP reaction (Fixed concentration of CAN of 1 mmol).

Samples	PCLMA conc. (mM)	FRGP dur. (min)	Onset Temp. ($°C$)	Degrad. Temp. ($°C$)	Wt. loss rate (-)($\%.min^{-1}$)	Char (wt.%)
BC*			304.4	316.8	4.95	0.3
PCLMA †	1	15	231.1	344.9	1.22	21.1
-g-BC	1	30	215.6	346.7	0.98	23.7
	1	60	208.8	346.7	0.64	25.4
	1	120	213.4	339.8	0.63	26.6
PCLMA †	5	15	237.7	387.6	0.99	7.5
-g-BC	5	30	215.0	396.8	0.76	5.2
	5	60	223.8	404.0	0.72	4.1
	5	120	224.5	399.8	0.61	12.3

*HCl hydrolysed BC nanofibrils; † Fixed concentration of CAN of 1 mmol for FRGP reaction of PCLMA.

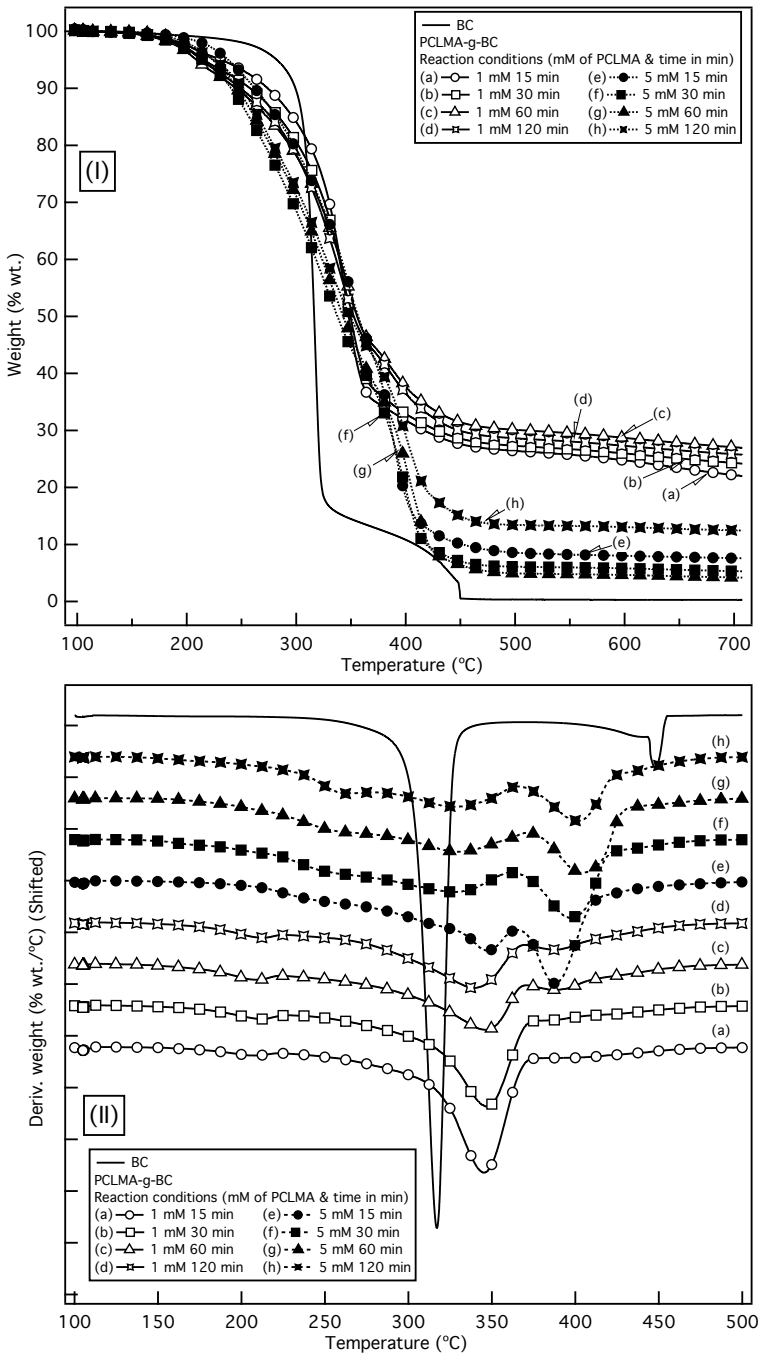


Figure 7.8: I) Thermal degradation behaviour and **II**) derivative weight loss of HCl hydrolysed BC and PCLMA-g-BC nanofibrils produced using various concentrations of PCLMA (*i.e.*, 1 mmol and 5 mmol) and increasing time of FRGP reaction (*i.e.*, 15 min, 30 min, 1 hr and 2 hr) in N_2 atmosphere (Fixed conc. of CAN, 1 mmol).

7.3.5 Surface characterisation of PCLMA−g−BC nanofibrils

The change in hydrophobicity of dried paper-like samples ("nanopaper") composed of HCl hydrolysed BC nanofibrils and PCLMA-g-BC nanofibrils is shown in Figure 7.9 as a function of duration of FRGP reaction and concentration of PCLMA used for FRGP. Contact angle measurements of sessile drops of H_2O carried out on BC nanopapers exhibited a quasi-instantaneous soaking of a H_2O droplet into their surfaces, as a result of the high degree of hydrophilicity of BC nanofibrils and the presence of a meso- and micro-porous network inherent to the nanopaper. The advancing apparent contact angle of PCLMA-g-BC nanopapers revealed a more hydrophobic nature of the surfaces of PCLMA-g-BC nanofibrils as compared to unmodified BC nanofibrils (Figure 7.9). Moreover, the concentration of PCLMA used for the FRGP reaction, 1 mmol and 5 mmol, respectively, resulted in to two distinct regimes (*i.e.*, moderate and high) of hydrophobicity of surfaces of PCLMA-g-BC nanofibrils. For a low concentration of PCLMA (1 mmol), the θ was ranged between 45° and 50° for an increasing reaction time. These θ values were significantly lower than the 80° reported by Biresaw *et al.*[451] for solvent-cast PCL films, thus denoting a non-uniformed surface coverage of PCLMA-g-BC with PCLMA. When higher concentrations of PCLMA (5 mmol) were used, the θ measured increased to value between 67° and 81° for an increasing reaction time, except for a duration of FRGP of 15 min. Therefore, a greater concentration of PCLMA drastically enhanced the degree of hydrophobicity of surfaces of PCLMA-g-BC nanofibrils, as compared to a lower one, which was ascribed to a denser coverage of PCLMA-g-BC surfaces by PCLMA. Habibi *et al.*[396,452] reported θ values between 70° and 80° for poly(ϵ-caprolactone)-grafted cellulose nanocrystals where the cellulose nanocrystals were grafted by ring-opening polymerisation of cyclic ϵ-caprolactone monomer using stannous octoate as catalyst and θ value of 75° for PCL-grafted cellulose nanocrystals; where the grafting of PCL chains of 10,000 $g{\cdot}mol^{-1}$) onto cellulose nanocrystals was performed via isocyanate-mediated reaction. Lonnberg *et al.*[424] also reported a θ of 95° for $\epsilon-$caprolactone ($\epsilon-$CL) grafted cellulose fibres (from Whatman no. 1 filter paper). The grafting reaction was performed by ring-opening polymerisation (ROP) using a tin octoate ($SnOct_2$) as the catalyst.

Photographs of suspensions of HCl hydrolysed BC and PCLMA-g-BC nanofibrils in DCM are shown in Figure 7.10. The suspension of non-modified BC nanofibrils was achieved after solvent exchange and intense sonication. The HCl hydrolysed BC nanofibrils formed a dense percolated network in DCM because of the formation of hydrogen bonds between

nanofibrils[453] which remained stable over time (Figure 7.10**a**, **c**). However, after a solvent exchange to DCM , PCLMA-g-BC nanofibrils formed a homogeneous suspension because of steric stabilisation of nanofibrils and solvation of chains of PCLMA in DCM. The suspension of PCLMA-g-BC nanofibrils partially flocculated over time (*i.e.*, 24 h). This behaviour was associated to heterogeneous coverage of PCLMA chains along the BC nanofibril, thus resulting in decrease of stability of PCLMA-g-BC suspensions.

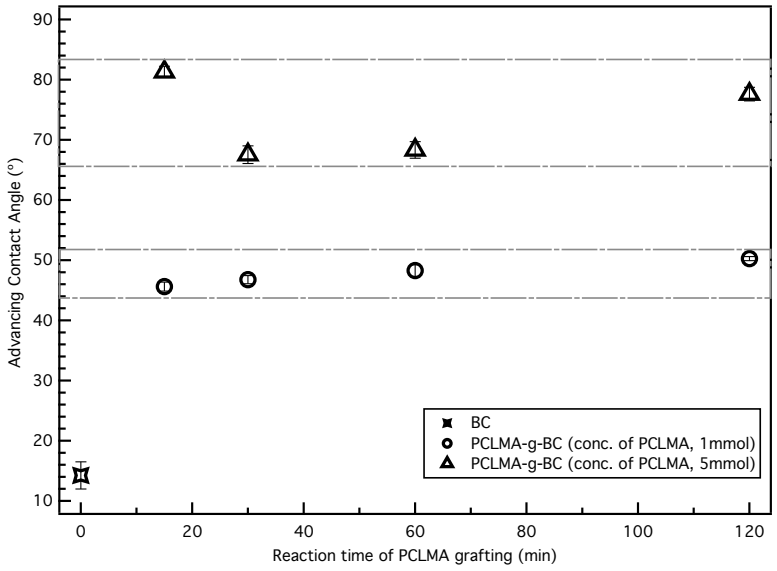


Figure 7.9: Evolution of advancing contact angles on surface of "nanopaper" made from HCl hydrolysed BC and PCLMA-g-BC nanofibrils, respectively, as function of duration of FRGP reaction and concentration of PCLMA used for FRGP reaction.

7.3.6 Surface morphology of PCLMA−g−BC nanofibrils

SEM micrographs of PCLMA-g-BC nanofibrils are presented in Figure 7.11. These PCLMA-g-BC nanofibrils were synthesised using concentrations of PCLMA of 1 mmol and 5 mmol, respectively and a reaction time of 30 min. In both cases, the morphology of the PCLMA-g-BC nanofibrils exhibited a less-defined structure of the individual nanofibrils as well as smoother surfaces than the HCl hydrolysed nanofibrils described in the previous Chapter 6 (see Figure 6.11).

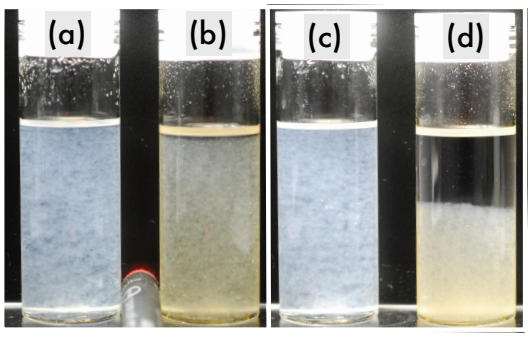


Figure 7.10: Photographs of suspension of (**a**, **c**) HCl hydrolysed BC nanofibrils and (**b**, **d**) PCLMA-g-BC* nanofibrils, respectively, with a concentration of 0.1% wt./v. in dichloromethane. After dispersion using an ultrasonic probe (**a**; **b**) and 24 h after sonication (**c**; **d**). (* conc. of PCLMA, 1 mmol; conc. of CAN, 1 mmol & duration FRGP 30 min)

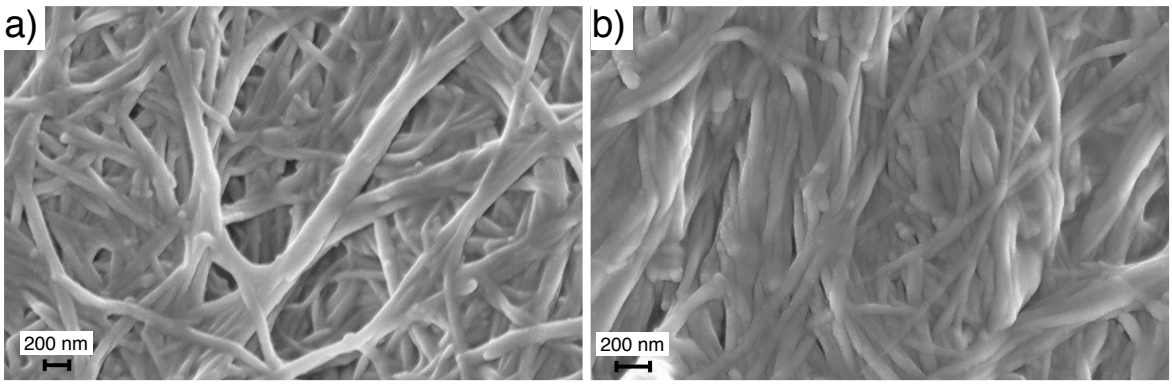


Figure 7.11: SEM micrographs of PCLMA-g-BC nanofibrils produced using a concentration of PCLMA of: **a**) 1 mmol and **b**) 5 mmol, respectively, at a fixed concentration of CAN of 1 mmol and a reaction time of 30 min.

7.4 Characterisation of bacterial-based nanocomposite films with PCLMA-g-BC nanofibrils

The following parts describe the thermal, viscoelastic and mechanical properties of PCLMA-g-BC reinforced PHB nanocomposites as a function of nanofiller content.

7.4.1 Thermal behaviour of PCLMA−g−BC nanofibril reinforced PHB nanocomposites

The thermal behaviour of neat PHB films and PHB nanocomposites containing HCl hydrolysed BC nanofibrils and PCLMA-g-BC nanofibrils, assessed using DSC are shown in Figure 7.12 and their associated properties are summarised in Table 7.4. The second heating curves of the neat PHB and PHB nanocomposites present the conventional endothermic peak associated with a complete melting of the PHB crystallites. The morphology of the melting peaks varied with the presence of nanofillers, the small shoulder located to the left of melting peak became more prominent with increasing nanofiller content, thus denoting the formation of significant smaller spherulites throughout the PHB matrix (Figure 7.12**I**). Similarly, the melting peak of PHB nanocomposites shifted to lower temperatures with increasing nanofiller content, this behaviour suggested as before, the presence of smaller spherulites (Table 7.4). The first cooling curves (cooling profile: high→low temperature) of nanocomposites distinctly showed the presence of a crystallisation peak, which shifted to higher temperatures with an increase of nanofiller content (Table 7.4), thus indicating that nanofillers acted as nucleation sites (*i.e.*, nucleating agents) for the growth of spherulites throughout the PHB matrix. A similar crystallisation behaviour was reported by Pei *et al.*[388] for silylated cellulose nanocrystal (2 wt.% of cellulose) reinforced PLLA matrix. Pei *et al.* ascribed the relative strengthening of the crystallisation peaks and the shift towards higher temperatures of crystallisation to the nucleation effect the homogeneous dispersion of cellulose nanocrystals in the PLLA matrix, which was facilitated by the silane-treatment, performed on the surfaces of the cellulose nanocrystals.

Moreover, the rapid completion of the spherulites growth upon cooling suggested that smaller spherulites were formed. For the neat PHB films the crystallisation peak occurred at a lower temperature than for PHB nanocomposites and occurred over a broad temperature (Figure 7.12**II** & Table 7.4), which denoted a slower growth and a greater size of spherulites, since they were only impinged by the formation of neighbouring spherulites in the bulk. It is

worth noting that neither neat PHB films nor PHB nanocomposites exhibited an identifiable glass transition temperature (T_g) in the DSC thermograms. This lack of visible T_g was also reported by Wong *et al.*[454] and was ascribed to the complete crystallisation of PHB matrix[389,390].

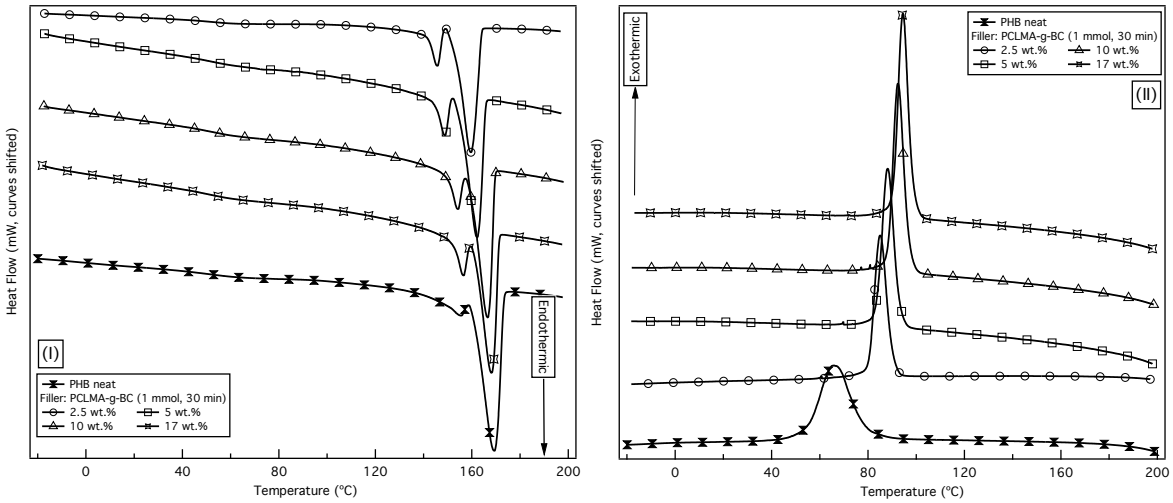


Figure 7.12: DSC thermograms of neat PHB and PCLMA-g-BC/PHB nanocomposites as a function of fraction (%wt.) of reinforcing nanofillers: **I**) second heating profile, **II**) first cooling profile, as described in Chapter 2

7.4.2 Dynamic mechanical analysis of PCLMA−g−BC nanofibril reinforced PHB nanocomposites

The dynamic mechanical analysis for the neat PHB films and various PHB nanocomposites is presented in Figure 7.13 as a function of nanofiller content (%wt.) and reaction conditions used to synthesised the PCLMA-g-BC nanofibrils. The evolution of the storage modulus (E') of the neat PHB films with respect to increase of temperature was typical for a crystalline polymer, where three different regions were identified: the glassy state (below $-25°C$), the mechanical glass transition (approximately between $-25°C$ and $35°C$) and the rubbery plateau (approximately between $35°C$ and $120°C$). As a consequence, the transition across these states with increasing temperature caused the $\tan\delta$ (damping factor) of the neat PHB films to pass through a maximum at $8°C$, thus, characteristic for the relaxation process of polymer chains. Moreover, a sudden drop of E' was observed around $60°C$ owing to a

Table 7.4: Summary of thermal characteristics of PHB nanocomposites reinforced with various fraction (%wt.) of PCLMA−g−BC† nanofibrils (conc. of PCLMA, 1 mmol; conc. of CAN, 1 mmol & duration FRGP, 30 min).

Nanofiller	Nanofiller content (%wt.)	Mech. $T_g{}^{\diamond}$ ($^{\circ}C$)	T_c ($^{\circ}C$)	T_m ($^{\circ}C$)	$\Delta H_f(T_m)$ ($J.g^{-1}$)	$X_c{}^*$ (%)
none		8	66	169	64	43.9
PCLMA	2.5	24	85	168	72	50.3
-g-BC†	5	20	88	167	66	49.6
	10	23	92	162	65	49.2
	17	26	94	160	60	49.5

Glass-rubber transition temperature (T_g), crystallisation temperature (T_c), melting temperature (T_m), associated heat of fusion ($\Delta H_f(T_m)$) and degree of crystallinity (X_c). $T_g{}^{\diamond}$ extracted from maximum $\tan\delta$ peak in Figure 7.13. $X_c{}^*$ determined as previously stated in Chapter 2 (Equation 2.19).

progressive softening of the PHB network induced by a greater mobility of its chains.

As seen in Figure 7.13, the addition of either BC or PCLMA-g-BC nanofibrils into PHB had a strong influence on the viscoelastic response of the various PHB nanocomposites, thus, independently of the nanofiller content and their state of chemical modification. A significant increase of E' over the neat PHB films was observed for the PHB nanocomposites, which denoted a stiffening of the PHB matrix cause by the establishment of a percolated network of BC or PCLMA-g-BC nanofibrils, which in either case restricted the mobility of polymer chains as seen by the increase in T_g. Moreover, the E' measured in glassy state of nanocomposites increased with increasing nanofiller content in the PHB matrix. Comparatively, the increase of E' between BC and PCLMA-g-BC nanofibril reinforced PHB was unarguably higher for those reinforced with the hydrophobic PCLMA-g-BC nanofibrils for an equivalent nanofiller content, thus showing their superior reinforcement capacity over neat PHB films and HCl hydrolysed BC reinforced PHB (Figure 7.13**I** & **III**). In addition, the E' of PHB nanocomposites exhibited only a marginal increase with increasing PCLMA grafting density, *i.e.* with greater hydrophobicity (*e.g.*, synthesised using a conc. of PCLMA of 5 mmol) (Figure 7.13**III** & **V**). Significant changes in the $\tan\delta$ response were observed between the neat PHB films and PHB nanocomposites. First, the intensity of $\tan\delta$ decreased

with increasing nanofiller content within the PHB matrix. Meanwhile, the peak location of $\tan\delta$ shifted to higher temperatures, which implied that the presence of BC or PCLMA-g-BC nanofibrils in the composition of PHB nanocomposites restricted the mobility of the polymer chains, thus increasing the thermomechanical stability of these PHB nanocomposites comparatively to the neat PHB films (Table 7.4). Secondly, comparison of $\tan\delta$ peaks between BC and PCLMA-g-BC nanofibrils reinforcing PHB nanocomposites, respectively, showed that the former exhibited a higher peak intensity of $\tan\delta$ than the latter one, which ascribed that the hydrophilic BC nanofibrils achieved lesser nanofiller-matrix interfacial interactions and load transfer than the hydrophobic PCLMA-g-BC nanofibrils (Figure 7.13**II** & **IV**). The hydrophobic chains of PCLMA grafted from the BC backbone during FRGP reaction of PCLMA-g-BC nanofibrils conferred a good affinity (*i.e.*, compatibility) with the hydrophobic network of PHB biopolymer. Moreover, comparison of peak intensity of $\tan\delta$ between PCLMA-g-BC nanofibrils synthesised using different concentrations of PCLMA, 1 mmol and 5 mmol, which exhibited advancing θ of 46° and 67°, respectively, revealed no further reduction in the peak intensity of $\tan\delta$ for their respective nanofiller content (Figure 7.13**IV** & **VI**). This suggested that a balance was reached between the nanofiller-matrix interfacial interaction and the degree of hydrophobicity of the reinforcing nanofillers in the PHB matrix.

Study of nanocomposite systems composed of poly(caprolactone) (PCL)-grafted cellulose nanocrystals (extracted from ramie fibres) reinforcing a PCL matrix reported by Habibi *et al.*[396,452] were in agreement with the thermomechanical behaviour described above. Roohani *et al.*[455] prepared cellulose whisker reinforced poly(vinyl alcohol) (PVA) matrix nanocomposites, for which Roohani *et al.* also observed a decrease in the magnitude of $\tan\delta$ peak with increasing weight fraction of cellulose whiskers. The change in damping properties of these PVA nanocomposites was ascribed to a decrease in the number of mobile units of polymer chains participating in the relaxation process since they were impeded by cellulose whiskers. Tingaut *et al.*[387] hydrophobised cellulose microfibrils (from wood pulp) by acetylation (using acetic anhydride) to reinforce a poly(lactic acid) (PLA) matrix. Surprisingly, Tingaut *et al.*[387] reported a decrease of T_g (measured from DMA) and a lowering of E' for PLA nanocomposites reinforced with hydrophobised cellulose microfibrils (*i.e.*, 17% acetylated) compared to PLA nanocomposites composed of unmodified cellulose microfibrils. Furthermore, Tingaut *et al.*[387] suggested that the degree of hydrophobicity and nanofiller content

needed to be adjusted to achieve adequate filler-matrix interactions in the PLA nanocomposites.

7.4.3 Mechanical properties of PCLMA−g−BC nanofibril reinforced PHB nanocomposites

The tensile strength and Young's modulus of bacterial-based nanocomposites are presented in Figure 7.14 and 7.15, as a function of nanofiller content and the state of chemical modification of these nanofillers. Tensile tests revealed that an addition of BC nanofibrils into a PHB matrix improved the tensile properties of PHB nanocomposites, demonstrating the reinforcing effect of BC nanofillers within the PHB matrix, irrespective of their state of chemical modification comparatively to neat PHB films. The tensile strength of PHB reinforced with HCl hydrolysed BC nanofibrils varied slightly with an increase of nanofiller content. For instance, the tensile strength of these nanocomposites increased by 45% and 24% for a nanofiller content (*i.e.*, HCl hydrolysed BC nanofibrils) of 2.5 wt.% and 17 wt.%, respectively. This suggested that the hydrophilic BC nanofibrils were poorly dispersed within the hydrophobic PHB matrix although an initial reinforcing effect of BC nanofibrils in the PHB matrix was initiated because of the formation of a percolated network of BC via hydrogen bonding[381], nonetheless, there was a poor adhesion between the nanofillers and the PHB matrix. In the case of PHB reinforced with PCLMA-g-BC nanofibrils (*i.e.*, conc. of PCLMA, 1 mmol; conc. of CAN, 1 mmol & duration FRGP, 30 min) the tensile strength increased gradually with increasing of nanofiller content. However, it reached its highest value for a nanofiller content of 10 wt.%, which corresponded to an increase of 101% as compared to the neat PHB film (22.7 MPa). However, significantly for increasing the PCLMA-g-BC loading fraction to 17 wt.% caused the tensile strength to decline significantly. Surprisingly, the tensile strength of PHB nanocomposites reinforced with more hydrophobic PCLMA-g-BC nanofibrils (*i.e.*, conc. of PCLMA, 5 mmol; conc. of CAN, 1 mmol & duration FRGP, 30 min) rose only by 60% for a nanofiller content of 10 wt.% comparatively to the neat PHB films (22.7 MPa). These findings ascribed that for the PCLMA-g-BC/PHB nanocomposite systems investigated here, the optimal tensile strength was attained for a nanofiller content of 10 wt.% using mildly hydrophobic PCLMA-g-BC nanofibrils (*i.e.*, with a CA of 46°). Accordingly, Lin *et al.*[403] reported that the optimal tensile strength of PLA reinforced with hydrophobised cellulose whiskers was attained for a nanofiller content of 8 wt.%, thus accounting for an increase of tensile strength by 85.5% in comparison with the neat PLA films

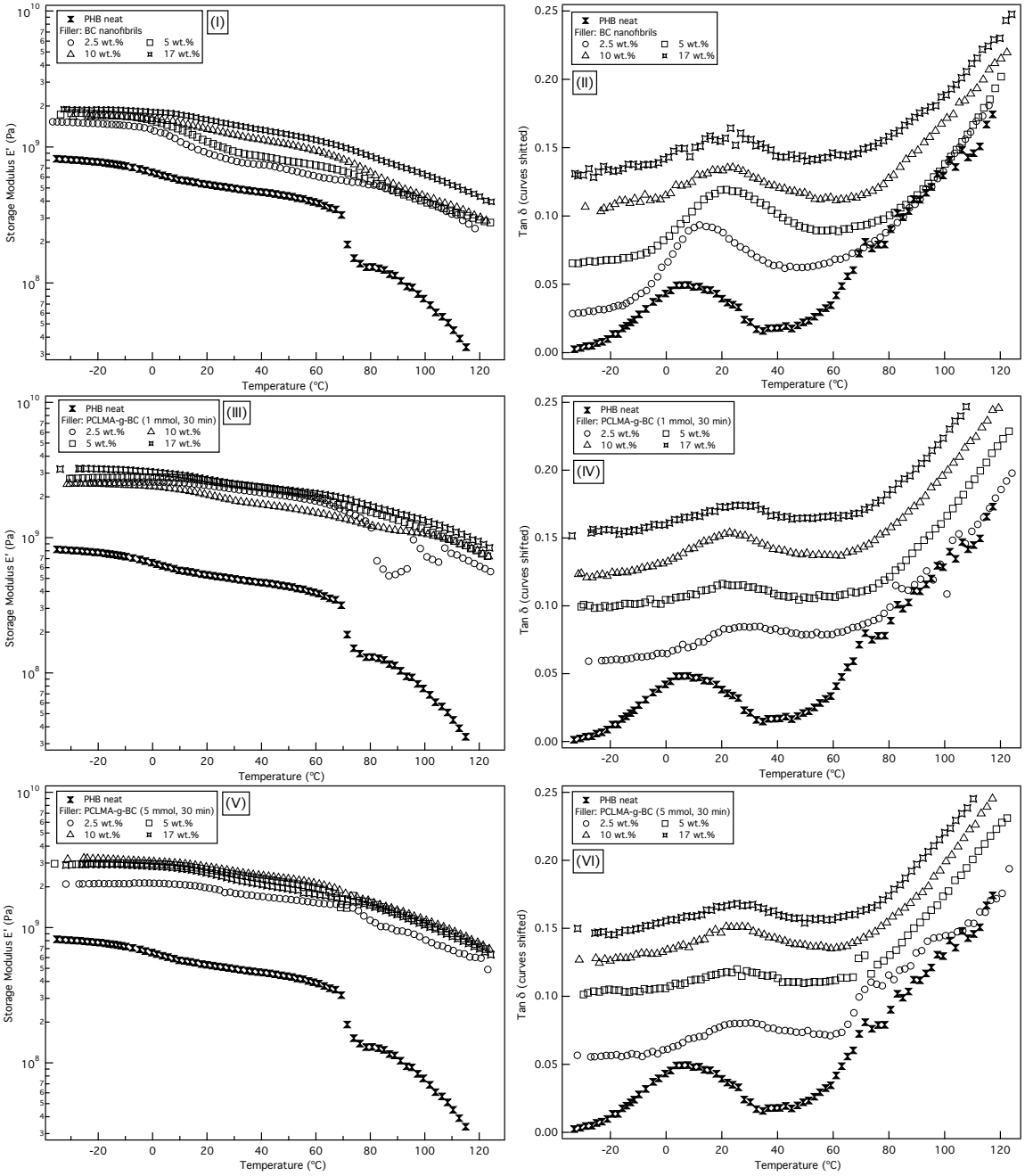


Figure 7.13: E′ and tan δ for neat PHB film and PHB nanocomposites as a function of nanofiller content and temperature: **I** & **II**, HCl hydrolysed BC nanofibrils; **III** & **IV**, PCLMA-g-BC nanofibrils (conc. of PCLMA, 1 mmol; conc. of CAN, 1 mmol & duration FRGP, 30 min); **V** & **VI**, PCLMA-g-BC nanofibrils (conc. of PCLMA, 5 mmol; conc. of CAN. 1 mmol & duration FRGP, 30 min)

(40.7 MPa). In their investigation, Lin *et al.* prepared the hydrophobic cellulose whiskers (from cotton linters) by surface-grafting of poly(caprolactone) (PCL) via microwave-assisted ring-opening polymerisation. Similarly, Tome *et al.*[412] reported the gradual improvement of both tensile and Young's modulus of PLA reinforced with acetylated BC nanofibrils (*i.e.*, CA of 64°) up to a nanofiller content of 6 wt.%. Those tensile properties were higher than the ones for neat PLA films and PLA nanocomposites reinforced with unmodified BC nanofibrils for an identical nanofiller content.

Moreover, the Young's modulus of PHB nanocomposites improved gradually with increasing nanofiller content (Figure 7.15). PHB reinforced with mildly hydrophobised PCLMA-g-BC nanofibrils exhibited the highest Young's modulus, increasing by 170% and 176% for a nanofiller content of 10 wt.% and 17 wt.%, respectively, as compared to neat PHB films with a Young's modulus of 1.5 GPa. Comparatively, the Young's modulus of PHB reinforced with very hydrophobic PCLMA-g-BC nanofibrils was markedly lower than those reinforced with mildly hydrophobic ones and even inferior than PHB nanocomposites reinforced with hydrophilic BC nanofibrils for a nanofiller content of 17 wt.%.

As a result, it is speculated that the under-performance of PHB reinforced with the most hydrophobic PCLMA-g-BC nanofibrils (*i.e.*, θ of 67°) could be attributed to the high density of chain of PCLMA on their surface, which created a hydrophobic shell surrounding the BC backbone, thus hindering the inter-penetration of polymer chains between the PHB and the PCLMA-g-BC nanofibrils. Moreover the decrease of the degree of crystallinity of these PCLMA-g-BC nanofibrils (see Section 7.3.1) and the much greater grafting density resulted in a lower loading with stiff BC, which may also have impaired the reinforcing capability of these PCLMA-g-BC nanofibrils in the PHB.

7.5 Conclusions

A novel strategy for the hydrophobicity of never-dried BC nanofibrils was demonstrated as well as the preparation of entirely bacterial-based nanocomposite, where hydrophobised BC nanofibril reinforced effectively a PHB matrix.

The hydrophobised BC nanofibrils were synthesised by FRGP of hydrophobic caprolactone 2-(methacryloyloxy)ethyl ester macromonomer from the BC backbone using a CAN redox initiation in an aqueous medium containing a suspension of PCLMA. Control over the concentration of reagents and the duration of FRGP enabled to tailor the hydrophobicity of

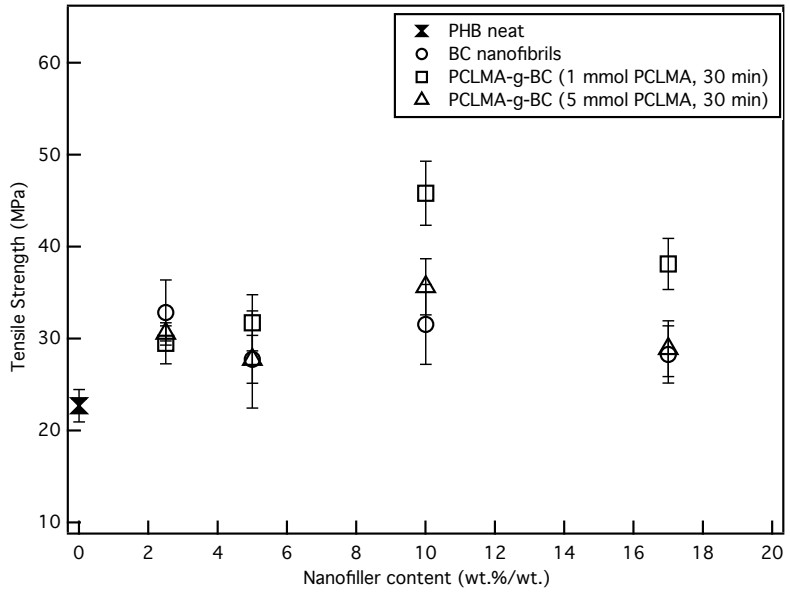


Figure 7.14: Tensile strength of bacterial-based nanocomposites reinforced with HCl hydrolysed BC and PCLMA-g-BC nanofibrils as a function of nanofiller content and state of chemical modification.

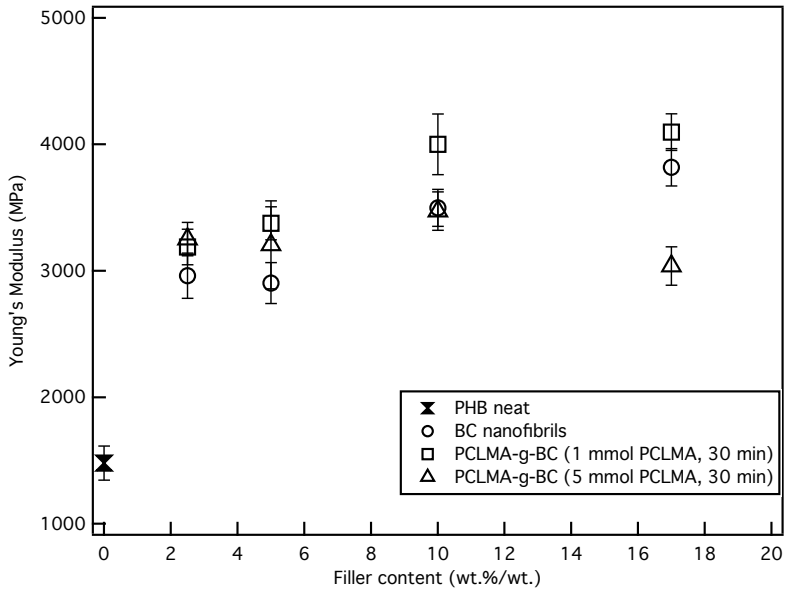


Figure 7.15: Young's modulus of bacterial-based PHB reinforced with HCl hydrolysed BC and PCLMA-g-BC nanofibrils as a function of nanofiller content and state of chemical modification.

PCLMA-g-BC nanofibrils, as expressed by variation of the water contact angle. Accordingly, an increase in the concentration of reagents or/and the duration of FRGP reaction resulted in a higher density of grafted PCLMA chains from the BC surface as deduced from the increase of the IR band assigned to the carboxyl groups. Likewise, the variations of thermal stability of PCLMA-g-BC nanofibrils were inherent characteristics resulting from an effective FRGP.

PCLMA-g-BC reinforced PHB with increasing nanofiller content were prepared by solution-casting of a dispersion of hydrophobised PCLMA-g-BC nanofibrils within a PHB solution. The use of hydrophobised nanofillers to reinforce the PHB matrix led to the improvements of both storage modulus and tensile properties of PCLMA-g-BC/PHB nanocomposites compared to the neat PHB films. The overall improvement of both thermomechanical and mechanical properties of these nanocomposites was attributed to improved nanofiller-matrix interfacial interaction, thus promoting an effective load transfer between the PHB and PCLMA-g-BC nanofibrils. Moreover, the tailoring of the degree of hydrophobicity of PCLMA-g-BC nanofibrils and the nanofiller content in the PHB matrix influenced the mechanical properties of PHB nanocomposites.

7.6 Future work

The future work should investigate the oxygen barrier properties of PCLMA-g-BC/PHB nanocomposites as a function of nanocomposite thickness and nanofiller content since these nanocomposites could be used in packaging applications owing to their renewable sourcing (*i.e.*, microorganisms) and the inherent biodegradability of the individual elements constituting them. By an adaptation of the solution-casting procedure, these PCLMA-g-BC/PHB nanocomposites will be shaped into small diameter tubes with a tailored wall-thickness and length. The use of bacterial-based nanocomposite tubings is currently being investigated in cardiovascular applications[456,457], vascular implants (*i.e.*, stents) owing to their mechanical, biodegradable and biocompatible properties.

8

General Conclusions

The aim of the research presented in this thesis was to investigate the use of bacterial cellulose for a wide range of innovative (nano-) materials. Bacterial cellulose, an extracellular product biosynthesised by cellulose-producing *Gluconobacter xylinus* strain has recently gained tremendous interest as an alternative source of cellulose owing to its outstanding chemical, physical and mechanical properties. Indeed, bacterial cellulose possesses the chemical composition and crystallographic structure of native cellulose originating from plants but, it is genuinely biosynthesised into individual nanofibrils (nano-sized fibrils), which are subsequently agglomerating during fermentation to form a hydrogel pellicle having an excellent water holding capacity. The main outcomes of the research described in the thesis are described, as follows.

8.1 Biosynthesis of bacterial cellulose by *Gluconobacter xylinus* BPR2001

The scaling up of *Gluconobacter xylinus* BPR2001 fermentation in stirred-tank bioreactor to increase the yield of bacterial cellulose production comparatively to culture in Erlenmeyer flasks was achieved. To further increase the bacterial cellulose yield, additional stainless-steel meshes located along the vessel wall and stirring shaft were introduced. These new surfaces in the bioreactor allowed for anchoring of *Gluconobacter xylinus* cells during the fermentation cycle, which resulted in a drastic increase of the bacterial cellulose biosynthesised.

8.2 Surface modification of sisal by bacterial cellulose coating and preparation of hierarchical all-cellulose composites

Bacterial cellulose was coated onto sisal fibres during the fermentation of *Gluconobacter xylinus* in a stirred-tank bioreactor. The effective deposition and immobilisation of a dense bacterial cellulose layer by extensive hydrogen bonds on the fibre surface was assessed and compared to characteristics of genuine sisal fibres.

Hierarchical all-cellulose composites, produced by reinforcing a regenerated cellulose matrix with bacterial cellulose coated sisal fibres (fibre weight fraction of 40 wt./wt.%) were produced. The concept of hierarchical all-cellulose composites consisted in combining cellulosic materials of different length scales, where, the regenerated cellulose matrix with tailored degree of crystallinity was used as a molecular binder, the sisal fibres as a micro-size reinforcement and the bacterial cellulose coating on the fibres as a nano-reinforcement. The matrix of hierarchical all-cellulose composites consisted of a self-reinforced regenerated cellulose, which was prepared by dissolution of microcrystalline cellulose in dimethylacetamide/lithium chloride and subsequent regeneration in water. Control over the dissolution time enable to tailor the fraction of undissolved cellulose crystals reinforcing a cellulose phase, which dictated the mechanical properties and response of the matrix alone. These, hierarchical all-cellulose composites reinforced by bacterial cellulose coated sisal fibres exhibited better mechanical properties than those reinforced by genuine sisal fibres, where both tensile strength and Young's modulus were increased by 12% and 15%, respectively. Moreover, hierarchical all-cellulose composites reinforced by bacterial cellulose coated sisal fibres presented an improved quality of the sisal fibres/regenerated cellulose matrix interface.

8.3 Preparation of bacterial cellulose based porous cryogel microspheres

Highly porous cryogel microspheres were produced by dissolution and regeneration of bacterial cellulose. The formation of cryogel microspheres from a bacterial cellulose solution was performed by fast-freezing of drops of a BC solution in liquid N_2, which fixed the microsphere shape prior to regeneration in water. The bacterial cellulose cryogel microspheres obtained after freeze-drying of regenerated bacterial cellulose gel possessed a high porosity with a distinctive morphology of the cellulose network consisting of partially dissolved and regenerated

bacterial cellulose. Both porosity and morphology of the cryogel microspheres varied with respect to the dissolution time in dimethylacetamide/lithium chloride cosolvent as well as concentration of the bacterial cellulose solution.

8.4 Thioether functionalisation of bacterial cellulose and synthesis of bioinorganic nanohybrids

An innovative synthesis route to functionalise bacterial cellulose nanofibrils with thioether moieties was developed using a "grafting from" approach. Radicals sites were created on the surface of bacterial cellulose by redox reaction between bacterial cellulose and cerium ammonium nitrate, subsequently, free radical grafting polymerisation of a monomer containing thioether moieties was initiated from the surfaces of bacterial cellulose nanofibrils. The reagent concentrations and reaction conditions of the free radical polymerisation influenced the length of the grafted homopolymer, and thus, the physical and thermal properties of thioether-functionalised bacterial cellulose nanofibrils varied accordingly.

Bioinorganic nanohybrid materials were prepared by decorating the thioether-functionalised bacterial cellulose nanofibrils with gold nanoparticles. *In situ* reduction of Au^{3+} solution into elemental gold nanoparticles in the presence of thioether-functionalised bacterial cellulose nanofibrils was chosen to obtain bacterial cellulose based bioinorganic nanohybrids. The gold nanoparticles chemisorbed onto the pendant thioether moieties grafted from the bacterial cellulose nanofibrils. Moreover, these gold functionalised bioinorganic nanohybrids exhibited surface plasmon resonance bands corresponding to those of colloidal suspensions of gold nanoparticles.

Alternatively, cadmium telluride quantum dots were used to decorate thioether-functionalised bacterial cellulose nanofibrils to prepare bioinorganic nanohybrids possessing optoelectronics properties. The nanohybrids were prepared by precipitation of quantum dots from suspension onto thioether-functionalised bacterial cellulose nanofibrils, followed by ligand transfer between the thioglycolic acid capped cadmium telluride quantum dots and the pendant thioether moieties grafted from the bacterial cellulose nanofibrils. Moreover, the cadmium telluride quantum dot functionalised bacterial cellulose exhibited a surface plasmon resonance band and photoluminescence properties when irradiated with UV light similar to that of a colloidal suspension of cadmium telluride quantum dots.

8.5 Hydrophobisation of bacterial cellulose nanofibrils and processing of bacterial-based nanocomposites

The synthesis of hydrophobised bacterial cellulose nanofibrils was performed using a "grafting from" approach previously developed for thioether functionalised bacterial cellulose nanofibrils. In that instance, an hydrophobic caprolactone-based macromonomer suspended in a aqueous medium was grafted from the radical sites created by the redox reaction on the bacterial cellulose nanofibrils via a free radical grafting polymerisation reaction. The reaction conditions of the free radical grafting polymerisation reaction allowed to tailor the degree of hydrophobicity of the synthesised polycaprolactone grafted bacterial cellulose nanofibrils. Similarly, the physical and thermal properties of this grafted copolymer were investigated.

Entirely bacterial-based nanocomposites composed of hydrophobised bacterial cellulose nanofibrils reinforcing a poly-3-hydroxybutyrate matrix were produced by solution casting. The effect of the degree of hydrophobicity of polycaprolactone grafted bacterial cellulose nanofibrils and the nanofiller content in the poly-3-hydroxybutyrate matrix were related respectively to the thermal, thermomechanical and mechanical properties of the bacterial-based nanocomposites. The mechanical properties of polycaprolactone grafted bacterial cellulose nanofibrils reinforced poly-3-hydroxybutyrate nanocomposites with a nanofiller content of 10 wt./wt.% exhibited an increase for both tensile strength and Young's modulus of 101% and 170%, respectively, as compared to the mechanical properties of the neat poly-3-hydroxybutyrate films. This demonstrated the effective reinforcement capacity of polycaprolactone grafted bacterial cellulose nanofibrils to reinforce a poly-3-hydroxybutyrate matrix.

8.6 Concluding remarks

The versatile use of bacterial cellulose was demonstrated in this thesis. Various usages, which included improvement of the interface quality of natural fibre/regenerated cellulose matrix composites, the preparation of macroporous micrometre-sized beads (*i.e.*, cryogels), the synthesis of functional bioinorganic nanohybrids composed of gold nanoparticles or quantum dots chemisorbed to thioether functionalised bacterial cellulose nanofibrils and the production of entirely bacterial-based nanocomposites reinforced with hydrophobised bacterial cellulose nanofibrils were investigated. Indeed, bacterial cellulose exhibits outstanding physical and chemical properties, which result from its intrinsic nano-sized structure subsequent to

bacterial biosynthesis. In conclusion, bacterial cellulose is increasingly becoming a favoured choice of raw material for the development of advanced renewable (nano-) materials.

References

[1] A Moores and F Goettmann. **The plasmon band in noble metal nanoparticles: an introduction to theory and applications**. *New Journal of Chemistry*, **30**(8):1121–1132, 2006. xi, 9

[2] Dieter Klemm, Brigitte Heublein, Hans-Peter Fink, and Andreas Bohn. **Cellulose: fascinating biopolymer and sustainable raw material**. *Angew Chem Int Ed Engl*, **44**(22):3358–93, 2005. xi, 1, 23, 25, 29

[3] S Salmon and SM Hudson. **Crystal morphology, biosynthesis, and physical assembly of cellulose, chitin, and chitosan**. *Polymer Reviews*, **37**(2):199–276, 1997. xi, 22, 23

[4] C Tokoh, K Takabe, M Fujita, and H Saiki. **Cellulose synthesized by Acetobacter xylinum in the presence of acetyl glucomannan**. *Cellulose*, **5**(4):249–261, 1998. xi, 24, 25

[5] C. H. Haigler. *Cellulose chemistry and its applications*, chapter The functions and biogenesis of native cellulose, pages 30–83. Ellis Horwood Ltd., Chichester, 1985. xii, 26

[6] T Heinze and A Koschella. **Solvents applied in the field of cellulose chemistry: a mini review**. *Polímeros: Ciência e Tecnologia*, **15**(2):84–90, 2005. xii, 49, 50

[7] M John and S Thomas. **Biofibres and biocomposites**. *Carbohydrate Polymers*, **71**(3):343–364, 2008. xii, 47, 49, 51

[8] A Bismarck, I AranberriAskargorta, J Springer, T Lampke, B Wielage, A Stamboulis, I Shenderovich, and HH Limbach. **Surface characterization of flax, hemp and cellulose fibers; Surface properties and the water uptake behavior**. *Polym. Compos.*, **23**(5):872–894, 2002. xii, 49, 51

[9] Alain Pierre and Gérard Pajonk. **Chemistry of aerogels and their applications**. *Chem Rev*, **102**(11):4243–4266, 2002. xiv, 82, 84, 85

[10] Falk Liebner, Emmerich Haimer, Martin Wendland, Marie-Alexandra Neouze, Kerstin Schlufter, Peter Miethe, Thomas Heinze, Antje Potthast, and Thomas Rosenau. **Aerogels from unaltered bacterial cellulose: application of scCO2 drying for the preparation of shaped, ultra-lightweight cellulosic aerogels**. *Macromol. Biosci.*, **10**(4):349–352, 2010. xiv, 85, 87, 88, 99

[11] Eduardo Ruiz-Hitzky, Margarita Darder, Pilar Aranda, and Katsuhiko Ariga. **Advances in biomimetic and nanostructured biohybrid materials**. *Adv. Mater.*, **22**(3):323–336, 2010. xv, 109, 110

[12] T Heinze. **Hot topics in polysaccharide chemistry–selected examples**. *Macromol. Symp.*, **280**(1):15–27, 2009. xviii, 158, 160

[13] B Zhao and WJ Brittain. **Polymer brushes: surface-immobilized macromolecules**. *Progress in Polymer Science*, **25**(5):677–710, 2000. xviii, 159, 160

[14] R Rai, T Keshavarz, J.A Roether, A.R Boccaccini, and I Roy. **Medium chain length polyhydroxyalkanoates, promising new biomedical materials for the future**. *Materials Science and Engineering: R: Reports*, 2011. xviii, 159, 161, 162

[15] K Sudesh, H Abe, and Y Doi. **Synthesis, structure and properties of polyhydroxyalkanoates: biological polyesters**. *Progress in Polymer Science*, **25**(10):1503–1555, 2000. xviii, 161, 162

[16] Lawrence Hrubesh. **Aerogel applications**. *Journal of Non-Crystalline Solids*, **225**(1):335–342, 1998. xxi, 85, 86

[17] T. Heinze D. Klemm, H.-P. Schmauder. *Biopolymers*, **6**, pages 290–292. Wiley-VCH, Weinheim, 2002. 1

[18] S Eichhorn. **Cellulose nanowhiskers: promising materials for advanced applications**. *Soft Matter*, **7**(2):303–315, 2011. 1, 155

[19] I Siró and D Plackett. **Microfibrillated cellulose and new nanocomposite materials: a review**. *Cellulose*, **17**(3):459–494, 2010. 1, 155

[20] S Hestrin and M Schramm. **Synthesis of cellulose by Acetobacter xylinum. II. Preparation of freeze-dried cells capable of polymerizing glucose to cellulose**. *Biochem J*, **58**(2):345–352, Oct 1954. 2, 25, 27

[21] M Schramm and S Hestrin. **Factors affecting production of cellulose at the air/liquid interface of a culture of Acetobacter xylinum**. *Microbiology*, **11**(1):123, 1954. 2, 26, 29, 30

[22] Robert Cannon and Steven Anderson. **Biogenesis of bacterial cellulose**. *Critical Reviews in Microbiology*, **17**(6):435–447, 1991. 2, 24

[23] K Watanabe, M Tabuchi, Y Morinaga, and F Yoshinaga. **Structural features and properties of bacterial cellulose produced in agitated culture**. *Cellulose*, **5**(3):187–200, 1998. 2, 27, 28, 38, 55

[24] S Yamanaka, K Watanabe, N Kitamura, M Iguchi, S Mitsuhashi, Y Nishi, and M Uryu. **The structure and mechanical properties of sheets prepared from bacterial cellulose**. *Journal of Materials Science*, **24**(9):3141–3145, 1989. 2, 29, 156

[25] M Iguchi, S Yamanaka, and A Budhiono. **Bacterial cellulose—a masterpiece of nature's arts**. *Journal of Materials Science*, **35**(2):261–270, 2000. 2, 28, 29, 33, 34

[26] R.M. Brown. **Cellulose structure and biosynthesis: What is in store for the 21st century?** *J. Polym. Sci. A Polym. Chem.*, **42**(3):487–495, 2004. 2, 22

[27] WK Czaja, DJ Young, M Kawecki, and RM Brown Jr. **The future prospects of microbial cellulose in biomedical applications**. *Biomacromolecules*, **8**(1):1–12, 2007. 2, 29, 30

[28] A Svensson, E Nicklasson, T Harrah, B Panilaitis, DL Kaplan, M Brittberg, and P Gatenholm. **Bacterial cellulose as a potential scaffold for tissue engineering of cartilage**. *Biomaterials*, **26**(4):419–431, 2005. 2, 29, 30

[29] M Samir, F Alloin, and A Dufresne. **Review of recent research into cellulosic whiskers, their properties and their application in nanocomposite field**. *Biomacromolecules*, **6**(2):612–626, 2005. 2, 30, 155

[30] Jerry Workman and Art W. Springsteen. *Applied Spectroscopy: A Compact Reference for Practitioners*. Academic Press, 1998. 7

[31] P Mulvaney. **Surface plasmon spectroscopy of nanosized metal particles**. *Langmuir*, **12**(3):788–800, 1996. 8

[32] T Klar, M Perner, S Grosse, G Von Plessen, W Spirkl, and J Feldmann. **Surface-plasmon resonances in single metallic nanoparticles**. *Physical Review Letters*, **80**(19):4249–4252, 1998. 8

[33] RM Drake and JE Gordon. **Mie scattering**. *American Journal of Physics*, **53**:955, 1985. 8

[34] E Hutter and JH Fendler. **Exploitation of localized surface plasmon resonance**. *Adv. Mater.*, **16**(19):1685–1706, 2004. 8

[35] Leroy E. Alexander. *X-Ray Diffraction Methods in Polymer Science*. Wiley-Interscience, 1969. 10, 11

[36] L. Segal, J.J. Creely, Jr Martin, A.E., and C.M. Conrad. **An empirical method for estimating the degree of crystallinity of native cellulose using the X-ray diffractometer**. *Textile Research Journal*, **29**(10):786–794, 1959. 11, 38, 71

[37] KSW Sing, DH Everett, RAW Haul, L Moscou, RA Pierotti, J Rouquerol, and T Siemieniewska. **Reporting physisorption data for gas/solid systems, with special reference to the determination of surface area and porosity (recommendations 1984)**. *Pure Appl Chem*, **57**(4):603–619, 1985. 12

[38] S. Lowell, Joan E. Shields, Martin A. Thomas, and Matthias Thommes. *Characterization of porous solids and powders: surface area, pore size, and density*. Particle technology series. Springer, 2004. 12

[39] M Thommes. **Physical adsorption characterization of nanoporous materials**. *Chemie Ingenieur Technik*, **82**(7), 2010. 12

[40] EP Barrett, LG Joyner, and PP Halenda. **The determination of pore volume and area distributions in porous substances. I. Computations from nitrogen isotherms**. *J Am Chem Soc*, **73**(1):373–380, 1951. 12

[41] A. Broido. **A simple, sensitive graphical method of treating thermogravimetric analysis data**. *Journal of Polymer Science Part A-2: Polymer Physics*, **7**(10):1761–1773, 1969. 14

[42] N. A. Liu and W. C. Fan. **The kinetic methods for which no assumption about the order of reaction is needed**. *Fire and Materials*, **22**(5):219–220, 1998. 14

[43] Musa Momoh, A. N. Eboatu, E. G. Kolawole, and A. R. Horrocks. **Thermogravimetric studies of the pyrolytic behaviour in air of selected tropical timbers**. *Fire and Materials*, **20**(4):173–181, 1996. 14

[44] M. Teodorovic, Lj. Majdanac, D. Cosic, and V. Nesovic. **The thermal behaviour of cellulose samples with different structure**. *Journal of Thermal Analysis and Calorimetry*, **38**(4):907–916, April 1992. 14

[45] Y Kong and JN Hay. **The measurement of the crystallinity of polymers by DSC**. *Polymer*, **43**(14):3873–3878, 2002. 15

[46] GR Saad, YJ Lee, and H Seliger. **Synthesis and characterization of biodegradable poly(ester-urethanes) based on bacterial poly(R-3-hydroxybutyrate)**. *Journal of Applied Polymer Science*, **83**(4):703–718, Jan 2002. 15

[47] PJ Barham, A Keller, EL Otun, and PA Holmes. **Crystallization and morphology of a bacterial thermoplastic: poly-3-hydroxybutyrate**. *Journal of Materials Science*, **19**(9):2781–2794, Jan 1984. 15

[48] DS Jones. **Dynamic mechanical analysis of polymeric systems of pharmaceutical and biomedical significance**. *Int J Pharm*, **179**(2):167–178, 1999. 15

[49] R.E Wetton, R.D.L Marsh, and J.G Van-de Velde. **Theory and application of dynamic mechanical thermal analysis**. *Thermochimica acta*, **175**(1):1–11, Feb 1991. 15

[50] Kevin P. Menard. *Dynamic Testing and Instrumentation*. CRC Press, May 2008. doi:10.1201/9781420053135.ch5. 16

[51] Debashish Roy, Mona Semsarilar, James T Guthrie, and Sebastien Perrier. **Cellulose modification by polymer grafting: a review**. *Chem Soc Rev*, **38**(7):2046–2064, 2009. 22, 159

[52] Daniel J Cosgrove. **Growth of the plant cell wall**. *Nature Reviews Molecular Cell Biology*, **6**(11):850, Nov 2005. 22

[53] HJ Wellard. **Variation in the lattice spacing of cellulose**. *Journal of Polymer Science*, **13**(71):471–476, 1954. 23

[54] A Sarko, J Southwick, and J Hayashi. **Packing analysis of carbohydrates and polysaccharides. 7. Crystal structure of cellulose IIII and its relationship to other cellulose polymorphs**. *Macromolecules*, **9**(5):857–863, 1976. 23

[55] J Sugiyama, H Chanzy, and JF Revol. **On the polarity of cellulose in the cell wall of Valonia**. *Planta*, **193**(2):260–265, 1994. 23

[56] RH Atalla and DL Vanderhart. **Native cellulose: a composite of two distinct crystalline forms**. *Science*, **223**:283–285, 1984. 23

[57] Y Horikawa and J Sugiyama. **Localization of crystalline allomorphs in cellulose microfibril**. *Biomacromolecules*, **10**(8):2235–2239, 2009. 23

[58] AC O'Sullivan. **Cellulose: the structure slowly unravels**. *Cellulose*, **4**(3):173–207, 1997. 23

[59] E.J Vandamme, S De Baets, A Vanbaelen, K Joris, and P De Wulf. **Improved production of bacterial cellulose and its application potential**. *Polym Degrad Stabil*, **59**(1-3):93–99, Jan 1998. 24

[60] Rainer Jonas and Luiz Farah. **Production and application of microbial cellulose**. *Polym Degrad Stabil*, **59**(1-3):101–106, Jan 1998. 24

[61] Takayoshi Matsumoto, Daisuke Tatsumi, Nobutake Tamai, and Tatsuya Takaki. **Solution properties of celluloses from different biological origins in LiCl - DMAc**. *Cellulose*, **8**(4):275 – 282, 2002. 24, 49, 53, 56

[62] Y Yamada. **Transfer of Acetobacter oboediens Sokollek et al. 1998 and Acetobacter intermedius Boesch et al. 1998 to the genus Gluconacetobacter as Gluconacetobacter oboediens comb. nov. and Gluconacetobacter intermedius comb. nov**. *International Journal of Systematic and Evolutionary Microbiology*, **50**(6):2225, 2000. 24

[63] M Shoda and Y Sugano. **Recent advances in bacterial cellulose production**. *Biotechnology and Bioprocess Engineering*, **10**(1):1–8, 2005. 24, 31

[64] W Williams and Robert Cannon. **Alternative environmental roles for cellulose produced by Acetobacter xylinum**. *Applied and Environmental Microbiology*, **55**(10):2448, Oct 1989. 24, 25, 26, 27

[65] F Yoshinaga, N Tonouchi, and K WATANABE. **Research progress in production of bacterial cellulose by aeration and agitation culture and its application as a new industrial material**. *Bioscience, biotechnology, and biochemistry*, **61**(2):219–224, 1997. 24, 27, 28

[66] K Watanabe, M Tabuchi, A Ishikawa, H Takemura, T Tsuchida, Y Morinaga, and F Yoshinaga. **Acetobacter xylinum mutant with high cellulose productivity and an ordered structure**. *Bioscience, biotechnology, and biochemistry*, **62**(7):1290–1292, 1998. 24

[67] H Toyosaki, Y Kojima, T Tsuchida, KI Hoshino, Y Yamada, and F Yoshinaga. **The characterization of an acetic acid bacterium useful for producing bacterial cellulose in agitation cultures: The proposal of Acetobacter xylinum subsp. sucrofermentans subsp. nov.** *The Journal of General and Applied Microbiology*, **41**(4):307–314, 1995. 24

[68] A Ishikawa, M Matsuoka, T Tsuchida, and F Yoshinaga. **Increase in cellulose production by sulfaguanidine-resistant mutants derived from Acetobacter xylinum subsp. sucrofermentans**. *Bioscience, biotechnology, and biochemistry*, **59**(12):2259–2262, 1995. 24

[69] P De Wulf, K Joris, and EJ Vandamme. **Improved cellulose formation by an Acetobacter xylinum mutant limited in (keto) gluconate synthesis**. *Journal of Chemical Technology & Biotechnology*, **67**(4):376–380, 1996. 24

[70] B Hungund and S Gupta. **Strain improvement of Gluconacetobacter xylinus NCIM 2526 for bacterial cellulose production**. *African Journal of Biotechnology*, Jan 2010. 24

[71] Rui-Qin Wu, Zhi-Xi Li, Jia-Ping Yang, Xiao-Hui Xing, Dong-Yan Shao, and Kang-Lin Xing. **Mutagenesis induced by high hydrostatic pressure treatment: a useful method to improve the bacterial cellulose yield of a Gluconoacetobacter xylinus strain**. *Cellulose*, **17**(2):399–405, Apr 2010. 24

[72] P Ross, R Mayer, and M Benziman. **Cellulose biosynthesis and function in bacteria**. *Microbiological Reviews*, **55**(1):35–58, Mar 1991. 24, 25, 27, 28, 34

[73] U Römling. **Molecular biology of cellulose production in bacteria**. *Research in microbiology*, **153**(4):205–212, 2002. 24

[74] Nicholas Carpita and Claudia Vergara. **A recipe for cellulose**. *Science*, **279**(5351):672–673, 1998. 24

[75] NS Han and JF Robyt. **The mechanism of Acetobacter xylinum cellulose biosynthesis: direction of chain elongation and the role of lipid pyrophosphate intermediates in the cell membrane**. *Carbohydrate Research*, **313**(2):125–133, 1998. 24

[76] M Benziman and N Eizen. **Pyruvate-phosphate dikinase and the control of gluconeogenesis in Acetobacter xylinum**. *J Biol Chem*, **246**(1):57–61, Jan 1971. 25

[77] RM Brown, JH Willison, and CL Richardson. **Cellulose biosynthesis in Acetobacter xylinum: visualization of the site of synthesis and direct measurement of the in vivo process**. *Proceedings of the National Academy of Sciences of the United States of America*, **73**(12):4565, 1976. 25

[78] A Sani and Y Dahman. **Improvements in the production of bacterial synthesized biocellulose nanofibres using different culture methods**. *Journal of Chemical Technology & Biotechnology*, **85**(2):151–164, 2010. 26, 27

[79] S Moonmangmee, H Toyama, O Adachi, G Theeragool, N Lotong, and K Matsushita. **Purification and characterization of a novel polysaccharide involved in the pellicle produced by a thermotolerant Acetobacter strain**. *Bioscience, biotechnology, and biochemistry*, **66**(4):777–783, 2002. 26

[80] W Borzani and SJ Souza. **Mechanism of the film thickness increasing during the bacterial production of cellulose on non-agitaded liquid media**. *Biotechnol Lett*, **17**(11):1271–1272, 1995. 26

[81] A Krystynowicz, W Czaja, A Wiktorowska-Jezierska, M Gonçalves-Miśkiewicz, M Turkiewicz, and S Bielecki. **Factors affecting the yield and properties of bacterial cellulose**. *Journal of Industrial Microbiology and Biotechnology*, **29**(4):189–195, 2002. 26

[82] Y Chao, T Ishida, Y Sugano, and M Shoda. **Bacterial cellulose production by Acetobacter xylinum in a 50-L internal-loop airlift reactor**. *Biotechnol Bioeng*, **68**(3):345–352, 2000. 27, 31

[83] HJ Son, HG Kim, KK Kim, HS Kim, YG Kim, and SJ Lee. **Increased production of bacterial cellulose by Acetobacter sp V6 in synthetic media under shaking culture conditions**. *Bioresource Technology*, **86**(3):215–219, Jan 2003. 27

[84] T Oikawa, T Ohtori, and M Ameyama. **Production of cellulose from D-mannitol by Acetobacter xylinum KU-1**. *Biosci Biotech Bioch*, **59**(2):331–332, Jan 1995. 27

[85] Sangok Bae and Makoto Shoda. **Bacterial cellulose production by fed-batch fermentation in molasses medium**. *Biotechnol Prog*, **20**(5):1366–71, Jan 2004. 27

[86] T Kouda, H Yano, and F Yoshinaga. **Effect of agitator configuration on bacterial cellulose productivity in aerated and agitated culture**. *Journal of Fermentation and Bioengineering*, **83**(4):371–376, Jan 1997. 27

[87] Hyo-Jeong Song, Hongxian Li, Jin-Ho Seo, Myong-Jun Kim, and Seong-Jun Kim. **Pilot-scale production of bacterial cellulose by a spherical type bubble column bioreactor using saccharified food wastes**. *Korean J Chem Eng*, **26**(1):141–146, Jan 2009. 27

[88] Kuan-Chen Cheng, Jeff M Catchmark, and Ali Demirci. **Enhanced production of bacterial cellulose by using a biofilm reactor and its material property analysis**. *J Biol Eng*, **3**:12, Jan 2009. 27, 37

[89] Kuan-Chen Cheng, Ali Demirci, and Jeffrey M Catchmark. **Advances in biofilm reactors for production of value-added products**. *Applied Microbiology and Biotechnology*, **87**(2):445–56, Jun 2010. 27

[90] W Czaja, D Romanovicz, and R Brown. **Structural investigations of microbial cellulose produced in stationary and agitated culture**. *Cellulose*, Jan 2004. 27, 40, 93, 95

[91] OM Astley, E Chanliaud, AM Donald, and MJ Gidley. **Structure of Acetobacter cellulose composites in the hydrated state**. *International Journal of Biological Macromolecules*, **29**(3):193–202, 2001. 28, 34

[92] S Yamanaka and J Sugiyama. **Structural modification of bacterial cellulose**. *Cellulose*, Jan 2000. 28, 34

[93] G Guhados, W Wan, and JL Hutter. **Measurement of the elastic modulus of single bacterial cellulose fibers using atomic force microscopy**. *Langmuir*, **21**(14):6642–6646, 2005. 28

[94] Fumio Tanaka and Tadahisa Iwata. **Estimation of the elastic modulus of cellulose crystal by molecular mechanics simulation**. *Cellulose*, **13**(5):509–517, 2006. 29

[95] Y Nishi, M Uryu, S Yamanaka, K WATANABE, N Kitamura, M Iguchi, and S Mitsuhashi. **The structure and mechanical properties of sheets prepared from bacterial cellulose**. *Journal of Materials Science*, **25**(6):2997–3001, 1990. 29

[96] M Seifert, S Hesse, V Kabrelian, and D Klemm. **Controlling the water content of never dried and reswollen bacterial cellulose by the addition of water-soluble polymers to the culture medium**. *J. Polym. Sci. A Polym. Chem.*, **42**(3):463–470, 2004. 29

[97] Nadine Hessler and Dieter Klemm. **Alteration of bacterial nanocellulose structure by in situ modification using polyethylene glycol and carbohydrate additives**. *Cellulose*, **16**(5):899–910, Oct 2009. 29

[98] C Legnani, C Vilani, V L Calil, H S Barud, W G Quirino, C A Achete, S J L Ribeiro, and M Cremona. **Bacterial cellulose membrane as flexible substrate for organic light emitting devices**. *Thin Solid Films*, **517**(3):1016–1019, Jan 2008. 29

[99] A Nakagaito, S Iwamoto, and H Yano. **Bacterial cellulose: the ultimate nano-scalar cellulose morphology for the production of high-strength composites**. *Applied Physics A: Materials Science & Processing*, **80**(1):93–97, 2005. 29, 156

[100] BR Evans, HM O'Neill, VP Malyvanh, I Lee, and J Woodward. **Palladium-bacterial cellulose membranes for fuel cells**. *Biosensors and Bioelectronics*, **18**(7):917–923, 2003. 29

[101] J Shah and R Malcolm Brown. **Towards electronic paper displays made from microbial cellulose**. *Applied Microbiology and Biotechnology*, **66**(4):352–355, 2005. 29

[102] W Czaja, A Krystynowicz, S Bielecki, and RM Brown. **Microbial cellulose—the natural power to heal wounds**. *Biomaterials*, **27**(2):145–151, 2006. 29

[103] Henrik Bäckdahl, Bo Risberg, and Paul Gatenholm. **Observations on bacterial cellulose tube formation for application as vascular graft**. *Materials Science & Engineering C*, pages 1–8, Aug 2010. 29

[104] Z Cai and J Kim. **Preparation and characterization of novel bacterial cellulose/gelatin scaffold for tissue regeneration using bacterial cellulose hydrogel**. *Journal of Nanotechnology in Engineering and ...*, Jan 2010. 29

[105] Nattakan Soykeabkaew, Chandeep Sian, Saharman Gea, Takashi Nishino, and Ton Peijs. **All-cellulose nanocomposites by surface selective dissolution of bacterial cellulose**. *Cellulose*, **16**(3):435–444, 2009. 29, 48, 93, 94, 101

[106] Julasak Juntaro, Marion Pommet, Gerhard Kalinka, Athanasios Mantalaris, Milo S. P Shaffer, and Alexander Bismarck. **Creating hierarchical structures in renewable composites by attaching bacterial cellulose onto sisal fibers**. *Adv. Mater.*, **20**(16):3122–3126, 2008. 30, 52

[107] Marion Pommet, Julasak Juntaro, Jerry Y. Y. Heng, Athanasios Mantalaris, Adam F. Lee, Karen Wilson, Gerhard Kalinka, Milo S. P. Shaffer, and Alexander Bismarck. **Surface modification of natural fibers using bacteria: depositing bacterial cellulose onto natural fibers to create hierarchical fiber reinforced nanocomposites**. *Biomacromolecules*, **9**(6):1643–1651, 2008. 30, 70

[108] HS Barud, C Barrios, T Regiani, RFC Marques, M Verelst, J Dexpert-Ghys, Y Messaddeq, and SJL Ribeiro. **Self-supported silver nanoparticles containing bacterial cellulose membranes**. *Materials Science and Engineering: C*, **28**(4):515–518, 2008. 30, 96, 111, 113

[109] T Zhang, W Wang, D Zhang, X Zhang, Y Ma, Y Zhou, and L Qi. **Biotemplated synthesis of gold nanoparticle-bacteria cellulose nanofiber nanocomposites and their application in biosensing-bacteria cellulose nanofiber nanocomposites and their application in biosensing**. *Advanced Functional Materials*, **20**(7):1152–1160, 2010. 30, 113, 116, 139

[110] Wei Wang, Hong-Yi Li, De-Wen Zhang, Jing Jiang, Yi-Ran Cui, Shuang Qiu, Ying-Lin Zhou, and Xin-Xiang Zhang. **Fabrication of bienzymatic glucose biosensor based on novel gold nanoparticles-bacteria cellulose nanofibers nanocomposite**. *Electroanalysis*, **22**(21):2543–2550, 2010. 30, 113, 116

[111] D Sun, J Yang, and X Wang. **Bacterial cellulose/TiO2 hybrid nanofibers prepared by the surface hydrolysis method with molecular precision**. *Nanoscale*, **2**(2):287–292, 2010. 30, 112, 113

[112] YK Yang, SH Park, JW Hwang, WR Pyun, and YS Kim. **Cellulose production by Acetobacter xylinum BRC5 under agitated condition**. *Journal of Fermentation and Bioengineering*, **85**(3):312–317, Jan 1998. 35

[113] Y. Marechal and H. Chanzy. **The hydrogen bond network in I cellulose as observed by infrared spectrometry**. *Journal of Molecular Structure*, **523**:183–196, Jan 2000. 40

[114] A Carrillo, X Colom, JJ Sunol, and J Saurina. **Structural FTIR analysis and thermal characterisation of lyocell and viscose-type fibres**. *European Polymer Journal*, **40**(9):2229–2234, 2004. 40, 41, 58, 59

[115] H Huang, L Chen, S Lin, C Hsu, and H Chen. **In situ modification of bacterial cellulose network structure by adding interfering substances during fermentation**. *Bioresource Technology*, Jan 2010. 40, 41

[116] SY Oh, DI Yoo, Y Shin, HC Kim, HY Kim, YS Chung, WH Park, and JH Youk. **Crystalline structure analysis of cellulose treated with sodium hydroxide and carbon dioxide by means of X-ray diffraction and FTIR spectroscopy**. *Carbohydrate Research*, **340**(15):2376–2391, 2005. 40, 41

[117] J Lojewska, P Miskowiec, T Lojewski, and LM Proniewicz. **Cellulose oxidative and hydrolytic degradation: In situ FTIR approach**. *Polym Degrad Stabil*, **88**(3):512–520, 2005. 40, 41

[118] S Wong, S Kasapis, and Y Tan. **Bacterial and plant cellulose modification using ultrasound irradiation**. *Carbohydrate Polymers*, Jan 2009. 40, 41

[119] S Zhou, K Tashiro, T Hongo, H Shirataki, C Yamane, and T Iis. **Influence of water on structure and mechanical properties of regenerated cellulose studied by an organized combination of infrared spectra, X-ray diffraction, and dynamic viscoelastic data measured as functions of temperature and humidity**. *Macromolecules*, **34**(5):1274–1280, 2001. 40, 41

[120] M Kauráková, AC Smith, MJ Gidley, and RH Wilson. **Molecular interactions in bacterial cellulose composites studied by 1D FT-IR and dynamic 2D FT-IR spectroscopy**. *Carbohydrate Research*, **337**(12):1145–1153, 2002. 40, 41

[121] J Sugiyama, J Persson, and H Chanzy. **Combined infrared and electron diffraction study of the polymorphism of native celluloses**. *Macromolecules*, **24**(9):2461–2466, 1991. 40, 41

[122] H Yamamoto, F Horii, and A Hirai. **In situ crystallization of bacterial cellulose II. Influences of different polymeric additives on the formation of celluloses I_α and I_β at the early stage of incubation**. *Cellulose*, **3**(1):229–242, 1996. 40

[123] J Alongi, J Tata, and Alberto Frache. **Hydrotalcite and nanometric silica as finishing additives to enhance the thermal stability and flame retardancy of cotton**. *Cellulose*, 2010. 42

[124] A.K. Mohanty, M. Misra, L.T. Drzal, S.E. Selke, B.R. Harte, and G. Hinrichsen. *Natural Fibers, Biopolymers and Biocomposites: An Introduction.* CRC Press, 2005. Chap: 1. 47, 51

[125] G Marsh. **Composites that grow in fields**. *Reinforced Plastics*, **52**(10):16–17, 2008. 47

[126] P Wambua, J Ivens, and I Verpoest. **Natural fibres: can they replace glass in fibre reinforced plastics?** *Composites Science and Technology*, **63**(9):1259–1264, 2003. 47

[127] K. C. Khemani and C Sholz. *Degradable Polymers and Materials: Principles and Practice.* American Chemical Society, 2005. 47

[128] J Summerscales, N Dissanayake, and A Virk. **A review of bast fibres and their composites. Part 2-composites**. *Composites Part A: Applied Science and Manufacturing*, **41**(10):1336–1344, 2010. 47

[129] James Holbery and Dan Houston. **Natural-fiber-reinforced polymer composites applications in automotive**. *Jom-Us*, **58**(11):80–86, 2006. 47

[130] S. K. Garkhail, R. W. H. Heijenrath, and T. Peijs. **Mechanical properties of natural-fibre-mat-reinforced thermoplastics based on flax fibres and polypropylene**. *Applied Composite Materials*, **7**(5):351–372, 2000. 47

[131] Yan Li, Yiu-Wing Mai, and Lin Ye. **Sisal fibre and its composites: a review of recent developments**. *Composites Science and Technology*, **60**(11):2037–2055, 2000. 47, 51

[132] Robert Kohler and Kai Nebel. **Cellulose-nanocomposites: towards high performance composite materials**. *Macromolecular Symposia*, **244**(1):97–106, 2006. 47

[133] Denis Mihaela Panaitescu, Dan Donescu, Cristiana Bercu, Dumitru Mircea Vuluga, Michaela Iorga, and Marius Ghiurea. **Polymer composites with cellulose microfibrils**. *Polym Eng Sci*, **47**:1228–1234, 2007. 47

[134] K. Wötzel, R. Wirth, and M. Flake. **Life cycle studies on hemp fibre reinforced components and ABS for automotive parts**. *Die Angewandte Makromolekulare Chemie*, **272**(1):121–127, 1999. 47

[135] Xun Xu, Krishnan Jayaraman, Caroline Morin, and Nicolas Pecqueux. **Life cycle assessment of wood-fibre-reinforced polypropylene composites**. *Journal of Materials Processing Technology*, **198**(1-3):168 – 177, 2008. 47

[136] R Kumar, MK Yakubu, and RD Anandjiwala. **Biodegradation of flax fiber reinforced poly lactic acid**. 2010. 47

[137] NM Barkoula, SK Garkhail, and T Peijs. **Biodegradable composites based on flax/polyhydroxybutyrate and its copolymer with hydroxyvalerate**. *Industrial Crops and Products*, **31**(1):34–42, 2010. 47

[138] AK Bledzki and A Jaszkiewicz. **Mechanical performance of biocomposites based on PLA and PHBV reinforced with natural fibres-a comparative study to PP**. *Composites Science and Technology*, **70**(12):1687–1696, 2010. 47

[139] JT Kim and AN Netravali. **Mechanical, thermal, and interfacial properties of green composites with ramie fiber and soy resins**. *J Agr Food Chem*, **58**(9):5400–5407, 2010. 47, 48, 109

[140] A.K. Mohanty, A. Wibowo, M. Misra, and L.T. Drzal. **Effect of process engineering on the performance of natural fiber reinforced cellulose acetate biocomposites**. *Composites Part A: Applied Science and Manufacturing*, **35**(3):363 – 370, 2004. 48

[141] Arief C. Wibowo, Amar K. Mohanty, Manjusri Misra, and Lawrence T. Drzal. **Chopped industrial hemp fiber reinforced cellulosic plastic biocomposites: Thermomechanical and morphological properties**. *Industrial and Engineering Chemistry Research*, **43**(16):4883 – 4888, 2004. 48

[142] Wolfgang Gindl and Jozef Keckes. **Tensile properties of cellulose acetate butyrate composites reinforced with bacterial cellulose**. *Composites Science and Technology*, **64**(15 SPEC ISS):2407 – 2413, 2004. 48, 156

[143] AAS Curvelo, AJF De Carvalho, and JAM Agnelli. **Thermoplastic starch-cellulosic fibers composites: preliminary results**. *Carbohydrate Polymers*, **45**(2):183–188, 2001. 48

[144] P Pan, B Zhu, W Kai, S Serizawa, M Iji, and Y Inoue. **Crystallization behavior and mechanical properties of bio-based green composites based on poly(L-lactide) and kenaf fiber**. *Journal of Applied Polymer Science*, **105**(3):1511–1520, 2007. 48

[145] M Shibata, S Oyamada, S Kobayashi, and D Yaginuma. **Mechanical properties and biodegradability of green composites based on biodegradable polyesters and ....** *Journal of Applied Polymer Science*, **92**(6):3857–3863, 2004. 48

[146] R. Bhardwaj, A.K. Mohanty, L.T. Drzal, F. Pourboghrat, and M. Misra. **Renewable resource-based green composites from recycled cellulose fiber and Poly(3-hydroxybutyrate-¡i¿co¡/i¿-3-hydroxyvalerate) bioplastic**. *Biomacromolecules*, **7**(6):2044–2051, 2006. 48

[147] K. Oksman, M. Skrifvars, and J. F. Selin. **Natural fibres as reinforcement in polylactic acid (PLA) composites**. *Composites Science and Technology*, **63**(9):1317–1324, 2003. 48

[148] W. Gindl and J. Keckes. **All-cellulose nanocomposite**. *Polymer*, **46**(23):10221 – 10225, 2005. Nanocomposite films;Self-reinforcement;Failure strain;. 48, 55, 58, 64

[149] W. Gindl, T. Schoberl, and J. Keckes. **Structure and properties of a pulp fibre-reinforced composite with regenerated cellulose matrix**. *Applied Physics A: Materials Science and Processing*, **83**(1):19 – 22, 2006. 48, 64, 74, 75

[150] Takashi Nishino, Ikuyo Matsuda, and Koichi Hirao. **All-cellulose composite**. *Macromolecules*, **37**(20):7683 – 7687, 2004. 48, 73, 75

[151] Haisong Qi, Jie Cai, Lina Zhang, and Shigenori Kuga. **Properties of films composed of cellulose nanowhiskers and a cellulose matrix regenerated from alkali/urea solution**. *Biomacromolecules*, **10**(6):1597–1602, 2009. 48

[152] Young-Keun Hong, Kyung-Ho Chung, and Wha-Seop Lee. **Structure of regenerated cellulose fibers from DMAc/LiCl solution**. *Textile Research Journal*, **68**(1):65–69, 1998. 48

[153] Benoit J. C. Z Duchemin, Roger H Newman, and Mark P Staiger. **Phase transformations in microcrystalline cellulose due to partial dissolution**. *Cellulose*, **14**(4):311–320, 2007. 48, 58

[154] T Dawsey and C McCormick. **The lithium cloride/dimethylacetamide solvent for cellulose: a literature review**. *Polymer Reviews*, **30**(3-4):405 – 440, 1990. 48, 49

[155] Qiang Zhao, Richard C. M Yam, Baoqing Zhang, Yingkui Yang, Xinjian Cheng, and Robert K. Y Li. **Novel all-cellulose ecocomposites prepared in ionic liquids**. *Cellulose*, **16**(2):217–226, 2009. 48, 73

[156] Takashi Nishino and Noriko Arimoto. **All-cellulose composite prepared by selective dissolving of fiber surface**. *Biomacromolecules*, **8**(9):2712–2716, 2007. 48, 64

[157] Nattakan Soykeabkaew, Takashi Nishino, and Ton Peijs. **All-cellulose composites of regenerated cellulose fibres by surface selective dissolution**. *Composites Part A*, **40**(4):321–328, 2009. 48, 73

[158] Richard P Swatloski, Scott K Spear, John D Holbrey, and Robin D Rogers. **Dissolution of cellulose with ionic liquids**. *J Am Chem Soc*, **124**(18):4974–4975, 2002. 48, 49

[159] Benoît J C Duchemin, Roger H Newman, and Mark P Staiger. **Structure–property relationship of all-cellulose composites**. *Composites Science and Technology*, **69**(7-8):1225–1230, 2009. 48, 55, 65, 77

[160] Donglin Han and Lifeng Yan. **Preparation of all-cellulose composite by selective dissolving of cellulose surface in PEG/NaOH aqueous solution**. *Carbohydrate Polymers*, **79**(3):614–619, 2010. 48

[161] Hiroyuki Matsumura, Junji Sugiyama, and Wolfgang G. Glasser. **Cellulosic nanocomposites. I. Thermally deformable cellulose hexanoates from heterogeneous reaction**. *Journal of Applied Polymer Science*, **78**(13):2242–2253, 2000. 48

[162] Hiroyuki Matsumura and Wolfgang G. Glasser. **Cellulosic nanocomposites. II. Studies by atomic force microscopy**. *Journal of Applied Polymer Science*, **78**(13):2254–2261, 2000. 48

[163] Albin F. Turbak. **Recent developments in cellulose solvent systems.** *Tappi Journal*, **67**(1):94 – 96, 1984. 49

[164] Charles L. McCormick, Peter A. Callais, and Brewer H. Hutchinson. **Solution studies of cellulose in lithium chloride and N,N-dimethylacetamide**. *Macromolecules*, **18**(12):2394–2401, 1985. 49, 53, 56

[165] C. L. McCormick and P. A. Callais. **Derivation of cellulose in lithium chlroride and N,N-dimethylacetamide solutions**. *Polymer Preprints, Division of Polymer Chemistry, American Chemical Society*, **27**(2):91 – 92, 1986. 49

[166] A Striegel. **Theory and applications of DMAC/LICL in the analysis of polysaccharides**. *Carbohydrate Polymers*, **34**(4):267–274, 1997. 49

[167] Daisuke Ishii, Daisuke Tatsumi, Takayoshi Matsumoto, Kazuki Murata, Hisao Hayashi, and Hiroshi Yoshitani. **Investigation of the structure of cellulose in LiCl/DMAc solution and its gelation behavior by small-angle X-ray scattering measurements**. *Macromolecular Bioscience*, **6**(4):293 – 300, 2006. 49

[168] C Woodings. **The development of advanced cellulosic fibres**. *International Journal of Biological Macromolecules*, **17**(6):305–309, 1995. 49

[169] Nahla A El-Wakil and Mohammad L Hassan. **Structural changes of regenerated cellulose dissolved in FeTNa, NaOH/thiourea, and NMMO systems**. *Journal of Applied Polymer Science*, **109**(5):2862–2871, 2008. 49

[170] H Boerstoel, H Maatman, J Westerink, and B Koenders. **Liquid crystalline solutions of cellulose in phosphoric acid**. *Polymer*, **42**(17):7371–7379, 2001. 49

[171] MA Aziz, P Paramasivam, and SL Lee. **Prospects for natural fibre reinforced concretes in construction**. *International Journal of Cement Composites and Lightweight Concrete*, **3**(2):123–132, 1981. 51

[172] F Pacheco-Torgal and S Jalali. **Cementitious building materials reinforced with vegetable fibres: A review**. *Construction and Building Materials*, 2010. 51

[173] J Summerscales, N Dissanayake, and A Virk. **A review of bast fibres and their composites. Part 1-fibres as reinforcements**. *Composites Part A: Applied Science and Manufacturing*, **41**(10):1328–1335, 2010. 51

[174] PS Mukherjee and KG Satyanarayana. **Structure and properties of some vegetable fibres Part 1 Sisal fibre**. *Journal of Materials Science*, **19**(12):3925–3934, 1984. 51, 72

[175] Navin Chand and S. A. R. Hashmi. **Mechanical properties of sisal fibre at elevated temperatures**. *Journal of Materials Science*, **28**(24):6724–6728, 1993. 51, 72

[176] F. L. Matthews and R. D. Rawlings. *Composite materials: Engineering and science*. Woodhead Publising Ltd., 1994. 52

[177] J. Rout, M. Misra, S. S. Tripathy, S. K. Nayak, and A. K. Mohanty. **The influence of fibre treatment on the performance of coir-polyester composites**. *Composites Science and Technology*, **61**(9):1303–1310, 2001. 52

[178] L. Y. Mwaikambo and M. P. Ansell. **Hemp fibre reinforced cashew nut shell liquid composites**. *Composites Science and Technology*, **63**(9):1297–1305, 2003. 52

[179] Mohamed Naceur Belgacem and Alessandro Gandini. **The surface modification of cellulose fibres for use as reinforcing elements in composite materials**. *Composite Interfaces*, **12**:41–75, 2005. 52

[180] J George, MS Sreekala, and S Thomas. **A review on interface modification and characterization of natural fiber reinforced plastic composites**. *Polym. Eng. Sci.*, **41**(9):1471–1485, 2001. 52

[181] X Li, LG Tabil, and S Panigrahi. **Chemical treatments of natural fiber for use in natural fiber-reinforced composites: A review**. *J Polym Environ*, **15**(1):25–33, 2007. 52, 73

[182] Y Xie, CAS Hill, Z Xiao, H Militz, and C Mai. **Silane coupling agents used for natural fiber/polymer composites: A review**. *Composites Part A: Applied Science and Manufacturing*, 2010. 52

[183] A Baltazar-Y-Jimenez and A Bismarck. **Surface modification of lignocellulosic fibres in atmospheric air pressure plasma**. *Green Chemistry*, **9**:1057–1066, 2007. 52

[184] A Baltazar-Y-Jimenez, J Juntaro, and A Bismarck. **Effect of atmospheric air pressure plasma treatment on the thermal behaviour of natural fibres and dynamical mechanical properties of randomly-oriented short fibre composites**. *Journal of Biobased Materials and Bioenerg*, **2**(3):264–273, 2008. 52

[185] A Baltazar-Y-Jimenez, M Bistritz, and E Schulz. **Atmospheric air pressure plasma treatment of lignocellulosic fibres: Impact on mechanical properties ...**. *Composites Science and Technology*, **68**(1):215–227, 2008. 52

[186] J. Juntaro, M. Pommet, A. Mantalaris, M. Shaffer, and A. Bismarck. **Nanocellulose enhanced interfaces in truly green unidirectional fibre reinforced composites**. *Composite Interfaces*, **14**(7-9):753–762, 2007. 52

[187] Ludmila Ramos, Jose Assaf, Omar El Seoud, and Elisabete Frollini. **Influence of the supramolecular structure and physicochemical properties of cellulose on its dissolution in a lithium chloride/N,N-dimethylacetamide solvent system**. *Biomacromolecules*, **6**(5):2638–2647, 2005. 55

[188] T. Kondo, E. Togawa, and R.M. Brown. **"Nematic ordered cellulose": a concept of glucan chain association**. *Biomacromolecules*, **2**(4):1324–1330, 2001. 55, 59

[189] Choo-Won Kim, Dae-Sik Kim, Seung-Yeon Kang, Manuel Marquez, and Yong Lak Joo. **Structural studies of electrospun cellulose nanofibers**. *Polymer*, **47**(14):5097–5107, 2006. 55, 59

[190] F. G. Hurtubise and Hans Krassig. **Classification of fine structural characteristics in cellulose by infrared spectroscopy. Use of potassium bromide pellet technique**. *Analytical Chemistry*, **32**(2):177–181, 1960. 58, 59

[191] Mary L. Nelson and Robert T. O'Connor. **Relation of certain infrared bands to cellulose crystallinity and crystal latticed type. Part I. Spectra of lattice types I, II, III and of amorphous cellulose**. *Journal of Applied Polymer Science*, **8**(3):1311–1324, 1964. 58, 59

[192] S Ouajai and RA Shanks. **Composition, structure and thermal degradation of hemp cellulose after chemical treatments**. *Polym Degrad Stabil*, **89**:327–335, 2005. 58, 59

[193] Ute Richter, Thomas Krause, and Walter Schempp. **Untersuchungen zur alkalibehandlung von cellulosefasern. Teil 1. Infrarotspektroskopische und rntgenographische beurteilung der nderung des ordnungszustandes**. *Angewandte Makromolekulare Chemie*, **185**(1):155–167, 1991. 59

[194] Margaretha Akerholm, Barbara Hinterstoisser, and Lennart Salmen. **Characterization of the crystalline structure of cellulose using static and dynamic FT-IR spectroscopy**. *Carbohydrate Research*, **339**(3):569–578, 2004. 59

[195] Yu-Chuan Lin, Joungmo Cho, Geoffrey A Tompsett, Phillip R Westmoreland, and George W Huber. **Kinetics and mechanism of cellulose pyrolysis**. *J Phys Chem C*, **113**(46):20097–20107, 2009. 61

[196] A. A. Saafan and A. M. Habib. **Influence of changes in fine structure on thermal properties of cotton fibres**. *Journal of Thermal Analysis and Calorimetry*, **32**(5):1345–1354, 1987. 61

[197] MZ Rong, MQ Zhang, Y Liu, GC Yang, and HM Zeng. **The effect of fiber treatment on the mechanical properties of unidirectional sisal-reinforced epoxy composites**. *Composites Science and Technology*, **61**(10):1437–1447, 2001. 71

[198] S Ouajai, A Hodzic, and RA Shanks. **Morphological and grafting modification of natural cellulose fibers**. *Journal of Applied Polymer Science*, **94**(6):2456–2465, 2004. 71

[199] Vera A. Alvarez, Roxana A. Ruscekaite, and Analia Vazquez. **Mechanical properties and water absorption behavior of composites made from a biodegradable matrix and alkaline-treated sisal fibers**. *Journal of Composite Materials*, **37**(17):1575–1588, 2003. 72

[200] Alexander Bismarck, Amar K. Mohanty, Ibon Aranberri-Askargorta, Syliva Czapla, Manjusri Misra, Georg Hinrichsen, and Jurgen Springer. **Surface characterization of natural fibers; surface properties and the water up-take behavior of modified sisal and coir fibers**. *Green Chemistry*, **3**(2):100–107, 2001. 73

[201] ETN Bisanda. **The effect of alkali treatment on the adhesion characteristics of sisal fibres**. *Applied Composite Materials*, **7**(5):331–339, 2000. 75

[202] Nattakan Soykeabkaew, Noriko Arimoto, Takashi Nishino, and Ton Peijs. **All-cellulose composites by surface selective dissolution of aligned ligno-cellulosic fibres**. *Composites Science and Technology*, **68**(10-11):2201–2207, 2008. 75

[203] SN Pandey. **Ramie fibre: part I. Chemical composition and chemical properties. A critical review of recent developments**. *Textile Progress*, **39**(1):1–66, 2007. 77

[204] Y Li, YP Hu, CJ Hu, and YH Yu. **Microstructures and mechanical properties of natural fibers**. *Advanced Materials Research*, **33**:553–558, 2008. 77

[205] Arthur Geoffrey Norman. **The composition of some vegetable fibres with particular reference to jute**. *The Rothamstead memoirs on agricultural science*, **30**(5):831–838, 1937. 77

[206] Benoît J C Duchemin, Aji P Mathew, and Kristiina Oksman. **All-cellulose composites by partial dissolution in the ionic liquid 1-butyl-3-methylimidazolium chloride**. *Composites Part A*, **40**(12):2031–2037, 2009. 77

[207] S. S. Kistler. **Coherent expanded aerogels and jellies.** *Nature*, **127**:741, 1931. 82

[208] Nicola Husing and Ulrich Schubert. **Aerogels-airy materials: chemistry, structure, and properties**. *Angew. Chem. Int. Ed.*, **37**(1):22–45, 1998. 82

[209] S Kistler. **Coherent expanded-aerogels**. *The journal of physical chemistry*, **36**(1):52–64, 1932. 82, 83, 85

[210] M. B. Bryning, D. E. Milkie, M. F. Islam, L. A. Hough, J. M. Kikkawa, and A. G. Yodh. **Carbon nanotube aerogels**. *Adv. Mater.*, **19**(5):661–664, 2007. 82

[211] Nadja C. Bigall, Anne-Kristin Herrmann, Maria Vogel, Marcus Rose, Paul Simon, Wilder Carrillo-Cabrera, Dirk Dorfs, Stefan Kaskel, Nikolai Gaponik, and Alexander Eychmüller. **Hydrogels and aerogels from noble metal nanoparticles**. *Angew. Chem. Int. Ed.*, **48**(51):9731–9734, 2009. 82

[212] Indika Arachchige and Stephanie Brock. **Solgel assembly of CdSe nanoparticles to form porous aerogel networks**. *J Am Chem Soc*, **128**(24):7964–7971, 2006. 82

[213] Indika Arachchige and Stephanie Brock. **Highly luminescent quantum-dot monoliths**. *J Am Chem Soc*, **129**(7):1840–1841, 2007. 82

[214] Nikolai Gaponik, Andreas Wolf, Romy Marx, Vladimir Lesnyak, Kristian Schilling, and Alexander Eychmüller. **Three-dimensional self-assembly of thiol-capped CdTe nanocrystals: gels and aerogels as building blocks for nanotechnology**. *Adv. Mater.*, **20**(22):4257–4262, 2008. 82

[215] R Pekala. **Organic aerogels from the polycondensation of resorcinol with formaldehyde**. *Journal of Materials Science*, **24**(9):3221–3227, 1989. 83

[216] Dale Schaefer, Richard Pekala, and Greg Beaucage. **Origin of porosity in resorcinol-formaldehyde aerogels**. *Journal of Non-Crystalline Solids*, **186**:159–167, 1995. 83

[217] G Biesmans, D Randall, E Francais, and M Perrut. **Polyurethane-based organic aerogels' thermal performance**. *Journal of Non-Crystalline Solids*, **225**(1):36–40, 1998. 83

[218] A Rigacci, J C Marechal, M Repoux, M Moreno, and P Achard. **Preparation of polyurethane-based aerogels and xerogels for thermal superinsulation**. *Journal of Non-Crystalline Solids*, **350**:372–378, 2004. 83

[219] F Fischer, A Rigacci, R Pirard, S Berthon-Fabry, and P Achard. **Cellulose-based aerogels**. *Polymer*, **47**(22):7636–7645, 2006. 83, 87

[220] S Mine, K Prasad, H Izawa, K Sonoda, and J Kadokawa. **Preparation of guar gum-based functional materials using ionic liquid**. *J. Mater. Chem.*, 2010. 83

[221] C Jeffrey Brinker and George W. Scherer. *Sol-gel science: the physics and chemistry of sol-gel processing*. Gulf Professional Publishing, 1990. 83

[222] Alain C. Pierre. *Introduction to sol-gel processing*. Kluwer Academic Publishers, 1998. 83

[223] H Gesser and P Goswami. **Aerogels and related porous materials**. *Chem Rev*, **89**(4):765–788, 1989. 84, 85

[224] S Dai, YH Ju, HJ Gao, JS Lin, SJ Pennycook, and CE Barnes. **Preparation of silica aerogel using ionic liquids as solvents**. *Chem Commun*, **2000**(3):243–244, 2000. 84

[225] María Gutiérrez, María Ferrer, and Francisco del Monte. **Ice-templated materials: sophisticated structures exhibiting enhanced functionalities obtained after unidirectional freezing and ice-segregation-induced self-assembly**. *Chem. Mater.*, **20**(3):634–648, 2008. 85

[226] J Fricke and A Emmerling. **Aerogels-recent progress in production techniques and novel applications**. *Journal of Sol-Gel Science and Technology*, **13**(1):299–303, 1998. 85

[227] M Schmidt and F Schwertfeger. **Applications for silica aerogel products**. *Journal of Non-Crystalline Solids*, **225**(1):364–368, 1998. 85, 88

[228] Raluca Horga, Francesco Di Renzo, and Françoise Quignard. **Ionotropic alginate aerogels as precursors of dispersed oxide phases**. *Applied Catalysis A: General*, **325**(2):251–255, 2007. 85

[229] T Mehling, I Smirnova, U Guenther, and R.H.H Neubert. **Polysaccharide-based aerogels as drug carriers**. *Journal of Non-Crystalline Solids*, **355**(50-51):2472–2479, 2009. 85

[230] F Quignard, R Valentin, and FD Renzo. **Aerogel materials from marine polysaccharides**. *New Journal of Chemistry*, **32**(8):1300–1310, 2008. 85

[231] Costas Tsioptsias, Chrysoula Michailof, George Stauropoulos, and Costas Panayiotou. **Chitin and carbon aerogels from chitin alcogels**. *Carbohydrate Polymers*, **76**(4):535–540, 2009. 85

[232] S Cardea, P Pisanti, and E Reverchon. **Generation of chitosan nanoporous structures for tissue engineering applications using a supercritical fluid assisted process**. *The Journal of Supercritical Fluids*, **54**(3):290–295, 2010. 85

[233] Xinhong Chang, Dairong Chen, and Xiuling Jiao. **Chitosan-based aerogels with high adsorption performance**. *J. Phys. Chem. B*, **112**(26):7721–7725, 2008. 85

[234] Karine Molvinger, Françoise Quignard, Daniel Brunel, Michel Boissière, and Jean-Marie Devoisselle. **Porous chitosan-silica hybrid microspheres as a potential catalyst**. *Chem. Mater.*, **16**(17):3367–3372, 2004. 85, 89

[235] Xinhong Chang, Dairong Chen, and Xiuling Jiao. **Starch-derived carbon aerogels with high-performance for sorption of cationic dyes**. *Polymer*, **51**(16):3801–3807, 2010. 85

[236] R. C. Weatherwax and D. F. Caulfield. **Cellulose aerogels: an improved method for preparing a highly expanded form of dry cellulose**. *TAPPI (Technical Association of the Pulp and Paper Industry)*, **54**(6):985–986, 1971. 86

[237] R. Weatherwax. **Collapse of cell-wall pores during drying of cellulose**. *Journal of Colloid And Interface Science*, **62**(3):432–446, 1977. 86

[238] ME Smith and EH Finke. **Critical point drying of soft biological material for the scanning electron microscope**. *Investigative Ophthalmology & Visual Science*, **11**(3):127, 1972. 86

[239] R. Weatherwax and D. Caulfield. **The pore structure of papers wet stiffened by formaldehyde crosslinking II. Results from nitrogen sorption**. *Journal of Colloid And Interface Science*, **67**(3):506–515, 1978. 86

[240] J Innerlohinger, HK Weber, and G Kraft. **Aerocellulose: aerogels and aerogel-like materials made from cellulose**. *Macromol. Symp.*, **244**(1):126–135, 2006. 86, 89

[241] M Pääkkö, J Vapaavuori, R Silvennoinen, H Kosonen, M Ankerfors, T Lindström, LA Berglund, and O Ikkala. **Long and entangled native cellulose I nanofibers allow flexible aerogels and hierarchically porous templates for functionalities**. *Soft Matter*, **4**(12):2492–2499, 2008. 86

[242] Houssine Sehaqui, Michaela Salajková, Qi Zhou, and Lars A Berglund. **Mechanical performance tailoring of tough ultra-high porosity foams prepared from cellulose I nanofiber suspensions**. *Soft Matter*, **6**(8):1824–1832, 2010. 86, 88

[243] Sandra Hoepfner, Lorenz Ratke, and Barbara Milow. **Synthesis and characterisation of nanofibrillar cellulose aerogels**. *Cellulose*, **15**(1):121–129, 2008. 86, 87, 89, 99

[244] Hao Jin, Yoshiharu Nishiyama, Masahisa Wada, and Shigenori Kuga. **Nanofibrillar cellulose aerogels**. *Colloids and Surfaces A: Physicochemical and Engineering Aspects*, **240**(1-3):63–67, 2004. 86, 87

[245] Lindy Heath and Wim Thielemans. **Cellulose nanowhisker aerogels**. *Green Chemistry*, **12**(8):1448–1453, 2010. 86, 87, 88, 99

[246] Benoît J. C Duchemin, Mark P Staiger, Nick Tucker, and Roger H Newman. **Aerocellulose based on all-cellulose composites**. *Journal of Applied Polymer Science*, **115**(1):216–221, 2010. 86, 88

[247] C. Tan, B. Fung, J. Newman, and C. Vu. **Organic aerogels with very high impact strength**. *Adv. Mater.*, **13**(9):644–646, 2001. 87

[248] A Bisson, A Rigacci, D Lecomte, and P Achard. **Effective thermal conductivity of divided silica xerogel beds**. *Journal of Non-Crystalline Solids*, **350**:379–384, 2004. 87

[249] H. Maeda, M. Nakajima, T. Hagiwara, T. Sawaguchi, and S. Yano. **Preparation and properties of bacterial cellulose aerogel**. *Japanese Journal of Polymer Science and Technology*, **63**(2):135–137, 2006. 87, 88

[250] Matthew D Gawryla, Otto van den Berg, Christoph Weder, and David A Schiraldi. **Clay aerogel/cellulose whisker nanocomposites: a nanoscale wattle and daub**. *J. Mater. Chem.*, **19**(15):2118–2124, 2009. 88

[251] S Kuga. **The porous structure of cellulose gel regenerated from calcium thiocyanate solution**. *Journal of Colloid And Interface Science*, **77**(2):413–417, 1980. 89

[252] Roxane Gavillon and Tatiana Budtova. **Aerocellulose: New highly porous cellulose prepared from cellulose-NaOH aqueous solutions**. *Biomacromolecules*, **9**(1):269–277, 2008. 89, 99

[253] Romain Sescousse and Tatiana Budtova. **Influence of processing parameters on regeneration kinetics and morphology of porous cellulose from cellulose–NaOH–water solutions**. *Cellulose*, **16**(3):417–426, 2009. 89

[254] Meiling Deng, Qian Zhou, Anke Du, Johannes van Kasteren, and Yuzhong Wang. **Preparation of nanoporous cellulose foams from cellulose-ionic liquid solutions**. *Materials Letters*, **63**(21):1851–1854, 2009. 89, 99, 101

[255] H Kawaguchi. **Functional polymer microspheres**. *Progress in Polymer Science*, **25**(8):1171–1210, 2000. 89

[256] Xudong Shi, Lei Sun, Jian Jiang, Xiaolin Zhang, Wenjun Ding, and Zhihua Gan. **Biodegradable polymeric microcarriers with controllable porous structure for tissue engineering**. *Macromol. Biosci.*, **9**(12):1211–1218, 2009. 89

[257] Kyunga Na, Jaeyeon Jung, Jonghwan Lee, and Jinho Hyun. **Thermoresponsive pore structure of biopolymer microspheres for a smart drug carrier**. *Langmuir*, **26**(13):11165–11169, 2010. 89

[258] Quanchao Zhang, Jing Liu, Xiaojun Wang, Minxiong Li, and Jie Yang. **Controlling internal nanostructures of porous microspheres prepared via electrospraying**. *Colloid Polym Sci*, **288**(14-15):1385–1391, 2010. 89

[259] Yichen Cao, Bo You, and Limin Wu. **Facile fabrication of hollow polymer microspheres through the phase-inversion method**. *Langmuir*, **26**(9):6115–6118, 2010. 89

[260] EA Stefanescu. **Influence of key parameters on the morphology of ethylcellulose microcapsules prepared via room-temperature spray drying**. *Cellulose*, **17**(3):617–626, 2010. 89

[261] Gregory Glenn, Artur Klamczynski, Delilah Woods, BorSen Chiou, William Orts, and Syed Imam. **Encapsulation of plant oils in porous starch microspheres**. *J Agr Food Chem*, **58**(7):4180–4184, 2010. 89

[262] D Arcos, A López-Noriega, E Ruiz-Hernández, O Terasaki, and M Vallet-Regí. **Ordered mesoporous microspheres for bone grafting and drug delivery**. *Chem. Mater.*, **21**(6):1000–1009, 2009. 90

[263] TA Ostomel, Q Shi, CK Tsung, H Liang, and GD Stucky. **Spherical bioactive glass with enhanced rates of hydroxyapatite deposition and hemostatic activity**. *Small*, **2**(11):1261–1265, 2006. 90

[264] Yu Tang, Qi Zhang, Long Wang, Peng-Wei Pan, and Gang Bai. **Preparation of cellulose magnetic microspheres with "the smallest critical size" and their application for microbial immunocapture**. *Langmuir*, **26**(13):11266–11271, 2010. 90

[265] Young Song, Douglas Adler, Feng Xu, Emre Kayaalp, Aida Nureddin, Raymond Anchan, Richard Maas, and Utkan Demirci. **Vitrification and levitation of a liquid droplet on liquid nitrogen**. *Proceedings of the National Academy of Sciences*, **107**(10):4596–4600, 2010. 92

[266] S Park, JO Baker, ME Himmel, PA Parilla, and DK Johnson. **Cellulose crystallinity index: measurement techniques and their impact on interpreting cellulase performance**. *Biotechnology for Biofuels*, **3**(1):10, 2010. 93, 125

[267] HG Shirk and GA Greathouse. **Infrared spectra of bacterial cellulose**. *Anal Chem*, **24**(11):1774–1775, 1952. 95

[268] Yang Hu and Jeffrey Catchmark. **Formation and characterization of spherelike bacterial cellulose particles produced by Acetobacter xylinum JCM 9730 strain**. *Biomacromolecules*, **11**(7):1727–1734, 2010. 101

[269] P Gomez-Romero. **Hybrid organic-inorganic materials-in search of synergic activity**. *Adv. Mater.*, **13**(3):163–174, 2001. 109

[270] C Sanchez. **State of the art developments in functional hybrid materials**, Jan 2005. 109

[271] Peter Fratzl. **Biomimetic materials research: what can we really learn from nature's structural materials?** *Journal of The Royal Society Interface*, **4**(15):637–642, 2007. 109

[272] C Sanchez, H Arribart, and M Guille. **Biomimetism and bioinspiration as tools for the design of innovative materials and systems**. *Nature Materials*, **4**:277–288, 2005. 109

[273] R Lakes. **Materials with structural hierarchy**. *Nature*, **361**:511–515, 1993. 109

[274] Benedicte Lebeau and Plinio Innocenzi. **Hybrid materials for optics and photonics**. *Chem. Soc. Rev.*, 2011. 109

[275] D Avnir, T Coradin, O Lev, and J Livage. **Recent bio-applications of sol-gel materials**. *J. Mater. Chem.*, **16**(11):1013–1030, 2006. 109

[276] Dominik Eder. **Carbon NanotubeInorganic Hybrids**. *Chem Rev*, **110**(3):1348–1385, 2010. 109

[277] HB Yao, MR Gao, and SH Yu. **Small organic molecule templating synthesis of organic-inorganic hybrid materials: their nanostructures and properties**. *Nanoscale*, **2**(3):323–334, 2010. 109

[278] J Portier, JH Choy, and MA Subramanian. **Inoganic-organic-hybrids as precursors to functional materials**, 2001. 109

[279] C Sanchez, B Julián, P Belleville, and M Popall. **Applications of hybrid organic–inorganic nanocomposites**. *J. Mater. Chem.*, **15**(35-36):3559–3592, 2005. 109, 114

[280] C Sanchez, L Rozes, F Ribot, C Laberty-Robert, D Grosso, C Sassoye, C Boissiere, and L Nicole. **"Chimie douce": A land of opportunities for the designed construction of functional inorganic and hybrid organic-inorganic nanomaterials**. *Comptes rendus-Chimie*, **13**(1-2):3–39, 2010. 109

[281] J Wen and GL Wilkes. **Organic/Inorganic Hybrid Network Materials by the SolGel Approach**. *Chem. Mater*, **8**(8):1667–1681, 1996. 109

[282] RJP Corriu, A Mehdi, C Reyé, and C Thieuleux. **Control of coordination chemistry in both the framework and the pore channels of mesoporous hybrid materials**. *New Journal of Chemistry*, **27**(6):905–908, 2003. 110

[283] CT Kresge, ME Leonowicz, WJ Roth, JC Vartuli, and JS Beck. **Ordered mesoporous molecular sieves synthesized by a liquid-crystal template mechanism**. *Nature*, **359**(6397):710–712, 1992. 110

[284] GJ de AA Soler-Illia, C Sanchez, B Lebeau, and J Patarin. **Chemical strategies to design textured materials: from microporous and mesoporous oxides to nanonetworks and hierarchical structures**. *Chem. Rev*, **102**(11):4093–4138, 2002. 110

[285] S Mann, SL Burkett, SA Davis, CE Fowler, NH Mendelson, SD Sims, D Walsh, and NT Whilton. **Sol Gel Synthesis of Organized Matter**. *Chem. Mater*, **9**(11):2300–2310, 1997. 110

[286] Ciprian M. Cirtiu, Alexandre F. Dunlop-Brière, and Audrey Moores. **Cellulose nanocrystallites as an efficient support for nanoparticles of palladium: application for catalytic hydrogenation and Heck coupling under mild conditions**. *Green Chem.*, 2011. 110, 114, 115

[287] Tao Niu, Yuanqing Gu, and Jianguo Huang. **Luminescent cellulose sheet fabricated by facile self-assembly of cadmium selenide nanoparticles on cellulose nanofibres**. *J. Mater. Chem.*, **21**:651–656, 2011. 110, 111, 112, 113, 115, 146

[288] HS Barud, RMN Assunção, MAU Martines, J Dexpert-Ghys, RFC Marques, Y Messaddeq, and SJL Ribeiro. **Bacterial cellulose-silica organic-inorganic hybrids**. *Journal of Sol-Gel Science and Technology*, **46**(3):363–367, 2008. 110, 113, 115

[289] Thawatchai Maneerung, Seiichi Tokura, and Ratana Rujiravanit. **Impregnation of silver nanoparticles into bacterial cellulose for antimicrobial wound dressing**. *Carbohydrate Polymers*, **72**(1):43–51, 2008. 110, 113, 115

[290] Jinping Zhou, Ran Li, Shilin Liu, Qian Li, Linzhi Zhang, Lina Zhang, and Jianguo Guan. **Structure and magnetic properties of regenerated cellulose/Fe3O4 nanocomposite films**. *Journal of Applied Polymer Science*, **111**(5):2477–2484, 2009. 110, 114, 115

[291] Zhiming Liu, Mei Li, Lyudmila Turyanska, Oleg Makarovsky, Amalia Patanè, Wenjian Wu, and Stephen Mann. **Self-Assembly of Electrically Conducting Biopolymer Thin Films by Cellulose Regeneration in Gold Nanoparticle Aqueous Dispersions**. *Chem. Mater.*, **22**(8):2675–2680, 2010. 110, 114, 115

[292] Tiffany Abitbol and Derek Gray. **CdSe/ZnS QDs Embedded in Cellulose Triacetate Films with Hydrophilic Surfaces**. *Chem. Mater.*, **19**(17):4270–4276, 2007. 110

[293] Tiffany Abitbol and Derek Gray. **Incorporation into paper of cellulose triacetate films containing semiconductor nanoparticles**. *Cellulose*, **16**(2):319–326, 2009. 110

[294] IS Bayer, A Steele, PJ Martorana, E Loth, and L Miller. **Superhydrophobic cellulose-based bionanocomposite films from Pickering emulsions**. *Applied Physics Letters*, **94**(16):163902, 2009. 110, 115

[295] Ana Maria Ferraria, Sami Boufi, Nicolas Battaglini, Ana Maria Botelho Do Rego, and Manuel Reivilar. **Hybrid Systems of Silver Nanoparticles Generated on Cellulose Surfaces**. *Langmuir*, **26**(3):1996–2001, 2010. 110

[296] AN Generalova, SV Sizova, VA Oleinikov, VP Zubov, MV Artemyev, L Spernath, A Kamyshny, and S Magdassi. **Highly fluorescent ethyl cellulose nanoparticles containing embedded semiconductor nanocrystals**. *Colloids and Surfaces A: Physicochemical and Engineering Aspects*, **342**(1-3):59–64, 2009. 110, 116

[297] SH Hwang, CN Moorefield, P Wang, KU Jeong, SZD Cheng, KK Kotta, and GR Newkome. **Construction of CdS quantum dots via a regioselective dendritic functionalized cellulose template**. *Chem Commun*, (33):3495–3497, 2006. 110, 112, 145

[298] Xin Li, Shiyan Chen, Weili Hu, Shuaike Shi, Wei Shen, Xiang Zhang, and Huaping Wang. **In situ synthesis of CdS nanoparticles on bacterial cellulose nanofibers**. *Carbohydrate Polymers*, **76**(4):509–512, 2009. 110, 113, 114, 148

[299] Loan T. T Trinh, Anna-Lena Kjøniksen, Kaizheng Zhu, Kenneth D Knudsen, Sondre Volden, Wilhelm R Glomm, and Bo Nyström. **Slow salt-induced aggregation of citrate-covered silver particles in aqueous solutions of cellulose derivatives**. *Colloid Polym Sci*, **287**(12):1391–1404, 2009. 110

[300] A Kadib, K Molvinger, T Cacciaguerra, Mosto Bousmina, and Daniel Brunel. **Chitosan Templated Synthesis of Porous Metal Oxide Microspheres with Filamentary Nanostructures**. *Microporous and Mesoporous Materials*, 2010. 110, 115

[301] DS dos Santos, PJG Goulet, NPW Pieczonka, ON Oliveira, and RF Aroca. **Gold nanoparticle embedded, self-sustained chitosan films as substrates for surface-enhanced Raman scattering**. *Langmuir*, **20**(23):10273–10277, 2004. 110

[302] H Yao, Z Tan, H Fang, and Shu-Hong Yu. **Artificial nacrelike bionanocomposite films from the selfassembly of chitosan–montmorillonite hybrid building blocks**. *Angew. Chem. Int. Ed.*, **49**(52):10127–101131, 2010. 110, 115

[303] Rajeshwar. **Luminescence probe studies on naked and cadmium sulfide modified cellulose matrices**. *Langmuir*, **5**(1):255–260, 1989. 111, 114

[304] J He, T Kunitake, and A Nakao. **Facile in situ synthesis of noble metal nanoparticles in porous cellulose fibers**. *Chem. Mater*, **15**(23):4401–4406, 2003. 111, 112, 116

[305] Mohammad L. Hassan, Azza A. Ward, and Mahmoud A. Eid. **Mechanical, optical, and electrical properties of cellulosic semiconductor nanocomposites**. *Journal of Applied Polymer Science*, **115**(5):2847–2854, 2010. 111

[306] Yongsoon Shin, In-Tae Bae, Bruce W Arey, and Gregory J Exarhos. **Facile stabilization of gold-silver alloy nanoparticles on cellulose nanocrystal**. *J Phys Chem C*, **112**(13):4844–4848, 2008. 111, 112

[307] R El-Shishtawy, A Asiri, N Abdelwahed, and M Al-Otaibi. **In situ production of silver nanoparticle on cotton fabric and its antimicrobial evaluation**. *Cellulose*, **18**(1):75–82, 2010. 111

[308] Chunyang Zhu, Jianfeng Xue, and Junhui He. **Controlled In-Situ Synthesis of Silver Nanoparticles in Natural Cellulose Fibers Toward Highly Efficient Antimicrobial Materials**. *J. Nanosci. Nanotech.*, **9**(5):3067–3074, 2009. 111, 112

[309] X Chen, Y Liu, H Lu, H Yang, X Zhou, and J Xin. **In-situ growth of silica nanoparticles on cellulose and application of hierarchical structure in biomimetic hydrophobicity**. *Cellulose*, **17**(6):1103–1113, 2010. 111, 112

[310] Sonal Padalkar, J. R Capadona, S. J Rowan, C Weder, Yu-Ho Won, Lia A Stanciu, and Robert J Moon. **Natural Biopolymers: Novel Templates for the Synthesis of Nanostructures**. *Langmuir*, **26**(11):8497–8502, 2010. 112, 114, 142

[311] J Cai, S Kimura, M Wada, and S Kuga. **Nanoporous cellulose as metal nanoparticles support**. *Biomacromolecules*, **10**(1):87–94, 2009. 112, 114

[312] Y Sun, Y Yin, BT Mayers, T Herricks, and Y Xia. **Uniform silver nanowires synthesis by reducing AgNO3 with ethylene glycol in the presence of seeds and poly (vinyl pyrrolidone)**. *Chem. Mater.*, **14**(11):4736–4745, 2002. 112

[313] Karima Benaissi, Lee Johnson, Darren A Walsh, and Wim Thielemans. **Synthesis of platinum nanoparticles using cellulosic reducing agents**. *Green Chemistry*, **12**(2):220, 2010. 112, 115

[314] Paula Marques, Tito Trindade, and Carlos Neto. **Titanium dioxide/cellulose nanocomposites prepared by a controlled hydrolysis method**. *Composites Science and Technology*, **66**(7-8):1038–1044, 2006. 112

[315] Qi Xu, Melvin Tucker, Phil Arenkiel, Xin Ai, Garry Rumbles, Junji Sugiyama, Michael Himmel, and Shi-You Ding. **Labeling the planar face of crystalline cellulose using quantum dots directed by type-I carbohydrate-binding modules**. *Cellulose*, **16**(1):19–26, 2009. 112, 116

[316] J Tormo, R Lamed, A J Chirino, E Morag, E A Bayer, Y Shoham, and T A Steitz. **Crystal structure of a bacterial family-III cellulose-binding domain: a general mechanism for attachment to cellulose**. *EMBO J*, **15**(21):5739–51, 1996. 112

[317] Peng Zhang. **Investigation of Novel Quantum Dots/Proteins/Cellulose Bioconjugate Using NSOM and Fluorescence**. *Journal of Fluorescence*, **16**(3):349–353, 2006. 113, 116

[318] Weili Hu, Shiyan Chen, Xin Li, Shuaike Shi, Wei Shen, Xiang Zhang, and Huaping Wang. **In situ synthesis of silver chloride nanoparticles into bacterial cellulose membranes**. *Materials Science & Engineering C*, **29**(4):1216–1219, 2009. 113

[319] S Ifuku, M Tsuji, M Morimoto, H Saimoto, and H Yano. **Synthesis of Silver Nanoparticles Templated by TEMPO-Mediated Oxidized Bacterial Cellulose Nanofibers**. *Biomacromolecules*, **10**(9):2714–2717, 2009. 113

[320] Luiz Claudio de Santa Maria, Ana L C Santos, Philippe C Oliveira, Hernane S Barud, Younés Messaddeq, and Sidney J L Ribeiro. **Synthesis and characterization of silver nanoparticles impregnated into bacterial cellulose**. *Materials Letters*, **63**(9-10):797–799, 2009. 113

[321] Dayong Zhang and Limin Qi. **Synthesis of mesoporous titania networks consisting of anatase nanowires by templating of bacterial cellulose membranes**. *Chem. Commun.*, (21):2735–7, 2005. 113

[322] Jian Zeng, Shilin Liu, Jie Cai, and Lina Zhang. **TiO2 Immobilized in Cellulose Matrix for Photocatalytic Degradation of Phenol under Weak UV Light Irradiation**. *The Journal of Physical Chemistry C*, **114**(17):7806–7811, 2010. 114

[323] Chunyu Chang, Jun Peng, Lina Zhang, and Dai-Wen Pang. **Strongly fluorescent hydrogels with quantum dots embedded in cellulose matrices**. *J. Mater. Chem.*, **19**(41):7771, 2009. 114, 115, 116

[324] Dong Ruan, Qilin Huang, and Lina Zhang. **Structure and Properties of CdS/Regenerated Cellulose Nanocomposites**. *Macromol. Mater. Eng.*, **290**(10):1017–1024, 2005. 114, 115

[325] K Xie, Y Yu, and Y Shi. **Synthesis and characterization of cellulose/silica hybrid materials with chemical crosslinking**. *Carbohydrate Polymers*, **78**(4):799–805, 2009. 115

[326] TT Hien Pham, C Cao, and SJ Sim. **Application of citrate-stabilized gold-coated ferric oxide composite nanoparticles for biological separations**. *Journal of Magnetism and Magnetic Materials*, **320**(15):2049–2055, 2008. 114

[327] Ricardo J B Pinto, Paula A A P Marques, Carlos Pascoal Neto, Tito Trindade, Sara Daina, and Patrizia Sadocco. **Antibacterial activity of nanocomposites of silver and bacterial or vegetable cellulosic fibers**. *Acta Biomaterialia*, **5**(6):2279–2289, 2009. 114

[328] I Matsui. **Nanoparticles for electronic device applications: A brief review**. *Journal of chemical engineering of Japan*, **38**(8):535–546, 2005. 114

[329] J Yang, D Sun, J Li, X Yang, J Yu, Q Hao, W Liu, J Liu, Z Zou, and J Gu. **In situ deposition of platinum nanoparticles on bacterial cellulose membranes and evaluation of PEM fuel cell performance**. *Electrochimica Acta*, **54**(26):6300–6305, 2009. 114

[330] Umesh Kumar, Kusum Kumari, Shailesh Sharma, Mahesh Kumar, V Vankar, Rita Kakkar, and Vikram Kumar. **Role of surface modification of colloidal CdSe quantum dots on the properties of hybrid organic–inorganic nanocomposites**. *Colloid & Polymer Science*, **288**(8):841–849, 2010. 116

[331] KW Hu, FY Jhang, CH Su, and CS Yeh. **Fabrication of Gd2O(CO3)2.H2O/silica/gold hybrid particles as a bifunctional agent for MR imaging and photothermal destruction of cancer cells**. *J. Mater. Chem.*, **19**(15):2147–2153, 2009. 116

[332] N Gaylord. **A proposed new mechanism for catalyzed and uncatalyzed graft polymerization onto cellulose**. *Journal of Polymer Science Part C: Polymer Symposia*, **37**(1):153–172, 1972. 116, 117

[333] AY Kulkarni and PC Mehta. **Ceric ion-induced redox polymerization of acrylonitrile on cellulose**. *Journal of Applied Polymer Science*, **12**(6):1321–1342, 1968. 117

[334] JC Arthur, PJ Baugh, and O Hinojosa. **ESR study of reactions of cellulose initiated by the ceric ion method**. *Journal of Applied Polymer Science*, **10**(10):1591–1606, 1966. 117

[335] KC Gupta and S Sahoo. **Grafting of acrylonitrile and methyl methacrylate from their binary mixtures on cellulose using ceric ions**. *Journal of Applied Polymer Science*, **79**(5):767–778, 2001. 118

[336] Puja Goyal, Vineet Kumar, and Pradeep Sharma. **Graft copolymerization onto Tamarind Kernel Powder: Ceric(IV)-initiated graft copolymerization of acrylonitrile**. *Journal of Applied Polymer Science*, **114**(1):377–386, Oct 2009. 118

[337] J Turkevich. **A study of the nucleation and growth processes in the synthesis of colloidal gold**. *Discussions of the Faraday Society*, **11**, 1951. 118

[338] S Kumar, KS Gandhi, and R Kumar. **Modeling of Formation of Gold Nanoparticles by Citrate Method**. *Ind. Eng. Chem. Res*, **46**(10):3128–3136, 2007. 119

[339] Joerg Polte, T. Torsten Ahner, Friedmar Delissen, Sergey Sokolov, Franziska Emmerling, Andreas F Thuenemann, and Ralph Kraehnert. **Mechanism of Gold Nanoparticle Formation in the Classical Citrate Synthesis Method Derived from Coupled In Situ XANES and SAXS Evaluation**. *J Am Chem Soc*, **132**(4):1296–1301, 2010. 119

[340] Joseph B Schlenoff, Jayesh R Dharia, Hong Xu, Liqing Wen, and Ming Li. **Adsorption of thiol-containing copolymers onto gold**. *Macromolecules*, **28**(12):4290–4295, 1995. 119

[341] T. J. Lenk, V. M. Hallmark, J. F. Rabolt, L. Haeussling, and H. Ringsdorf. **Formation and Characterization of Self-Assembled Films of Sulfur-Derivatized Poly(methyl methacrylates) on Gold**. *Macromolecules*, **26**(6):1230–1237, 1993. 119, 120

[342] KG Marra, DDA Kidani, and EL Chaikof. **Cytomimetic biomaterials .2. In-situ polymerization of phospholipids on a polymer surface**. *Langmuir*, **13**(21):5697–5701, 1997. 120

[343] Robert Menzel, Michael Q Tran, Angelika Menner, Christopher W. M Kay, Alexander Bismarck, and Milo S. P Shaffer. **A versatile, solvent-free methodology for the functionalisation of carbon nanotubes**. *Chem Sci*, **1**(5):603–608, 2010. 120

[344] N Gaponik, DV Talapin, AL Rogach, K Hoppe, EV Shevchenko, A Kornowski, A Eychmuller, and H Weller. **Thiol-capping of CdTe nanocrystals: an alternative to organometallic synthetic routes**. *J Phys Chem B*, **106**(29):7177–7185, 2002. 120, 144, 146

[345] Andrey L Rogach, Thomas Franzl, Thomas A Klar, Jochen Feldmann, Nikolai Gaponik, Vladimir Lesnyak, Alexey Shavel, Alexander Eychmueller, Yuri P Rakovich, and John F Donegan. **Aqueous synthesis of thiol-capped CdTe nanocrystals: State-of-the-art**, 2007. 120, 122

[346] Beverly A Rzigalinski and Jeannine S Strobl. **Cadmium-containing nanoparticles: Perspectives on pharmacology and toxicology of quantum dots**. *Toxicology and Applied Pharmacology*, **238**(3):280–288, 2009. 122

[347] Per Stenstad, Martin Andresen, Bjørn Steinar Tanem, and Per Stenius. **Chemical surface modifications of microfibrillated cellulose**. *Cellulose*, **15**(1):35–45, Feb 2008. 124

[348] G Canche-Escamilla, JI Cauich-Cupul, E Mendizabal, JE Puig, H Vazquez-Torres, and PJ Herrera-Franco. **Mechanical properties of acrylate-grafted henequen cellulose fibers and their application in composites**. *Composites Part A: Applied Science and Manufacturing*, **30**(3):349–359, 1999. 124

[349] C Radhakumary, Prabha D Nair, C. P. Reghunadhan Nair, and Suresh Mathew. **Chitosan-comb-graft-polyethylene glycol monomethacrylate-Synthesis, characterization, and evaluation as a biomaterial for hemodialysis applications**. *Journal of Applied Polymer Science*, **114**(5):2873–2886, Dec 2009. 124, 126

[350] Zhenglong Wan, Zhouyi Xiong, Heling Ren, Yuanyuan Huang, Huaxi Liu, Hanguo Xiong, Yiqiang Wu, and Jian Han. **Graft copolymerization of methyl methacrylate onto bamboo cellulose under microwave irradiation**. *Carbohydrate Polymers*, Jan 2010. 126, 136

[351] XL Wang, Y Huang, J Zhu, YB Pan, R He, and YZ Wang. **Chitosan-graft poly (p-dioxanone) copolymers: preparation, characterization, and properties**. *Carbohydrate Research*, **344**(6):801–807, 2009. 126

[352] B. S Kaith and S Kalia. **Graft copolymerization of MMA onto flax under different reaction conditions: a comparative study**. *Express Polymer Letters*, **2**(2):93–100, 2008. 126

[353] DY Kim, Y Nishiyama, and S Kuga. **Surface acetylation of bacterial cellulose**. *Cellulose*, **9**(3):361–367, 2002. 128

[354] A Neira, M Tarraga, and R Catalan. **Degradation of acrylic acid-grafted cellulose in aqueous medium with radical initiators**. *Journal of the Chilean Chemical Society*, **53**:1399–1403, 2008. 128, 129

[355] CY Liang and RH Marchessault. **Infrared spectra of crystalline polysaccharides. II. Native celluloses in the region from 640 to 1700 cm. 1**. *Journal of Polymer Science*, **39**(135):269–278, 1959. 128, 129

[356] JC Arthur and O Hinojosa. **Oxidative reactions of cellulose initiated by free radicals**. *J Polym Sci Pol Sym*, (36):53–71, Jan 1971. 128

[357] George Socrates. *Infrared and Raman Characteristic Group Frequencies: Tables and Charts*. John Wiley and Sons, 3 edition, 2004. 129

[358] SH Yoon, HJ Jin, MC Kook, and YR Pyun. **Electrically conductive bacterial cellulose by incorporation of carbon nanotubes**. *Biomacromolecules*, **7**(4):1280–1284, Jan 2006. 131

[359] RR Navarro, K Sumi, and M Matsumura. **Improved metal affinity of chelating adsorbents through graft polymerization**. *Water Research*, **33**(9):2037–2044, Jan 1999. 131

[360] BR Nayak and RP Singh. **Synthesis and characterization of grafted hydroxypropyl guar gum by ceric ion induced initiation**. *European Polymer Journal*, **37**(8):1655–1666, 2001. 131

[361] D. S. Varma and Veena Narasimhan. **Thermal behavior of graft copolymers of cotton cellulose and acrylate monomers**. *Journal of Applied Polymer Science*, **16**(12):3325–3339, 1972. 133

[362] Kuisma Littunen, Ulla Hippi, Leena-Sisko Johansson, Monika Österberg, Tekla Tammelin, Janne Laine, and Jukka Seppälä. **Free radical graft copolymerization of nanofibrillated cellulose with acrylic monomers**. *Carbohydrate Polymers*, 2010. 133

[363] JA Creighton, CG Blatchford, and MG Albrecht. **Plasma resonance enhancement of Raman scattering by pyridine adsorbed on silver or gold sol particles of size comparable to the excitation wavelength**. *Journal of the Chemical Society, Faraday Transactions 2*, **75**:790–798, 1979. 138

[364] KC Grabar, RG Freeman, MB Hommer, and MJ Natan. **Preparation and Characterization of Au Colloid Monolayers**. *Anal Chem*, **67**(4):735–743, 1995. 138, 139

[365] Eunkeu Oh, Kimihiro Susumu, Ramasis Goswami, and Hedi Mattoussi. **One-Phase Synthesis of Water-Soluble Gold Nanoparticles with Control over Size and Surface Functionalities**. *Langmuir*, **26**(10):7604–7613, 2010. 138

[366] Layal L Rouhana, Jad A Jaber, and Joseph B Schlenoff. **Aggregation-resistant water-soluble gold nanoparticles**. *Langmuir*, **23**(26):12799–12801, 2007. 138, 139, 140

[367] JJ Storhoff, RC Mucic, and CA Mirkin. **Strategies for organizing nanoparticles into aggregate structures and functional materials**. *Journal of Cluster Science*, **8**(2):179–216, 1997. 138

[368] T Kim, K Lee, MS Gong, and SW Joo. **Control of gold nanoparticle aggregates by manipulation of interparticle interaction**. *Langmuir*, **21**(21):9524–9528, 2005. 138, 139

[369] J Kimling, M Maier, B Okenve, V Kotaidis, H Ballot, and A Plech. **Turkevich method for gold nanoparticle synthesis revisited**. *J. Phys. Chem. B*, **110**(32):15700–7, 2006. 138

[370] J Liao, Y Zhang, W Yu, L Xu, C Ge, J Liu, and N Gu. **Linear aggregation of gold nanoparticles in ethanol**. *Colloids and Surfaces A: Physicochemical and Engineering Aspects*, **223**:177–183, 2003. 139

[371] KH Su, QH Wei, X Zhang, JJ Mock, DR Smith, and S Schultz. **Interparticle coupling effects on plasmon resonances of nanogold particles**. *Nano Letters*, **3**(8):1087–1090, 2003. 139

[372] S Zhang, W Ni, X Kou, MH Yeung, L Sun, J Wang, and C Yan. **Formation of gold and silver nanoparticle arrays and thin shells on mesostructured silica nanofibers**. *Advanced Functional Materials*, **17**(16):3258–3266, 2007. 139

[373] Richard Hoogenboom. **Thiol-Yne Chemistry: A Powerful Tool for Creating Highly Functional Materials**. *Angew. Chem. Int. Ed.*, **49**(20):3415–3417, 2010. 152

[374] WJ Work, K Horie, M Hess, and RFT Stepto. **Definitions of terms related to polymer blends, composites, and multiphase polymeric materials (IUPAC recommendations 2004)**. *Pure Appl Chem*, **76**(11):1985–2007, 2004. 154

[375] LS Schadler, LC Brinson, and WG Sawyer. **Polymer nanocomposites: a small part of the story**. *JOM Journal of the Minerals, Metals and Materials Society*, **59**(3):53–60, 2007. 154

[376] V Favier, H Chanzy, and J Cavaille. **Polymer Nanocomposites Reinforced by Cellulose Whiskers**. *Macromolecules*, **28**(18):6365–6367, 1995. 155

[377] M Labet, W Thielemans, and A Dufresne. **Polymer grafting onto starch nanocrystals**. *Biomacromolecules*, **8**(9):2916–2927, 2007. 155

[378] W Thielemans, MN Belgacem, and A Dufresne. **Starch nanocrystals with large chain surface modifications**. *Langmuir*, **22**(10):4804–4810, 2006. 155

[379] W Helbert, J Cavaille, and A Dufresne. **Thermoplastic Nanocomposites Filled With Wheat Straw Cellulose Whiskers. Part I: Processing and Mechanical Behavior**. *Polym. Compos.*, **17**(4):604–611, 1996. 155

[380] Gilberto Siqueira, Houssein Abdillahi, Julien Bras, and Alain Dufresne. **High reinforcing capability cellulose nanocrystals extracted from Syngonanthus nitens (Capim Dourado)**. *Cellulose*, **17**(2):289–298, 2010. 155

[381] Gilberto Siqueira, Julien Bras, and Alain Dufresne. **Cellulose Whiskers versus Microfibrils: Influence of the Nature of the Nanoparticle and its Surface Functionalization on the Thermal and Mechanical Properties of Nanocomposites**. *Biomacromolecules*, **10**(2):425–432, 2009. 155, 180

[382] Leonardo E Millon, Ganesh Guhados, and Wankei Wan. **Anisotropic polyvinyl alcohol-Bacterial cellulose nanocomposite for biomedical applications**. *J. Biomed. Mater. Res.*, **86B**(2):444–452, 2008. 155

[383] Aji P Mathew, W Thielemans, and Alain Dufresne. **Mechanical properties of nanocomposites from sorbitol plasticized starch and tunicin whiskers**. *Journal of Applied Polymer Science*, **109**(6):4065–4074, 2008. 155

[384] Dagang Liu, Tuhua Zhong, Peter R Chang, Kaifu Li, and Qinglin Wu. **Starch composites reinforced by bamboo cellulosic crystals**. *Bioresource Technology*, **101**(7):2529–2536, 2010. 155

[385] K Oksman, A.P Mathew, D Bondeson, and I Kvien. **Manufacturing process of cellulose whiskers/polylactic acid nanocomposites**. *Composites Science and Technology*, **66**(15):2776–2784, 2006. 155

[386] KY Lee, JJ Blaker, and A Bismarck. **Surface functionalisation of bacterial cellulose as the route to produce green polylactide nanocomposites with improved properties**. *Composites Science and Technology*, **69**(15-16):2724–2733, 2009. 155, 157, 158

[387] Philippe Tingaut, Tanja Zimmermann, and Francisco Lopez-Suevos. **Synthesis and characterization of bionanocomposites with tunable properties from poly(lactic acid) and acetylated microfibrillated cellulose**. *Biomacromolecules*, **11**(2):454–464, 2010. 155, 179

[388] Aihua Pei, Qi Zhou, and Lars A Berglund. **Functionalized cellulose nanocrystals as biobased nucleation agents in poly(l-lactide) (PLLA) – Crystallization and mechanical property effects**. *Composites Science and Technology*, **70**(5):815–821, 2010. 155, 176

[389] L Jiang, E Morelius, J Zhang, M Wolcott, and J Holbery. **Study of the poly (3-hydroxybutyrate-co-3-hydroxyvalerate)/cellulose nanowhisker composites prepared by solution casting and melt processing**. *Journal of Composite Materials*, **42**(24):2629–2645, 2008. 155, 158, 177

[390] E Ten, J Turtle, D Bahr, L Jiang, and M Wolcott. **Thermal and Mechanical Properties of Poly (3-hydroxybutyrate-co-3-hydroxyvalerate)/cellulose nanowhiskers Composites**. *Polymer*, **51**:2652–2660, 2010. 155, 158, 177

[391] Cai Zhijiang, Yang Guang, and Jaehwan Kim. **Biocompatible nanocomposites prepared by impregnating bacterial cellulose nanofibrils into poly(3-hydroxybutyrate)**. *Current Applied Physics*, **11**(2):247–249, 2011. 155, 159, 161

[392] Cai Zhijiang and Yang Guang. **Optical nanocomposites prepared by incorporating bacterial cellulose nanofibrils into poly(3-hydroxybutyrate)**. *Materials Letters*, **65**(2):182–184, 2011. 155, 158

[393] Z Cai and J Kim. **Bacterial cellulose/poly (ethylene glycol) composite: characterization and first evaluation of biocompatibility**. *Cellulose*, **17**(1):83–91, 2010. 155

[394] Otto Van Den Berg, Michael Schroeter, Jeffrey R Capadona, and Christoph Weder. **Nanocomposites based on cellulose whiskers and (semi)conducting conjugated polymers**. *J. Mater. Chem.*, **17**(26):2746, 2007. 155

[395] Maria Peresin, Youssef Habibi, Justin Zoppe, Joel Pawlak, and Orlando Rojas. **Nanofiber Composites of Polyvinyl Alcohol and Cellulose Nanocrystals: Manufacture and Characterization**. *Biomacromolecules*, **11**(3):674–681, 2010. 155

[396] Y Habibi, AL Goffin, N Schiltz, E Duquesne, P Dubois, and A Dufresne. **Bionanocomposites based on poly (-caprolactone)-grafted cellulose nanocrystals by ring-opening polymerization**. *J. Mater. Chem.*, **18**(41):5002–5010, 2008. 155, 173, 179

[397] S Eichhorn, A Dufresne, M Aranguren, N Marcovich, J Capadona, S Rowan, C Weder, W Thielemans, M Roman, S Renneckar, W Gindl, S Veigel, J Keckes, H Yano, K Abe, M Nogi, A Nakagaito, A Mangalam, J Simonsen, A Benight, A Bismarck, L Berglund, and T Peijs. **Review: current international research into cellulose nanofibres and nanocomposites**. *Journal of Materials Science*, **45**(1):1–33, 2010. 155

[398] MA Hubbe, OJ Rojas, LA Lucia, and M Sain. **Cellulosic nanocomposites: A review**. *BioResources*, **3**(3):929–980, 2008. 155

[399] H Yano, J Sugiyama, AN Nakagaito, M Nogi, T Matsuura, M Hikita, and K Handa. **Optically transparent composites reinforced with networks of bacterial nanofibers**. *Adv. Mater.*, **17**(2):153–155, 2005. 156

[400] M Nogi, S Ifuku, K Abe, K Handa, AN Nakagaito, and H Yano. **Fiber-content dependency of the optical transparency and thermal expansion of bacterial nanofiber reinforced composites**. *Applied Physics Letters*, **88**:133124, 2006. 156

[401] M Nogi and H Yano. **Transparent nanocomposites based on cellulose produced by bacteria offer potential innovation in the electronics device industry**. *Adv. Mater.*, **20**(10):1849–1852, 2008. 156

[402] Eliane Trovatti, Lúcia Oliveira, Carmen S.R Freire, Armando J.D Silvestre, Carlos Pascoal Neto, José J.C Cruz Pinto, and Alessandro Gandini. **Novel bacterial cellulose-acrylic resin nanocomposites**. *Composites Science and Technology*, **70**(7):1148–1153, 2010. 156, 158

[403] N Lin, G Chen, J Huang, A Dufresne, and PR Chang. **Effects of polymer-grafted natural nanocrystals on the structure and mechanical properties of poly (lactic acid): A case of cellulose whisker-graft-polycaprolactone**. *Journal of Applied Polymer Science*, **113**(5):3417–3425, 2009. 156, 180

[404] EE Brown and MPG Laborie. **Bioengineering bacterial cellulose/poly (ethylene oxide) nanocomposites**. *Biomacromolecules*, **8**(10):3074–3081, 2007. 156

[405] Cristian J Grande, Fernando G Torres, Clara M Gomez, Omar P Troncoso, Josep Canet-Ferrer, and Juan Martínez-Pastor. **Development of self-assembled bacterial cellulose-starch nanocomposites**. *Materials Science and Engineering: C*, **29**(4):1098–1104, 2009. 157

[406] IMG Martins, SP Magina, L Oliveira, CSR Freire, AJD Silvestre, CP Neto, and A Gandini. **New biocomposites based on thermoplastic starch and bacterial cellulose**. *Composites Science and Technology*, **69**(13):2163–2168, 2009. 157, 158

[407] YZ Wan, H Luo, F He, H Liang, Y Huang, and XL Li. **Mechanical, moisture absorption, and biodegradation behaviours of bacterial cellulose fibre-reinforced starch biocomposites**. *Composites Science and Technology*, **69**(7-8):1212–1217, 2009. 157

[408] M Woehl, C Canestraro, and A Mikowski. . . . **Bionanocomposites of thermoplastic starch reinforced with bacterial cellulose nanofibres: Effect of enzymatic treatment on mechanical properties**. *Carbohydrate Polymers*, **80**(3):866–873, 2010. 157, 158

[409] SCM Fernandes, L Oliveira, CSR Freire, AJD Silvestre, CP Neto, A Gandini, and J Desbriéres. **Novel transparent nanocomposite films based on chitosan and bacterial cellulose**. *Green Chemistry*, **11**(12):2023–2029, 2009. 157, 158

[410] Y Kim, R Jung, H Kim, and H Jin. **Transparent nanocomposites prepared by incorporating microbial nanofibrils into poly(l-lactic acid)**. *Current Applied Physics*, **9**(1):S69–S71, 2009. 157

[411] F Quero, M Nogi, H Yano, K Abdulsalami, SM Holmes, BH Sakakini, and SJ Eichhorn. **Optimization of the Mechanical Performance of Bacterial Cellulose/Poly (l-lactic) Acid Composites**. *ACS Appl. Mater. Interfaces*, **2**(1):321–330, 2009. 157

[412] Liliana C. Tomé, Ricardo J. B. Pinto, Eliane Trovatti, Carmen S. R. Freire, Armando J. D. Silvestre, Carlos Pascoal Neto, and Alessandro Gandini. **Transparent bionanocomposites with improved properties prepared from acetylated bacterial cellulose and poly (lactic acid) through a simple approach**. *Green Chem.*, 2011. 157, 158, 182

[413] Y Habibi, LA Lucia, and OJ Rojas. **Cellulose nanocrystals: chemistry, self-assembly, and applications**. *Chem Rev*, **110**(6):3479–3500, 2010. 158, 159

[414] CSR Freire, AJD Silvestre, C Pascoal Neto, A Gandini, P Fardim, and B Holmbom. **Surface characterization by XPS, contact angle measurements and ToF-SIMS of cellulose fibers partially esterified with fatty acids**. *Journal of Colloid And Interface Science*, **301**(1):205–209, 2006. 158

[415] B Braun and JR Dorgan. **Single-Step Method for the Isolation and Surface Functionalization of Cellulosic Nanowhiskers**. *Biomacromolecules*, **10**(2):334–341, 2008. 158

[416] Ana Gisela Cunha and Alessandro Gandini. **Turning polysaccharides into hydrophobic materials: a critical review. Part 1. Cellulose**. *Cellulose*, **17**(5):875–889, 2010. 158, 159

[417] C Goussé, H Chanzy, G Excoffier, and L Soubeyrand. **Stable suspensions of partially silylated cellulose whiskers dispersed in organic solvents**. *Polymer*, **43**(9):2645–2651, 2002. 158

[418] C Gousse, H Chanzy, M Cerrada, and E Fleury. **Surface silylation of cellulose microfibrils: preparation and rheological properties**. *Polymer*, **45**(5):1569–1575, 2004. 158

[419] M Tabuchi, K Watanabe, Y Morinaga, and F Yoshinaga. **Acetylation of bacterial cellulose: Preparation of cellulose acetate having a high degree of polymerization**. *Biosci Biotech Bioch*, **62**(7):1451–1454, 1998. 158

[420] H Yuan, Y Nishiyama, M Wada, and S Kuga. **Surface acylation of cellulose whiskers by drying aqueous emulsion**. *Biomacromolecules*, **7**(3):696–700, 2006. 158

[421] G Morandi, L Heath, and W Thielemans. **Cellulose Nanocrystals Grafted with Polystyrene Chains through Surface-Initiated Atom Transfer Radical Polymerization (SI-ATRP)**. *Langmuir*, **25**(14):8280–8286, 2009. 158

[422] E Lasseuguette. **Grafting onto microfibrils of native cellulose**. *Cellulose*, **15**(4):571–580, 2008. 158

[423] M Tizzotti, A Charlot, E Fleury, M Stenzel, and J Bernard. **Modification of Polysaccharides Through Controlled/Living Radical Polymerization Grafting—Towards the Generation of High Performance Hybrids**. *Macromol. Rapid Commun.*, **31**:1751–1772, 2010. 158

[424] H Lönnberg, Q Zhou, H Brumer III, TT Teeri, E Malmström, and A Hult. **Grafting of Cellulose Fibers with Poly (-caprolactone) and Poly (l-lactic acid) via Ring-Opening Polymerization**. *Biomacromolecules*, **7**(7):2178–2185, 2006. 158, 173

[425] Thomas Gädda, Janne Kylmä, Jukka Tuominen, Hannu Mikkonen, Aki Laine, Soili Peltonen, and Jukka Seppälä. **Poly(-caprolactone)-grafted acetylated anhydroglucose oligomer by**

ring-opening polymerization—Synthesis and characterization. *Journal of Applied Polymer Science*, **100**(2):1633–1641, 2006. 158

[426] D Roy, JT Guthrie, and S Perrier. **RAFT Graft Polymerization of 2-(Dimethylaminoethyl) Methacrylate onto Cellulose Fibre**. *Australian Journal of Chemistry*, **59**(10):737–741, 2006. 158

[427] D Roy, JS Knapp, JT Guthrie, and S Perrier. **Antibacterial cellulose fiber via RAFT surface graft polymerization**. *Biomacromolecules*, **9**(1):91–99, 2007. 158

[428] S Philip, T Keshavarz, and I Roy. **Polyhydroxyalkanoates: biodegradable polymers with a range of applications**. *Journal of Chemical Technology & Biotechnology*, **82**(3):233–247, 2007. 159

[429] SY Lee. **Plastic bacteria? Progress and prospects for polyhydroxyalkanoate production in bacteria**. *Trends in Biotechnology*, **14**(11):431–438, 1996. 159

[430] Suchada Chanprateep. **Current trends in biodegradable polyhydroxyalkanoates**. *Journal of Bioscience and Bioengineering*, **110**(6):621–32, 2010. 159

[431] M. Lemoigne. **Products of dehydration and of polymerization of Beta-hydroxybutyric acid.** *Bull. Soc. Chem. Biol.*, **8**:770–782, 1926. 159

[432] RH Marchessault. **Polyhydroxyalkanoate (PHA) History at Syracuse University and Beyond**. *Cellulose*, **16**(3):357–359, 2009. 159

[433] AJ Anderson and EA Dawes. **Occurrence, metabolism, metabolic role, and industrial uses of bacterial polyhydroxyalkanoates.** *Microbiology and Molecular Biology Reviews*, **54**(4):450, 1990. 161

[434] RM Weiner. **Biopolymers from marine prokaryotes**. *Trends in Biotechnology*, **15**(10):390–394, 1997. 161

[435] T Keshavarz and I Roy. **Polyhydroxyalkanoates: bioplastics with a green agenda**. *Current Opinion in Microbiology*, **13**(3):321–326, 2010. 161

[436] M Zinn, B Witholt, and T Egli. **Occurrence, synthesis and medical application of bacterial polyhydroxyalkanoate**. *Adv Drug Deliv Rev*, **53**(1):5–21, 2001. 161

[437] M Koller, A Salerno, M Dias, A Reiterer, and G Braunegg. **Modern Biotechnological Polymer Synthesis: A Review**. *Food Technology and Biotechnology*, **48**(3):255–269, 2010. 161

[438] P Tian, L Shang, H Ren, Y Mi, D Fan, and M Jiang. **Biosynthesis of polyhydroxyalkanoates: Current research and development**. *African Journal of Biotechnology*, **8**(5):709–714, 2010. 161

[439] E Akaraonye, T Keshavarz, and I Roy. **Production of polyhydroxyalkanoates: the future green materials of choice**. *Journal of Chemical Technology & Biotechnology*, **85**(6):732–743, 2010. 161

[440] Yutaka Tokiwa and Buenaventurada P Calabia. **Review Degradation of microbial polyesters**. *Biotechnol Lett*, **26**(15):1181–1189, 2004. 161

[441] J Merrick and M Doudoroff. **Depolymerization of poly-beta-hydroxybutyrate by an intracellular enzyme system.** *The Journal of Bacteriology*, **88**(1):60–71, 1964. 161

[442] Nicholas Thomson, Ipsita Roy, David Summers, and Easan Sivaniah. **In vitro production of polyhydroxyalkanoates: achievements and applications**. *Journal of Chemical Technology & Biotechnology*, **85**(6):760–767, 2009. 161

[443] SF Williams, DP Martin, DM Horowitz, and OP Peoples. **PHA applications: addressing the price performance issue: I. Tissue engineering**. *International Journal of Biological Macromolecules*, **25**(1-3):111–121, 1999. 161

[444] XH Qu, Q Wu, J Liang, B Zou, and GQ Chen. **Effect of 3-hydroxyhexanoate content in poly (3-hydroxybutyrate-co-3-hydroxyhexanoate) on in vitro growth and differentiation of smooth muscle cells**. *Biomaterials*, **27**(15):2944–2950, 2006. 161

[445] J Araki, M Wada, and S Kuga. **Steric stabilization of a cellulose microcrystal suspension by poly(ethylene glycol) grafting**. *Langmuir*, **17**(1):21–27, 2001. 165

[446] Elisabeth Kloser and Derek Gray. **Surface Grafting of Cellulose Nanocrystals with Poly(ethylene oxide) in Aqueous Media**. *Langmuir*, **26**(16):13450–13456, 2010. 165

[447] L Heux, G Chauve, and C Bonini. **Nonflocculating and chiral-nematic self-ordering of cellulose microcrystals suspensions in nonpolar solvents**. *Langmuir*, **16**(21):8210–8212, 2000. 165

[448] MM de Souza Lima and R Borsali. **Rodlike cellulose microcrystals: Structure, properties, and applications**. *Macromol. Rapid Commun.*, **25**(7):771–787, 2004. 165

[449] J Lu, P Askeland, and LT Drzal. **Surface modification of microfibrillated cellulose for epoxy composite applications**. *Polymer*, **49**(5):1285–1296, 2008. 165

[450] Gilberto Siqueira, Julien Bras, and Alain Dufresne. **New Process of Chemical Grafting of Cellulose Nanoparticles with a Long Chain Isocyanate**. *Langmuir*, **26**(1):402–411, 2010. 165

[451] G Biresaw and CJ Carriere. **Correlation between mechanical adhesion and interfacial properties of starch/biodegradable polyester blends**. *J. Polym. Sci. B Polym. Phys.*, **39**(9):920–930, 2001. 173

[452] Youssef Habibi and Alain Dufresne. **Highly Filled Bionanocomposites from Functionalized Polysaccharide Nanocrystals**. *Biomacromolecules*, **9**(7):1974–1980, 2008. 173, 179

[453] David Viet, Stephanie Beck-Candanedo, and Derek G Gray. **Dispersion of cellulose nanocrystals in polar organic solvents**. *Cellulose*, **14**(2):109–113, 2007. 174

[454] S Wong, R Shanks, and A Hodzic. **Properties of poly (3-hydroxybutyric acid) composites with flax fibres modified by plasticiser absorption**. *Macromol. Mater. Eng.*, **287**(10):647–655, 2002. 177

[455] M Roohani, Y Habibi, NM Belgacem, G Ebrahim, AN Karimi, and A Dufresne. **Cellulose whiskers reinforced polyvinyl alcohol copolymers nanocomposites**. *European Polymer Journal*, **44**(8):2489–2498, 2008. 179

[456] AP Bonartsev, VL Myshkina, DA Nikolaeva, EK Furina, TA Makhina, VA Livshits, AP Boskhomdzhiev, EA Ivanov, AL Iordanskii, and GA Bonartseva. **Biosynthesis, biodegradation, and application of poly (3-hydroxybutyrate) and its copolymers-natural polyesters produced by diazotrophic bacteria**. *Communicating Current Research and Educational Topics and Trends in Applied Microbiology, Ed: A. Méndez-Vilas, Formatex, Spain*, **1**:295–307, 2007. 184

[457] GQ Chen and Q Wu. **The application of polyhydroxyalkanoates as tissue engineering materials**. *Biomaterials*, **26**(33):6565–6578, 2005. 184